Numerical Simulation of Binary Black Hole Spacetimes and a Novel Approach to Outer Boundary Conditions

Von der Fakultät für Mathematik und Physik
der Gottfried Wilhelm Leibniz Universität Hannover
zur Erlangung des Grades
Doktorin der Naturwissenschaften
– Dr. rer. nat. –
genehmigte Dissertation
von

Jennifer Seiler

geboren am 5. Mai, 1983 in Washington, DC, USA

●

· 2010 ·

Referent: Prof. Bernard Schutz, *Institut für Gravitationsphysik*
Koreferent: Prof. Jeffrey Winicour, *University of Pittsburgh*
Tag der Promotion: 5. Februar, 2010

Dedicated to Thomas Radke.

He had a rare combination of brilliance, character, and humility. Both the scientific community and society are handicapped by his loss.

Abstract

With ground-based gravitational wave detectors at design sensitivity, and a space-based detector in planning stages, the need for accurate gravitational wave templates for signal recognition by detector pipelines has become an urgent problem. With that in mind, and the fact that binary black hole inspirals and mergers are the strongest potential source for gravitational wave signals for online detectors, my research has focused on improving the accuracy and well-posedness of numerical simulations, and on the generation of gravitational waveforms from numerical simulations both for detector template generation and for astrophysical predictions.

For simulations of highly dynamical relativistic vacuum space-times I derived accurate and well-posed formulations of the Einstein equations for numerical evolutions. I herein propose a set of well-posed, constraint-preserving boundary conditions for artificial boundaries for a first order in time and second order in space 'generalized harmonic' formulation of the Einstein equations. I tested these conditions both for black hole space-times and for a series of robust stability tests, and show that these conditions reduce noise, reduce constraint violation, and increase stability for relativistic simulations. Additionally, I propose novel, well-posed, constraint-preserving boundary conditions for the more commonly used BSSN evolution system for standard "$1 + \log$" and Gamma-driver gauge conditions.

I carried out numerical evolutions of symmetric and asymmetric binary black hole mergers in large numbers to explore the parameter space of binary black hole inspirals and derive a statistical and phenomenological view of the physical qualities of binary merger remnants. I ran binary black hole inspiral simulations using both quasi-circular and post-Newtonian derived initial orbital binary inspiral parameters, and "puncture" initial data, and extracted physics from a number of initial data sequences in order to establish bounds on phenomenological formulae for the final spin and recoil velocity of merged black holes from arbitrary initial data parameters.

With the data from those parameter studies we focus on gravitational-wave emission to quantify how much spin effects contribute to the signal-to-noise ratio and to the relative event rates for the representative ranges in masses and detectors. I show that equal-spin binaries with maximum spin aligned with the orbital angular momentum are more than "three times as loud" as the corresponding binaries with anti-aligned spins. Finally, we derive a simple expression for the energy radiated in gravitational waves and find that the binaries have efficiencies $E_{\rm rad}/M$ between 3.6% and 10%.

Finally, I present an analytical inspiral-merger-ringdown gravitational waveforms from black-hole (BH) binaries with non-precessing spins by matching a post-Newtonian description of the inspiral to our numerical calculations, we obtain a waveform family with a conveniently small number of physical parameters. These waveforms will allow us to detect a larger parameter space of BH binary coalescence, to explore various scientific questions related to GW astronomy, and could dramatically improve the expected detection rates of GW detectors.

Keywords: boundary conditions, binary black holes, numerical relativity

Zusammenfassung

Da heutige erdgebundene Gravitationswellendetektoren ihre Designsensitivität erreicht haben und weltraumgestützte Detektoren in der Planungsphase sind, ist es notwendig, genaue Gravitationswellenschablonen zwecks Signalerkennung in den Detektor-Pipelines zur Verfügung zu haben. Mit dieser Problemstellung im Hinterkopf, und der Tatsache, daß binäre Schwarzlochverschmelzungsprozesse potentiell die stärksten Quellen gravitativer Strahlung für derzeit operierende Detektoren darstellt, hat sich meine Forschung dadrauf konzentriert, die Genauigkeit und korrekte Stellung numerischer Simulationen zu verbessern, sowie gravitative Wellenformen durch numerische Simulationen für Detektorschablonenerzeugung und astrophysikalische Vorhersagen zu berechnen.

Für Simulationen hochdynamischer, relativistischer Vakuumraumzeiten habe ich genaue und korrekt gestellte Formulierungen der Einsteingleichungen für numerische Evolutionen hergeleitet. Hierbei entwerfe ich einen Satz korrekt gestellter, zwangsbedingungserfüllender Randbedingungen für künstliche Ränder und für eine "generalisierte harmonische" Formulierung der Einsteingleichungen erster Ordnung in der Zeit und zweiter Ordung im Raum. Verschiedene Tests an Schwarzlochraumzeiten und Stabilitätstests zeigen, daß diese Bedingungen numerisches Rauschen und Verletzungen der Zwangsbedingungen reduzieren, sowie die Stabilität erhöhen. Desweiteren entwickele ich neue korrekt gestellte, zwangbedingungserfüllende Randbedingungen für das weitverbreitete BSSN Evolutionssystem mit der "1+log" Gamma-Treiber Eichbedingung.

Ich habe eine große Anzahl numerischer Evolutionen symmetrischer und asymmetrischer Schwarzlochverschmelzungen durchgeführt, um den Parameterraum zu untersuchen, und um eine statistische und phänomenologische Ansicht physikalischer Größen des verschmolzenen schwarzen Loches zu erhalten. Ich habe Simulationen von Binärsystemen mit quasi-zirkulären und post-Newtonisch abgeleiteten orbitalen Punktions-Anfangsparametern durchgeführt, und habe phänomenologische Formeln für den finalen Spin und Rückstoß des verschmolzenen schwarzen Loches für beliebige Anfangsdaten bestimmt.

Desweiteren habe ich mich mit den Daten dieser Parameterstudien auf deren gravitative Wellenemission konzentriert, um den Effekt von Spin auf das Signal-zu-Rausch Verhältnis und relativen Ereignisraten für verschiedene Massen und Detektoren zu bestimmen. Ich zeige, daß Binärsysteme mit gleichem und maximal ausgerichteten Spin mehr als dreimal "lauter" sind, als entsprechende Systeme mit anti-ausgerichtetem Spin. Zudem leite ich einen einfachen Ausdruck für die abgestrahlte Energie in Gravitationswellen her, und zeige, daß eine Effizienz zwischen 3.6% und 10% in $E_{\rm rad}/M$ erreicht werden kann.

Zuletzt präsentiere ich eine Familie analytischer und vollständiger Wellenformen für Binärsysteme mit nicht-präzedierendem Spin, die mit einem hinreichend kleinen Satz an freien physikalischen Parametern auskommt. Um dies zu erreichen, habe ich post-Newtonische Wellenformen an numerisch berechnete angepasst. Diese Wellenformen werden es ermöglichen, einen großen Bereich des Schwarzloch-Parameterraums aufzuspühren, verschiedene Aspekte der Gravitationswellenastronomie zu beantworten, und die Detektionsraten erheblich zu verbessern.

Schlagworte: Randbedingungen, Schwarzlochverschmelzungen, Numerisches Relitivität

Contents

Acknowledgments **ix**

List of Figures **xi**

List of Tables **xxvi**

1 Introduction **1**

2 Background **5**

2.1 General Relativity and Gravitational Waves 6

2.2 Numerical Relativity 8

2.3 Decomposing the Einstein Equations 10

2.3.1 The ADM decomposition 11

2.3.2 The BSSNOK Formulation 13

2.3.3 The Harmonic Formulation 16

2.4 Initial Data 19

2.4.1 Time Symmetric Schwarzschild 20

2.4.2 Brill-Lindquist Data 21

2.4.3 Excision 22

2.4.4 Punctures 23

2.5 Numerical Methods and Implementation 26
    2.5.1 The Finite Difference Approximation 26
    2.5.2 Method of Lines 28
    2.5.3 Numerical Dissipation 31
2.6 Simulation Physics 31
    2.6.1 Apparent Horizon Finder 32
    2.6.2 Isolated Horizon Finder 34
    2.6.3 Gravitational Wave Extraction 35
    2.6.4 Proving Well-posedness 44
    2.6.5 Boundary Conditions 46
2.7 Running Numerical Simulations 50
    2.7.1 Cactus and Carpet 51
2.8 Outline of Thesis 52
    2.8.1 Units and Notation 52

3 Boundary conditions 55

3.1 Boundaries for the Harmonic Formulation 56
    3.1.1 Discretization 57
    3.1.2 Finite Differencing 60
    3.1.3 Summation By Parts 62
    3.1.4 Well-posed Boundary Conditions 63
    3.1.5 Constraint-Preservation 67
    3.1.6 Results 68
    3.1.7 Discussion 81

3.2 ADM -BSSN 82
3.2.1 Boundary Conditions for the BSSN System 84
3.2.2 Propagation of the Constraints 87
3.2.3 Propagation of the Weyl Curvature 89
3.2.4 Propagation of Lapse and Shift 94
3.2.5 Numerical Implementation 96
3.2.6 Discussion 97

4 Physics from Numerical Simulations 99

4.1 Simulations 100
4.1.1 Initial data 104
4.1.2 Convergence tests 107
4.2 Kicks 113
4.2.1 Kick measurements via Ψ_4 115
4.2.2 Kick measurements via gauge-invariant perturbations 117
4.2.3 Results 119
4.2.4 Initial transients in the waveforms 122
4.2.5 Recoil velocities 126
4.2.6 Mode contributions to the recoil velocity 131
4.2.7 Angular Momentum and Mass Conservation 131
4.3 Spins 137
4.3.1 Methods and Results 138
4.3.2 Results 142
4.3.3 Discussion 151

5 Gravitational Wave Detector Data Analysis 157

5.1 Detectability 158

5.1.1 Numerical Setup and Initial Data 161

5.1.2 NR waveforms 161

5.1.3 Matching PN and NR waveform amplitudes 163

5.1.4 Radiated Energy 166

5.1.5 SNR, Horizon Distances and Event Rates 167

5.1.6 Results 168

5.1.7 Influence of higher ℓ-modes 172

5.1.8 Match between different models 174

5.1.9 Accuracy of NR waveform amplitudes 177

5.1.10 SNR Fits 180

5.1.11 Radiated Energy Fits 182

5.1.12 Discussion 186

5.2 Spin Templates 187

5.2.1 Numerical simulations 188

5.2.2 Constructing hybrid waveforms 189

5.2.3 Efficiency of non-spinning IMR templates to search for binaries with non-precessing spins 190

5.2.4 Waveform templates for non-precessing binaries 191

5.2.5 Efficiency of the new templates 192

5.2.6 Discussion 194

6 Conclusions 197

6.1 Boundary Conditions 197

6.2 Physics 198

6.3 Analysis 200

A Appendix 203

A.1 Well-posed boundary terms with SAT 203

A.1.1 Second Derivatives 204

A.1.2 Wave Equation in Flat Space 205

A.1.3 Wave Equation in General 206

A.2 Proper Boundaries for Harmonic 208

A.3 Constraint Preserving Boundary Conditions 210

A.4 On the convergence tests 211

A.5 Details on the extraction of Ψ_4 211

A.6 A comparison of wave-extraction methods 214

A.7 On the influence of orbital eccentricity 216

A.8 Sensitivity curves 217

Bibliography 217

Curriculum Vitae 231

Acknowledgments

I have felt extremely privileged to have been able to perform my doctoral studies at the Albert Einstein Institute. I am forever indebted to the Max-Planck Society and the Max-Planck-Institut für Gravitationsphysik as a whole for its support in terms of funding, facilities, and commitment to quality research and collaboration. I am grateful to the director of the Astrophysical Relativity division of the institute, Bernard Schutz for his support and guidance throughout this process. I am especially indebted to the group leader of my numerical relativity group, Luciano Rezzolla. He has always tried to help me not only along the process of obtaining a Ph.D. and on a personal level, but also with a view on my career as a whole. He was always supportive of getting my name known to the community and encouraged me to present my work at every conference and workshop that gave me the opportunity. He has always shown patience with my stubborn independence, and indulged my personal ideas for research directions, which may have been occasionally separate from the group's research directions.

The biggest privilege from being at the Albert Einstein Institute has not been the computer resources or facilities, but the people that my position at the institute has allowed me to communicate and collaborate with these past four years. I have had the benefit of consulting with some of the greatest minds in the field. I am very lucky to have been able to work closely with researchers like Bela Szilagyi, Denis Pollney, Sascha Husa, Erik Schnetter, Mark Hannam, Dario Nuñez, Nils Dorband, and Peter Diener. I am especially grateful to Bela, Denis, and Sascha, who have been inordinately magnanimous with their time and patience to help me in my research and daily endeavors.

I am very lucky to have been able to work with and know Thomas Radke, who we recently lost. Any problem anyone had related to the code or the computer clusters, he was quick to find an answer, and never seemed bothered to help. He was a brilliant programmer, an eager and curious learner, and an amazing human being. He will be missed and never forgotten.

I would also like to thank our cluster administrator, Nico Budewitz. He somehow managed to be a student and a double-time employee as administrator, despite his part-time title. He seemed ready to quickly respond to cluster issues 24 hours a day, 7 days a week. He was always helpful and patient with new users, always eager to find efficient and optimal ways to run the cluster, and tried to meet all users' needs as best as possible.

Much credit is due to my fellow students these past four years: Christian Reisswig, Lucia Santamaria, Tilman Vogel, Michaela Chirvasa, Filippo Galeazzi, and Anil Zenginoglu. Their support, encouragement, translation skills, fruitful discussion and helpful input both scientific and administrative has been invaluable throughout this process. Their curiosity, commitment, and eagerness for scientific discussion and discovery has been an inspirational and motivational force for me.

This thesis would not have been possible without the direction of Saul Teukolsky who set me on the path to numerical relativity and supported me with personal, scientific, and professional advice throughout my undergraduate studies. Without him, I would never have found the Albert Einstein Institute, or had the opportunity to visit and fall in love with it the summer before I left Cornell.

I would also like to support Katarina Henke, Dörte Bänge, and Ute Schlichting for helping me get through all of the administrative muddle required for me to live and work in Germany and submit and defend this Ph.D. thesis.

Finally, I am grateful to my mother and father, Steven and Gretchen Seiler. They have never ceased to believe in me, and never wavered in their support of my every decision, even to move half a world away from them. They have been a constant source inspiration to me, and I only hope I can live to be half the human beings that they each are. I also want to thank my brother, Geoffrey. He has always told his friends and acquaintances that I am some genius cosmologist solving the Universe, and their interest and excitement has always been a reminder to me that no matter how few people read this thesis, the world does care, and the work does make a difference.

JENNIFER SEILER

Max-Planck-Institut für Gravitationsphysik,
Potsdam, GERMANY
June 2009

> *Friendship is unnecessary, like philosophy, like art …It has no survival value; rather it is one of those things that give value to survival…*
>
> C.S. Lewis

List of Figures

2.1 The effect of gravitational waves on a ring of particles. The wave propagation is perpendicular to the ring. The top row shows the effect of the wave + polarized, while the bottom row shows the effect of × polarization. 6

2.2 A spacetime diagram illustrating the definition of the lapse function α and the shift vector β^a. 11

2.3 A diagram illustrating the various described methods of initial data formulation. Image (a) represents the $N + 1$ sheet description from of Brill-Lindquist data and the puncture approach; image (b) represents Misner data and the Bowen-York solution, and image (c) represents Misner's wormhole solution. 24

2.4 A diagram illustrating a cross-section of a 3-coordinate shape (the curvy line) which is not Strahlkörper about the local coordinate origin (the central point). The arrows show rays from the origin which intersect the shape more than once. 32

2.5 A diagram illustrating the use or artificial time-like outer boundaries, Ω in spacelike slices of the evolution domain, Σ. 46

3.1 The evolution of ϕ for flat-space wave equations with a constant shift in the x-direction. As initial data I have used a spherical Gaussian pulse of amplitude 1.0 and width 1.0, on a grid 8 (121 grid points) units in size. Thin lines are the Sommerfeld-type boundary conditions without the SAT terms applied, whereas thick lines use the SAT boundary treatment given by Eq. (3.49). 69

3.2 The same as in Fig. 3.1 but shown in a logarithmic scale for $||\Phi_{00}||_\infty$ and on a longer timescale. Note that standard Sommerfeld boundary conditions are unstable for $|\beta^i| > 1$. 70

3.3 The L_2-norm of the Hamiltonian constraint for a Teukolsky wave, comparing my constraint-preserving boundary conditions with the standard non-SBP Sommerfeld conditions, as well as the purely Sommerfeld SAT algorithm to ensure well-posedness. The boundaries for this simulation are at a radius of 7M from the center of initial Gaussian pulse. 71

3.4 The L_2-norm of the harmonic constraints for a Brill wave of amplitude 0.5, comparing constraint-preserving boundary conditions with the standard Sommerfeld conditions, as well as the purely Sommerfeld SAT algorithm to ensure well-posedness. The boundaries in these simulations are also at a radius of 7M from the center. 73

3.5 The tt component of the metric for a Brill wave of amplitude $a = 0.5$, comparing constraint-preserving boundary conditions with the standard Sommerfeld conditions. The above plot shows a two-dimensional cut in the xy plane at various times. On the right is the evolution of the Brill wave with constraint-preserving SAT and on the left is the same simulation but with standard Sommerfeld type boundary conditions. 75

3.6 Evolution of Q^{00} component of the harmonic data for a Brill wave perturbed by random noise of a kernel amplitude of $\epsilon \pm 0.075$, over all the grid points. This is placed on top of Brill wave initial data with an amplitude of $a = 0.5$. 76

3.7 Evolution of the L_2-norm of the harmonic constraints for a Brill wave ($a = 0.5$) perturbed by a checkerboard noise pattern of amplitude $\epsilon \pm 0.1$, over all the grid points, in order to excite the highest frequency grid mode. 77

3.8 The infinity norm of the error in $\tilde{g}_{xx}$ relative to the exact solution, $\mathcal{E}$, for 2D shifted gauge wave simulations with amplitude $A = 0.01$, $d = 2$, and boundary width $x, y \in [-7, 7]$. The resolutions presented here are $dx, dy = 0.05, 0.1, 0.2$ doubled relative to the next lowest resolution. The solution with standard boundary conditions blows up at early times and is shown as the dashed line with $dx = 0.1$. 78

3.9 The L_2-norm of the harmonic constraints for a head-on collision of two black holes each of mass $0.5M$ starting from an initial separation of $3M$ and with boundaries at $144M$, comparing constraint-preserving boundary conditions with the standard Sommerfeld conditions. 80

3.10 The $\ell = 2, m = 0$ component of the Zerilli scalar for the extracted gravitational radiation for a head-on collision of two black holes each of mass $0.5M$ starting from an initial separation of $3M$ and with boundaries at $144M$, comparing constraint-preserving boundary conditions with the standard Sommerfeld conditions. 80

4.1 Position in the (a_1, a_2) space of the five sequences r, ra, s, t, and u for which the inspiral and merger has been computed. 102

4.2 The L_∞ norm of the Einstein tensor Eq. (4.19) as a function of time. During the periods of strong dynamics (*i.e.*, when the time derivatives of the evolution variables are large) the convergence order is dominated by the accuracy of the time-interpolation algorithm used at mesh refinement boundaries, thus yielding third-order accuracy. At the times when these time-derivatives are small, the fourth-order finite-differencing algorithm becomes the dominant source of the error. Note that the very large violations (of $\mathcal{O}(300)$ at the medium resolution) are confined to a *single* grid point on the trailing edge of the apparent horizon and are produced by the very steep gradients in the shift. As discussed later, this does not affect the fourth-order convergence of the waveforms. At the time of the merger a common apparent horizon forms and its excision from the calculation of the L_∞ norm is responsible for the drop in the violation. 109

4.3 Convergence of the fiducial waveform Q^+_{22} for the binary system $r0$ before and after the time-shift defined in Eqs. (A.38)–(A.40). In the upper graph we show the difference between Q^+_{22} when computed at different resolutions, scaled for fourth-order convergence and using raw data (*i.e.*, without time-shifting). The overlap between the curves is rather poor indicating an over-convergence (*i.e.*, the truncation error appears to be smaller than expected). In the lower panel we show the same data but after time-shifting. The very good overlap of the scaled curves on the indicates that the time-shifting is essential for obtaining properly scaling differences between runs of various resolutions. 112

4.4 Accuracy of the fiducial waveform Q^+_{22} for the binary system $r0$. In the upper graph we show the waveforms at the three different resolutions: very-high (continuous line), high (dashed line), medium (dotted line). The accuracy is very good already with the lowest resolution and the curves cannot be distinguished. The lower panels show magnifications of some relevant portions of the waveform, with the lower-left panel concentrating on the initial transient radiation produced by the truncation error. The lower-right panel, on the other hand, refers to the quasi-normal ringing and shows that it is well-captured at all resolutions. 113

4.5 Amplitude of $r_{\rm E,sch}|\Psi_4|$ for extraction spheres at $r_{\rm E} = 30\,M$, $40\,M$, $50\,M$ and $60\,M$, demonstrating that Ψ_4 does indeed fall off as required by the peeling property. There is a slight decrease in amplitude with larger radius, suggesting that dissipative effects may become important at larger radii. Results in this paper use waveforms from the $r_{\rm E} = 50\,M$ extraction sphere, unless indicated otherwise. 116

4.6 Recoil velocity as function of time for a binary system of nonspinning black holes with a mass ratio of $2/3$ at an initial separation $4.1\,M$. The set of curves *(a)* and *(b)* differ in the choice of the integration constant, while the solid and dashed lines show the two independent computations of the momentum flux [eqs. (4.29) and (4.36)]. 120

4.7 Recoil velocity as function of time for the sequence of runs *i.e.,* from $r0$ with $-a_1 = a_2 = 0.586$, to r4 with $a_1 = 0, a_2 = 0.586$). Note that the merger is delayed for smaller values of $|a_1|$. 120

4.8 The recoil velocity of the binary $r0$ is compared to those of the same system but with either a larger or a smaller initial separation (*i.e.,* $r0l$ and $r0s$, respectively). Note the same recoil velocity is obtained when the integration constant is properly taken into account, while an error as large as $\sim 13\%$ is made otherwise. 121

4.9 Kick velocities and error bars for different spin ratios; the dashed lines show a linear fit of all the data when the point at $a_1/a_2 = 1$ is given an infinite weight since $|v|_{\rm kick} = 0$ for $a_1 = a_2$. 122

4.10 *Left panel:* Evolution in velocity space of the recoil-velocity vector. Very little variation is recorded before the radiation reaches the observer at $r_{\rm E} = 50\,M$ (dotted lines in the two insets). The absence of the proper linear momentum in the initial data triggers a rapid and an almost straight-line motion (dashed line) of the center of the spiral away from the origin of coordinates during the initial stages of the evolution. After this transient motion, the evolution is slower, with the spiral progressively opening up (solid line). The vector to the center of the spiral corresponds to the initial linear momentum of the spacetime and is used as integration constant for Eqs. (4.29) and (4.36). The final part of the evolution is characterized by a change in the spiral pattern (long-dashed line) as a result of the interaction of different modes in the ringdown of the final black hole. Note that the figure has been rotated clockwise of about 30° to allow for the two insets. *Right panel:* Initial behavior of the recoil velocity (upper graph) and of the waveform (Q^+_{22}) for model $r0$ (lower graph). This figure should be compared with the initial vector evolution of the recoil velocity shown in the left panel where the same types of lines have been used for the different stages of the evolution. 124

4.11 *Left panel:* The same as in the left panel of Fig. 4.10 but for system $r7$. Shown in the inset is the sudden re-orientation of the recoil velocity vector during ringdown and corresponding to a new spiral with different aperture (long-dashed line). Although more pronounced in $r7$, the appearance of this “hook” at ringdown is seen all the members of the sequence. *Right panel:* The same as in the left panel of Fig. 4.10 but for system $r7$. The upper graph concentrates on the final stages of the evolution in of the recoil velocity and on the appearance of a second peak during ringdown (long-dashed curve). The lower graph shows the same but in terms of the Q^{+}_{22} waveform. A discussion of these final stages of the evolution is made in Sect. 4.2.6. 125

4.12 *Left panel:* Recoil velocity as a function of the spin asymmetry parameter a_1/a_2 for the models listed in Table 4.1. Indicated with a continuous lines are the results obtained via Ψ_4, while a dashed line is used for the gauge-invariant quantities $Q^{+,\times}_{\ell m}$. *Right panel:* Final recoil velocity calculated with both the use Ψ_4 (empty circles) and the gauge-invariant quantities (stars). Shown in the inset is the incorrect scaling obtained when the correction for the integration constant is not made. 127

4.13 *Upper panel:* Comparison of the computed data for the recoil velocity (open circles) with the least-squares fits using either a linear (dotted line) or a quadratic dependence (dashed line). *Lower panel:* Point-wise residuals computed with the linear (dotted line) or a quadratic fit (dashed line). 129

4.14 The total kick calculated via Eq. (4.36) up to $\ell = 7$ is compared to the contributions of individual terms q_1 and q_2, as well as the sum of term excluding these. In the case of the $r0$ system (left panel) the spins are anti-aligned and the q_2 term is dominant and the q_1 term does not provide a significant contribution. In the case of the $r7$ system (right panel), on the other hand, the spins are essentially aligned and the while the q_2 term is still dominant, the q_1 term also makes a significant contribution. 130

4.15 *Left panel:* Dependence on the spin ratio of the initial total angular momentum $J_{\rm ini}$ [as computed from Eq. (4.48)], of the radiated angular momentum $J_{\rm rad}$ [as computed through the gauge-invariant waveforms], and of the final spin of the black hole $J_{\rm fin}$. All quantities show a linear behavior, whose coefficient are collected in Table 4.4. *Right panel:* Relative error $\Delta J/J_{\rm ini}$ in the conservation of the angular momentum [*cf.*, Eq. (4.55)]. Different curves refer to whether the final spin of the black hole is computed using the isolated/dynamical horizon formalism (triangles) or the distortion of the apparent horizon (squares). In both cases the error is of about 1% at most for simulations at the medium resolution. . . 133

4.16 *Left panel:* Dependence on the spin ratio of the ADM mass $M_{\rm ADM}$, of the scaled radiated energy $M_{\rm rad}$ [as computed through the gauge-invariant waveforms and scaled by a factor of 10 to make it visible], and of the final mass of the black hole $M_{\rm fin}$. All quantities show linear behaviors, whose coefficients are collected in Table 4.4. *Right panel:* Relative error $\Delta M/M_{\rm ini}$ in the conservation of the energy [*cf.*, Eq. (4.57)]. Note that the error is of about 0.5% at most for simulations at the medium resolution. 134

4.17 Global dependence of the final spin on the symmetric mass ratio and on the initial spins as predicted by expression (4.63). Squares refer to numerical estimates while circles to the EMRL constraints. 140

4.18 *Upper panel:* Comparison of the numerical data with the 2D fit through (4.63) in the case of equal-mass binaries, ($\nu = 1/4$). Empty circles indicate the AEI data [1], stars the FAU-Jena data [2]], a long-dashed line the BKL, and a short-dashed one the fit. *Lower panel:* residuals between the different estimates and the fit. 141

4.19 *Upper panel:* Comparison of the numerical data with the 2D fit through (4.63) in the case of nonspinning binaries. Empty circles indicate the Jena data [3], stars the Goddard data [4]], a long-dashed line the quadratic EOB fit [5] and a short-dashed line our 2D fit. *Lower panel:* residuals between the different estimates and the 2D fit. 142

4.20 *Upper panel:* Set of initial spins and mass ratios leading to a final Schwarzschild BH: *i.e.*, $a_{\rm fin}(a, \nu) = 0$. The two curves refer to the BKL estimate (long dashed) and to the 2D fit (short dashed), respectively. Indicated with a star is a numerical example leading to $a_{\rm fin} = 0.005$. *Lower panel:* Comparison between the BKL prediction (symbols) and the 2D fit (solid, dashed and long-dashed lines) near the EMRL. Different curves refer to different values of ν and the match is complete for $\nu = 0$. 144

4.21 Critical values of the initial spin and mass ratio leading to a final BH having the same spin as the initial ones *i.e.*, $a_{\rm fin}(a, \nu) = a$. A magnification is shown in the inset, where the dashed/non-dashed region refers to binaries *spun-down/up* by the merger. 145

4.22 *Left panel:* Rescaled residual for aligned binaries. The circles refer to equal-mass, equal-spin binaries presented in refs. [1–3, 6–8], triangles to equal-mass, unequal-spin binaries presented in ref. [1, 6], and squares to unequal-mass, equal-spin binaries presented in refs. [3, 6–8]. Here and in the right panel the "binary order number" is just a dummy index labelling the different configurations. *Right panel:* The top part reports the final spin computed for misaligned binaries. Hexagons refer to data from [9] (labelled "RIT"), squares to the data Table 4.7 (labelled "AEI"), circles to data from [10] (labelled "FAU"), and triangles to data from [11] (labelled "PSU-UTA"). Note that these latter data points refer to the aligned component $a^{\|}_{\rm fin}$ since this is the only component available from ref. [11]. The bottom part of this panel shows instead the rescaled residuals for these misaligned binaries. 149

4.23 Using the same data (and convention for the symbols) as in the right panel of Fig. 4.22, we here report the angle between the final spin vector and the initial orbital angular momentum $\theta_{\rm fin}$. Shown instead with asterisks and circles are the values predicted for the data from refs [10, 11] by our analytic fit (asterisks) and by the point-particle approach suggested in ref. [4] (circles). 151

4.24 Contour plots of $|v_{\rm kick}|$ as a function of the spin parameters a_1 and a_2. The diagram has been computed using expressions (6.3) and (6.4). 153

4.25 Contour plots of $a_{\rm fin}$ as a function of the spin parameters a_1 and a_2. The diagram has been computed using expressions (6.7) and (6.8). 154

5.1 Schematic representation in the (a_1, a_2) plane, also referred to as the "spin diagram", of the initial data collected in Table 5.1. These sequences cover most important portions of the space of parameters which is symmetric with respect to the $a_1 = a_2$ diagonal. 162

5.2 Noise strain for the Advanced LIGO and Virgo detectors and the Fourier-transformed amplitude of the PN and NR waveform at $\theta = 0, \phi = 0$ for a total mass $M = 200\,M_{\odot}$ at a distance $d = 100\,\mathrm{Mpc}$ for the maximally spinning model s_8. The glueing frequency is at $f_{\rm glue} = 27.14$ Hz. 165

5.3 Averaged and maximum horizon distance $d_H = d_H(a, M)$ for the LIGO detector (top left panel), for the Virgo detector (top right panel), and for the advanced versions of both detectors (bottom left and right panels, respectively). The horizon distance has been computed at a reference SNR $\rho = 8.0$. 169

5.4 Maximum SNR $\rho_{\rm max} = \rho(a,\, M)$ for the LIGO detector for a given set of masses at a distance $d = 100\,\mathrm{Mpc}$. Note that the growth of $\rho_{\rm max}$ with a is very well described with a low-order polynomial which is of 4th order for the optimal mass (*cf.* discussion in Sect. 5.1.10). Note also that the dependence on a becomes stronger for masses $M > 200\,M_{\odot}$, for which the NR-part of the waveform and hence the plunge and ringdown phase dominate. In these cases, the SNR is more then doubled between $a = -1$ and $a = +1$. 170

5.5 Averaged and maximum SNR $\rho = \rho(a, M)$ for the planned LISA mission and for sources at $d = 6.4\,\mathrm{Gpc}$ $(z = 1)$. 171

5.6 *Left panel:* maximum SNR $\rho_{\rm max}$ as a function of the mass for the highly spinning model s_8 and for the present detectors LIGO and Virgo. Different lines refer to the SNRs computed using only the $\ell = 2$ multipoles (continuous line), or up to the $\ell = 4$ multipoles (dashed line). *Right panel:* ratio between maximum and averaged SNR ρ as a function of the spins $a_1 = a_2$ for $M = 200\,M_{\odot}$ ($M = 3.53 \times 10^6\,M_{\odot}$) by including modes up to $\ell = 2$ and $\ell = 4$ for LIGO (LISA). In contrast to the case $\ell = 2$, the $\ell = 4$-curve is not constant but depends on the initial spins a_1, a_2 173

5.7 Best and minmax match as a function of mass for a waveform containing only the $\ell = 2, m = 2$ contribution and referring to the LIGO detector. Very similar behaviors can be shown also for the other detectors. 175

5.8 Best match as a function of the total projected spin a for a waveform containing only the $\ell = 2, m = 2$ contribution. The top/lower panels refers to binary with a total mass ($200/400\,M_\odot$) which are close to the optimal ones for the LIGO/Virgo or advanced detectors, respectively. In both panels the dotted line shows the minimum best match (0.965) needed for a detection. While the data have been computed for the LIGO detector, very similar behaviors can be shown also for the other detectors. 176

5.9 As in Fig. 5.8 but now different lines represent the matches obtained when comparing the numerical waveforms of the binary r_0 computed at different resolutions. The matches are computed for the LIGO detector, but very similar behaviors can be shown also for the other detectors. 179

5.10 Different symbols show the numerically computed values of $\rho_{\rm max}(a, M_{\rm opt})$ for the different detectors and represent therefore the cross section along the optimal mass of Figs. 5.3 and 5.5. Note that the SNR for the advanced detectors have been divided by 7 to make them fit onto the same scale. . . 181

5.11 Energy radiated during the numerical calculation $E^{\rm NR}_{\rm rad}$ (crosses), the total radiated energy $E_{\rm rad} = E^{\rm NR}_{\rm rad} + E^{\rm PN}_{\rm rad}$ (squares) along the diagonal of the spin diagram, *i.e.*, for $a_1 = a_2$. Shown as a continuous line is the analytic expressions given here (AEI fit), while the dashed line is the one suggested in ref. [12] (RIT fit). Note that the lines represent 1-dimensional cuts of 2-dimensional surfaces and hence are not expected to fit well all points. Finally, indicated with a dotted line is the prediction for the radiated energy coming from the point-particle approach of [4] and refined in [13]. 185

5.12 Phenomenological parameters ψ_k, f_1, f_2, f_3 and σ computed from the *equal-spin* hybrid waveforms (dots), and the analytical fits given by Eq. (5.32) (surfaces). Test-mass limit is indicated by black traces. η is the symmetric mass ratio and χ is the spin parameter. 188

5.13 Fitting factor and faithfulness (in LIGO noise spectrum) of non-spinning phenomenological templates with spinning hybrid waveforms constructed from NR simulations sets (1), (2) and (3). 190

5.14 Fitting factor and faithfulness of the spinning templates with *equal-spin* hybrid waveforms (using Initial LIGO noise spectrum). 192

5.15 Fitting factor of the spinning templates with *unequal-spin* hybrid waveforms (using Initial LIGO noise spectrum). Parameters (q, χ_1, χ_2) of the hybrid waveforms are shown in legends. 194

5.16 Match and FF of *non-spinning* IMR templates proposed in [14, 15] with the equal-spin hybrid waveforms. A comparison with Fig. 5.15 demonstrates the effect of neglecting spins. 195

5.17 Effective distance to optimally-oriented, equal-mass binaries with (equal) spin χ producing optimal SNR 8 in Initial LIGO. 196

A.1 *Left panel:* Evidence that the conditions for the Peeling theorem are met also for Ψ_3, which scales as r^{-2} when extracted at isotropic radii $r_{\rm E} = 30\,M$, $40\,M$, $50\,M$, and $60\,M$. This figure should be compared to the corresponding Fig. 4.5. *Right panel:* The same as the left panel but for the gauge-invariant quantity Q^{+}_{22}, which is shown to be constant when extracted at isotropic radii $r_{\rm E} = 30\,M$, $40\,M$, $50\,M$, and $60\,M$. 212

A.2 Comparison of the two polarization amplitudes h_+ (upper graph) and $h_\times$ (lower graph) as computed with Ψ_4 (continuous black line) or with the gauge invariant quantities $Q^+_{\ell m}$ (dashed red line). Note the two polarizations are computed using the lowest (and dominant) multipole $\ell = 2,\ m = 2$ and are extracted at $r_{\rm E} = 50\,M$. 215

A.3 *Left panel:* Coordinate trajectories for one of the black holes for the $r0$ compared with similar models where the initial linear momenta have been changed by $\pm 3\%$ in order to modify the eccentricity of the inspiral. *Right panel:* Recoil velocity for the $r0$ case is compared with similar models for which the initial eccentricity has been increased by adding and subtracting 3% of the initial linear momentum of the black holes relative to the $r0$ values. The effect of increased eccentricity in the final merger is to increase the size of the kick, by about 4% in both cases. 216

List of Tables

3.1 Boundary conditions for the BSSN variables. Nine sufficient and necessary conditions at the boundary for the geometric variables, where x is the direction perpendicular to the boundary, and A stands for the other two directions. 86

4.1 The puncture initial data parameters defining the binaries: location $\pm x/M$, linear momenta $\pm p/M$, mass parameters m_i/M, spins S_i/M^2, dimensionless spins a_i, ADM mass $M_{\rm ADM}$ measured at infinity, and ADM angular momentum $J_{\rm ADM}$ computed from Eq. (4.48). Note that we set $M_1 = M_2 = 1/2$ [*cf.*, Eq. (4.17)]. 105

4.2 Binary sequences for which numerical simulations have been carried out, with different columns referring to the puncture initial location $\pm x/M$, the linear momenta $\pm p/M$, the mass parameters m_i/M, the dimensionless spins a_i, the normalized ADM mass $\widetilde{M}_{\rm ADM} \equiv M_{\rm ADM}/M$ measured at infinity, and the normalized ADM angular momentum $\widetilde{J}_{\rm ADM} \equiv J_{\rm ADM}/M^2$. Finally, the last six columns contain the numerical and fitted values for $|v_{\rm kick}|$ (in $\rm km/s$), $a_{\rm fin}$ and the corresponding errors. 111

4.3 Final kick velocities in units of $\mathrm{km/s}$ for the models listed in Tab. 4.1. Columns two and three show the values obtained using the gauge-invariant quantities $Q^{\times,+}_{\ell m}$ and Ψ_4 respectively and taking into account the integration constant. Columns four and five, on the other hand, show the results obtained when ignoring the integration constant. The same data are shown in the right panel of Fig. 4.12. 128

4.4 Coefficients for the phenomenological expressions (4.53) and (4.54) (and the corresponding coefficients for $\Delta M_{\rm rad,\,fin}/M$) by means of which it is possible to compute the relative losses of energy and angular momentum, as well as the final mass and spin of the black hole in binary mergers in which the spins are orthogonal to the orbital plane. 136

4.5 Final and radiated angular momenta and masses, computed from the gauge-invariant waveforms. Shown is also the radiated spin and mass relative to their initial values, which are listed in Tab. 4.1. 136

4.6 Initial parameters of the new binaries computed at the AEI. The different columns contain the initial spin a, the symmetric mass ratio ν, half of the initial separation $x/M = \frac{1}{2}(x_1 - x_2)$, the dimensionless initial angular momentum $\tilde{J} = J/(\mu M)$, the numerical and fitted values for $a_{\rm fin}$ and the corresponding relative error. 139

4.7 Initial parameters of the new misaligned AEI binaries. 150

5.1 Binary sequences for which numerical simulations have been carried out, with various columns referring to the puncture initial location $\pm x/M$, the mass parameters m_i/M, the dimensionless spins a_i, and the normalized ADM mass $\widetilde{M}_{_{\rm ADM}} \equiv M_{_{\rm ADM}}/M$ measured at infinity. Finally, the last four columns contain the numerical values of the energy radiated during the simulation using the two methods described in the text and the corresponding errors between them, as well as the error to the fitted values. . . 160

5.2 Initial instantaneous frequencies $M\omega_{\rm ini}$ and associated minimum masses $M_{\rm min}$ of the NR waveforms for the different models and for each detector according to the corresponding lower cut-off frequency (*i.e.,* at 30 Hz for Virgo, at 40 Hz for eLIGO, at 10 Hz for AdLIGO/AdVirgo, and at 10^{-4} Hz for LISA). All the values for the masses are in units of solar masses. . 164

5.3 Properties of the “optimal” aligned binaries for the different detectors. Shown in the different rows are the optimal total aligned spin a, the optimal total mass in solar masses, the optimal maximum $\rho_{\rm max}$ and average $\rho_{\rm avg}$ SNRs, the optimal horizon distance d_H (expressed in ${\rm Mpc}$ and where cH^{-1} is the Hubble radius), the lower bound for the optimal relative event rate R, and the glueing frequency $f_{\rm glue}$ for the optimal binary. The masses have been sampled with an accuracy of $2.5\,M_\odot$ for the ground-based detectors and of $2.5\times10^4\,M_\odot$ for LISA. 172

5.4 Best and minmax matches as computed for the LIGO detector for binaries with different spins in the spin diagram. Different columns show $\mathcal{M}_{\rm best}$ and $\mathcal{M}_{\rm minmax}$ for waveforms computed either using only the $\ell=2, m=2$ contribution (third and fourth columns), only the $\ell=3, m=2$ contribution (fifth and sixth columns), or the sky-averaged contributions of all modes up to $\ell=4$ (last two columns). Finally the last eight rows show the matches at different resolutions (*i.e.,* $\Delta x/M=0.024, 0.020, 0.018$ or low, medium and high, respectively) for the binary r_0. 178

5.5 Fitting coefficients for the maximum SNR computed for the optimal mass [Eq. (6.5)]. The different rows refer to the various detectors and have been computed including all modes up to $\ell=4$. 182

5.6 Coefficients describing the amplitude and phase of the phenomenological waveforms. See Eq. (5.32). 193

A.1 Integrated convergence rates of the Zerilli-Moncrief gauge-invariant variables providing the dominant contribution in the kick-velocity measurements. As the numbers indicate, we achieve at least third order convergence both in amplitude and phase. A time-shift as given by Eqs. (A.38)–(A.40) was made on the raw data to remove the near cancellation of the lowest-order error terms. 213

Abbreviations

Adaptive mesh-refinement - AMR

Apparent horizon - AH

Arnowitt-Deser-Misner - ADM

Baumgarte-Shapiro-Shibata-Nakamura - BSSN

Binary black-hole - BBH

Black-hole - BH

Effective one body - EOB

Extreme mass-ratio inspiral - EMRI

Extreme mass-ratio limit - EMRL

First order symmetric hyperbolic system - FOSH

Fitting factor - FF

Fourth-order Runge-Kutta - RK4

General Relativity - GR

Gravitational wave - GW

Initial-boundary-value problem - IBVP

Initial data - ID

Initial-value problem - IVP

Innermost stable circular orbit - ISCO

Inspiral-merger-ringdown - IMR

Isolated horzon - IH

Iterated Crank-Nicholson - ICN

Laser Interferometer Gravitational Wave Observatory - LIGO

Laser Interferometer Space Antenna - LISA

Marginally outer trapped surface - MOTS

Numerical Injection Analysis - NINJA

Numerical-relativity - NR

Ordinary differential equation - ODE

Partial differential equations - PDE

Post-Newtonian - PN

Signal-to-noise ratio - SNR

Simultaneous approximation penatly terms - SAT

Summation by parts - SBP

Transverse traceless - TT

Well-posed - WP

Chapter 1

Introduction

> *Every time we walk along a beach some ancient urge disturbs us so that we find ourselves shedding shoes and garments or scavenging among seaweed and whitened timbers like the homesick refugees of a long war . . . Mostly the animals understand their roles, but man, by comparison, seems troubled by a message that, it is often said, he cannot quite remember or has gotten wrong . . . Bereft of instinct, he must search continually for meanings . . . Man was a reader before he became a writer, a reader of what Coleridge once called the mighty alphabet of the universe.*
>
> Loren Eiseley

In 1915 Einstein's theory of general relativity proposed that the geometry of spacetime could be as dynamic and informative as the electromagnetic universe. He proposed that matter and energy define the structure of the surrounding spacetime, and that that structure, in turn, effects the motion of the bodies within it. The objective of all work accomplished here is for the improvement of computational models and modeling techniques for general relativistic simulations. These simulations are relevant for the prediction of gravitational wave (GW) signals to be used for the improvement of GW signal detection rates and accuracy of parameter estimation by gravitational wave observatories. The use of such numerically generated signals is essential for such observatories to be able to distinguish GW signals, and such observations would provide an entirely new spectrum of observation for understanding the dynamics of our Universe.

Optical, radio, and x-ray astronomy have provided us with abundant evidence that many galaxies contain massive black holes in their central nuclei. These nuclear black holes have a profound effect on the formation, dynamics, and entire history of the surrounding galaxy. There is some evidence that the formation of such black hole populations can be described by a multistage process of binary inspiral, merger, and accretion. Thus, the detection and analysis of gravitational waves produced by such events would be the first detailed description and the first direct evidence of such processes, and would give new insight into the formation of all galaxies– our own included.

The measurement and understanding of gravitational waves is an entirely new regime of astronomical observation. Studying this new regime will convey new information about the behavior, structure, and history of spacetime, as well as being one of the fist direct non-local tests of our theories with regard the physical force of gravity and the dynamics of the fabric of spacetime.

This dissertation is concerned with the derivation and implementation of a well-posed numerical treatment of the Einstein equations for general relativity in full 3+1 dimensions on a finite discrete domain of evolution. I will discuss the use of these codes for the evolution of binary black hole (BBH) spacetimes and the exploration of the parameter space for such constructions. I will also discuss the extraction of relevant physical information (such as gravitational waves, spins, and recoil velocities) from those simulations, and the analysis of those results for use in gravitational wave detection and in generating astrophysical predictions for the behaviour of merged black holes binaries. Much of the work discussed herein has been collaborative work with other researchers at the Max-Planck Institute for gravitational physics. Collaborators will be credited in the relevant chapters.

I will first spend the next chapter introducing the background, motivations, and computational and mathematical methods required for the generation of numerical relativity simulations and analysis. My thesis covers almost a global scope of the stages required to generate a well-posed numerical simulation and of the analysis of the resultant data required to provide useful information to gravitational wave (GW) and astrophysics communities:

- In Chapter [2] I describe the physics, mathematics, and computational methods and background required to understand the simulations and research done for this thesis. I start by explaining the decomposition of the Einstein equations for use in numerical simulations, follow with the derivation and application of initial data for such simulations, and then discuss the numerical methods required to evolve said data forward in time. I explain the different methods used to extract gravitational waveforms and black horizon properties. I explain how we prove numerical and physical accuracy and stability for our simulations, and follow with a discussion of the specific qualities of the codes used in this these.

- In Chapter [3] I describe the derivation, implementation and testing of two new kinds of boundary conditions for two different kinds of evolution systems common in numerical relativity. These new methods are designed to improve the numerical and physical accuracy and stability of numerical simulations with truncated evolution domains by artificial outer boundaries. I prove their well-posedness, accuracy and stability and show a series of tests showing this improved performance against standard methods for the Harmonic formulation of the Einstein Equations, and derive constraint preserving conditions for the BSSN system whcih are well-posed in theconformally flat constant coeeficient limit.

- In Chapter [4] I characterize phenomenological formulae for the prediction of the final spin and recoil velocity of merged binary black holes from arbitrary initial parameters derived from data extracted from our numerical simulations. This work is the result of the fitting physical knowledge and assumptions to data obtained from an extensive study of the parameter space of black hole binaries by sequences of numerical simulations performed on a variety of initial data parameters. Quite surprisingly, these relations highlight a nonlinear behavior, not predicted by the PN estimates, and can be readily employed in astrophysical studies on the evolution of binary black holes in massive galaxies.

- In Chapter [5] I will discuss the uses of gravitational waveforms extracted from numerical simulations for use in gravitational wave detector data analysis pipelines. Using the previous chapter's parameter studies I explore how much spin effects contribute to the signal-to-noise ratio and to event rates for a representative range of masses and detectors. I also present an analytical inspiral-merger-ringdown gravitational waveform for black hole binaries with non-precessing spins by matching a post-Newtonian description of the inspiral to numerical calculations to obtain a generic waveform with a conveniently small number of parameters.

I follow with a discussion of the outlook for the numerical methods discussed and the potential extensions of the work discussed. I will conclude with a summary of the work done in this thesis and an analysis of the results shown followed by Appendices to discuss technical details which do not suit the main body of the text.

Chapter 2

Background

We do not know the past in chronological sequence. It may be convenient to lay it out anesthetized on the table with dates pasted on here and there, but what we know we know by ripples and spirals eddying out from us and from our own time.

Ezra Pound

The simulation of general relativistic spacetimes requires the explanation of background for both the physics motivations, experimental objectives, theoretical and mathematical challenges, and numerical/computational requirements, as well as the details of implementation used for the research in this thesis. The research in this thesis deals with both the details of the mathematical and computational methods employed to make numerical simulation of the Einstein equations possible, the methods for the extraction of physical information from simulation data, as well as the use of results of such simulations for astrophysical predictions, for the production of waveforms for use in gravitational wave detector pipelines, and to establish the detectability and accuracy of parameter estimation of gravitational waveforms by said detectors. Thus I need to give background of both astrophysical and computational nature in order to explain the results described in the later chapters.

In this section I will try to highlight the most important foundations of the methods and results described in this thesis. I will first explain physical theory and the relevance of gravitational waves in general relativity, astrophysics, and cosmology. I will explain why numerical relativity is necessary to describe and predict the gravitational waves resultant from massive astrophysical events. I will then follow with a description of the steps necessary for the creation of a numerical relativity simulation and a description of the methods and code used for the simulations in this thesis. This requires an elaboration of the decomposition of the Einstein equations, the choice of coordinates, the methods for choosing initial data, and the numerical methods employed to discretize space and time and integrate on those discrete grids. I will then explain how gravitational waveforms and black hole horizon data is obtained from simulations, and how we prove physical accuracy. I then explain the importance of boundary conditions, and discuss the details of

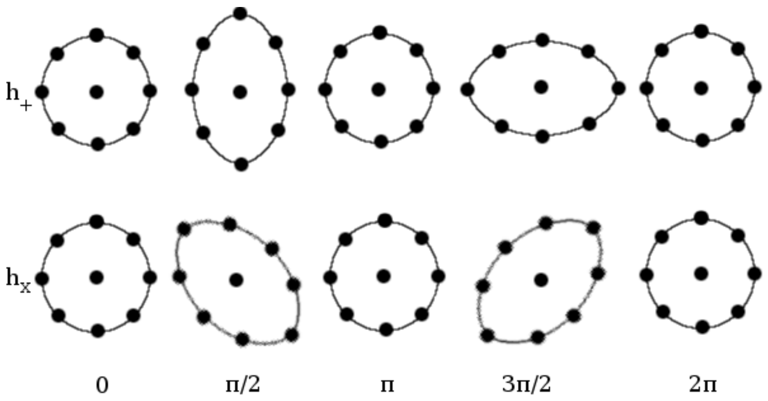

Figure 2.1: The effect of gravitational waves on a ring of particles. The wave propagation is perpendicular to the ring. The top row shows the effect of the wave + polarized, while the bottom row shows the effect of × polarization.

the codes used for this research. I will conclude the chapter with an outline of the thesis, which should make clear how the background given herein supports the material of the thesis to follow.

2.1 General Relativity and Gravitational Waves

Einstein's theory of gravitation, general relativity (GR), asserts that gravity is the result of curvature in spacetime. This curvature is determined by the matter and energy distribution in that spacetime. This coaction between matter and curvature is described by the Einstein Equations:

$$G_{\mu\nu} = 8\pi T_{\mu\nu} \tag{2.1}$$

This equation gives ten nonlinear partial differential equations (PDE) to describe the full 4 dimensional spacetime metric and matter fields. Where $G_{\mu\nu}$ represents the Einstein tensor and $T_{\mu\nu}$ is the stress energy tensor for the matter in the spacetime. In this dissertation I will discuss only black hole, and perturbed black hole spacetimes. Thus we limit our focus to the general relativistic prediction for systems containing only black holes. We can then set the matter term, $T_{\mu\nu}$, to be everywhere zero. In other words, we treat here only vacuum problems. However, many of the methods derived here (ICN and boundary conditions) may be applied to matter problems, as well.

Even with this vacuum simplification, however, few analytical solutions are known to

$$G_{\mu\nu} = R_{\mu\nu} - \frac{1}{2} g_{\mu\nu} R = 0 \tag{2.2}$$

for realistic astrophysical spacetimes. Here $R_{\mu\nu}$ is the Ricci curvature tensor, R is the scalar curvature, and $g_{\mu\nu}$ is the metric tensor for our spacetime of interest.

Einstein's motives for developing GR were mainly theoretical. At the time there were no strong observational reasons to abandon Newtonian gravity. Still, today, evidence of some predictions of GR have only been observed indirectly. Therefore, the study of weak gravitational fields is an extremely important test of Einstein's theory. In such a weak field regime we may say that such a region corresponds to a nearly flat spacetime. Thus, we may say that such a spacetime has coordinates such that the metric tensor is defined as some finite deviation from Minkowski spacetime

$$g_{\mu\nu} = \eta_{\nu\mu} + h_{\nu\mu}\,, \qquad |h_{\nu\mu}| \ll 1. \tag{2.3}$$

Working as if we have this flat spacetime with a tensor field $h_{\mu\nu}$ we can derive linearized filed equations in GR

$$\partial^\alpha \partial_{(\mu} \bar{h}_{\nu)\alpha} - \frac{1}{2}\left(\partial_\alpha \partial^\alpha \bar{h}_{\mu\nu} + \eta_{\mu\nu} \partial^\alpha \partial^\beta \bar{h}_{\alpha\beta}\right) = 8\pi T_{\mu\nu}\,, \tag{2.4}$$

where $\bar{h}_{\mu\nu} = h_{\mu\nu} - \frac{1}{2}\eta_{\mu\nu} h$ and $h = \eta^{\mu\nu} h_{\mu\nu}$ If we make a gauge transformation to the Lorentz gauge we may simplify the field equations to $\Box \bar{h}_{\mu\nu} = 16\pi T_{\mu\nu}$, where $\Box := g^{\mu\nu}\nabla_\mu \nabla_\nu$ is the flat space d'Alembertian operator. In flat vacuum spacetime we obtain

$$\Box \bar{h}_{\mu\nu} = (-\partial_t^2 + \nabla^2)\bar{h}_{\mu\nu} = 0. \tag{2.5}$$

This gives us a wave equation for a spacetime perturbation propagating at the speed of light transverse to the direction of propagation. Thus, the Einstein field equations tell us that if masses accelerate asymmetrically around in a spacetime, the curvature of that spacetime will warp to reflect the motions of those objects.

In the same way that electromagnetic radiation accompanies acceleration of electric charges, gravitational radiation accompanies quadrupolar acceleration of any massive objects. In highly dynamical spacetimes, cross-polarized transverse quadrupolar ripples in spacetime will radiate out longitudinally from this system, giving a metric perturbation

$$h_{ij} = h_+ (e_+)_{ij} - h_\times (e_\times)_{ij} \tag{2.6}$$

for the spatial part where $e_{+,\times}$ are basis tensors in the transverse traceless (TT) gauge. These ripples are gravitational waves.

The strongest gravitational waves are generated by accelerating systems with the largest gravitational fields, GM/R. Potential sources of strong gravitational waves are binary systems of massive compact objects such as black holes or neutron stars. The orbital motion of the two massive objects in a quasi-Keplerian orbit will produce gravitational waves. These gravitational waves propagate outward at the speed of light and a distant observer will see that the distances between objects will oscillate as these waves pass. Any gravitational waves seen from earth will never be much more than a fractional change in size (h) of 1 in 10^{-20}, if the predictions of general relativity are accurate. Currently there are many ground based detectors online which are designed to detect such passing gravitational waves (LIGO, VIRGO, TAMA, GEO). The detection of gravitational waves by these detectors can provide a view into regions of the universe that other observational techniques cannot. These are the first observatories that would observe the Universe with a spectrum other than the electromagnetic. Additionally, the detection of gravitational waves could potentially give us the first large scale direct confirmation of general relativity, or it could give us the first evidence that an alternate or modified theory of gravity is necessary. But, of course, any important result from gravitational wave detection hinges on the ability to correctly distinguish and analyze the detector's output.

Among the most promising sources for gravitational wave detectors are the inspiral and merger of compact binaries of black holes and neutron stars. Even for these sources, the signal strength is likely to be much less than the level of the detector noise [16]. Thus, data analysis techniques are required to extract the signal from the noise. One technique which is used for this purpose is *matched filtering*, in which the detector output is cross-correlated with a catalog of theoretically predicted waveforms. Therefore, chances of detecting a generic astrophysical signal depend on the size, scope, and accuracy of the theoretical signal template bank. The success of gravitational wave detectors depends on accurate theoretical models of compact binary inspirals [17]. The work discussed in this thesis is a small part of the effort required for the detection, recognition, and analysis of gravitational waves through the creation of such template waveforms. The main focus of this thesis will be the generation of waveforms and astrophysical predictions for binary black hole (BBH) inspirals and mergers.

2.2 Numerical Relativity

> *Far better an approximate answer to the right question, which is often vague, than an exact answer to the wrong question, which can always be made precise.*
>
> John W. Tukey

Binary systems of compact objects are potentially some of the most important sources of gravitational waves. The general Newtonian solution to the binary problem is given by Keplerian orbits. In general relativity, however, these orbits will decay due to the emission of gravitational radiation. This decay will lead to the inspiral and eventual merger of the two objects. Thus the emitted waves contain important astrophysical information about the dynamics of the system. The entire inspiral and merger of compact binaries can be separated into four different phases:

1. The longest being the initial quasi-equilibrium *inspiral* phase. In order to predict the behaviour of astrophysically relevant events in this weak field regime, we can approximate GR by perturbative methods called post-Newtonian expansions, which are expansions in terms of the relative speed of the black holes.

2. Those quasi-circular orbits become unstable at the innermost stable circular orbit (ISCO), where the inspiral enters the *plunge* phase. As we approach the ISCO the post-Newtonian approximation breaks down. Here a full-GR solution is required, but as an exact solution is rarely possible, this is where a numerical solution becomes relevant.

3. After the plunge, the black holes will merge to become a single distorted black hole. In this *merger* phase, numerical evolutions and phenomenological approximations

fit to numerical results are the only source of accurate waveforms. This will be the strongest signal in terms of amplitude.

4. This distorted black hole will ringdown to an equilibrium state. This *ringdown* stage of a merged black hole can be treated with perturbative methods for know quasinormal ringdown frequencies for given black hole spins for Kerr black hole solutions [18].

Eventually the black hole will approach an equilibrium state, and can be described by known spacetime formulations from exact solutions. However, in the treatment of strong dynamical fields, such as close inspiral and merger of two black holes, we need to treat the full non-linear Einstein equations. Here fully self-consistent numerical relativity (NR) simulations become essential.

This becomes more and more relevant today as gravitational wave detectors approach final design sensitivity. The ground-based detectors (LIGO, VIRGO, GEO, TAMA) will produce a data stream that contains noise. Therefore, accurate knowledge of potential signal waveforms will be needed *a priori* in order to successfully identify meaningful signals in the data stream. However, in order for numerical waveforms to be used for binary black hole signal detection, detector pipelines require matching against a large database of template waveforms that cover the full parameter space of binary black hole attributes– such as spin magnitude and orientation, and binary mass ratio. Numerical simulations are computationally expensive and time consuming. It thus becomes necessary to make extrapolations from numerical results and to derive phenomenological formulae for waveform generation and for predictions for other physical quantities such as the final spin and velocity of the merged black hole. I will discuss such formulae in Chapter [4]. Finally, I will discuss the use of numerical waveforms for detector data analysis in Chapter [5] where I will discuss detectability, signal-to-noise ratio, parameter estimation for detections and phenomenological waveforms for GW detection templates.

Historically, lacking exact or numerical results from full general relativity, data analysis methods for such events had to be developed based on perturbative methods called post-Newtonian expansions. Before numerical relativity could successfully model the binary black hole problem the GW detector observational community could not test or tune such methods with actual or accurate numerical BH merger waveforms. Now, the field of numerical relativity has finally reached a stage where accurate simulations for a range of astrophysical situations can be provided to the GW data analysis community, and the challenges of how to extend the capabilities of numerical relativity simulations have become more clear.

Until recently, the challenges of vacuum numerical relativity made progress toward waveform production slow, if not occasionally stagnant. Those problems included the inherent difficulty of evolving a singularity in a numerically stable way, finding appropriate gauge conditions for stable evolution, and the problems of efficiency and accuracy given limited resolution and limited computational resources. However, beginning with the first successful orbit of two black holes in a simulation [19], through the first demonstration of the merger and ringdown [20–23], and finally the discovery of a robust method for stably evolving any number of orbits through the merger and ringdown without excising the black hole within the horizon, stable and accurate numerical simulations are now common and rapidly developing, and the field of numerical relativity has become a fast moving and competitive field just when it has become most urgent for the field of astrophysics. This thesis builds on this previous work and works to improve the accuracy, efficiency, and scope of these codes.

After decades of research to develop stable, accurate, functioning, and efficient numerical codes for the evolution of fully general relativistic dynamical spacetimes, the field of numerical relativity has now reached a stage where it is possible to accurately simulate a range of astrophysical situations and provide waveforms to the GW data analysis community. In particular, numerical relativists have simulated BH binaries through 15 orbits, merger and ringdown, and simulations have been performed with a variety of initial configurations, providing important astrophysical information [24]. Numerical relativists are now able to provide the GW detector community with accurate waveforms, and for a wide enough spectrum of initial parameter that we can soon provide a phenomenological formula for generating arbitrary template waveforms for detector pipelines.

The earliest solutions to the Einstein equations were constructed by considering the Einstein equations in their covariant form [2.1] and by imposing convenient symmetries. In numerical relativity we think of the Einstein equations as an initial value problem (IVP). Initial data is specified on a particular slicing of spacetime in a discretised numerical domain, and then evolution equations are used to move forward to neighboring slices. Thus obtaining a time evolution of our full three-dimensional slice. In order to obtain such an evolution one first needs to split up the equations [2.2] in such a way that we choose three ’spatial’ variables and one ’time’ variable dimension along which we step forward our evolution. This freedom of coordinate choice is related to the fact that general relativity is a gauge theory. This gauge freedom gives us the freedom to split our four dimensional space as we see fit. I will discuss some commonly chosen approaches to this ’3+1’ decomposition in the sections that follow, as well as methods for choosing initial data, numerical methods required for simulations in vacuum spacetimes, and motivations for using numerical evolutions.

2.3 Decomposing the Einstein Equations

> *Divide each difficulty into as many parts as is feasible and necessary to resolve it.*
>
> Rene Descartes

In other theories of classical physics we are given a spacetime background and our only task is to determine the time evolution of quantities within that background. As discussed in the previous two sections, Einstein’s theory of general relativity asserts that spacetime structure and gravity may be related by describing a metric, $g_{\mu\nu}$, on a manifold, M, where the curvature of $g_{\mu\nu}$ is related to the matter distribution by the Einstein equations 2.1. Written in this form, the Einstein equations are manifestly covariant. That is, there is no way to distinguish spatial coordinates from a time coordinate. While this is a natural and sensible form for the equations to take from a geometrical standpoint, for the sake of gaining a more intuitive view, and for numerical evolutions, it is necessary to

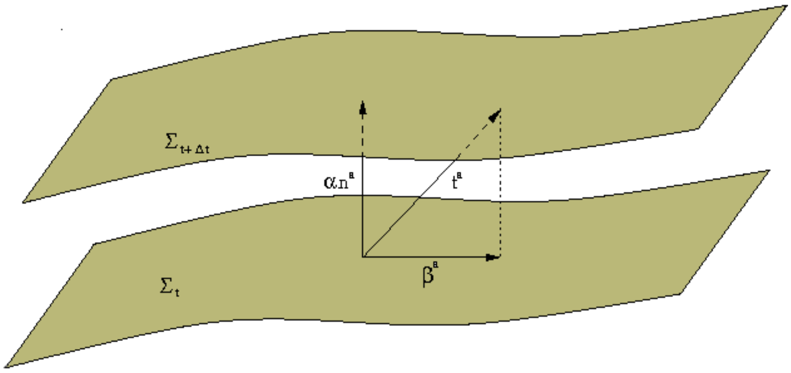

Figure 2.2: A spacetime diagram illustrating the definition of the lapse function α and the shift vector β^a.

separate your spatial coordinates from time in order to have a path along which to evolve some initial data through time. Thus, the first thing that needs to be done is to reformulate the Einstein equations as a *Cauchy problem*, that is, give a set of initial conditions that sufficiently determine the future evolution of the system.

Since the Einstein equations give us ten equations and ten independent components of the four metric $g_{\mu\nu}$, we have the same number of equations as unknowns. Only six of these ten equations involve second time-derivatives of the metric. The other four equations, thus, are not evolutions equations. We call these our constraint equations. The four constraint equations appear as a result of the general covariance of the Einstein equations. This gives us the freedom to apply general coordinate transformations to each of the four coordinates.

If we consider the Einstein equations as a Cauchy problem, we may separate our ten equations into a set of four constraint equations and six evolution equations. If these four constraint equations are satisfied on some initial hypersurface, then the Bianchi identities

$$\nabla_\nu G^{\mu\nu} \equiv 0 \tag{2.7}$$

guarantee that the evolution equations preserve the constraints on all future spacelike hypersurfaces during the evolution. This freedom means that the Einstein Equations can be formulated in several ways that will allow us to evolve the dynamics of any relativistic simulations. I will discuss some of the most common approaches to this freedom in the sections which follow.

2.3.1 The ADM decomposition

To make the Einstein equations suitable for numerical treatment, one typically introduces a foliation of spacetime into three-dimensional hypersurfaces. The most frequently used approach is to choose the hypersurfaces to be spacelike, which leads to the 3+1 or Cauchy formulation of general relativity [25, 26]. Here we reformulate the Einstein equations in such a way that we can describe the time evolution of our metric quantities by foliating our spacetime, (M, g_{ij}), by a set of 3-dimensional spacelike Cauchy surfaces, Σ_t, as parameterized by some time function, t. If we let n^a be a future-pointing timelike unit normal vector field to our hypersurface, Σ_t, we can extract our spatial metric from the spacetime metric, g_{ij}, as a three dimensional Riemannian metric on each Σ_t

$$\gamma_{ij} = g_{ij} + n_i n_j. \tag{2.8}$$

We then define a vector field from t that satisfies $t^a \nabla_a t = 1$. We decompose t^a into normal and tangential parts relative to Σ_t by defining the *lapse function*, α, and the *shift vector*, β_i, respectively

$$\alpha \quad = -t^i n_i = (n^i \nabla_i t)^{-1}\,, \tag{2.9}$$

$$\beta_i \quad = \gamma_{ij} t^j\,. \tag{2.10}$$

These *gauge functions* define how coordinates move forward in time from slice, Σ_t to $\Sigma_{t+\Delta t}$. Here, the lapse function, α, sets the proper interval as measured by an observer as we move between hypersurfaces, as illustrated in Figure [2.2], and the shift function β_i is the relative velocity of Eulerian observers and the lines of constant spatial coordinates. These four parameters, α and β_i, are a manifestation of the gauge freedom in the Einstein equations. We can now rewrite the interval as

$$ds^2 = -\alpha^2 dt^2 + \gamma_{ij}(dx^i + \beta^i dt)(dx^j + \beta^j dt). \tag{2.11}$$

Since the Einstein equations are second order, in order to distinguish between the intrinsic curvature of the internal geometry of a hypersurface and the *extrinsic* curvature associated with the embedding of that hypersurface in the spacetime for. We must then introduce something like a time derivative of our metric, γ_{ij}. Thus, we introduce the *extrinsic curvature tensor*, K_{ij}, to define a time derivative of our spatial metric γ_{ij} on our hypersurface Σ_t

$$K_{ij} = \gamma_a^c \nabla_c n_b = -\frac{1}{2}\mathcal{L}_n \gamma_{ij}\,, \tag{2.12}$$

where $\mathcal{L}_n$ is the Lie derivative with respect to n^a. This extrinsic curvature tensor describes the change of the normal vector on our hypersurface under parallel transport, and is a purely spatial tensor.

The appropriate initial data should, thus, provide definitions for $(\Sigma, \gamma_{ij}, K_{ij})$ on a hypersurface, where Σ is a three-dimensional manifold, γ_{ij} is a Riemannian metric, and K_{ij} is a symmetric tensor field on Σ. That is, the metric, γ_{ij}, depends on how Σ_t is embedded in the full spacetime. We can derive relations between the curvature ${}^{(3)}R^l_{ijk}$ of Σ and the spacetime curvature R^l_{ijk} and obtain

$$D_i K^i_j - D_j K^i_i = R_{kl} n^l h^k_j. \tag{2.13}$$

These are known as the *Gauss-Codacci relations*. We can now use our notions of an induced metric γ_{ij} and extrinsic curvature K_{ij} and these relations in our analysis of the Einstein equations. Combining these conditions with the vacuum Einstein equations, we obtain

$$\partial_t K_{ij} = \alpha\left[\bar{R}_{ij} - 2K_{il}K^l_j + KK_{ij}\right] - \bar{\nabla}_i\bar{\nabla}_j\alpha$$
$$+\beta^i\bar{\nabla}_l K_{ij} + K_{il}\bar{\nabla}_j\beta^l + K_{jl}\bar{\nabla}_i\beta^l. \tag{2.14}$$

Here, $\bar{\nabla}_i$ is the spatial covariant derivative on γ_{ij}, and $\bar{R_{ij}}$ is the associated Ricci tensor with γ_{ij}. Our set of second order evolution equations for the metric is then completed by rewriting our definition of extrinsic curvature using that fact that in our coordinates, $\mathcal{L}_t \equiv \partial_t$

$$\partial_t\gamma_{ij} = -2\alpha K_{ij} + \bar{\nabla}_i\beta_j + \bar{\nabla}_j\beta_i. \tag{2.15}$$

Equations [2.14] and [2.15] give us a complete set of first order evolution equations given a well-posed initial value problem for γ_{ij} and K_{ij}. Following the same procedure, we also get the constraint equations

$$\bar{R} + K^2 - K_{ij}K^{ij} = 0 \tag{2.16}$$
$$\bar{\nabla}_j\left(K^{ij} - \gamma^{ij}K\right) = 0. \tag{2.17}$$

Equation [2.16] is known as the *Hamiltonian constraint* and it constrains the three metric γ_{ij}, while equation [2.17] is the *momentum constraint* which constrains our extrinsic curvature K_{ij}. Valid initial data must satisfy these constraints on our initial slice. If this condition is met, the Bianchi identities guarantee that they will continue to be satisfied for all future slices in the evolution. This decomposition is known as the *Arnowitt-Deser-Misner* (ADM) scheme.

We are now left with the freedom to choose five components of the three metric and three components of the extrinsic curvature. The metric retains full three dimensional coordinate invariance on each slice. Each hypersurface represents a $t = const.$ slice of the spacetime, so we choose how the initial hypersurface it embedded in spacetime is represented by the trace of our extrinsic curvature K. We must now choose a method for decomposing our constraint equations to address this freedom.

One of the first problems to solve in numerical relativity is to find a formulation of the Einstein equations which gives a stable and accurate longterm evolution. In the ADM approach, the Einstein equations split into elliptic constraint equations within the spacelike hypersurfaces and hyperbolic evolution equations governing the time evolution normal to the hypersurfaces. These constraints can be enforced within the evolution or left as a test of the accuracy of the evolution. In addition, certain gauge variables appear that can be freely specified and that reflect the general covariance of general relativity – the field equations are invariant under transformations of the spacetime coordinates. These properties create two new problems: how best to choose the gauge, and how to deal with the evolution of the constraints. I discuss these two issues in the next sections.

2.3.2 The BSSNOK Formulation

Although the ADM formulation can work for some models of gravitational collapse or cosmological models in numerical treatments, it does not satisfy the requirements for stable longterm evolution necessary for simulating the inspiral, merger, and ringdown of compact binaries. This is because first order form of the ADM equations is only weakly hyperbolic. It was recognized by Shiabata, Nakamura and Oohara and Kojima [27, 28] and later elaborated further by Baumgarte and Shapiro [29] that a conformal traceless decomposition of the ADM variables results in a scheme that allows for stable longterm evolutions numerically. This scheme is known as the BSSNOK system. The ADM decomposition gives us evolution equations for the metric γ_{ij} in equation [2.15] and the extrinsic curvature K_{ij} in equation [2.14]. We further transform these variables as follows.

The three metric, γ_{ij}, is conformally transformed via

$$\phi = \frac{1}{12} \ln \det \gamma_{ij} \, , \qquad \tilde{\gamma}_{ij} = e^{-4\phi} \gamma_{ij} \tag{2.18}$$

Here the conformal factor ϕ is evolved as an independent variable, and $\tilde{\gamma}_{ij}$ is subject to the constraint $det \tilde{\gamma}_{ij} = 1$. The extrinsic curvature is subjected to the same transformation, and its trace, $\mathrm{tr}\, K_{ij}$, is additionally evolved as an independent variable

$$K \equiv \mathrm{tr}\, K_{ij} = g^{ij} K_{ij} \, , \qquad \tilde{A}_{ij} = e^{-4\phi} \left(K_{ij} - \frac{1}{3} \gamma_{ij} K \right) , \tag{2.19}$$

where $\mathrm{tr}\, A_{ij} = 0$. Lastly, we introduce the new evolution variables $\tilde{\Gamma}^i = \tilde{\gamma}^{jk} \tilde{\Gamma}^i_{jk}$, defined in terms of the Christoffel symbols of the conformal three metric. These connection coefficients are introduced to better calculate the Ricci curvature, and to make our system of evolution equations reproduce the wave equation in the linear limit.

Now that we have introduced the variables $(\phi, \tilde{\gamma}_{ij}, K, \tilde{A}_{ij}, \tilde{\Gamma}^i)$ to replace (γ_{ij}, K_{ij}), the Einstein equations specify a set of evolution equations for these new variables

$$\begin{aligned}
(\partial_t - \mathcal{L}_\beta) \tilde{\gamma}_{ij} &= -2\alpha \tilde{A}_{ij} \, , && (2.20) \\
(\partial_t - \mathcal{L}_\beta) \phi &= -\frac{1}{6} \alpha K \, , && (2.21) \\
(\partial_t - \mathcal{L}_\beta) \tilde{A}_{ij} &= e^{-4\phi} \left[-D_i D_j \alpha + \alpha R_{ij} \right]^{TF} + \alpha \left(K \tilde{A}_{ij} - 2 \tilde{A}_{ik} \tilde{A}^k_j \right) , && (2.22) \\
(\partial_t - \mathcal{L}_\beta) K &= -D^i D_i \alpha + \alpha \left(\tilde{A}_{ij} \tilde{A}^{ij} + \frac{1}{3} K^2 \right) , && (2.23) \\
(\partial_t - \mathcal{L}_\beta) \tilde{\Gamma}^i &= \tilde{\gamma}^{jk} \partial_j \partial_k \beta^i + \frac{1}{3} \tilde{\gamma}^{ij} \partial_j \partial_k \beta^k + \beta^j \partial_j \tilde{\Gamma}_i - \tilde{\Gamma}_j \partial_j \beta^i + \frac{2}{3} \tilde{\Gamma}^i \partial_j \beta^i && (2.24) \\
&- 2 \tilde{A}^{ij} \partial_j \alpha + 2\alpha \left(\tilde{\Gamma}^i_{jk} \tilde{A}^{jk} + 6 \tilde{A}^{ij} \partial_j \phi - \frac{2}{3} \tilde{\gamma}^{ij} \partial_j K \right) ,
\end{aligned}$$

where TF denotes the trace free part of the tensors in the brackets ($T^{TF}_{ij} \equiv T_{ij} - g_{ij} g^{kl} T_{kl}/3$ for any tensor T_ij). This system gives us seventeen dynamical variables $(\phi, \tilde{\gamma}_{ij}, K, \tilde{A}_{ij}, \tilde{\Gamma}^i)$, four gauge quantities (α, β^i), and nine constraint quantities (from equations [2.16] and [2.17]) and the constraints on the new variables

$$\begin{aligned}
\mathcal{H} &= e^{-4\phi}\left[\tilde{R} - 8\tilde{D}^j\tilde{D}_j\phi - 8(\tilde{D}^j\phi)(\tilde{D}_j\phi)\right] + \\
&\quad \frac{2}{3}\left[K^2 - \tilde{A}_{ij}\tilde{\gamma}^{ij}\right] - \tilde{A}_{ij}\tilde{A}^{ij}\,, && (2.25)\\
\mathcal{M}_i &= 6\tilde{A}^j_i(\tilde{D}_j\phi) - 2\tilde{A}_{ij}\tilde{\gamma}^{ij}(\tilde{D}_i\phi) - \frac{2}{3}(\tilde{D}_iK) + \tilde{\gamma}^{kj}(\tilde{D}_i\tilde{A}_{ki})\,, && (2.26)\\
\mathcal{A} &= \tilde{A}_{ij}\tilde{\gamma}^{ij}\,, && (2.27)\\
\mathcal{S} &= \det\tilde{\gamma}_{ij} - 1\,, && (2.28)\\
\mathcal{G}^i &= \tilde{\Gamma}^i - \tilde{\gamma}^{jk}\tilde{\Gamma}^i_{jk}, && (2.29)
\end{aligned}$$

and we are left with four degrees of freedom for the gravitational polarization modes– two in the conformal three metric $\tilde{\gamma}_{ij}$, and two in the transverse traceless part of the extrinsic curvature A^{ij}_{TT}. All other freedoms either represent coordinate freedoms or are fixed by the constraint equations. These constraint equations are independent of the kinematical variables α and β^i that govern how our coordinates move through spacetime. The BSSN code used in this thesis enforces our coordinate constraints $(\mathcal{A},\mathcal{S})$ but the physical constraints $(\mathcal{H},\mathcal{M}^i)$ are not actively enforced, and are allowed to evolve freely, as they are used to monitor the accuracy of our evolutions [30]. We find that the BSSN system allows for a variety of gauge conditions for α and β but for stable evolutions through merger there is a commonly used and convenient standard for contemporary numerical relativity.

Now, in order to evolve the system we have to specify conditions on the lapse α and shift β^i. The simplest approach is to set $\alpha = 1$ and $\beta^i = 0$, but this leads to a formulation which is not strongly hyperbolic. Called *geodesic slicing*, this can cause the slice to touch the coordinate singularity in the data [31]. Since one does not normally know in advance what spacetime the initial data one specifies on the initial hypersurface will evolve to, one would not like to specify the gauge as a fixed function of spacetime. Rather, we would like to tie it to the dynamics so that it can adapt itself to the solution. One common approach to evolve the lapse is according to the “1+log” slicing condition [32]

$$\partial_t\alpha - \beta^i\partial_i\alpha = -2\alpha(K - K_0)\,, \tag{2.30}$$

where K_0 is the initial value of the trace of the extrinsic curvature. One can then evolve the shift according to a hyperbolic ‘Γ-driver’ condition [33]

$$\begin{aligned}
\partial_t\beta^i - \beta^j\partial_j\beta^i &= \frac{3}{4}\alpha B^i\,, && (2.31)\\
\partial_t B^i - \beta^j\partial_j B^i &= \partial_t\tilde{\Gamma}^i - \beta^j\partial_j\tilde{\Gamma}^i - \eta B^i\,, && (2.32)
\end{aligned}$$

where η is a damping coefficient. The advection terms on the right-hand-sides of these equations are required to account for the advection of the punctures in “moving-puncture” evolutions, which will be discussed in Section [2.4.4]. These are the gauge conditions chosen for all BSSN evolutions discussed in this dissertation. This system is symmetric hyperbolic (the significance of which will be discussed in Section [2.6.4]) in the linear approximation and the corresponding linear initial value problem is, thus, well-posed. Since in this case the evolution system for the constraint variables can also be reduced to a symmetric hyperbolic system, it follows that the constraints are satisfied for all time if satisfied initially.

This variation of the ADM equations containing additional auxiliary evolution terms, known as the BSSN formulation, has been implemented with great success. The evolution equations will have a set of eigenvalues and eigenvectors which indicate the presence of modes that travel at or below the speed of light. However, superluminal modes will permit error from inside the horizon to escape, and zero speed modes will create an accumulation of error on the evolution grid which will not advect away. The virtue of the BSSN formulation is that all constraint-violating modes travel at the speed of light. This is not the case for the ADM equations. In addition, while the ADM system is known to only be weakly hyperbolic, the BSSN formulation has been shown to be strongly hyperbolic in the linear regime [34]. In the next section I describe a decomposition of the Einstein equations which is manifestly symmetric hyperbolic in the full nonlinear regime.

2.3.3 The Harmonic Formulation

The decomposition of the Einstein tensor into evolution equations and constraints leaves four degrees of freedom in the spacetime metric that are not set by the field equations themselves, but can be freely specified. In a $3+1$ approach, these four degrees of freedom are determined by the choice of the lapse and shift, which amounts to specifying four out of ten metric components. The Arnowitt-Deser-Misner (“ADM”) equations [26] are a well known reduction of the Einstein system corresponding to this style of gauge choice.

An alternate approach to fixing the gauge degrees of freedom specifies the action of the wave operator on the coordinates, regarded as four scalar quantities. This is done by first choosing four functions $F^\alpha(x^\rho, g^{\rho\sigma})$, known as our *gauge source functions*, and then constructing a coordinate map x^α subject to the condition [35] that the d’Alembertian of each coordinate is

$$\nabla_\mu \nabla^\mu x^\alpha = \frac{1}{\sqrt{-g}} \partial_\mu \left(\sqrt{-g} g^{\mu\beta} \partial_\beta x^\alpha \right) = -F^\alpha \,. \tag{2.33}$$

We may rewrite Eqs. (2.33) as constrained variables

$$C^\alpha := \nabla_a \nabla^a x^\alpha - F^\alpha = 0 \,, \tag{2.34}$$

and using them in combination with the Einstein tensor $G^{\mu\nu}$ one obtains the *generalized harmonic* evolution system

$$E^{\mu\nu} := G^{\mu\nu} - \nabla^{(\mu} \Gamma^{\nu)} + \frac{1}{2} g^{\mu\nu} \nabla_\alpha \Gamma^\alpha \,. \tag{2.35}$$

Here Γ^ν is treated formally as a vector in construction the covariant derivative $\nabla^\mu \gamma^\nu$. When the constraints C^α are satisfied, this gives a manifestly hyperbolic evolution system

$$E^{\mu\nu} = -\nabla^{(\mu} F^{\nu)} + \frac{1}{2} g^{\mu\nu} \nabla_\rho F^\rho \,. \tag{2.36}$$

If the gauge source functions are chosen such that they do not depend on derivatives of the metric, they will not enter the principle part of the system and will not affect its well-posedness or stability numerically. In terms of these variables, the vacuum Einstein equations are a system of ten wave equations acting on the metric components, coupled through the coefficients of the wave operator and the source terms. The principle part of the Einstein equations, thus, reduces to a second order hyperbolic form. This method is the called the 'generalized harmonic' formulation of the Einstein equations. Harmonic coordinates were first introduced by deDonder [36] in 1921 to reduce the Einstein equations to 10 quasilinear wave equations. They were later used by Choquet-Bruhat [25] to give the first well-posed version of the Cauchy problem for the gravitational field. The first successful numerical evolutions of the binary black hole problems was solved in harmonic coordinates by Pretorius [19] in 2005. Many researchers have implemented numerical evolutions schemes for harmonic formulations of the Einstein equations [37–41] and since successfully solved the inspiral and merger of binary black hole problems.

For the formulation used in this dissertation we use a densitized inverse metric $\tilde{g}^{\mu\nu} := \sqrt{-g}g^{\mu\nu}$ as evolution variables, the harmonic constraints Eqs. (2.34) take the form

$$C^\alpha = -\frac{1}{\sqrt{-g}}\partial_\beta\tilde{g}^{\alpha\beta} - F^\alpha = 0\,, \tag{2.37}$$

while for the evolution equations we obtain

$$\begin{aligned}
\partial_\rho\left(g^{\rho\sigma}\partial_\sigma\tilde{g}^{\mu\nu}\right) \quad &- \quad 2\sqrt{-g}g^{\rho\sigma}g^{\tau\lambda}\Gamma^\mu_{\rho\tau}\Gamma^\nu_{\sigma\lambda} - \sqrt{-g}(\partial_\rho g^{\rho\sigma})(\partial_\sigma g^{\mu\nu}) + \frac{g^{\rho\sigma}}{\sqrt{-g}}(\partial_\rho g^{\mu\nu})(\partial_\sigma g) \\
&+ \quad \frac{1}{2}g^{\mu\nu}\left(\frac{g^{\rho\sigma}}{2g\sqrt{-g}}(\partial_\rho g)(\partial_\sigma g) + \sqrt{-g}\Gamma^\tau_{\rho\sigma}\partial_\tau g^{\rho\sigma} + \frac{1}{\sqrt{-g}}(\partial_\sigma g)\partial_\rho g^{\rho\sigma}\right) \\
&+ \quad 2\sqrt{-g}\nabla^{(\mu}F^{\nu)} - \sqrt{-g}g^{\mu\nu}\nabla_\rho F^\rho + \sqrt{-g}A^{\mu\nu} = 0\,,
\end{aligned} \tag{2.38}$$

which takes the form of a quasilinear wave equation, where in the final term we have allowed for a constraint adjustment function which may depend on the metric and its first derivatives,

$$A^{\mu\nu} := C^\rho A^{\mu\nu}_\rho(x^\rho, g_{\rho\sigma}, \partial_\tau g_{\rho\sigma})\,. \tag{2.39}$$

These constraint adjustments implemented in the code are given from [42] and have the form

$$A^{\mu\nu} := -\frac{a_1}{\sqrt{-g}}C^\rho\partial_\rho\tilde{g}^{\mu\nu} + \frac{a_2 C^\rho\nabla_\rho t}{\varepsilon + \epsilon_{\sigma\tau}C^\sigma C^\tau}C^\mu C^\nu - \frac{a_3}{\sqrt{-g^{tt}}}C^{(\mu}\nabla^{\nu)}t\,, \tag{2.40}$$

where the $a_i > 0$ are adjustable parameters, $\epsilon_{\sigma\tau}$ is the natural metric associated with the Cauchy slicing, and ε is a small positive number chosen to ensure regularity. These terms vanish when the constraints are satisfied, and thus do not affect the principle part of the evolution system. The effect of these terms is to suppress long wavelength instabilities in standardized tests for periodic boundary conditions. The first and second term in the adjustments suppress constraint violations in the nonlinear regime, while the third term leads to constraint damping in the linear regime.

Assuming that the gauge source functions F^α are also chosen such that they do not depend on derivatives of the metric, then the principle part of Eq. (2.38) consists of only its first term. That is, we have a set of ten wave equations of the form

$$\partial_\rho \left(g^{\rho\sigma} \partial_\sigma \tilde{g}^{\mu\nu} \right) = S^{\mu\nu} \,, \tag{2.41}$$

where $S^{\mu\nu}$ are non-principle source terms consisting of at most first derivatives of the evolution variables. By implication, this system inherits the property of the well-posedness of the initial-boundary value problem for the wave equation.

Note that we do not explicitly enforce the harmonic constraints during the evolution. Instead, we invoke the Bianchi identities, which for wave equations of the homogeneous form gives

$$g^{\rho\sigma} \partial_\rho \partial_\sigma C^\mu + L^{\mu\rho}_\sigma \partial_\rho C^\sigma + M^\mu_\sigma C^\sigma = 0 \,, \tag{2.42}$$

where the matrices L and M are functions of the metric and its first and second derivatives. It is essential to have all of the initial data constructed in a way that satisfies the conditions

$$C^\rho = 0 \,, \qquad \partial_t C^\rho = 0 \,, \tag{2.43}$$

as well as a construction of the boundary data that implies a homogeneous boundary condition for the constraints. However, by satisfying these conditions, we arrive at a well-posed initial boundary value problem (IBVP) for the constraint propagation system. Work by Kreiss, Winicour, Reula and Sarbach [43] demonstrates that it is possible to construct such boundary data while keeping the IBVP of the evolution system of the metric variables well-posed. In Section [3.1] we implement and test such boundary conditions and compare them with simpler (unconstrained SAT and non-SAT) boundary treatments for a number of test-problems. Since the harmonic constraints imply evolution equations for the ‘lapse’ and ‘shift’, the only remaining free initial data (in addition to the three metric and extrinsic curvature of the Cauchy hypersurface) are the initial choices of lapse and shift through the choice of gauge source functions.

In order to understand the feasibility of Eq. (2.38) as an unconstrained evolution system, one needs to have insight into the associated constraint propagation system [44–46]

$$\nabla \nabla C^\rho = S^\rho(g, \partial g, \partial^2 g, C, \partial C, A, \partial A) \,, \tag{2.44}$$

where S^ρ is a source term dependent on the metric, the constraints, the constraint adjustment term, and their derivatives. The principal part of Eq. (2.44) is, again, that of a wave operator, implying the connection to results regarding the well-posedness of the IBVP for the wave equation.

This harmonic decomposition is second order in time. In the code discussed in this dissertation, we found it more convenient to discretize and use the method of lines to time-integrate an evolution system which is first order in time. The reduction to first order in time con be done in a number of ways. We have implemented the generalized harmonic evolution system Eqs. (2.38), cast in a form that is first differential-order in time, and second-differential order in space. We introduced the auxiliary variables

$$Q^{\mu\nu} \equiv n^\rho \partial_\rho \tilde{g}^{\alpha\beta} \,, \tag{2.45}$$

are used to eliminate the second time-derivatives, where n^ρ is time-like and tangential to the outer boundary [40]. The resulting evolution system takes the form

$$\partial_t \tilde{g}^{\mu\nu} = -\frac{g^{it}}{g^{tt}}\partial_i \tilde{g}^{\mu\nu} + \frac{1}{g^{tt}} Q^{\mu\nu}\,, \tag{2.46}$$

$$\partial_t Q^{\mu\nu} = -\partial_i\left(\left(g^{ij} - \frac{g^{it}g^{jt}}{g^{tt}}\right)\partial_j \tilde{g}^{\mu\nu}\right) - \partial_i\left(\frac{g^{it}}{g^{tt}}Q^{\mu\nu}\right) + \tilde{S}^{\mu\nu}(\tilde{g}, \partial\tilde{g}, F, \partial F)\,, \tag{2.47}$$

where $\tilde{S}^{\mu\nu}(\tilde{g}, \partial\tilde{g}, F, \partial F)$ are non-principle source terms consisting of at most first derivatives of the evolution variables and are determined by our choice of gauge.

The AEI harmonic code used in this dissertation in Section [3.1] is a fourth-order accurate finite-difference code based on the University of Pittsburgh Harmonic code, Abigel [47], which incorporates theorems establishing well-posedness and numerical stability of the harmonic initial-boundary value problem. As noted earlier, the gauge source functions F^μ may be chosen to be arbitrary functions of the spacetime coordinate metric. They can be viewed as differential gauge conditions on the densitized metric. For most of the tests in this dissertation we set our gauge source functions $F^\mu = 0$ and thus evolve a strictly harmonic system. The exceptions are for analytic convergence tests, where we set

$$F^\mu = -\frac{1}{\sqrt{-\det g^{\mu\nu}_{(0)}}}\partial_\nu \tilde{g}^{\mu\nu}_{(0)}\,, \tag{2.48}$$

where $g^{\mu\nu}_{(0)}$ is our analytic metric; and for black hole spacetimes, where we set

$$F^\mu = \frac{\omega}{\sqrt{-\det g^{\mu\nu}}}(\tilde{g}^{t\nu} - \eta^{t\mu})\,, \tag{2.49}$$

where $\eta^{\mu\nu}$ is the Minkowski metric, and ω is a smooth, weighting function. In our binary black hole simulations, we have found that this choice of gauge source function keeps the lapse and shift under reasonable control as the black holes evolve. The rest of the simulations performed in this thesis are purely harmonic (*i.e.* $F^\mu = 0$).

Unlike mixed hyperbolic-elliptic formulations, hyperbolic formulations, such as this one have the advantage that there are a well-developed mathematical methods for analyzing the well-posedness of the IBVP. For both harmonic and BSSN formulations, this hinges on the boundary conditions that one imposes at the outer boundaries of the computational domain. Obtaining stable boundary conditions that avoid spurious reflections and preserve well-posedness is a main focus of this thesis and will be discussed for both formulations discussed in this section and in Chapter [3].

2.4 Initial Data

Let us watch well our beginnings, and results will manage themselves.

Alexander Clark

General relativity, as all classical physics, is deterministic– the behaviour of our system is completely dependent on initial conditions. If data is derived that gives “appropriate initial data” such that it specifies an initial slice that uniquely determines the system for all subsequent evolution, we say that we have an initial value formulation. If, additionally, small changes in initial data result only in locally small changes in the solution, and changes in the system are causally bounded, then we may say that we have a *well-posed* initial data formulation. All numerical relativity simulations must start with a hypersurface that describes our gravitational field at some initial slice in space-time. This is our initial data (ID). We must evolve this data into neighboring hypersurfaces according to our evolution equations, as defined by our decomposition of the Einstein equations, as discussed in the previous section [2.3]. The Einstein equations also constrain our choices for initial data. Because of the non-linearity there is no unique way of choosing which parts of our initial data may be freely specified, and which parts may be constrained. When constructing solutions of the Einstein initial value equations we are free to specify the topology of the initial data hypersurface. The Einstein equations place no constraints on the topology of the spacetime they describe, or of the hypersurfaces that foliate it. In this section we will introduce some common methods for describing binary black hole initial data in the two coordinate systems introduced in the previous section.

Two methods have been developed to deal with the singularity problem of numerical relativity – namely the *puncture* method [48, 49], which generalizes the Brill-Lindquist prescription [50] for initial data of black holes at rest and uses the Bowen-York extrinsic curvature [51] to solve the Hamiltonian constraint numerically for moving spinning black hole initial data [49,52]; and the *excision* method [53], in which a portion of the spacetime containing the singularity is not evolved and the horizon surrounding it is treated as in inner boundary. In this section we introduce these two methods. I will also discuss and compare two methods used for obtaining physical orbital parameters spins needed for to prescribe the initial data described here – namely quasi-circular, and post-Newtonian derived parameters. First, as an illustration I will describe single black hole data, and then I will move forward to multiple black hole initial data specification.

2.4.1 Time Symmetric Schwarzschild

The simplest black hole solution is the Schwarzschild solution, as it represents a static spherically symmetric single black hole connecting two causally disconnected asymptotically flat surfaces. The simplest representations of the Schwarzschild solution are time-symmetric ($K_{ij} = 0$), and thus exist on a “maximally embedded” hypersurface ($K = 0$). This fixes our choice of foliation for Σ. The interval for Schwarzschild may be written

$$ds^2 = -\left(\frac{1 - \frac{M}{2\tilde{r}}}{1 + \frac{M}{2\tilde{r}}}\right)^2 dt^2 + \left(1 + \frac{M}{2\tilde{r}}\right)^4 \left(d\tilde{r}^2 + \tilde{r}^2 d\theta^2 + \tilde{r}^2 sin^2\theta d\phi^2\right). \tag{2.50}$$

M represents the mass of the black hole as measured at spacelike infinity. By choosing a time-symmetric initial data hypersurface, we immediately get $K_{ij} = 0$, eliminating the need to solve the momentum constraints. If we choose a conformal three geometry given by a flat metric the Hamiltonian constraint becomes $\tilde{\nabla}^2\phi = 0$ as we approach infinite distance. The simplest solution of this equation is

$$\phi = 1 + \frac{M}{2\tilde{r}}, \tag{2.51}$$

we now have the full Cauchy data representing a single stationary black hole. All that is left is to choose a lapse and shift before we can integrate the evolution equations in [2.14] and [2.15]. In this case we may demand that $\partial_t K$ vanishes. This yields a *maximal slicing* equation for the lapse, which takes the form

$$\tilde{\nabla}^2(\alpha\phi) = 0\,. \tag{2.52}$$

It is convenient, in these coordinates, to choose boundary conditions such that the lapse is frozen at the event horizon ($a(\tilde{r} = M/2) = 0$) and such that it goes to one at infinity

$$\alpha = \frac{1 - \frac{M}{2\tilde{r}}}{1 + \frac{M}{2\tilde{r}}},\,. \tag{2.53}$$

If we now choose $\beta^i = 0$, we find that the left hand side of the evolution equations vanish and we have a static solution for the Einstein equations.

With this choice for the lapse and shift, frozen at the event horizon, we find that the solution covers only the black hole exterior. To cover the interior would require the use of a non-spacelike slice. This is what happens when the usual Schwarzschild areal-radial coordinates are used. At $r = 2M$ we would encounter a coordinate singularity, which is not possible to evolve numerically. This frozen lapse and shift at the horizon also creates an incompatible over-specification of the gauge for the horizon boundary.

2.4.2 Brill-Lindquist Data

As we saw in the previous section, the easiest way to generate initial data is to assume time symmetry and a conformally flat three geometry. One approach for generating time-symmetric multiple black hole data is Brill-Lindquist initial data [50]. We again assume a flat conformal geometry, and we have to solve for a Hamiltonian constraint of the form $\tilde{\nabla}^2 = 0$. We can use the linearity of the Hamiltonian constraint to choose the solution to be a superposition of each black hole solution. For N black holes

$$\phi = 1 + \sum_{\sigma=1}^{N} \frac{\mu_\sigma}{2 \mid x - C_\sigma \mid}\,, \tag{2.54}$$

where $\mid x - C_\sigma \mid$ is the distance from C_σ to the position of the hole in Euclidean space, and μ_σ are constants related to the masses of the holes. Each point $x = C_\sigma$ represents infinity in a different causally disconnected universe, giving $N + 1$ asymptotically flat hypersurfaces connected through N black holes. The universe containing N black holes cannot be isometric to any of the other universes connected to each hole, unlike in the Schwarzschild solution. Brill-Lindquist data have N singular points representing an image of infinity as seen through the throat of the black hole connecting to ’our’ universe.

Misner [54] found a construction for the time-symmetric Hamiltonian constraint which has two isometric asymptotically flat hypersurfaces for N black holes. The analytic representation of Misner initial data can only be made in terms of an infinite series expansion. This data contains an infinite number of singular points for each hole. In the next sections I will address two ways by which these singularities are dealt with numerically, and the formulation of more generic, more physically relevant initial data.

2.4.3 Excision

Time-symmetric black-hole solutions of the constraint equations such as those in the previous section are useful as test cases, because they have analytic solutions. However, they are not physically accurate or relevant. To generate time-asymmetric solutions for moving and/or spinning black holes we may make generalizations of the Misner and Brill-Lindquist data formulations. The first approach to be developed (and the approach used in our black hole spacetimes for all harmonic coordinate simulations) is a generalization of Misner data. This choice was made because two isometric universes means solving for one universe gives you both solutions, rather than trying to solve constraints for $N+1$ manifolds. The fact that the throats of the black holes are fixed-point sets in the isometry allows you to specify boundary conditions on the horizons and thus excise the black hole interiors. This generalization was developed by York and his collaborator [51, 55–58] in 1979, and was for a very long time the standard choice for intial data in numerical relativity for binary black hole spacetimes. This approach begins with a set of assumptions about the geometry of the solution

$$\begin{aligned} K &= 0\,, & maximal\,slicing\,, \\ \tilde{\gamma} &= f_{ij}\,, & conformal\,flatness\,, \\ \phi\,|_\infty &= 1\,, & asymptotic\,flatness\,, \end{aligned} \tag{2.55}$$

where f_{ij} represents a flat metric in the chosen coordinate system. One feature of the assumption of conformal flatness is that, for the BSSN system, we find that the momentum constraints decouple from the Hamiltonian constraint. This is important because it allow one to choose analytic solutions for black holes with both momenta and spins.

The solution of the momentum constraints gives us the trace-free part of the extrinsic curvature

$$\begin{aligned} \tilde{A}_{ij} &= \frac{3}{2r^2}\left[P_i n_j + P_j n_i - (f_{ij} - n_i nj)P^k n_k\right] \\ &+ \frac{3}{r^3}\left[\epsilon_{kil} S^l n^k n_j + \epsilon_{kjl} S^l n^k n_i\right]\,, \end{aligned} \tag{2.56}$$

where P^i and S^i are vector parameters and n^i is the outward pointing unit normal of the sphere in flat conformal space. Using this solution and the assumptions in [2.55] we can set physical values for the linear and angular momentum of each black hole in our intial data construction. We find that the linear momentum of the hypersurface is given by P^i and the angular momentum by S^i. Because the momentum constraints are linear we can add any number of solutions for any collection of momenta.

By the method of images we can make the tensors in our solution inversion symmetric, like those in the Misner solution. There are two inversion symmetric solutions for the extrinsic curvature of a single black hole

$$\begin{aligned}\tilde{A}^{\pm}_{ij} &= \frac{3}{2r^2}\left[P_i n_j + P_j n_i - (f_{ij} - n_i nj)P^k n_k\right] \\ &\mp \frac{3a^2}{2r^4}\left[P_i n_j + P_j n_i + (f_{ij} - 5n_i nj)P^k n_k\right] \\ &+ \frac{3}{r^3}\left[\epsilon_{kil}S^l n^k n_j + \epsilon_{kjl}S^l n^k n_i\right] ,\end{aligned} \tag{2.57}$$

where a is the radius of the throat of the black hole. This $r = a$ surface is where we set our excision boundary conditions. For more than one black hole the process for making the solution inversion symmetric gives and infinite series solution. However this solution converges rapidly and is easy to evaluate numerically.

Once we have an inversion symmetric extrinsic curvature, we can find a likewise inversion symmetric solution for the Hamiltonian constraint. With the assumptions in [2.55] the Hamiltonian constraint for our solution is

$$\tilde{\nabla}^2\phi + \frac{1}{8}\phi^{-7}\tilde{A}_{ij}\tilde{A}^{ij} = 0\,. \tag{2.58}$$

The isometry condition gives us a condition on the conformal factor, ϕ, at the throat of each hole

$$n^i_\sigma \tilde{\nabla}_i \phi \mid_{a_\sigma} = -\frac{\phi}{2r_\sigma} \mid_{a_\sigma} , \tag{2.59}$$

where n^i_σ is the outward pointing unit normal to the σ^{th} throat and a_σ is the coordinate radius of the σ^{th} throat. We can plug this condition into our equation for the Hamiltonian constraint [2.58] as a boundary condition on the horizons of the throats when solving the region exterior to the throats. Finally, all that is left is to choose an outer boundary condition. This is needed in order for the quasilinear elliptic equations above to be solved as a well-posed boundary-value problem. This final condition comes from the fact that we have an asymptotically flat solution. Thus, the solution behaves as

$$\phi = 1 + \frac{E}{2r} + \mathcal{O}(r^{-2})\,, \tag{2.60}$$

where E is the total ADM energy content of the initial hypersurface. In Chapter [3] and Section [2.6.5] we will discuss some solutions to this boundary value problem.

2.4.4 Punctures

In 1997 Brandt and Brügmann [49] realized a method to factor out analytically the behavior of the singular points in the Euclidean manifold of the $N + 1$ sheet Brill-Lindquist approach. This “puncture” method allows us to rewrite the constraint equations on an $N + 1$ hypersurface manifold as equations for different functions on a simple Euclidean manifold. This approach was first successfully used for numerical simulations of binary black hole inspirals in 2005 [20–22, 33, 59, 60], and has since become the standard initial

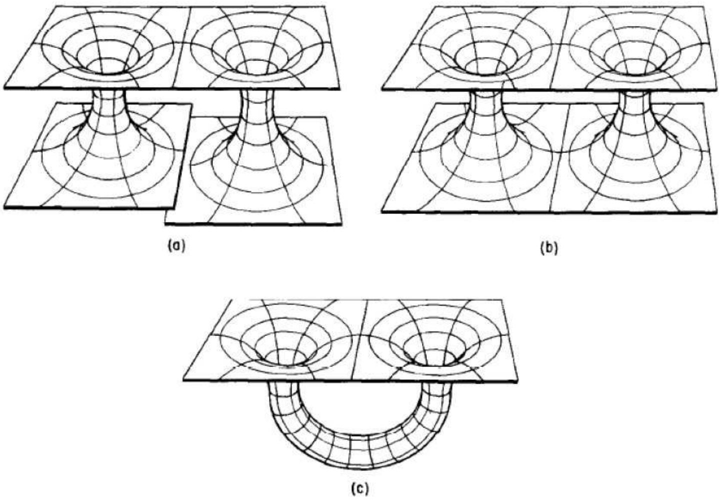

Figure 2.3: A diagram illustrating the various described methods of initial data formulation. Image (a) represents the $N + 1$ sheet description from of Brill-Lindquist data and the puncture approach; image (b) represents Misner data and the Bowen-York solution, and image (c) represents Misner's wormhole solution.

data formulation for binary black hole simulations in the BSSN evolution system.

The generalization of the Brill-Lindquist data begins with the same assumptions as the Bowen-York approach [2.55]. We, therefore, again have the trace-free part of the extrinsic curvature from the solution of the momentum constraints

$$\begin{aligned} \tilde{A}_{ij} &= \frac{3}{2r^2}\left[P_i n_j + P_j n_i - (f_{ij} - n_i nj)P^k n_k\right] \\ &+ \frac{3}{r^3}\left[\epsilon_{kil} S^l n^k n_j + \epsilon_{kjl} S^l n^k n_i\right] , \end{aligned} \tag{2.61}$$

where P^i and S^i are vector parameters and n^i is the outward pointing unit normal of the sphere in flat conformal space. Then, based on a time-symmetric solution we may assume a conformal factor of the form

$$\phi = \frac{1}{\chi} + u , \qquad \frac{1}{\chi} \equiv \sum_{\sigma=1}^{N} \frac{\mu_0}{2 \mid x - C_\sigma \mid} . \tag{2.62}$$

Here we require asymptotic flatness and a smooth function for u, and thus require $u = 1 + \mathcal{O}(r^{-1})$. Substituting the Hamiltonian constraint gives

$$\tilde{\nabla}^2 u + \eta(1 + \chi u)^{-7} = 0 , \qquad \eta = \frac{1}{8}\chi^7 \tilde{A}_{ij}\tilde{A}^{ij} . \tag{2.63}$$

Near each singularity, or "puncture", we obtain $\chi \approx \mid x - C_\sigma \mid$. The trace-free part of the extrinsic curvature $\tilde{A}_{ij}\tilde{A}^{ij}$ behaves no worse than $\mid x - C_\sigma \mid^{-6}$, and so η will vanish at each puncture faster than $\mid x - C_\sigma \mid$. This gives us a unique C^2 solution of our modified Hamiltonian constraint, and an approach which allows us to specify the mass and position of our black holes as parameterized by μ_0 and C_σ respectively. The linear momenta and spins are, again, parameterized by P_σ and S_σ respectively in the conformal extrinsic curvature of each hole. We only need to obtain a solution for u on a simple Euclidean manifold. With this formulation there is no need for inner boundary conditions, as the singularity is avoided if we choose a grid for our evolution domain such that C_σ is between grid points, and u is continuous. This is a significant advantage, as dealing with excision boundaries accurately in highly dynamic numerical simulations is one of the biggest challenges of the Bowen-York approach. Both because of the numerical and physical inaccuracies created by artificial boundaries, and more significantly because of the constraints on the gauge.

In this fixed puncture prescription, the black hole singularity is split into singular and nonsingular pieces, with the singular piece being handled analytically and not evolved. Because the coordinates of the punctures are fixed, the coordinate system becomes distorted as the binary is evolved, eventually causing any numerical code to crash. However, by choosing appropriate gauge conditions, and by taking advantage of the discrete nature of finite differencing codes used in numerical relativity, it was found that the singular part of the puncture could be evolved along with the nonsingular part, thus avoiding coordinate distortion [61]. This breakthrough, referred to as the “moving puncture” method, opened the door for many numerical relativity groups studying black hole binaries to successfully run long-term stable simulations from inspiral smoothly through merger and ringdown without tuning.

To avoid problems with evolving the interior of the hole we need to make sure no derivatives of the extrinsic curvature show up in our evolution equations. We, therefore, must choose a shift vector which vanishes, and a lapse for which its first derivatives vanish at the punctures. This is not a problem, because for grids staggered about the punctures, the first derivatives of the lapse α are sufficiently close to zero near the punctures that they cause no discontinuities in the evolved data. Thus, an important element in achieving stable evolution of the binary black hole problem in the BSSN formulation is choosing coordinates that allow the punctures to move through the grid without allowing any evolution at the location of the puncture itself. The conditions for lapse α and shift β^i that have been most successful thus far are known as *1+log slicing* and the *Gamma driver shift* conditions

$$\begin{aligned}
\partial_t \alpha - \beta^i \partial_i \alpha &= -2\alpha (K - K_0)\,, && (2.64)\\
\partial_t \beta^i - \beta^j \partial_j \beta^i &= \frac{3}{4} \alpha B^i\,, && (2.65)\\
\partial_t B^i - \beta^j \partial_j B^i &= \partial_t \tilde{\Gamma}^i - \beta^j \partial_j \tilde{\Gamma}^i - \eta B^i\,, && (2.66)
\end{aligned}$$

as discussed in section [2.3.2], where K_0 is the initial value of the trace of the extrinsic curvature. Common initial conditions are $\beta^i = B^i = 0$ and $\alpha = 1/\phi_{BL}^2$, where $\phi_{BL} = 1 + \sum_i \frac{m_i}{2|x - C_\sigma|}$ is the Brill-Linquist conformal factor used for the puncture ID.

The problem with both the initial data generation methods described is that they assume $K = 0\,, \tilde{M}^{ij} = 0$ and that the conformal geometry is flat. These assumptions are not necessarily compatible with the physical system we are trying to simulate. For either method the solution for a single spinning black hole does not generate a Kerr solution, as the Kerr solution is not a conformally flat geometry. Since the Kerr solution is stationary, conformally flat intial data will always contain a non-vanishing dynamical component. Thus, when we evolve either of the initial data prescriptions described, the system will emit non-physical gravitational radiation, as it attempts to settle to the Kerr geometry. This means that all simulations from these initial data will generate some unphysical ‘junk’ radiation which will contaminate the initial signal. Fortunately, such junk radiation will radiate off the evolution domain and leave us evolving physically realistic data. However, this inaccuracy must always be taken into account, and reflections of the junk radiation are an important reason for wanting better boundary conditions.

2.5 Numerical Methods and Implementation

> *Man inhabits a realm half in and half out of nature, his mind reaching forever beyond the tool, the uniformity, the law, into some realm which is that of the mind alone.*
>
> Loren Eiseley

Now that we have a set of evolution equations, gauge conditions, and initial data, we need to choose a method to evolve this system numerically. Achieving a numerical implementation of a PDE system is a difficult task. We are trying to model an infinite continuum spacetime with a finite discrete numerical representation. Modelling the Einstein equations in black hole spacetimes is wrought with problems. Lack of a preferred frame, gauge issues, a system of ten tightly coupled equations, singularities, artificial boundaries, accelerating dynamics all complicate the task of successfully evolving an accurate representation of the physical system. A crucial component to any numerical code is the choice of numerical methods, which, for large simulations must, deal with a balance of accuracy and efficiency, in addition to the problems specific to the modelling of binary black hole spacetimes. Here I give a partial description of the methods used to address these problems. In the next section [2.7] I will describe the implementation and execution of these methods and the framework under which they were implemented.

2.5.1 The Finite Difference Approximation

To evolve our evolution equations numerically we must first discretize our continuum intial data and solve our PDEs on this discrete grid. In the finite difference approach one covers the simulation domain by a discrete grid and the numerical approximation is represented by its values at the grid points. Using Taylor series expansions, we replace a partial differential equation with an algebraic equation on a discrete computational grid in order to discretize the form of the equation. Solving the discretized partial differential equation consists of a finite series of basic floating point operations which can be performed rapidly on modern computer clusters.

Thus we must evolve our system using a discrete grid. To do this the numerical domain is covered by an equidistant grid, where a Cartesian grid is represented by points at the values (for a grid staggered about the origin)

$$\begin{aligned} x_i &= (i-\frac{1}{2})h_x\,, \qquad 0 \leq i \leq N_x\,, && (2.67)\\ y_j &= (j-\frac{1}{2})h_y\,, \qquad 0 \leq j \leq N_y\,, && (2.68)\\ z_k &= (k-\frac{1}{2})h_z\,, \qquad 0 \leq k \leq N_z\,. && (2.69) \end{aligned}$$

Here N_x , N_y, and N_z are the total number of grid points in each direction, and h is the grid spacing in each direction,

$$h_x = \frac{(x_{max}-x_{min})}{N_x}\,, \qquad h_y = \frac{(y_{max}-y_{min})}{N_y}\,, \qquad h_z = \frac{(z_{max}-z_{min})}{N_z}\,. \quad (2.70)$$

The finite difference approach approximates a continuum expression using the Taylor series expansion. By taking Taylor series expansions about a point, a discrete approximation to the derivative operator at that point is obtained. For example, for centered differencing in first order convergent form

$$\begin{aligned} f(x+h) &= f(x) + h\frac{df}{dx}\,|_x + \frac{h^2}{2}\frac{d^2 f}{dx^2}\,|_x + \frac{h^3}{6}\frac{d^3 f}{dx^3}\,|_x + \ldots && (2.71)\\ f(x-h) &= f(x) - h\frac{df}{dx}\,|_x - \frac{h^2}{2}\frac{d^2 f}{dx^2}\,|_x - \frac{h^3}{6}\frac{d^3 f}{dx^3}\,|_x + \ldots && (2.72)\\ \frac{df}{dx} &= \frac{f(x+h)-f(x-h)}{2h} - \frac{1}{6}f'''(\zeta)h^2\,, && (2.73) \end{aligned}$$

where $x - h \leq \zeta \leq x + h$ and h is the grid spacing from Eq. [2.70]. The discrete approximation differs from the continuum expression by a truncation error related to the computational grid spacing. All simulations in this thesis are with fourth or sixth order convergent differencing operators. Fourth order operators are:

$$\begin{aligned} \frac{df}{dx} &= \frac{-f(x+2h)+8f(x+h)-8f(x-h)+f(x-2h)}{12h}\,, && (2.74)\\ \frac{d^2 f}{dx^2} &= \frac{-f(x+2h)+16f(x+h)-30f(x)+16f(x-h)-f(x+2h)}{12h^2} && (2.75) \end{aligned}$$

with a five point stencil for second derivatives. Most simulations in this dissertation are done using summation by parts (SBP) satisfying derivative operators, with weighted sideways differencing on the boundary. The derivation and implementation of the first and second derivative operators will be discussed in Section [3.1.3].

Assuming that we have a well-behaved solution which allows a Taylor series expansion, we may relate the numerical solution $\tilde{S}$ to the analytical solution S via

$$\tilde{S} = S + \mathcal{O}(h^\sigma)\,, \quad (2.76)$$

where σ is the convergence rate. σ may be measured by running a given simulation at multiple resolutions with the same conditions. Given three discretized solutions, $\tilde{S}(h)$, $\tilde{S}(h/q)$ and $\tilde{S}(h/q^2)$ we obtain

$$\begin{aligned} L &\equiv \tilde{S}(h/q) - \tilde{S}(h) = \mathcal{O}((h/q)^\sigma - h^\sigma\,, \\ M &\equiv \tilde{S}(h/q^2) - \tilde{S}(h/q) = \mathcal{O}((h/q^2)^\sigma - (h/q)^\sigma\,, \\ \frac{L}{M} &= \frac{q^{-\sigma}-1}{q^{-2\sigma}-q^{-\sigma}} = q^\sigma\,, \qquad \sigma = \frac{\log(\frac{L}{M})}{\log q}\,. \end{aligned} \tag{2.77}$$

In addition to proving that our discrete system approximates a continuum solution as $h \to 0$, from σ we may extrapolate our numerical results to a continuum solution.

Convergence in numerical simulations is a necessary condition for code verification. This is particularly true for the numerical relativity case for ninary black hole simulations, because we have no exact solutions and no data to compare against. If the solutions produced by a code run for the same parameters at different resolutions does not converge at the expected rate, then there is a source of divergence somewhere in the code and something is broken. Courant, Friedrichs, and Lewy introduced the significance of this problem in numerical simulations in 1928 [62]. No finite differencing simulation can claim to solve a differential equation accurately unless it can show convergence of the proper order. All simulations in this thesis were tested for convergence for various test cases. All spatial differences used in this thesis are fourth order, and thus have a truncation error proportional to h^4. The harmonic simulations have second order differencing on the boundaries and thus converge to second order as those inaccuracies spread to the rest of the simulation domain. This convergence order depends not only on the order of the spatial differencing methods, but also on the order of the method used for time integration, which will be discussed in the next section.

2.5.2 Method of Lines

Now that we have discretized our simulation domain and defined approximations to the continuum spatial differential operators, we need to define a way to step forward in time by integrating our hyperbolic evolution equations. The general method we use to do this in all simulations discussed in this thesis is called the method of lines (MoL). The idea is to finite-difference the spatial derivatives of the PDE as described in the previous section, leaving the time derivatives continuous. This leads to a coupled set of ordinary differential equations (ODE) for the time dependence of the variables $u = (u_{ij})$ at the spatial grid points,

$$\partial_t u = f(t, u)\,, \tag{2.78}$$

With the initial conditions $u(t_0) = u_0$. A suitable ODE integrator is then used to integrate these ODEs forward in time. There are many different possibilities for this, but in the simulations discussed in this dissertation, we used either the iterative Crank Nicolson scheme, or the 4th order Runge-Kutta scheme.

The ODE integrators we consider here belong to the class of explicit Runge-Kutta schemes. Given the unknowns u^n at time t^n, these compute an approximation u^{n+1} at time $t^{n+1} = t^n + \Delta t$ as follows:

$$\begin{aligned}
k_1 &= f(t^n, u^n)\,, \\
k_2 &= f(t^n + c_2\Delta t\,,\; u^n + a_{21}\Delta t k_1)\,, \\
k_3 &= f(t^n + c_3\Delta t\,,\; u^n + a_{31}\Delta t k_1 + a_{32}\Delta t k_2)\,, \\
&\vdots \\
k_s &= f(t^n + c_s h\,,\; u^n + a_{s1}\Delta t k_1 + a_{s2}\Delta t k_2 + \;\ldots\; + a_{s,s-1}\Delta t k_{s-1})\,, \\
u^{n+1} &= u^n + \Delta t(b_1 k_1 + \ldots + b_s k_s)\,,
\end{aligned}$$

for an s stage time stepping scheme. Any particular integration scheme is uniquely defined by the coefficients a_{ij}, b_i and c_i, which may be written as a tableau

$$\begin{array}{c|ccccc}
0 & & & & & \\
c_2 & a_{21} & & & & \\
c_3 & a_{31} & a_{32} & & & \\
\vdots & \vdots & \vdots & \ddots & & \\
c_s & a_{s1} & a_{s2} & \cdots & a_{s,s-1} & \\
\hline
 & b_1 & b_2 & \cdots & b_{s-1} & b_s
\end{array} \tag{2.79}$$

Consistency requires that $\sum_{k=0}^{s} b_k = 1$. The method is said to be pth order for a smooth function f if

$$\parallel u^{n+1} - u^n \parallel = \mathcal{O}(\Delta t^{p+1}) \tag{2.80}$$

The simplest Runge-Kutta method is the Euler method

$$u^{n+1} = u^n + \Delta t f(t^n\,, u^n)\,, \tag{2.81}$$

which is first-order and is represented by the tableau

$$\begin{array}{c|c}
0 & \\
\hline
 & 1
\end{array} \tag{2.82}$$

Two second-order Runge-Kutta methods are given by the tableaux

$$\begin{array}{c|cc}
0 & & \\
1 & 1 & \\
\hline
 & \frac{1}{2} & \frac{1}{2}
\end{array}
\qquad
\begin{array}{c|cc}
0 & & \\
\frac{1}{2} & \frac{1}{2} & \\
\hline
 & 0 & 1
\end{array} \tag{2.83}$$

The first is known as the *trapezoidal rule*, the second as the *midpoint rule*. Two examples of third-order methods are

$$\begin{array}{c|ccc}
0 & & & \\
\frac{1}{3} & \frac{1}{3} & & \\
\frac{2}{3} & 0 & \frac{2}{3} & \\
\hline
 & \frac{1}{4} & 0 & \frac{1}{4}
\end{array}
\qquad
\begin{array}{c|ccc}
0 & & & \\
1 & 1 & & \\
\frac{1}{2} & \frac{1}{4} & \frac{1}{4} & \\
\hline
 & \frac{1}{6} & \frac{1}{6} & \frac{2}{3}
\end{array} \tag{2.84}$$

The first is *Heun's (third order) method*, the second is derived in Shu and Osher [63]. There are many known fourth-order Runge-Kutta (RK4) methods, the one used in the simulations in this dissertation is as follows

$$\begin{array}{c|cccc} 0 & & & & \\ \frac{1}{2} & \frac{1}{2} & & & \\ \frac{1}{2} & 0 & \frac{1}{2} & & \\ 1 & 0 & 0 & 1 & \\ \hline & \frac{1}{6} & \frac{1}{3} & \frac{1}{3} & \frac{1}{6} \end{array} \tag{2.85}$$

For orders $p > 4$, it is one can no longer construct a method with $s = p$ stages.

Another method that in very popular in numerical relativity is the *iterative Crank-Nicolson(ICN) method* [64], which was developed by Choptuik from the *implicit Crank Nicolson scheme* [65]. ICN is given by the iteration equations

$$\begin{aligned} k_1 &= f(t^n, u^n)\,, \\ k_2 &= f(t^n + \frac{1}{2}\Delta t\,,\, u^n + \frac{1}{2}\Delta t k_1)\,, \\ k_3 &= f(t^n + \frac{1}{2}\Delta t\,,\, u^n + \frac{1}{2}\Delta t k_2)\,, \\ &\vdots \\ k_s &= f(t^n + \frac{1}{2}\Delta t\,,\, u^n + \frac{1}{2}\Delta t k_{s-1})\,, \\ u^{n+1} &= u^n + \Delta t k_s)\,. \end{aligned}$$

In the limit $s \to \infty$ this yields the implicit Crank-Nicolson method

$$\frac{u^{n+1} - n^n}{\Delta t} = f\left(\frac{u^n + u^{n+1}}{2}\right)\,. \tag{2.86}$$

As you can see from equation [2.86], the iterative version of ICN can also be seen as an explicit Runge-Kutta scheme with

$$\begin{array}{c|ccccc} 0 & & & & & \\ \frac{1}{2} & \frac{1}{2} & & & & \\ \frac{1}{2} & 0 & \frac{1}{2} & & & \\ \vdots & \vdots & \vdots & \ddots & & \\ \frac{1}{2} & 0 & 0 & \dots & \frac{1}{2} & \\ \hline & 0 & 0 & \dots & 0 & 1 \end{array} \tag{2.87}$$

As you can see, the ICN method is always second order, regardless of the number of steps. Thus it is worth while to compare with the implicit Crank-Nicolson scheme, to minimize the computational time spent on time integration while maximizing the regime of values of Δt which preserve a stable evolution. All of the simulations discussed in this thesis use RK4 time integration in order to preserve fourth order convergence.

2.5.3 Numerical Dissipation

For complicated systems of PDEs there exist solutions in the integration of the system that grow exponentially, like $e^{at/h}$, for some positive value of a and grid spacing h. These unstable modes are not present in the continuum problem but appear as a result of the finite difference approximation [2.5.1]. The instabilities may arise because high frequency modes may appear and grow because they cannot be resolved on the discrete grid. For this reason we need to apply a filter to suppress these artificially growing high frequency modes. We call this approach numerical dissipation.

One of the most popular approaches for the elimination of these spurious modes is known as *Kreiss-Oliger dissipation* [66, 67]. We may apply this method of dissipation to the right-hand-side (RHS) of our time integration equation [2.78] via an operator such as

$$(D_4 u)_j = -\frac{1}{16} h^{-1} (u_{j-2} - 4u_{j-1} + 6u_j - 4u_{j+1} + u_{j+2}) \, , \tag{2.88}$$

from the Taylor expansion

$$(D_4 u)_j = -\frac{1}{16} h^3 (u'''')_j + \mathcal{O}(h^5) \, . \tag{2.89}$$

For our simulations we use sixth order dissipation. Because our finite-differencing is forth-order accurate, the order of accuracy is not changed when adding $D_6 u$ to the right-hand-side,

$$\partial_t u = f(t, u) + \epsilon_D D_6 u \, . \tag{2.90}$$

We see that adding dissipation will decrease the amplification factor of high frequency modes. The same argument as above for the advection equation shows that

$$\mid \frac{\Delta t}{h} \epsilon_D \mid \leq 1 \tag{2.91}$$

is needed for stability. We apply the sixth-order operator both in all coordinate directions and add it to the right-hand-side of the discretized evolution equations at all grid points. This is applied to all simulations performed for this thesis.

2.6 Simulation Physics

With the tools described in the previous section we can now evolve the Einstein equations using one of the formulations described in section 2.3 on a relativistic space time described by one of the initial data formulations described by 2.4. We can the integrate that system on a numerical grid using finite differencing 2.5.1 and method of lines 2.5.2 to evolve our initial data according to our chosen evolution system. The primary output of such numerical relativity simulations are some approximate and discrete representation of the spacetime geometry. Now that I have described the tools necessary to make such a working code, I need to explain how we extract further physical data from these evolutions.

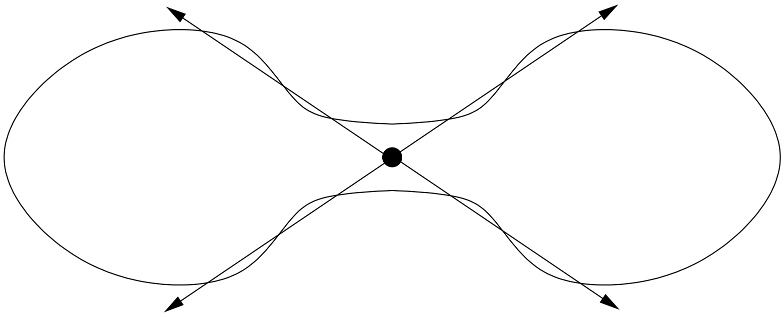

Figure 2.4: A diagram illustrating a cross-section of a 3-coordinate shape (the curvy line) which is not Strahlkörper about the local coordinate origin (the central point). The arrows show rays from the origin which intersect the shape more than once.

For the sake of analysis and diagnostics one needs to extract data such as the motion of the black holes, the properties of their horizons, and the emitted gravitational radiation. We need to extract these properties from the metric quantities evaluated in our numerical relativity code. Further, I will explain how we determine and prove the accuracy of this data and of the code itself. In this section I will explain how we extract information from the simulations in this thesis from the discrete spacetime geometry given us directly by the simulations. In the section following this I will explain the specifics of the implementation used for all the described tools, and with that I will be ready to discuss the results of my research and the work involved therein.

2.6.1 Apparent Horizon Finder

A key diagnostic for numerical evolutions of black hole spacetimes, and a key source of astrophysical data comes from analysis of the black hole horizons. An *event horizon* of an asymptotically flat spacetime is the boundary between the space for which a future-pointing null geodesics can reach future null infinity $\mathscr{J}$. This continuous null surface is defined *non-locally* in time [68]. As a global property of the entire spacetime it can only be obtained as part of post-processing for any simulation that evolves forward in time. However, for any numerical run it is important to monitor the properties of your black holes to make sure you are evolving real physics, without having to wait for the simulation to reach completion. For this purpose, we calculate the properties of the *apparent horizon* (AH) of the black holes. An apparent horizon is defined *locally* in time on a spacelike slice, and can thus be calculated “on the fly” at each time-step in a computational simulation.

A *marginally outer trapped surface* (MOTS) is a smooth closed 2-surface in a slice whose congruence of future-pointing outgoing null geodesics have *zero* expansion Θ. There may be several such surfaces, some nested inside others. An *apparent horizon* is defined to be the *outermost* marginally trapped surface. That is, it cannot be contained in any other MOTS. In terms of our $3+1$ variables, an apparent horizon satisfies the equation

$$\Theta \equiv \nabla_i n^i + K_{ij} n^i n^j - K = 0 \tag{2.92}$$

for the expansion Θ of the outgoing null geodesics, where n^i is the outward-pointing unit normal to the apparent horizon, and ∇_i is the covariant derivative operator associated with the 3-metric g_{ij} in the slice [69]. This condition is a nonlinear elliptic PDE containing the 3-metric g_{ij} and its spatial derivatives, the extrinsic curvature K_{ij}, and the conformal factor ϕ. This outermost surface is coincident with the boundary of a "trapped surface" – i.e. a surface whose future-pointing outgoing null geodesics have *negative* expansion. The existence of such a surface automatically implies the existence of a black hole (given certain technical assumptions are met, including energy conditions and a reasonable gauge).

To parameterize a horizon's shape, one method is to assume that one can define some local coordinate origin inside the S^2 surface such that the spatial coordinate shape around that point is a *Strahlkörper* (or star-shaped region) defined as

> a region in Euclidean space containing a surface for which all rays radiating from the 'origin' intersect only one point on that surface.

Thus, the shape in figure 2.4 is not a Strahlkörper shape because there is no point inside the surface for which there does not exist lines which intersect the surface three times. Given this Strahlkörper assumption we may parameterize our surface by

$$r = h(\theta, \phi) \tag{2.93}$$

where $r \equiv [\sum_i (x^i - x_0^i)^2]^{1/2}$ is the Euclidean distance from the local coordinate origin, x_0^i, to a surface point, thus $h : S^2 \rightarrow \Re^+$ describes all points on the horizon surface.

To write the expansion Θ (2.92) in terms of this parameterization one must define a scalar function which vanishes on the surface $h(\theta, \phi)$ and increases outward from the origin, ${}^{(3)}F \equiv r - h(\theta, \phi)$. We take the outward-pointing normal co-vector to the AH surface as the gradient of F,

$$s_i \equiv^{(3)} s_i \equiv \nabla_i^{(3)} F = \partial_i r - \partial_i h = \frac{x^i}{r} - X_i^u \partial_u h, \tag{2.94}$$

where the coefficients $X_i^u \equiv \partial y^u / \partial x^i$ and $y^u \equiv (\theta, \phi)$. This gives us the outward normal to the AH surface

$$n^i = \frac{s^i}{||s^k||} = \frac{g^{ij} s_j}{(g^{kl} s_k s_l)^{1/2}} \tag{2.95}$$

which gives us the expansion

$$\begin{aligned} \Theta &\equiv \nabla_i n^i + K_{ij} n^i n^j - K \qquad (2.96) \\ &= \partial_i \frac{g^{ij} s_j}{(g^{kl} s_k s_l)^{1/2}} + \partial_i (\ln \sqrt{g}) \frac{g^{ij} s_j}{(g^{kl} s_k s_l)^{1/2}} + \frac{K^{ij} s_i s_j}{g^{kl} s_k s_l} - K \end{aligned}$$

If we set this expansion to zero and $r = h$ we can obtain the shape and position of the AH surface in terms of the metric, its derivatives and the extrinsic curvature:

$$\Theta \equiv \Theta(h, \partial_u h, \partial_{uv} h; g_{ij}, K_{ij}, \partial_k g_{ij}) = 0 \tag{2.97}$$

With this equation for an apparent horizon, we then need an algorithm to solve this equation on the fly in our simulations.

We can use a direct elliptic solver to take the level surface $H(r, \theta, \phi) = r - h(\theta, \phi)$, and interpret the horizon equation (2.92) as a nonlinear second order elliptic differential equation for the function $h(\theta, \phi)$. We may simply calculate all derivatives using finite differences and then apply Newton's method to solve the resulting system. Thus, our system (as written by Jonathan Thornburg [70]) computes the Jacobian $J[\Theta(h)]$ of the expansion $\Theta = \Theta(h)$ of a trial horizon surface $r = h(\theta_i, \phi_j)$ from the metric data in the Schwarzschild/Eddington-Finkelstein metric g_{ij} and K_{ij}.

This system, of course, requires a good initial guess to converge on a solutions for the horizon, otherwise Newton's method will diverge. Therefore, the initial parameters must be specified to the horizon finding algorithm where the horizons sit in the initial data, and what sort of geometry the initial data defines. So long as the horizons are found with enough frequency in time-steps relative to the velocity of the black hole through the coordinate space that the horizon has not moved too far from it's previously known location between iterations, this system will remain accurate and efficient. Thus we have a method for tracking the coordinate movement and shapes of the black hole horizons in our simulations.

2.6.2 Isolated Horizon Finder

Information such as the horizon spins, relative velocities, and masses can be extracted now that we know how to solve for the shape and coordinate motion of our black hole horizons. The notions of *isolated* and *dynamical* horizons allow us to define the mass and angular momentum associated with these holes on the fly during a dynamical simulation [71]. This theory works by defining a *non-expanding horizon* as a null hypersurface H that is foliated by marginally trapped surfaces. For a stationary horizon, this means stacking apparent horizons at spatial hypersurfaces to form a non-expanding world-tube. An *isolated horizon* may be defined as a non-expanding horizon H whose intrinsic geometry is not evolving along the null generators [72]. This allows one to use the Hamiltonian formulation to define our mass and angular momentum.

The formula for the angular momentum of the horizon can be derived with the assumption that our horizons are axisymmetric, and thus have a ϕ Killing vector field

$$\mathcal{L}_\phi q_{ij} = 0\,, \tag{2.98}$$

where $q_{ij} := \gamma_{ij} - s_i s_j$ is the induced metric on the horizon for outward-pointing normals s_i. We can then derive the magnitude of the angular momentum from

$$J_H = \frac{1}{8\pi} \oint_S \phi^\ell s^m K_{\ell m} dA\,. \tag{2.99}$$

This is identical to the ADM angular momentum with the exception that it is calculated on the horizon instead of at infinity.

From the angular momentum and horizon surface we can then obtain the mass of the black hole from the equation

$$M_H^2 = \frac{A_H}{16\pi} + \frac{4\pi J_H^2}{A_H}\,, \tag{2.100}$$

where A_H is the horizon area. Thus, we have extracted all information classically available from a stationary black hole horizon. We may then use the notion of a *dynamical horizon* as a *spacelike* hypersurface H that is foliated by marginally trapped surfaces to define fluxes and balance laws for mass and angular momentum for non-stationary horizons. Therefore, we can accurately measure the mass and spin of our simulated black holes throughout any simulation.

2.6.3 Gravitational Wave Extraction

The primary goal of numerical relativity simulations is the extraction of gravitational waveforms for analysis as template waveforms for gravitational wave detector detection pipelines. There are multiple ways to extract the radiation component from the numerical metric data. In this section I will explain how we extract the waveforms by using a Newman-Penrose [73] null tetrad to represent the metric to extract the Ψ_4 component of the Weyl tensor and how we relate that to h_+ and $h_\times$ polarizations of the metric perturbation waveforms. Second I will show another approach by which we treat h_+ and $h_\times$ as linear perturbations on a Schwarzschild solution to extract the radiation data via the Regge Wheeler [74] and Zerilli [75] radiation equations [76]. Both of the methods described in this section were used for most of the black hole simulations discussed in this dissertation, and have been shown to give comparable results to high accuracy (see Appendix [A.6] for the details of this comparison).

Weyl

While the tensor components evolved in an ADM evolution of Einstein's equations carry the geometrical information which define the spacetime, they do not directly provide an interpretation of the geometrical content of a spacetime. The problem is that the tensor components are not coordinate independent, the value of each component (for a non-vanishing tensor) can vary arbitrarily with coordinate change. We must calculate several more geometrically defined quantities. The complex valued Weyl scalars, Ψ_0,Ψ_1,Ψ_2,Ψ_3,Ψ_4 are coordinate independent, but do depend on a choice of tetrad (an orthonormal complex basis for the tangent space of the spacetime) in which they are evaluated. In order to analyze the gravitational radiation being emitted by the simulated binary system, we must choose a null tetrad to decompose the gravitational radiation. This radiation is contained in the Weyl tensor, C_{abcd}, so we would like a tetrad that separates the radiation part of the Weyl tensor from the non-radiation content. The tetrad is defined in relation to the numerical grid coordinates, but the resulting Ψ's are less sensitive to coordinate freedom.

The Newman-Penrose formalism was developed to introduce spinor calculus into general relativity [73]. It gives us a special kind of tetrad calculus based on null geodesics through a specified choice of basis vectors. For this discussion, we choose the following tetrad: given $\hat{\tau}$, the time-like unit vector normal to a given hypersurface and $\hat{r}$, the radial unit vector. Using spherical coordinates we obtain the tetrad

$$\begin{aligned} \overrightarrow{l} &\equiv \frac{1}{\sqrt{2}}(\hat{\tau}-\hat{r})\,, \qquad \overrightarrow{n} \equiv \frac{1}{\sqrt{2}}(\hat{\tau}+\hat{r})\,, \\ \overrightarrow{m} &\equiv \frac{1}{\sqrt{2}}(\hat{\theta}-i\hat{\phi})\,, \qquad \overrightarrow{\bar{m}} \equiv \frac{1}{\sqrt{2}}(\hat{\theta}+i\hat{\phi})\,, \end{aligned} \tag{2.101}$$

where $\overrightarrow{l}$ and $\overrightarrow{n}$ are the in-going and outgoing null vectors respectively, and $\overrightarrow{m}$ and $\overrightarrow{\bar{m}}$ are the complex null vectors with the standard spherical metric

$$ds^2 = -d\tau^2 + dr^2 + r^2(d\theta^2 + sin^2\theta d\psi^2). \tag{2.102}$$

The orthogonality relations of this tetrad are

$$\begin{aligned} \overrightarrow{l}\cdot\overrightarrow{l} &= \overrightarrow{n}\cdot\overrightarrow{n} = \overrightarrow{m}\cdot\overrightarrow{m} = \overrightarrow{\bar{m}}\cdot\overrightarrow{\bar{m}} = 0\,, \\ \overrightarrow{l}\cdot\overrightarrow{n} &= -\overrightarrow{m}\cdot\overrightarrow{\bar{m}} = -1\,, \\ \overrightarrow{l}\cdot\overrightarrow{m} &= \overrightarrow{l}\cdot\overrightarrow{\bar{m}} = \overrightarrow{n}\cdot\overrightarrow{m} = \overrightarrow{n}\cdot\overrightarrow{\bar{m}} = 0\,, \end{aligned} \tag{2.103}$$

so that in the spacetime metric can be described as

$$g_{ab} = 2m_{(a}\bar{m}_{b)} - 2n_{(a}l_{b)}$$

In specifying a tetrad of the form [2.101] we have reduced the number of degrees of freedom associated with the choice of orthonormal tetrad from six to three. The remaining three degrees of freedom are fixed by specifying the directions of $\hat{r}$ and the component of $\hat{\theta}$ orthogonal to $\hat{r}$ relative to the local metric. The rest of the components of $\hat{r}$, $\hat{\theta}$, and $\hat{\phi}$ are fixed by orthonormalization.

The Ψ's are defined as components of the Weyl tensor C_{abcd} which in the vacuum case is identical to the antisymmetrised Riemann tensor R_{abcd}. In terms of this tetrad, the complex Weyl scalars Ψ is given by

$$\begin{aligned} \Psi_0 &= C_{abcd}\, l^a\, m^b\, l^c\, m^d \\ \Psi_1 &= C_{abcd}\, l^a\, n^b\, l^c\, m^d \\ \Psi_2 &= C_{abcd}\, l^a\, n^b\, m^c\, \bar{m}^d \\ \Psi_3 &= C_{abcd}\, n^a\, l^b\, n^c\, \bar{m}^d \\ \Psi_4 &= C_{abcd}\, n^a\, \bar{m}^b\, n^c\, \bar{m}^d\,. \end{aligned}$$

Here, the Weyl scalar Ψ_0 is in-going gravitational (transverse) radiation, Ψ_1 is the outgoing gauge (longitudinal) radiation, Ψ_2 is the static gravitational ("Coulomb") field, Ψ_3 is the in-going gauge (longitudinal) radiation, and Ψ_4 is the out-going gravitational (transverse) radiation. Each Ψ_n should have a $1/r^{1+n}$ falloff.

With a tetrad of the form [2.101], these components can be expressed directly in terms of spatial quantities.

$$\begin{aligned}\Psi_0 &= C_{ab}\, m^a\, m^b \\ \Psi_1 &= \frac{1}{\sqrt{2}} C_{ab}\, m^a\, \hat{r}^b \\ \Psi_2 &= \frac{1}{2} C_{ab}\, \hat{r}^a\, \hat{r}^b \\ \Psi_3 &= \frac{-1}{\sqrt{2}} C_{ab}\, \bar{m}^a\, \hat{r}^b \\ \Psi_4 &= C_{ab}\, \bar{m}^a\, \bar{m}^b\end{aligned}$$

where m^a is as defined above. C_{ab} is the symmetric, trace-free, complex-valued tensor

$$C_{ab} = R_{ab} - K\, K_{ab} + K_a^{\ c}\, K_{cb} - i\epsilon_a^{\ cd}\, \nabla_d\, K_{bc}$$

given in terms of the Ricci curvature R_{ab} of the *spatial* metric and the extrinsic curvature K_{ab}. Only Ψ_4 is of interest for our purpose here because it contains the outbound radiation content of the system. Ψ_4 can be related to the gravitational radiation in the following way: in the transverse-traceless (TT) gauge, in the conformally flat limit as we approach infinity

$$\begin{aligned}\frac{1}{4}(\ddot{h}^{TT}_{\hat{\theta}\hat{\theta}} - \ddot{h}^{TT}_{\hat{\phi}\hat{\phi}}) &= -R_{\hat{\tau}\hat{\theta}\hat{\tau}\hat{\theta}} = -R_{\hat{\tau}\hat{\phi}\hat{r}\hat{\phi}} = -R_{\hat{r}\hat{\theta}\hat{r}\hat{\theta}} \qquad (2.104) \\ &= R_{\hat{\tau}\hat{\phi}\hat{\tau}\hat{\phi}} = R_{\hat{\tau}\hat{\theta}\hat{r}\hat{\theta}} = R_{\hat{r}\hat{\phi}\hat{r}\hat{\phi}}\,, \\ \frac{1}{2}\ddot{h}^{TT}_{\hat{\theta}\hat{\phi}} &= -R_{\hat{\tau}\hat{\theta}\hat{\tau}\hat{\phi}} = -R_{\hat{r}\hat{\theta}\hat{r}\hat{\phi}} = R_{\hat{\tau}\hat{\theta}\hat{r}\hat{\phi}} = R_{\hat{r}\hat{\theta}\hat{\tau}\hat{\phi}}\,. \qquad (2.105)\end{aligned}$$

We can then set the h_+ and $h_\times$ polarizations of the radiation to

$$\ddot{h}_+ = \frac{1}{2}(\ddot{h}^{TT}_{\hat{\theta}\hat{\theta}} - \ddot{h}^{TT}_{\hat{\phi}\hat{\phi}})\,, \qquad \ddot{h}_\times = \ddot{h}^{TT}_{\hat{\theta}\hat{\phi}}\,. \tag{2.106}$$

Finally, we can use the equality of the Riemann and Weyl tensors in vacuum, to yield a relationship between Ψ_4 and the radiation, $R_{abcd} = C_{abcd}(G_{\mu\nu} = 0)$, to yield the final relation between Ψ_4 and the radiation as a metric perturbation in terms of polarizations

$$\Psi_4 = -(\ddot{h}_+ - i\ddot{h}_\times)\,. \tag{2.107}$$

The final step in analyzing the gravitational radiation using Ψ_4 is to decompose it into spherical harmonic components. This is a useful way to gain insight into the physical processes at work, as some processes may excite specific modes, and therefore can most effectively be analyzed individually. For instance, quadrupole radiation emits at twice the orbital frequency, and so will be constrained to the $\ell = 2, m = \pm 2$ harmonic modes. Since two factors of $\overrightarrow{m}$ appear in the definition of Ψ_4, and each carries a spin-weight of -1, we decompose Ψ_4 in terms of spin-weight -2 spherical harmonics ${}_{-2}Y_{\ell m}(\theta, \phi)$

given by

$$ {}_{\pm 2}Y_{\ell m}(\theta,\phi) = \left[\frac{(\ell-2)!}{(\ell+2)!}\right]^{1/2} \left[\alpha^{\pm}_{(\ell m)}(\theta)\}Y_{\ell m}(\theta,\phi) + \beta^{\pm}_{(\ell m)}(\theta)Y_{(\ell-1)m}(\theta,\phi)\right] \tag{2.108} $$

for $l \geq 2$ and $\mid m \mid \leq l$, and with the functional coefficients

$$ \begin{aligned} \alpha^{\pm}_{(\ell m)}(\theta) &= \frac{2m^2-\ell(\ell+1)}{\sin\theta^2} \mp 2m(\ell-1)\frac{cot\theta}{\sin\theta} + \ell(\ell-1)cot^2\,, && (2.109) \\ \beta^{\pm}_{(\ell m)}(\theta) &= 2\left[\frac{2\ell+1}{2\ell-1}(\ell^2-m^2)\right]^{1/2}\left(\pm\frac{m}{\sin\theta^2}+\frac{cot\theta}{\sin\theta}\right)\,. && (2.110) \end{aligned} $$

We can now decompose the dimensionless Weyl scalar Ψ_4, yielding

$$ \Psi_4(t,\overrightarrow{r}) = \frac{1}{Mr}\sum_{\ell=2}^{\infty}\sum_{m=-\ell}^{\ell} {}_{-2}C_{\ell m}(t)\,{}_{-2}Y_{\ell m}(\theta,\phi)\,, \tag{2.111} $$

where M is the total system mass, and r is the radial distance to the binary center of mass. The Newman Penrose formalism turns out to be an ideal framework for perturbative studies in general relativity. Price first showed that Ψ_4 and Ψ_0 could be used to described all non-trivial perturbations of a Schwarzschild black hole [18]. Teukolsky showed that the same is also true for Kerr spacetimes for any arbitrary spin [77].

This decomposition assumes a flat space background, and so the extraction surface of the radiation must be adequately far from the coalescing black hole binary to not be affected significantly by its gravitational potential. This is an important consideration in numerical relativity, as it requires the domain of evolution for all of our simulations to be sufficiently large in size that we may choose radiation extraction spheres on which a flat background metric is not a terribly inaccurate assumption, but large grids for numerical evolutions require a lot of computational power. Thus, accuracy requirements and efficiency requirements must be balanced. The area with the most dynamics is in the region closest to the two black holes, we require a high grid resolution near the holes, but as gravitational radiation is long wave length and extracted on a fixed radius sphere, we do not need such high resolution far out near our radiation extraction spheres. Therefore mesh refinement is used to layer grid of different resolutions to match the accuracy requirements of the different regions of our evolution domain, while not causing exponential drops in computational efficiency. We will discuss this technique in section [2.7]

Zerilli

Another approach to extract gravitational radiation data from numerical simulations is to calculate first order gauge invariant waveforms from a numerical spacetime, under the basic assumption that, at the spheres of extraction, the spacetime is approximately Schwarzschild. The stability problem for a Schwarzschild black hole in the form of a perturbation analysis on a “pure metric” was first presented by Regge and Wheeler in 1957 [74]. One result of this work was the formulation of a gauge transformation that allows a complete radial/angular separation of the Einstein equations for even and odd parities. So for some perturbation the Einstein equations

$$\begin{aligned}\delta G_{\mu\nu} &= \delta R_{\mu\nu} = \delta\Gamma^{\rho}_{\mu\nu,\rho} - \Gamma^{\rho}_{\mu\rho,\nu}\,, && (2.112)\\ \delta\Gamma^{i}_{jk} &= \frac{1}{2}g^{il}(h_{jl,k} + h_{kl,j} - h_{jk,l})\,, && (2.113)\end{aligned}$$

where $h \ll 1$ is the perturbation tensor, and $\delta\Gamma, \delta R, \delta G$ are the perturbed parts of the affine connections, Ricci, and Einstein tensors.

The Regge-Wheeler and Zerilli equations each describe one of the two degrees of freedom of linearized gravity as it propagates in a black hole background. Odd-parity perturbations are governed by the Regge-Wheeler equation, and even parity perturbations by the Zerilli equation. Odd-parity perturbations are often referred to as *axial perturbations* because they drag the inertial frame and thus cause rotation. Even-parity perturbations are often referred to as *polar perturbations* as they cause no such effects.

To begin we assume a spacetime $\gamma_{\alpha\beta}$ which can be written as a Schwarzschild background $\gamma^{Schwarz}_{\alpha\beta}$ with perturbations $h_{\alpha\beta}$:

$$\gamma_{\alpha\beta} = \gamma^{Schwarz}_{\alpha\beta} + h_{\alpha\beta} \tag{2.114}$$

with

$$\{\gamma^{Schwarz}_{\alpha\beta}\}(t,r,\theta,\phi) = \begin{pmatrix} -S & 0 & 0 & 0 \\ 0 & S^{-1} & 0 & 0 \\ 0 & 0 & r^2 & 0 \\ 0 & 0 & 0 & r^2\sin^2\theta \end{pmatrix} \qquad S(r) = 1 - \frac{2M}{r} \tag{2.115}$$

Since we are considering perturbations in which the background spacetime is expressed by the Schwarzschild metric it makes sense to expand the perturbations in spherical harmonics. The three-metric perturbations γ_{ij} can be decomposed using spherical harmonics, $Y_{\ell m}$ into $\gamma^{\ell m}_{ij}(t,r)$ where

$$\gamma_{ij}(t,r,\theta,\phi) = \sum_{\ell=0}^{\infty}\sum_{m=-\ell}^{\ell}\gamma^{\ell m}_{ij}(t,r) \tag{2.116}$$

and

$$\gamma_{ij}(t,r,\theta,\phi) = \sum_{k=0}^{6} p_k(t,r)\mathbf{V}_k(\theta,\phi) \tag{2.117}$$

where $\{\mathbf{V}_k\}$ is some basis for tensors on a two-sphere in three-dimensional Euclidean space. In Schwarzschild coordinates, the Regge Wheeler and Zerilli equations may be written

$$\begin{aligned}\partial_t^2\Psi^{(o)}_{\ell m} - \partial_r^2\Psi^{(o)}_{\ell m} + V^{(o)}_{\ell}\Psi^{(o)}_{\ell m} &= S^{(o)}_{\ell m}\,, && (2.118)\\ \partial_t^2\Psi^{(e)}_{\ell m} - \partial_r^2\Psi^{(e)}_{\ell m} + V^{(e)}_{\ell}\Psi^{(e)}_{\ell m} &= S^{(e)}_{\ell m}\,, && (2.119)\end{aligned}$$

respectively, where $S^{(o)}$ is the Regge-Wheeler source function, $S^{(e)}$ is the Zerilli source function, $V_\ell^{(o)}$ are $V_\ell^{(e)}$ are the Regge-Wheeler and Zerilli potential functions. From $\Psi_{lm}^{(o)}$ and $\Psi_{lm}^{(e)}$ we obtain the gravitational wave amplitude

$$h_+ - ih_\times = \frac{1}{r}\sum_{l,m}\sqrt{\frac{(\ell+2)!}{(\ell-2)!}}(\Psi_{\ell m}^{(e)} + \Psi_{\ell m}^{(o)})_{-2}Y^{\ell m}(\theta,\phi) + \mathcal{O}(\frac{1}{r^2}) \tag{2.120}$$

Working backwards we can use this formalism to extract the gravitational wave data from Regge Wheeler and Zerilli-Moncrief wave equations the perturbations from Schwarzschild on some extraction sphere according to even and odd harmonics.

Working with the Regge-Wheeler basis the three-metric is then expanded in terms of the (six) standard Regge-Wheeler functions $\{c_1^{\times\ell m}, c_2^{\times\ell m}, h_1^{+\ell m}, H_2^{+\ell m}, K^{+\ell m}, G^{+\ell m}\}$ [74], [76]. Where each of the functions is either *odd* ($\times$) or *even* ($+$) parity

$$\begin{aligned}\gamma_{ij}^{lm} &= c_1^{\times\ell m}(\hat{e}_1)_{ij}^{\ell m} + c_2^{\times\ell m}(\hat{e}_2)_{ij}^{\ell m} + h_1^{+\ell m}(\hat{f}_1)_{ij}^{\ell m} \\ &+ A^2H_2^{+\ell m}(\hat{f}_2)_{ij}^{\ell m} + R^2K^{+\ell m}(\hat{f}_3)_{ij}^{\ell m} + R^2G^{+\ell m}(\hat{f}_4)_{ij}^{\ell m}\end{aligned} \tag{2.121}$$

which we can write in an expanded form as

$$\gamma_{rr}^{\ell m} = A^2H_2^{+\ell m}Y_{\ell m} \tag{2.122}$$

$$\gamma_{r\theta}^{\ell m} = -c_1^{\times\ell m}\frac{1}{\sin\theta}Y_{\ell m,\phi} + h_1^{+\ell m}Y_{\ell m,\theta} \tag{2.123}$$

$$\gamma_{r\psi}^{\ell m} = c_1^{\times\ell m}\sin\theta Y_{\ell m,\theta} + h_1^{+\ell m}Y_{\ell m,\phi} \tag{2.124}$$

$$\gamma_{\theta\theta}^{\ell m} = c_2^{\times\ell m}\frac{1}{\sin\theta}(Y_{\ell m,\theta\phi} - \cot\theta Y_{\ell m,\phi}) + R^2K^{+\ell m}Y_{\ell m} + R^2G^{+\ell m}Y_{\ell m,\theta\theta} \tag{2.125}$$

$$\begin{aligned}\gamma_{\theta\psi}^{\ell m} &= -c_2^{\times\ell m}\sin\theta\frac{1}{2}\left(Y_{\ell m,\theta\theta} - \cot\theta Y_{\ell m,\theta} - \frac{1}{\sin^2\theta}Y_{\ell m}\right) \\ &\quad +R^2G^{+\ell m}(Y_{\ell m,\theta\phi} - \cot\theta Y_{\ell m,\phi})\end{aligned} \tag{2.126}$$

$$\begin{aligned}\gamma_{\psi\psi}^{\ell m} &= -\sin\theta c_2^{\times\ell m}(Y_{\ell m,\theta\phi} - \cot\theta Y_{\ell m,\phi}) + R^2K^{+\ell m}\sin^2\theta Y_{\ell m} \\ &\quad +R^2G^{+\ell m}(Y_{\ell m,\phi\phi} + \sin\theta\cos\theta Y_{\ell m,\theta})\end{aligned} \tag{2.127}$$

A similar decomposition allows the four gauge components of the four-metric to be written in terms of *three* even-parity variables $\{H_0, H_1, h_0\}$ and the *one* odd-parity variable $\{c_0\}$

$$\gamma_{tt}^{\ell m} = N^2H_0^{+\ell m}Y_{\ell m} \tag{2.128}$$

$$\gamma_{tr}^{\ell m} = H_1^{+\ell m}Y_{\ell m} \tag{2.129}$$

$$\gamma_{t\theta}^{\ell m} = h_0^{+\ell m}Y_{\ell m,\theta} - c_0^{\times\ell m}\frac{1}{\sin\theta}Y_{\ell m,\phi} \tag{2.130}$$

$$\gamma_{t\psi}^{\ell m} = h_0^{+\ell m}Y_{\ell m,\phi} + c_0^{\times\ell m}\sin\theta Y_{\ell m,\theta} \tag{2.131}$$

We can also get the lapse from $\gamma_{tt} = -\alpha^2 + \beta_i\beta^i$. We have

$$\alpha^{\ell m} = -\frac{1}{2}NH_0^{+\ell m}Y_{\ell m}\,. \tag{2.132}$$

To distinguish Zerilli and Regge wheeler modes it is useful to also write this with the perturbation split into even and odd parity parts:

$$\gamma_{\alpha\beta} = \gamma_{\alpha\beta}^{background} + \sum_{l,m} \gamma_{\alpha\beta}^{\ell m,o} + \sum_{l,m} \gamma_{\alpha\beta}^{\ell m,e}$$

where (dropping some superscripts)

$$\{\gamma_{\alpha\beta}^{o}\} = \begin{pmatrix} 0 & 0 & -c_0 \frac{1}{\sin\theta} Y_{\ell m,\phi} & c_0 \sin\theta Y_{\ell m,\theta} \\ . & 0 & -c_1 \frac{1}{\sin\theta} Y_{\ell m,\phi} & c_1 \sin\theta Y_{\ell m,\theta} \\ . & . & c_2 \frac{1}{\sin\theta}(Y_{\ell m,\theta\phi} - \cot\theta Y_{\ell m,\phi}) & c_2 \frac{1}{2}\left(\frac{1}{\sin\theta} Y_{\ell m,\phi\phi} + \cos\theta Y_{\ell m,\theta} - \sin\theta Y_{\ell m,\theta\theta}\right) \\ . & . & . & c_2(-\sin\theta Y_{\ell m,\theta\phi} + \cos\theta Y_{\ell m,\phi}) \end{pmatrix}$$

$$\{\gamma_{\alpha\beta}^{e}\} = \begin{pmatrix} N^2 H_0 Y_{\ell m} & H_1 Y_{\ell m} & h_0 Y_{\ell m,\theta} & h_0 Y_{\ell m,\phi} \\ . & A^2 H_2 Y_{\ell m} & h_1 Y_{\ell m,\theta} & h_1 Y_{\ell m,\phi} \\ . & . & R^2 K Y_{\ell m} + r^2 G Y_{\ell m,\theta\theta} & R^2(Y_{\ell m,\theta\phi} - \cot\theta Y_{\ell m,\phi}) \\ . & . & . & \begin{array}{c} R^2 K \sin^2\theta Y_{\ell m} + \\ R^2 G(Y_{\ell m,\phi\phi} + \sin\theta\cos\theta Y_{\ell m,\theta}) \end{array} \end{pmatrix}$$

For such a Schwarzschild background we can define two unconstrained gauge invariant quantities $Q^{\times}_{\ell m} = Q^{\times}_{\ell m}(c_1^{\times\ell m}, c_2^{\times\ell m})$ and $Q^{+}_{\ell m} = Q^{+}_{\ell m}(K^{+\ell m}, G^{+\ell m}, H_2^{+\ell m}, h_1^{+\ell m})$, which from [78] are

$$Q^{\times}_{\ell m} = \sqrt{\frac{2(l+2)!}{(l-2)!}} \left[c_1^{\times\ell m} + \frac{1}{2}\left(\partial_r c_2^{\times\ell m} - \frac{2}{r} c_2^{\times\ell m}\right)\right] \frac{S}{r} \tag{2.133}$$

$$Q^{+}_{\ell m} = \frac{1}{\Lambda}\sqrt{\frac{2(l-1)(l+2)}{l(l+1)}}(4rS^2 k_2 + l(l+1) r k_1) \tag{2.134}$$

$$\equiv \frac{1}{\Lambda}\sqrt{\frac{2(l-1)(l+2)}{l(l+1)}}\Big(l(l+1)S(r^2\partial_r G^{+\ell m} - 2h_1^{+\ell m}) + 2rS(H_2^{+\ell m} - r\partial_r K^{+\ell m}) + \Lambda r K^{+\ell m}\Big)\,, \tag{2.135}$$

where

$$k_1 = K^{+\ell m} + \frac{S}{r}(r^2 \partial_r G^{+\ell m} - 2h_1^{+\ell m}) \tag{2.136}$$

$$k_2 = \frac{1}{2S}\left[H_2^{+\ell m} - r\partial_r k_1 - \left(1 - \frac{M}{rS}\right) k_1 + S^{1/2}\partial_r(r^2 S^{1/2}\partial_r G^{+\ell m} - 2S^{1/2} h_1^{+\ell m})\right]$$

$$\equiv \frac{1}{2S}\left[H_2 - rK_{,r} - \frac{r-3M}{r-2M}K\right]. \tag{2.137}$$

These quantities only depend on the purely spatial Regge-Wheeler functions, and not the gauge parts. These quantities satisfy the wave equations

$$(\partial_t^2 - \partial_{r^*}^2) Q^{\times}_{\ell m} + S \left[\frac{l(l+1)}{r^2} - \frac{6M}{r^3} \right] Q^{\times}_{\ell m} = 0 \quad (2.138)$$

$$\begin{aligned}(\partial_t^2 - \partial_{r^*}^2) Q^{+}_{\ell m} + S \Bigg[\frac{1}{\Lambda^2} \Bigg(\frac{72M^3}{r^5} - & \quad (2.139)\\ \frac{12M}{r^3}(l-1)(l+2)\left(1 - \frac{3M}{r}\right)\Bigg) + \frac{l(l-1)(l+1)(l+2)}{r^2\Lambda} \Bigg] Q^{+}_{\ell m} = 0 &\end{aligned}$$

where

$$\begin{aligned} \Lambda &= (l-1)(l+2) + 6M/r & (2.140)\\ r^* &= r + 2M \ln(r/2M - 1)\,. & (2.141)\end{aligned}$$

We assume that the numerical solution, on a Cartesian grid, is approximately Schwarzschild on the spheres of constant $r = \sqrt{(}x^2 + y^2 + z^2)$ where the waveforms are extracted. The general procedure is to then project the required metric components, and radial derivatives of metric components, onto spheres of constant coordinate radius. This radius should be sufficiently large that Schwarzschild approximation does not cause errors significantly above numerical error. We may then transform the metric components and their derivatives on the selected two-spheres from Cartesian coordinates into a spherical coordinate system. We can calculate the physical metric on these spheres for our known conformal factor. We must then calculate the transformation from the coordinate radius to an areal radius for each sphere. The areal coordinate $\hat{r}$ of each sphere is calculated by

$$\hat{r} = \hat{r}(r) = \left[\frac{1}{4\pi} \int \sqrt{\gamma_{\theta\theta}\gamma_{\phi\phi}} d\theta d\phi \right]^{1/2} \quad (2.142)$$

from which

$$\frac{d\hat{r}}{d\eta} = \frac{1}{16\pi\hat{r}} \int \frac{\gamma_{\theta\theta,\eta}\gamma_{\phi\phi} + \gamma_{\theta\theta}\gamma_{\phi\phi,\eta}}{\sqrt{\gamma_{\theta\theta}\gamma_{\phi\phi}}}\, d\theta d\phi\,. \quad (2.143)$$

From there we can calculate the S factor on each sphere. Combined with the areal radius.

$$S(\hat{r}) = \left(\frac{\partial \hat{r}}{\partial r} \right)^2 \int \gamma_{rr}\, d\theta d\phi \quad (2.144)$$

This also produces an estimate of the mass.

$$M(\hat{r}) = \hat{r}\frac{1 - S}{2} \quad (2.145)$$

We can calculate the six Regge-Wheeler variables, and required radial derivatives, on these spheres by integration of combinations of the metric components over each sphere.

$$
\begin{aligned}
c_1^{\times\ell m} &= \frac{1}{l(l+1)}\int \frac{\gamma_{\hat{r}\phi}Y^*_{\ell m,\theta} - \gamma_{\hat{r}\theta}Y^*_{\ell m,\phi}}{\sin\theta}\,d\Omega \\
c_2^{\times\ell m} &= -\frac{2}{l(l+1)(l-1)(l+2)}\int \Bigg\{\left(-\frac{1}{\sin^2\theta}\gamma_{\theta\theta} + \frac{1}{\sin^4\theta}\gamma_{\phi\phi}\right)(\sin\theta Y^*_{\ell m,\theta\phi} \\
&- \cos\theta Y^*_{\ell m,\phi}) + \frac{1}{\sin\theta}\gamma_{\theta\phi}(Y^*_{\ell m,\theta\theta} - \cot\theta Y^*_{\ell m,\theta} - \frac{1}{\sin^2\theta}Y^*_{\ell m,\phi\phi})\Bigg\}\,d\Omega \\
h_1^{+\ell m} &= \frac{1}{l(l+1)}\int \left\{\gamma_{\hat{r}\theta}Y^*_{\ell m,\theta} + \frac{1}{\sin^2\theta}\gamma_{\hat{r}\phi}Y^*_{\ell m,\phi}\right\}d\Omega \\
H_2^{+\ell m} &= S\int \gamma_{\hat{r}\hat{r}}Y^*_{\ell m}\,d\Omega \\
K^{+\ell m} &= \frac{1}{2\hat{r}^2}\int \left(\gamma_{\theta\theta} + \frac{1}{\sin^2\theta}\gamma_{\phi\phi}\right)Y^*_{\ell m}\,d\Omega \\
&+ \frac{1}{2\hat{r}^2(l-1)(l+2)}\int \Bigg\{\left(\gamma_{\theta\theta} - \frac{\gamma_{\phi\phi}}{\sin^2\theta}\right)\Bigg(Y^*_{\ell m,\theta\theta} - \cot\theta Y^*_{\ell m,\theta} \\
&- \frac{1}{\sin^2\theta}Y^*_{\ell m,\phi\phi}\Bigg) + \frac{4}{\sin^2\theta}\gamma_{\theta\phi}(Y^*_{\ell m,\theta\phi} - \cot\theta Y^*_{\ell m,\phi})\Bigg\}\,d\Omega \\
G^{+\ell m} &= \frac{1}{\hat{r}^2 l(l+1)(l-1)(l+2)}\int \Bigg\{\left(\gamma_{\theta\theta} - \frac{\gamma_{\phi\phi}}{\sin^2\theta}\right)\Bigg(Y^*_{\ell m,\theta\theta} - \cot\theta Y^*_{\ell m,\theta} \\
&- \frac{1}{\sin^2\theta}Y^*_{\ell m,\phi\phi}\Bigg) + \frac{4}{\sin^2\theta}\gamma_{\theta\phi}(Y^*_{\ell m,\theta\phi} - \cot\theta Y^*_{\ell m,\phi})\Bigg\}\,d\Omega
\end{aligned}
$$

where

$$
\gamma_{\hat{r}\hat{r}} = \frac{\partial r}{\partial \hat{r}}\frac{\partial r}{\partial \hat{r}}\gamma_{rr}\,, \qquad \gamma_{\hat{r}\theta} = \frac{\partial r}{\partial \hat{r}}\gamma_{r\theta}\,, \qquad \gamma_{\hat{r}\phi} = \frac{\partial r}{\partial \hat{r}}\gamma_{r\phi}\,. \tag{2.146}
$$

From here we can construct the gauge invariant quantities from these Regge-Wheeler and Zerilli variables

$$
Q^{\times}_{\ell m} = \sqrt{\frac{2(l+2)!}{(l-2)!}}\left[c_1^{\times\ell m} + \frac{1}{2}\left(\partial_{\hat{r}}c_2^{\times\ell m} - \frac{2}{\hat{r}}c_2^{\times\ell m}\right)\right]\frac{S}{\hat{r}} \tag{2.147}
$$

$$
Q^{+}_{\ell m} = \sqrt{\frac{2(l-1)(l+2)}{l(l+1)}}\frac{(4\hat{r}S^2k_2 + l(l+1)\hat{r}k_1)}{(l-1)(l+2) + 6M/\hat{r}}\,. \tag{2.148}
$$

This formalism is convenient as it gives us h_+ and $h_\times$ already decomposed into ℓ and m modes with no extra integration stages required. This is a useful way to gain insight into the physical processes at work, as some processes may excite specific modes, and therefore can most effectively be analyzed individually. For instance, quadrupole radiation emits at twice the orbital frequency, and so will be constrained mostly to the $\ell = 2, m = \pm 2$ harmonic modes. This is also a convenient formalism in that with it we can extract a mass estimate calculated from g_{rr}, an estimate of ADM mass enclosed within each two-sphere, and an estimate of momentum at each two-sphere. In Chapter [5] I will discuss the relative advantages of each of the two gravitational wave extraction methods presented in this section.

2.6.4 Proving Well-posedness

For a system of partial differential equations of the form

$$\partial_t u = P(D)u \,, \tag{2.149}$$

where some n-dimensional vector-valued function u, and spatial derivative operators defined by D, the *initial value* problem (IVP) corresponds to finding a solution $u(t, x)$ starting from some known initial data $u(t = 0, x)$. The concept of a *well-posed* problem, introduced in 1902 by Hadamard [79], is generally understood to satisfy three criteria:

- a solution to the problem exists (existence)
- the solution is unique (uniqueness)
- the solution depends continuously on the intial data (stability).

We may define this third condition of well-posedness for the Cauchy problem as the following [80]

> *A system of partial differential equations is called well-posed if there exists constants K and α, independent of the data, that satisfy*
>
> $$\mid u(\cdot, t) \mid < K e^{\alpha t} \mid u(\cdot, 0) \mid \tag{2.150}$$
>
> *for all $t \geq 0$, where $\mid \cdot \mid$ is the norm of the function.*

That is to say that the norm of the solution can be bounded by the same exponential for all initial data.

Attempts to solve ill-posed problems in numerical simulations will result in unstable solutions, thus well-posedness is not only a mathematical condition, but also significant for formulating a functioning numerical code. While most physical problems naturally give well-posed evolution systems, it is not difficult to find rather simple systems which are not well-posed. One example which closely relates to the problem of the $3+1$ evolution equations is the simple system:

$$\partial_t u = M \partial_x u \,, \qquad M = \begin{pmatrix} 1 & 1 \\ 0 & 1 \end{pmatrix} . \tag{2.151}$$

If we consider the evolution of a single Fourier mode, and consider the solution

$$u_1 = (ikAt + B)e^{ik(t+x)} \,, \qquad u_2 = Ae^{ik(t+x)} \,, \tag{2.152}$$

where A and B are constants, we see that u_2 is oscillatory in time and, thus, clearly bounded. However, u_1 has an additional linear growth. As the solution cannot be bounded by an exponential independent of the initial data, because one can always choose a k

large enough to surpass such a bound, we must then declare the solution *ill-posed*. Such solutions can often appear in 3+1 solutions in numerical relativity. Thus we wish to be sure we choose a category of evolution equations with solutions which are always well-posed. One such category of partial differential equations which can be shown to be well-posed under arbitrary conditions are called *hyperbolic*.

Hyperbolicity is a necessary condition of well-posedness for the Cauchy problem. Hyperbolicity is a condition on the matrix of spatial derivatives A^{ij} in the first order system

$$\partial_t u = A^{ij} \nabla u + B(u) \,. \tag{2.153}$$

If all eigenvalues for A are real and A has a complete set of eigenvectors, we say that the system is *strongly hyperbolic*. If all eigenvalues for A are real but A does not have a complete set of eigenvectors, we say that the system is *weakly hyperbolic*. It has been shown that strong hyperbolicity is equivalent to a stringent condition for well-posedness [81]. This concept may be intuitively understood as a requirement that systems behave as generalizations of the simple wave equation, that have the property of having finite propagation speeds, and thus a finite past domain of dependence.

If a system is strongly hyperbolic one can always find a positive definite a Hermitian matrix $H(n_i)$ such that

$$HP - P^T H^T = HP - P^T H = 0 \,, \tag{2.154}$$

where $P := A^i n_i$ for some arbitrary unit vector n_i. With this symmetrizer H we then get a complete set of eigenvectors

$$P e_a = \lambda_a e_a \tag{2.155}$$

with eigenvalues of λ_a. We may say that a system is *symmetric hyperbolic* if all A^i are symmetric (i.e. H is independent of n_i). Symmetric hyperbolic systems are, thus, clearly strongly hyperbolic, but not all strongly hyperbolic systems are symmetric. We can then also define *strictly hyperbolic* as one for which all eigenvalues of P are both real and distinct for all n_i. This implies that the symbol P may be diagonalized and automatically strongly hyperbolic.

The importance of the Hermitian symmetrizer in showing well-posedness is related to the construction of the inner product for solutions of our differential equations

$$\begin{aligned} \langle u, v \rangle &:= u^T H v \,, \\ \mid u \mid^2 := \langle u, u \rangle &:= u^T H u \end{aligned} \tag{2.156}$$

which gives the *energy norm* for our system of equations. Thus, if we can show that there is a bound on this energy norm, we show that our system is well-posed. This tool has been used to show well-posedness for all systems in this thesis for some given assumptions.

A major criticism of the ADM formulation of the Einstein equations is that the evolution equations in this system are only weakly hyperbolic, except under very specific conditions. However, stable and convergent results have been and continue to be produced in the BSSN system by applying a system for constraint damping to the right hand sides of the evolution of the extrinsic curvature equations and by applying dissipation to

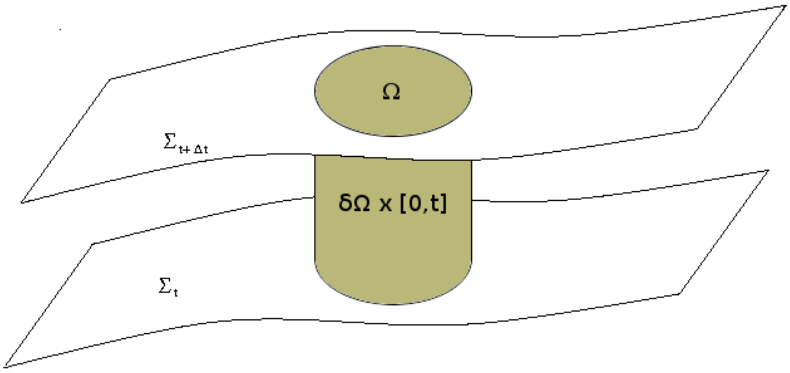

Figure 2.5: A diagram illustrating the use or artificial time-like outer boundaries, Ω in spacelike slices of the evolution domain, Σ.

the evolution system. One major advantage of the harmonic formulation of the Einstein equations is that the evolution equations in this system are manifestly strongly hyperbolic. However, gauge specification is less intuitive and techniques such as the moving puncture intial data are more challenging to implement for harmonic codes.

2.6.5 Boundary Conditions

To accurately study the asymptotic behavior of isolated systems, one needs to approach infinity. However, as a computer can only differentiate a finite number of points in a finite amount of real time in the simulation of such numerical systems, to deal with the finite memory of real computer clusters, we must operate on a finite number grid points. The simplest and most common approach to this problem in numerical relativity is to truncate the computational domain we wish to evolve by introducing an artificial time-like outer boundary at a finite distance from the region of interest in our evolution. The injection of this artificial boundary introduces an intial boundary value problem (IBVP). That is, we must solve the problem of well-posedness for this truncated system if we want to maintain a hyperbolic reduction of the Einstein equations which remains well-posed. This is a problem to both the mathematical and physical correctness of the numerical solution, as well as a problem for numerical accuracy. In order for this artificial boundary to work we need a boundary that:

1. controls incoming radiation,
2. are compatible with the constraints,
3. and are well-posed.

Point **1.** means that the simulation outer boundaries must be non-reflective and not introduce artificial in-going modes. Point **2.** means that those boundaries must also correspond to the same condition as the full system that the constraints are vanishing. Finally, point **3.** means that a unique solution must still exist which is continuously dependent on the initial data for the full system including the outer boundaries.

Generically, for such a set of artificial boundaries, the picture we have is that the metric, g is calculated on a manifold, $\mathcal{M}$, with boundary $\mathcal{S} \cup \mathcal{T}$ and an edge $\Sigma = \mathcal{S} \cap \mathcal{T}$, where $\mathcal{S}$ and $\mathcal{T}$ are space- and time- like hypersurfaces respectively for g and intersect on the spacelike hypersurface Σ. We will assume that $(\mathcal{M}, g)$ satisfy some global hyperbolicity and all fields to be smooth.

The first artificial outer boundary treatment has thus far been proposed which satisfies all of the above requirements for the fully nonlinear system was proposed by Friedrich and Nagy in 1998 [82]. However, this system is very specific and very hard to implement numerically. There do also exist alternative approaches to finite radius artificial boundaries. It is possible to compactify one's domain of evolution to include spatial infinity by a transformation of coordinates. However, given a finite number of points there could be some numerical error backscattered by the increasing changes in resolution, and the dissipation and damping required can often generate as much error as artificial boundaries for an even less efficient system. Another approach is to choose a slicing condition with the coordinate transformation to instead include null infinity. This problem remains a work in progress in the field of numerical relativity. Thus, the simplest approach remains the standard: timelike artificial outer boundaries.

In order to simplify the problem of obtaining well-behaved artificial outer boundaries, we may make some assumptions and assign some basic conditions. One wants an outgoing radiation boundary condition at an artificial outer boundary for the simulation domain that is at a sufficiently large radius

- to be causally disconnected from the highly dynamical parts of the simulation,
- which would allow for enough far-out wave extraction radii to accurately extrapolate the gravitational waveform at null infinity,
- and which is far enough out to allow for a perturbative treatment for the boundaries without becoming reflective, ill-posed, or interfering with the physics of the simulation.

Given a boundary at such a distance, we may consider a linearized approximant of the Einstein equations for the outer boundaries of our numerical simulations. Most astrophysically realistic spacetimes are asymptotically flat. This means that at large distances from the black holes (or neutron stars or other object of interest) the spacetime is flat plus some perturbation that falls off as $1/r$. These perturbations may be waves, gauge modes, or constraint violating modes that arise from numerical errors, which need to be able to smoothly leave the evolution domain without backscattering or causing further violation of the system constraints.

In the past few years there have been many such "linearized" boundary treatments proposed. Many of which maintain well-posedness and reduce incoming artificial radiation. In 2006 Kreiss and Winicour proposed a method for the Harmonic reduction of the Einstein equations that is well-posed and constraint preserving for the 1st order system [83] without requiring linearisation, only assuming that the boundaries are in the constant coefficient limit. In 2007 Buchman and Sarbach proposed an approximation that works by studying the reflection from a Psi-freezing constraint preserving outer boundary for an analytic problem and then subtracting those modes for corresponding modes in simulations [84]. Similarly Rinne proposed conditions for the first order harmonic system that control incoming radiation by specifying data for the incoming fields of the Weyl tensor [85]. In this thesis I propose two more sets of well-posed constraint preserving boundaries for the 'Generalized harmonic' and BSSN evolution systems.

In standard simulations we often use much simpler *ad hoc* conditions, simply using the fact that the boundaries are far enough away to be causally disconnected from the simulation. This, of course, limits the time that the simulation can remain accurate in the region of interest before it is saturated by noise from the outer boundaries, and pushing the boundaries far away is extremely computationally expensive. So the use of accurate, well-posed, and constraint preserving boundary conditions becomes more necessary as modern simulations become more stable and more often required to simulate longer physical times with greater accuracy and efficiency, so to be completed in a reasonable amount of time.

For simulations with causally disconnected outer boundaries, a simple "naive" boundary condition used in many primitive simulations are called *radiative* boundary conditions, called such because it allows incident radiation to flow smoothly out of the simulation grid. Such *ad hoc* conditions work on the assumption that far away all fields behave a outward travelling spherical waves $f \sim f(0) + u(r - vt)/r$. An example of a radiative boundary condition is

$$f = f_0 + \frac{u(r - vt)}{r} + \frac{h(r + vt)}{r} \tag{2.157}$$

for some outgoing and in-going functions u and h, and wave speed v, and assuming a $1/r$ falloff for outgoing waves. This leads to the differential equation

$$\frac{x^i}{r}\frac{\partial f}{\partial t} + v\frac{\partial f}{\partial x^i} + \frac{vx^i}{r^2}(f - f_0) = H\frac{vx^i}{r^2} \tag{2.158}$$

where x^i is the normal direction to the boundary, and $H = 2dh(s)/ds$.

These radiative boundary conditions work under the assumptions that:

1. the spacetime is asymptotically flat,
2. the sources of the gravitational field are localized in a small neighborhood far from the boundaries,
3. the shift is small enough at the boundary location that characteristic speeds may be neglected,
4. all fields move at or below the speed of light,
5. and there are no in-going fields at the boundary location.

Even if all of these assumptions were perfectly valid, such conditions do nothing to enforce preservation of the physical or coordinate constraints. Thus, even in an ideal, shift-free, linear wave-toy case it would be important to place the boundary far enough away to prevent incoming constraint violations from the boundary from interfering with the simulation results.

In addition to the problem of *ad hoc* conditions causing violations of the physical and coordinate constraints, the second important question for stability and accuracy of artificial boundaries is that of well-posedness. In the Einstein equations we have source terms, but these are typically quadratic in quantities that drop off to small values at large radii, and can be ignored at the boundaries. Also, not all fields in the Einstein equations propagate with the same speed, and thus we must be careful in our choice of v. However, in the BSSN system all eigenfields propagate along timelines or at the gauge speed. We can thus assign all speeds to 1 except the conformal factor and extrinsic curvature. For a second order ADM type reduction of the wave equation (and for the Einstein equations) we find that radiative boundary conditions are not well-posed in the spatial derivatives of the metric.

If, as in Section [2.6.4], we consider an evolution systems such as

$$\partial_t u = M^i \partial_i u \,, \tag{2.159}$$

where we constrain the domain of dependence to the region $\overrightarrow{x} \in \Omega$, and construct a principal symbol $P(n_i) = M^i n_i$. If we again assume that the system is symmetric hyperbolic with a Hermitian matrix such that $HP = P^T H$ then taking the energy norm gives

$$E(t) = \int_\Omega u^\dagger H u dV \,, \tag{2.160}$$

and taking the time derivative, we obtain

$$\frac{dE}{dt} = -\int_\Omega \partial_i (u^\dagger H M^i u) dV \,. \tag{2.161}$$

Finally, by applying divergence theorem we obtain

$$\frac{dE}{dt} = -\int_{\partial\Omega} (u^\dagger H M^i u) n_i dA = -\int_{\partial\Omega} (u^\dagger H P u) dA \,. \tag{2.162}$$

Thus, the well-posedness of our problem depends on the flux through the boundary $\partial\Omega$, and incoming fields must be bounded to have a bound on the energy growth of the system.

Boundary conditions in which one sets the inward eigenfields proportional to some small factor, S, times outward eigenfields are called *maximally dissipative* boundary conditions. We can generalize these and add some predefined function for incoming fields, $g(t)$. If S is set to zero we call these *Sommerfeld-type* boundary conditions, $S = -1$ are called *Dirichlet*, $S = 1$ are called *Newmann type* boundary conditions. Newmann and Dirichlet are reflective conditions for $g(t) = 0$. Thus, Sommerfeld-type boundaries are a natural choice for unknown and assumed to be negligible incoming fields. More generally, one may need to consider fields tangential to the boundary as well, in order to obtain well-posedness. This will be discussed in Section [3.2].

Additionally, many physical simulations allow some symmetries, which may be exploited to simplify the problem and improve computational efficiency. For example, it might be possible to simulate a rotating star by 'slicing' the space in half through the equatorial plane, simulating only one half, and placing a reflection boundary condition on the slicing plane, and thus we only have to evolve the simulation for half the number of grid points. Additionally, we might want to assume that this star has rotational symmetry about the axis of rotation of the star. In that case, it would be sufficient to simulate only one half of the $\phi =$ const plane of the star, and we only have to evolve one fourth of the simulation grid points. To increase efficiency in simulations we often take advantage of this in our choice of boundaries for the simulation domain. Within a simulation we may apply different conditions to different boundary faces. Rotating or reflective *symmetry* boundary conditions may be applied on some faces, and other physical boundary conditions on the other faces.

In Chapter [3] I will discuss boundary conditions I developed for the second order harmonic formulation of the Einstein equations, which are both well-posed and constraint preserving, and show that these improve constraint preservation, accuracy and stability over the bulk domain, relative to simple naive Sommerfeld-type boundaries. I will also present a set of constraint-preserving boundary conditions for the BSSN system.

2.7 Running Numerical Simulations

As is clear from the abundant amount of background information required to explain the workings of the numerical simulations involved in this thesis, it is clear that the execution of 3D relativistic numerical simulations of black hole spacetimes is a daunting and involved task. The focus of my work for this dissertation has been on the performance, accuracy, and well-posedness of such simulations, followed by parameter studies performed with this code with an eye on use of waveforms for GW detector data analysis. In order to perform the simulations involved here, and test the methods proposed, I used the Cactus computational toolkit.

The only codes I have myself contributed to in a significant portion (or all) of the development of are: the averaged ICN scheme, the initial data solver for Trumpet initial data, the mass solver for puncture initial data, the constraint preserving BSSN boundary conditions, the Padé extrapolation scheme for excision horizons, and most significantly the SBP and constraint preserving SBP boundary conditions for the Harmonic reduction of the Einstein equations. In much smaller proportion, I have contributed to: the development of the AEIHarmonic code for harmonic evolutions and the choice and implementation of gauges therein. AEIHarmonic was the project of Bela Szilagyi and his support in the encouraging implementation of my boundary conditions in his code was invaluable [40].

The BSSN evolution codes I used were developed by Miguel Alcubierre, Bernd Brügmann, Gabrielle Allen, and Denis Pollney [86, 87]. The Puncture initial data solver was written by Marcus Ansorg, Erik Schnetter, and Frank Loeffler, the PN initial data solver was a group effort described in [88]. The symmetry, interpolation, input and output, and coordinate algorithms are a major part of the Cactus computational toolkit described in [89–91]. Finally the mesh refinement code used is a package called Carpet and was developed and heavily supported by Erik Schnetter [92, 93].

2.7.1 Cactus and Carpet

The Cactus computational toolkit is a modular component-based computational framework for the development of applications for the solution complex multi-physics computational problems. The Cactus framework consists of a central infrastructure called the “flesh”, which consists of a module manager; and the components called “thorns” which can perform tasks such as setting up a computational grid, setting up coordinate systems, defining boundary and initial conditions, solving partial differential equations, and generating input and output. The Cactus Computational Toolkit provides a standard set of distributed thorns (such as grid setup, input and output and most of the previously listed functions) to provide basic functionality for the solution of computational physics problems.

Cactus provides the basic parallel framework that supports several different codes in the numerical relativity community used for modeling black holes, neutron stars and gravitational waves. The code employs a 3+1 decomposition of the Einstein equations described in Section [2.3] from [26, 94]. The equations are discretized using fourth order finite differences described in Section [2.5.1] with adaptive mesh refinement and using Runge-Kutta time integrators explained in Section [2.5.2].

The time evolution equations are formulated using a variant of the BSSN formulation described in [95] and coordinate conditions described in [33] and [60]. These are a set of 25 coupled partial differential equations which are first order in time and second order in space. The most important variable describing the geometry is the three-metric g^{ij} , which is a symmetric positive definite tensor defined everywhere in space, defining a scalar product which defines distances and angles. The code contains the formulation and discretisation of the right hand sides of the time evolution equations. Initial data and many analysis tools, as well as time integration and parallelization, are handled by other thorns already in Cactus. The current state of the time evolution, i.e., the three-metric g^{ij} and other variables, are communicated into and out of Cactus using a standard set of Cactus variables. Thus it is possible to use various pre-existing Cactus thorns with the thorns written for this thesis, such as initial data solvers and analysis tools.

Cactus provides infrastructure components for storage handling, parallelization, mesh refinement, and I/O methods are implemented by thorns in the same way as the computational physics thorns. Carpet [93] is a driver developed by Erik Schnetter that implements Berger-Oliger mesh refinement [96] to set up the computational grid variables used in the simulations in this thesis. Carpet ‘refines’ parts of the simulation domain by factors of two at prescribed distances from prescribed centers. Thus allowing us to place high resolution grid around the areas of interest in our simulation, while evolving low resolution grids in the outer areas of the simulation where spacetime is relatively flat and approximately linear. This significantly reduces the required memory and computational time for our simulations.

With these tools, I was able to implement my methods derived in the following Chapters as ’thorns’ and run simulations of a variety of initial data, including binary black hole simulations. I was able to run these simulations with initial data derived from quasi-circular and post-Newtonian solvers in cactus and Mathematica respectively to simulate a wide variety of binary black hole initial parameters some of which are described in Table [4.2].

2.8 Outline of Thesis

This background section should provide enough foundation to understand the research I have performed for this thesis:

- In Chapter [3] I will explain the derivation, implementation and testing of a set of well-posed constraint preserving boundary conditions for both the BSSN and Harmonic evolution systems described in sections [2.3.3] and [2.3.2]. The background for the details of well-posedness and the approach to artificial boundaries this section may be found in Section [2.6.4] and Section [2.6.5] respectively. The discrete nature of numerical simulations described in sections [2.5.2] and [2.5.1] should provide the background necessary to understand the importance of proving stability for the fully discrete system as well as for the continuum solution. I will show the results of tests which clearly show the advantages of well-posed boundary conditions and differencing techniques for efficient numerical simulations of any relativistic spacetimes.
- In Chapter [4] is discuss the results of a study of the parameter space of binary black hole simulations (spins and mass ratios). Simulations were strategically run in sequences with data throughout this parameter space. We extracted the final spins and recoil velocity for these simulations and fit to this data a phenomenological formula to predict the final spin and kick of a merged black hole from arbitrary binary initial data. The background provided in sections [2.1], [2.2], and all of [2.6] should provide most of the background required to understand the work in this chapter.
- Finally, in Chapter [5] I will discuss the use of the waveforms extracted from the simulations described in Chapter [4] to determine the effect of black hole spin on the signal to noise ratio of waveforms in various gravitational wave detector pipelines for a range of detectable binary masses. I will also discuss the use of similar waveforms combined with post-Newtonian inspiral waveforms to fit a set of analytical inspiral-merger-ringdown waveforms to take into account spin effects in binary inspiral and merger.

I will conclude this thesis with a summary of my findings for all of the aforementioned chapters, and ideas on how to progress and future outlook. Followed by relevant appendices for the results chapter and a bibliography of references.

2.8.1 Units and Notation

First, a note about units before I go into a discussion of my results and research. Unless otherwise noted, geometrized units are used throughout this thesis. This means $G = c =$

1. This allows us to express any observable quantities in terms of the total mass of the system, M, given that all observables for the black hole binary solution scale invariantly with the total system mass. Two convenient conversion factors are $1\,M_{\odot} = 5 \times 10^{-6}\,s$ for time measurements and $1\,M_{\odot} = 1.5\,km$ for distance measurements.

Greek indices are used to indicate a spacetime quantity, whereas Roman indices indicate a purely spatial quantity. This distinction is also made using a preceding parenthetically enclosed superscript of “3” for spatial quantities and “4” for space-time quantities, for example, ${}^{(3)}g_{ij}$ and ${}^{(4)}g\mu\nu$, respectively. However, in cases such as the examples given where the index convention specifies the dimensionality of the object and no further identification is needed, the superscript is omitted. Also, the metric signature will be $(-1, 1, 1, 1)$.

Partial derivatives are interchangeably denoted $\frac{\partial f}{\partial x}$, $\partial_i f$, or $f_{,i}$ depending on convenience and clarity.

Chapter 3

Boundary conditions

> *The box was a universe, a poem, frozen on the boundaries of human experience.*
>
> William Gibson

In numerical relativity, one commonly solves the Einstein equations in a bounded domain, and the question is then born about what boundary conditions ought to be provided at this artificial outer boundary. As explained in Section [2.6.5], specifying boundary conditions continues to be a challenge in numerical relativity in order to obtain a long time convergent numerical simulation of the Einstein equations in domains with artificial outer boundaries. The particular conditions that are enforced ideally satisfy a number of properties. Most importantly, in order to ensure stability of the system, they should be compatible with the interior evolution equations so that the discretised system forms a *well-posed* initial-boundary-value problem (IBVP). Secondly, they should take into account the fact that Einstein evolutions always involve constraint equations as well as time evolution equations, and satisfy the constraints at all times. Otherwise, constraint violations introduced by the boundaries are likely to drive the evolution away from an Einstein solution. Finally, the boundary conditions should be compatible with physical and numerical considerations affecting the accuracy of the solution: they should be transparent to outgoing radiation, and restrict the amount of spurious incoming radiation from beyond the computational domain, which is assumed to contain all of the dynamics of interest.

Finding appropriate boundary conditions that lead to a well-posed evolution system and maintain preservation of the constraints of the system is a difficult problem. It has been a subject of intense investigation in recent years and has been a major focus of my thesis research. In this chapter I present well-posed constraint preserving boundaries for the harmonic formulation, and a stable and constraint preserving system for conformally flat spacetimes in the BSSN formulation (introduced in in Section [2.3]) of the Einstein equations in 2nd order form. I present the derivation of these conditions, prove mathematically their well-posedness, and for the harmonic system I follow with thorough test of the well-posedness, convergence, stability, and constraint preservation of these conditions in numerical simulations of non-linear spacetimes.

3.1 Boundaries for the Harmonic Formulation

One of the challenges of numerical relativity is choosing a formalism to write the field equations that allows for long-term stable numerical evolution. In Section [2.3.3] I show the derivation of the harmonic coordinate condition, $\Box x^{\mu} = 0$ for the Einstein equations and explained why they are a practical set of evolution equations for numerical relativity simulations because, when written with this condition imposed, they take on a mathematically appealing form such that the principle part of the evolution equations takes on a manifestly symmetric hyperbolic form, and the principle part of each PDE satisfied for each metric component $g_{\mu\nu}$ becomes the scalar wave operator $\Box g_{\mu\nu}$, allowing for a clear existence and uniqueness proof. This system gives us four new constraints in addition to the physical (momentum and Hamiltonian) constraints in the form of the coordinate conditions. As the unbounded harmonic evolution system can offer well-posed solutions, what is left is to derive well-posed and constraint preserving set of conditions for the imposition of artificial outer boundaries. In this section I will explain the derivation, implementation and testing of boundary conditions formulated for the 2nd order harmonic formulation of the Einstein equations on a finite differenced Cartesian grid.

The approach which I introduce in this section is partially derived from a method first discussed in a series of related papers by Kreiss, Winicour and collaborators in [47,83,97], combined with the summation by parts (SBP) energy method discussed in Refs. [98–100]. By deriving energy estimates for the semi-discrete system using the “summation by parts” rule [3.1.3], one can ensure well-posedness [99, 101–103]. By applying this approach to boundary conditions which are radiation controlling and constraint-preserving, I am able to construct an IBVP which satisfies all of the above conditions.

The conditions are derived for a harmonic formulation of the Einstein equations which has been implemented in the code described in [40, 104] with the help of Bela Szilagyi. The evolution equations of the formulation, given explicitly in Section [2.3.3], are first-order in time, second-order in space. I approximate these equations using standard finite-difference techniques, however to ensure a well-posed discrete IBVP, I have worked out finite-difference operators for this system which satisfy the summation by parts property. Since the computational domain uses Cartesian coordinates on a cube, I have had to develop consistent operators for the corners and edges, as well. Following the developments of [83, 105] and [43, 106], I was able to construct boundary conditions of a Sommerfeld type, which are both well-posed and satisfy both the Einstein and harmonic constraints.

I have used the newly constructed boundary conditions in a number of practical tests and found them to perform extremely well in comparison with other standard techniques. Test evolutions include linear and nonlinear waves. In each case, the new boundary conditions are found to be more transparent to outgoing waves, as well as better at reducing the overall constraint violations on the grid. Further, the evolutions are stable against perturbations by high-frequency constraint violation (“noise”) added to the data, providing a strong demonstration of robustness. Tests were also done for black hole space-times. For head-on collisions and inspiral, the boundary conditions showed improvements in reducing reflections and constraint preservation, and thus improved the waveform accuracy. I published many of these results in [107].

3.1.1 Discretization

I start by introducing the system of evolution equations and numerical setup to which I wish to apply the proposed boundary conditions. The numerical implementation of the harmonic evolution equations in second differential order in space and first order in time form (2.46-2.47) from Section [2.3.3]

$$\partial_t \tilde{g}^{\mu\nu} = -\frac{g^{it}}{g^{tt}} \partial_i \tilde{g}^{\mu\nu} + \frac{1}{g^{tt}} Q^{\mu\nu} \,, \tag{3.1}$$

$$\partial_t Q^{\mu\nu} = -\partial_i \left(\left(g^{ij} - \frac{g^{it} g^{jt}}{g^{tt}} \right) \partial_j \tilde{g}^{\mu\nu} \right) - \partial_i \left(\frac{g^{it}}{g^{tt}} Q^{\mu\nu} \right) + \tilde{S}^{\mu\nu}(\tilde{g}, \partial\tilde{g}, F, \partial F) \,, \tag{3.2}$$

follows the “method of lines” approach [2.5.2], which applies to systems which can be cast in the form of an ordinary differential equation containing some spatial differential operator $\mathbf{L}$

$$\partial_t \mathbf{q} = \mathbf{L}(\mathbf{q}). \tag{3.3}$$

The time integration can be carried out using standard methods, such as the Runge-Kutta algorithm described in Section [2.5.2].

While it is possible to reduce this system to first order in space and time, it may not be a practical in numerical simulations. A reduction to first order in space increases the solution space leading to new constraints which must be satisfied during the evolution, and thus to more space for inaccuracy. Thus, I keep the system second order in space and derive differencing stencils which obey the SBP property and allow us to derive a well-posed semi-discrete boundary value problem.

For the system of interest in this thesis spatial derivatives on the right-hand-sides of (3.1-3.2) are computed by finite differencing on a uniformly spaced Cartesian grid. We introduce a grid of equidistant spatial points $x = (x_{i^1}, \ldots, x_{i^d})$. For this derivation I assume that in each direction I have the same number of points N, and $i_x = 0, \ldots, N-1$. I denote the grid spacing by h. I have implemented finite difference stencils which are fourth-order accurate over the interior grid and second-order accurate at the boundaries.

In the linear coefficient case, if the Cauchy problem is well-posed, as it is for the first order harmonic system, then the semi-discrete problem (discrete space, continuous time) is stable for these centered finite differencing stencils. Given that my evolutions are done with Runge-Kutta methods for time integration, the fully discrete system will remain well-posed for sufficiently small Courant factors. However, this property does not hold true for the second order system where second order spatial derivatives appear. In order to show well-posedness for this semi-discrete system I need to ensure that my second order derivatives also obey additional properties required for well-posedness, and this needs to be shown explicitly.

As an illustration of the derivation of the finite differencing for second differential order stencils in our code, we look at a system of partial differential equations, here illustrated as

$$\frac{d}{dt} v(t, \vec{x}) = P v(t, \vec{x}), v = (U, V)^T \,, \tag{3.4}$$

where $\vec{x} \in \Re, U : \Re \times \Re^d \to \Re^P, V : \Re \times \Re^d \to \Re^q$ and

$$P = \left[\begin{array}{cc} A^i\partial_i + B & C \\ D^{ij}\partial_{ij} + E^i\partial_i + F & G_i\partial_i + J \end{array} \right]. \tag{3.5}$$

Here the state vector v is split into the variables for which only first spatial derivatives appear, U, and which second appear, V.

Here I will temporarily treat the problem of well-posedness for second differential order in space systems in Fourier space. If we define the scalar product $(u, v) = \int_a^b u^\dagger v dx$, with the norm is $\|u\| = (u, u)$, then the set of functions $\{\frac{1}{2\pi} e^{\mathrm{i}\langle\vec{\omega},\vec{x}\rangle}, \vec{\omega} = (\omega_1, \omega_2, \ldots, \omega_d), \omega_r\}$ forms the orthonormal basis for the space of square integrable functions. In this space the functions $v(t, \vec{x})$ may be represented as

$$v(t, \vec{x}) = 2\pi \sum_{\vec{\omega}} e^{\mathrm{i}\langle\vec{\omega},\vec{x}\rangle} \hat{v}(t, \vec{\omega}), \tag{3.6}$$

where $\hat{v}(t, \vec{\omega})$ are the Fourier coefficients. By considering the partial derivatives $\partial_{i^1 i^2 \ldots}$ operating on the basis vectors $\frac{1}{2\pi} e^{\langle\vec{\omega},\vec{x}\rangle}$, one defines the Fourier symbols, $\hat{\partial}_{i^1 i^2 \ldots i^n} = (\mathrm{i}\omega_{i^1})(\mathrm{i}\omega_{i^2}) \ldots (\mathrm{i}\omega_{i^n})$. One can then Fourier transform the system $(P \to \hat{P})$ and reduce the evolution problem to a system of ordinary differential equations (ODEs). It is thus shown via a first order reduction in Fourier space, that the well-posedness is not influenced by the lower order terms of $\hat{P}$:

$$P = \left[\begin{array}{cc} \mathrm{i}\omega_0 A^n & C \\ \omega_0^2 D^{nn} & \mathrm{i}\omega_0 G^n \end{array} \right], \tag{3.7}$$

where $\omega_0 = |\vec{\omega}|, \omega_i = \omega_0 n_i$ and $M^n = M_i n_i$. It is shown in Section [2.6.4] that if there exists a positive definite a Hermitian matrix $H(n_i)$ such that $HP - P^T H^T = HP - P^T H = 0$ where $P := A^i n_i$ for some arbitrary unit vector n_i, with this symmetrizer H I then get a complete set of eigenvectors $Pe_a = \lambda_a e_a$ with eigenvalues of λ_a. We may say that a system is *symmetric hyperbolic* if all A^i are symmetric (i.e. H is independent of n_i). If there exists a positive constant K, such that $K^1 I_{\omega 0} \leq H \leq K I_{\omega 0}$ (where $I_{\omega 0} = diag(\omega_0^2 I_p, I_q)$, then the problem is well-posed in the norm

$$\|v\|_\partial^2 = \int \sum_{i=1}^{d} |\partial_i U|^2 + |V|^2 . \tag{3.8}$$

Then the problem is also well-posed in the norm $|v|_H$, defined as

$$\|v\|_H^2 = \sum_{\vec{\omega}} \hat{v}^\dagger \hat{H} \hat{v} . \tag{3.9}$$

On the discrete level a grid function is defined as $v = v(t, x, h)$ and the system above becomes

$$\frac{d}{dt}v = Pv, v = (U,V)^T\,, \tag{3.10}$$

$$P = \left[\begin{array}{cc} A^iD_i^{(}1,n) & C \\ D^{ij}D_{ij}^{(2,n)} + E^iD_i^{(1,n)} + F & G^iD_i^{(1,n)} + J \end{array}\right]. \tag{3.11}$$

D_i and D_{ij} are the $2n$-accurate centered discrete differencing stencils for first and second derivative operators. We now perform the same analysis in Fourier space, representing grid functions in terms of discrete Fourier coefficients. If I define the discrete scalar product of two grid functions

$$(u,v)_H = h_xh_yh_z\sum_{ijk}\sigma_i\sigma_j\sigma_k u_{ijk}\cdot v_{ijk}, \tag{3.12}$$

where σ_i, σ_j, σ_k are the coefficients of the corresponding inner product in each of the coordinate directions. The norm H is defined such that for a discrete inner product $\langle u,v\rangle_H = u^THv$, where $H = H^T > 0$. For diagonal H, the set of the exponential grid functions $\{\frac{1}{2\pi}e^{\mathrm{i}\langle\omega,x\rangle}, \omega = (\omega_1,\omega_2,\ldots,\omega_d)\,, \omega_r = -N/2+1,\ldots,N/2\}$ give an orthonormal basis in the space of the grid functions. The Euclidean scalar product $\langle x,y\rangle = \sum_{i=1}^d x_iy_i$, allowing us to decompose a grid function $v(t,x,h)$ to

$$v(t,x,h) = \frac{1}{(2\pi)^{d/2}}\sum_\omega e^{\mathrm{i}\langle\omega,x\rangle}v(t,\omega,h\omega). \tag{3.13}$$

The quantities $v(t,\omega,h\omega)$ represent the Fourier coefficients and they satisfy

$$v(t,\omega,h\omega) = \frac{1}{(2\pi)^{d/2}}\sum_x e^{-\mathrm{i}\langle\omega,x\rangle}v(t,x,h). \tag{3.14}$$

The discrete scalar product is then

$$(v,u)_h = \sum_\omega \hat{v}^\dagger\hat{u}\,, \tag{3.15}$$

the shift operator S_j^k applied to my grid function is

$$S_j^kv(t,x,h) = v(t,x',h) \qquad x = (x_{i_1},\ldots,x_j+kh,\ldots,x_{i_d})\,, \tag{3.16}$$

and the shift operator S_j^k acting on the basis $e^{\mathrm{i}\langle\omega,x\rangle}$ gives

$$S_j^ke^{\langle\omega,x\rangle} = \hat{S}k_j(h\omega_j)e^{\langle\omega,x\rangle}, \qquad \hat{S}_j^k(h\omega_j) = e^{\mathrm{i}kh\omega}\,. \tag{3.17}$$

A finite differencing operator D_j corresponding to the mth-order derivative in the j-direction, consists thus of a linear combination of shift operators such that $D_j =$

$h^m \sum_k a_k S_j^k$. Its Fourier symbol $\hat{D}_j$ satisfies

$$D_j e^{\langle\omega,x\rangle} = h^{-m} \sum_k a_k e^{ikh\omega_j} e^{\langle\omega,x\rangle} \tag{3.18}$$

Similarly, one can introduce the Fourier symbols of mixed derivatives. I can then perform a first order reduction as before, drop the lower order terms, and get the principle part

$$\hat{P}' = \begin{bmatrix} A^i \hat{D}_i^{(1,n)} & C \\ D^{ij} \hat{D}_{ij}^{(2,n)} & G^i \hat{D}_i^{(1,n)} \end{bmatrix} . \tag{3.19}$$

As with the continuum, stability can be shown in terms of a symmetrizer, $\hat{H}$. As in Section [2.6.4], if there exists a positive definite a Hermitian matrix $H(n_i)$ such that $HP - P^T H^T = HP - P^T H = 0$ where $P := A^i n_i$ for some arbitrary unit vector n_i. We may say that the semi-discrete system is *symmetric hyperbolic* if all A^i are symmetric (i.e. H is independent of n_i). If there exists a positive constant K, such that $K^1 I \leq \hat{H} \leq KI$ then the problem is well-posed in the norm

$$\|v\|_{h,D_\pm}^2 = \sum_{i=1}^{d} |D_{\pm i} U|_h^2 + |V|_h^2 . \tag{3.20}$$

With these relations I can show well-posedness in both the semi-discrete and the discrete regime by methods which are direct discrete analogs to the methods used to show well-posedness for the continuum solution.

3.1.2 Finite Differencing

For the purposes of the simulations for this proposed system I use finite differencing operators which obey the summation by parts property as explained in the next section, and which are weighted upwinded sideways derivatives at or near the boundary. The finite difference operators using $2n + 1$ points separated by a distance h that approximate a derivative of order m can be constructed as in Section [2.5.1] and obeying the properties described in the previous section. I construct these operators by Taylor expanding the function $f^{m,n,s}(x) = x^{n-s}(\log x)^m$ around a point $x_0 = 1$ up to the order $(x - x_0)^{2n}$. Here $s \in -n, \ldots, n$ is the offset of these points from symmetry with respect to the center ($s = 0$ for centered differencing). The coefficients of x in this expansion, $\bar{f}_{m,n,s,k}$, will be the weights of the points in the differencing stencil. The general finite differencing operator is thus a sum over the shift operator

$$D^{m,n,s} = \sum_{k=-n+s}^{n+s} \bar{f}_{m,n,s,k} S^k . \tag{3.21}$$

This operator will be accurate to $2n + 1 - m$ order convergence.

The centered first and second derivative operators are then

$$D^{1,n,s} = \frac{1}{h} \sum_{j=-n+s}^{n+s} \alpha_{n,s,j} S^j \tag{3.22}$$

$$D^{1,n} = \frac{1}{h} \sum_{j=1}^{n} \frac{j\beta_{n,j}}{2} (S^j - S^{-j}) \tag{3.23}$$

$$D^{2,n} = \frac{1}{h^2} \sum_{j=0}^{n} \beta_{n,j} (S^j + S^{-j}) \tag{3.24}$$

where the coefficients are obtained from

$$\alpha_{n,s,j} = \begin{cases} \frac{(-1)^{j+1}(n+|s|)!(n-|s|)!}{j(n+s-j)!(n-s+j)!} & j \neq 0 \\ \pm(H_{n-|s|} - H_{n+|s|}) & j = 0 \end{cases} \tag{3.25}$$

and

$$\beta_{n,j} = \begin{cases} 2(-1)^{j+1} \frac{(n)!^2}{j(n+j)!(n-j)!} & j \geq 0 \\ -\sum_{j=1}^{n} \beta_{n,j} & j = 0\,. \end{cases} \tag{3.26}$$

Here $j\beta_{n,j} = 2\alpha_{n,0,j}$ for $j \geq 1$ and $H_n = \sum_{i=1}^{n} \frac{1}{i}$ is the harmonic number. I define dimensionless finite difference operators

$$D_0^{(1)} = \frac{h}{2}(D_+ + D_-) \tag{3.27}$$

$$D_0^{(2)} = h(D_+ - D_-) = h^2 D_+ D_-\,, \tag{3.28}$$

where $D_+ v_i = (v_{i+1} - v_i)/h$ and $D_- v_i = (v_i - v_{i-1})/h$.

In order to maintain numerical stability for nonlinear problems, we add artificial dissipation to the right-hand-sides of the time evolution equations as described in Section [2.5.3]. This is must be done in a way that the dissipation term converges away fast enough that it does not change the convergence order of the system. Here I use the Kreiss-Oliger dissipation operator $\mathcal{D}^{(2m)}$ of order $2m$, as discussed in Section [2.5.3]

$$\mathcal{D}^{(2m)} = -\frac{(-1)^m}{2^{2m}} h^{2m-1} \sum_{j=1}^{d} \sigma_j (D_{+j})^m (D_{-j})^m\,, \tag{3.29}$$

for a $2m-2$ accurate scheme, where $\sigma_j \geq 0$ regulates the strength of the dissipation. This form of numerical dissipation has been proven to be numerically stable for non-constant-coefficient hyperbolic PDEs [67].

With the differencing operators and relations derived in the two previous sections I can now proceed in deriving a well-posed boundary treatment for a second order differencing in space, first order in time harmonic evolution system by setting a bound on the energy growth of the metric variables and their derivatives for the semi-discrete system.

3.1.3 Summation By Parts

In order to ensure the well-posedness of the semi-discrete system, we need to obtain an estimate on the energy growth of the system, as discussed in Section [2.6.4]. To do this, I have used difference operators D which satisfy the "summation by parts" (SBP) property. A discrete operator is said to satisfy SBP for a scalar product $E = \langle u, v\rangle = \int_a^b u \cdot v dx$ if

$$\langle u, Dv\rangle + \langle v, Du\rangle = (u \cdot v) \mid_a^b , \tag{3.30}$$

holds for all functions u, v in the domain $[a, b]$. This is the discrete analog of the integration by parts property for continuous functions. By integrating for the energy estimate using the SBP property of the difference operators, I ensure that boundedness properties of the continuum energy estimate carry over to the discretised system. I can construct these difference operators, including numerical boundary conditions in a consistent way, for the system of equations in (2.41)

$$\partial_\rho \left(g^{\rho\sigma} \partial_\sigma \tilde{g}^{\mu\nu}\right) = S^{\mu\nu} . \tag{3.31}$$

I follow the procedure outlined by Strand [102] in constructing finite difference stencils D of a given order, τ, such that

$$Du = \frac{du}{dx} + \mathcal{O}(h^\tau), \tag{3.32}$$

and which satisfy the SBP property (3.30). Briefly, given a state vector $u = (u_0, u_1, \ldots, u_n)^T$ on n grid points, I construct a finite difference operator D as a matrix acting on u. The coefficients of D can be represented as products of the standard operators

$$\begin{aligned} D_{0x} f_{i,j,k} &= \frac{1}{2h}\left(f_{i+1,j,k} - f_{i-1,j,k}\right) , \\ D_{+x} f_{i,j,k} &= \frac{1}{h}\left(f_{i+1,j,k} - f_{i,j,k}\right) , \\ D_{-x} f_{i,j,k} &= \frac{1}{h}\left(f_{i,j,k} - f_{i-1,j,k}\right) , \end{aligned} \tag{3.33}$$

described more generally in the previous section. They are determined up to the boundaries of the domain by solving the set of polynomials

$$Dx^m - \frac{dx^m}{dx} = 0, \qquad m = 0, 1, \ldots, \tau, \tag{3.34}$$

which establish the order of accuracy τ of the approximation. The SBP rule (3.30) provides an additional set of restrictions,

$$\langle u, Du\rangle = -\frac{1}{2} u^2(0) , \tag{3.35}$$

and

$$\langle u + v, D\left(u + v\right)\rangle_h = \langle D\left(u + v\right), u + v\rangle_h - \left(u_0 + v_0\right)^2 , \tag{3.36}$$

which should hold for all u, v in the half line divided into intervals of length $h > 0$. Following Strand [102], we can solve these conditions explicitly for the stencil coefficients of the first derivative operator D and obtain stencils like the ones describes in Sections [3.1.2] and [3.1.1]. It is trivial to obtain a second derivative operator simply by repeated application of the derived first derivative operator. However, this results in a very wide and thus impractical stencil, and instead I use the second derivative SBP operators described in [103, 108] and shown to be valid in Section [3.1.2]. The explicit expressions for the finite difference stencils which I use are given in [40].

The above considerations apply to the construction of difference operators along a single coordinate direction. I can derive a 3D SBP operator by applying the 1D operator along each coordinate direction. It can be shown that the resulting operator also satisfies SBP with respect to a diagonal scalar product

$$\langle u, v\rangle_H = h_x h_y h_z \sum_{ijk} \sigma_i \sigma_j \sigma_k u_{ijk} \cdot v_{ijk}, \tag{3.37}$$

where σ_i, σ_j, σ_k are the coefficients of the corresponding inner product in each of the coordinate directions. The norm H is defined such that for a discrete inner product $\langle u, v\rangle_H = u^T H v$, where $H = H^T > 0$. Note that this is only true if the norm, H, is diagonal. Here I restrict myself to this case.

3.1.4 Well-posed Boundary Conditions

I have constructed finite differencing operators which satisfy summation by parts, and thus can use the rule (3.30) as a tool for deriving an energy estimate and ensuring well-posedness of the semi-discrete system. For the continuum system, I have a well defined energy estimate which can be used to bound solutions. Through use of the SBP-compatible derivative operators defined in the previous section, I ensure that an energy estimate also holds for the semi-discrete system. If this energy estimate bounds the norm of the solution in a resolution independent way, then I have a stable semi-discrete system. Optimally, I would like the norm of the semi-discrete solution to satisfy the same estimate as the continuum solution.

To establish well-posedness I impose boundary conditions based upon the energy norm

$$\mathcal{E} = \|u(t, .)\|^2 = \langle u, u\rangle = \int_\Omega u \cdot H u dx \tag{3.38}$$

where $u(t, .)$ is the solution of the IBVP at time t, and H is a symmetric positive definite matrix on the bounded domain Ω. I require that

$$\mathcal{E}(t) \le C(t)\mathcal{E}(0)\,, \qquad t \ge 0\,, \tag{3.39}$$

with $C(t)$ independent of the initial and boundary data, so that the solution is bounded by the energy at time $t = 0$ for all t.

As an instructive example, which contains the essential features of the derivation for the Einstein equations, I derive explicitly the energy estimate for the wave equation with shift,

$$\partial_t^2 u = \left(\frac{-\gamma^{ij}}{\gamma^{tt}} \partial_i \partial_j - 2 \frac{\gamma^{it}}{\gamma^{tt}} \partial_i \partial_t \right) u. \tag{3.40}$$

where $-\frac{\gamma^{it}}{\gamma^{tt}}$ is the shift β^i, and $\beta^i \beta^j - \frac{\gamma^{ij}}{\gamma^{tt}}$ is the lapse.

I need to ensure that the energy, $\mathcal{E}^{(n)} = \| u(\cdot, t) \|^2$, satisfies that the energy of the system is bounded for the duration of the simulation. The time derivative of the energy of the system can be re-written in semi-discrete form as follows:

$$\begin{aligned} \frac{d}{dt}\mathcal{E} &= \frac{d}{dt} \left(\|u_t\|^2 + \left\| -\frac{\gamma^{ij}}{\gamma^{tt}} u_i u_j \right\| \right) \\ &= \left(\langle u_t, u_{tt} \rangle + \langle u_{tt}, u_t \rangle \right) - \frac{\gamma^{ij}}{\gamma^{tt}} \left(\langle u_i, u_{jt} \rangle + \langle u_{it}, u_j \rangle \right). \end{aligned} \tag{3.41}$$

This is only the energy for the system without the constraints. If the constraints are preserved throughout the evolution, then deriving a bound on this energy is proof of stability. However, without a bound on the constraint propagation system, this well-posedness proof only holds in the linear regime. Therefore, in the next section, I will derive a system to add constraint preserving terms to the SBP boundary conditions.

In this section my notation will follow that: I will use partial derivative symbols for continuum equations and subscripts for semi-discrete derivatives. To ensure that this quantity remains bounded in the semi-discrete case, I determine the energy growth which arises from the application of my boundary conditions, and remove this via the simultaneous approximation term (SAT, or "penalty") method described in [108]. I use a discrete second derivative stencil which also obeys SBP and more accurately approximates a second derivative than the wide stencil created from applying my first derivative twice as described in Section [3.1.1].

Since I use differencing operators which obey the SBP condition, we can make use of Eq. (3.30) to integrate Eq. (3.41). For the wave equation, after some algebra, this condition gives

$$\frac{d}{dt}\mathcal{E} = -2 \left[\frac{\gamma^{ij}}{\gamma^{tt}} (u_t u_j) \Big|_{x_i=0}^{x_i=N_i} + \frac{\gamma^{it}}{\gamma^{tt}} (u_t^2) \Big|_{x_i=0}^{x_i=N_i} \right]. \tag{3.42}$$

That is, the change in energy is determined by fluxes at the boundary points, $x_i = 0$ and $x_i = N_i$.

On the boundary faces, I impose a set of conditions which for the moment I write in a generic form

$$\left[\beta_{x_i=0} \partial_t + \alpha_{x_i=0} \partial_i + \delta_{x_i=0} \right] (u - u_0) = 0 \tag{3.43}$$

$$\left[\beta_{x_i=N} \partial_t - \alpha_{x_i=N} \partial_i - \delta_{x_i=N} \right] (u - u_0) = 0 \tag{3.44}$$

in terms of free parameters α, β, and δ which are indexed according to the grid face.

These are substituted into into the estimate, Eq. (3.42), leading to

$$\frac{d}{dt}\mathcal{E} = -2\left[\left(\frac{\alpha_{N_i}}{\beta_{N_i}}u_t^2 - \frac{\gamma^{it}}{\gamma^{tt}}u_t^2\right)\Bigg|_{x_i=N_i} - \left(\frac{\alpha_{0_i}}{\beta_{0_i}}u_t^2 - \frac{\gamma^{it}}{\gamma^{tt}}u_t^2\right)\Bigg|_{x_i=0}\right] , \quad (3.45)$$

where η^i is the normal to the boundary face i, and u_0 are data chosen to be consistent with the initial data.

The SAT method allows us to choose values for the free parameters in the boundary terms which conserve the energy in the system. I first write the original shifted wave equation, Eq. (3.40), in semi-discrete form, explicitly including the boundary terms:

$$\begin{aligned} u_{tt} = &-\frac{\gamma^{ij}}{\gamma^{tt}}H^{-1}D^{(2)}_{ij}u - 2\frac{\gamma^{it}}{\gamma^{tt}}H^{-1}D^{(1)}_i u_t + \tau_{0_i}H^{-1}E_{0_i}(\alpha_{0_i}u_t + \beta_{0_i}S_i u + \delta_{0_i}u) \\ &+\tau_{N_i}H^{-1}E_{N_i}(\alpha_{N_i}u_t + \beta_{N_i}S_i u + \delta_{N_i}u)\,. \end{aligned} \quad (3.46)$$

The E_a are vectors of length N defined as $E_{N_i} = (0, 0 \ldots 0, 1)^\top$ and $E_{0_i} = (1, 0 \ldots, 0)^\top$ to be zero everywhere except at the boundary points. S_i are sideways blended finite differencing stencils satisfying the SBP property, as described in the previous section.

I determine the time dependence of the energy for this new system in order to derive coefficients τ for my penalty terms which give a well-posed semi-discrete system. Substituting Eq. (3.46) into Eq. (3.41), and once again making use of the SBP property, Eq. (3.30), I arrive at

$$\begin{aligned} \frac{d}{dt}\mathcal{E} = &\left(\tau_{N_i}\alpha_{N_i} - \frac{\gamma^{it}}{\gamma^{tt}}\right)u_t^\top E_{N_i}u_t + 2\left(\tau_{0_i}\alpha_{0_i} + \frac{\gamma^{it}}{\gamma^{tt}}\right)u_t^\top E_{0_i}u_t \\ &+2\left(\tau_{N_i}\beta_{N_i} - \frac{\gamma^{ij}}{\gamma^{tt}}\right)u_t^\top E_{N_i}S_i u + 2\left(\tau_{0_i}\beta_{0_i} + \frac{\gamma^{ij}}{\gamma^{tt}}\right)u_t^\top E_{0_i}S_i u\,. \end{aligned} \quad (3.47)$$

The free parameters τ_0 and τ_N can be used to eliminate the $u_t^\top E_{N_i}S_i u$ terms, by setting $\tau_0\beta_0 = -\gamma^{ij}/\gamma^{tt}$ and $\tau_N\beta_N = \gamma^{ij}/\gamma^{tt}$. Then, the energy evolves according to

$$\begin{aligned} \frac{d}{dt}\mathcal{E} &= -2\left(\beta_{N_i}\frac{\gamma^{it}}{\gamma^{tt}} - \alpha_{N_i}\frac{\gamma^{ij}}{\gamma^{tt}}\right)\beta_{N_i}^{-1}u_t^\top E_{N_i}u_t \\ &\quad +2\left(\beta_{0_i}\frac{\gamma^{it}}{\gamma^{tt}} - \alpha_{0_i}\frac{\gamma^{ij}}{\gamma^{tt}}\right)\beta_{0_i}^{-1}u_t^\top E_{0_i}u_t = 0\,. \end{aligned} \quad (3.48)$$

The last equality is arrived at after some algebra, substituting the boundary conditions, Eq. (3.43–3.44), and making use of the original wave equation, Eq. (3.40).

The resulting semi-discrete evolution equation is given by

$$\begin{aligned} u_{tt} \;\; = \;\; & -\frac{\gamma^{it}}{\gamma^{tt}} H^{-1} D_i^{(1)} u_t - \frac{\gamma^{ij}}{\gamma^{tt}} H^{-1} D_{ij}^{(2)} u \\ & -\frac{\gamma^{ij}}{\gamma^{tt}\beta_{0_i}} H^{-1} E_{0_i} (\alpha_{0_i} u_t + \beta_{0_i} S_i u + \delta_{0_i} u) \\ & +\frac{\gamma^{ij}}{\gamma^{tt}\beta_{N_i}} H^{-1} E_{N_i} (\alpha_{N_i} u_t + \beta_{N_i} S_i u + \delta_{0_i} u)\,, \end{aligned} \tag{3.49}$$

which, as a result of the application of the SAT terms, satisfies the energy conservation equation $d\mathcal{E}/dt = 0$. This calculation may be found in more detail in the appendix [A.1].

I require that the energy, $\mathcal{E}^{(n)} = \|u\left(\cdot, t\right)\|^2$, satisfies (3.39) for positive times, that is, for the duration of a simulation the energy is bounded. The use of simultaneous approximation terms (the SAT or 'penalty') allows us to choose values for the free parameters in the boundary terms which conserve the energy in the system. I determine the time dependence of the energy for this system in order to derive coefficients for my penalty terms at the boundary points. This gives a well-posed semi-discrete system. The corresponding calculation for the Einstein equations, Eq. (2.46–2.47) mirrors this calculation in Appendix [A.1], except with the inclusion of source terms which do not themselves modify the boundary treatment. After the calculation described in Appendix [A.2] for the harmonic system, I obtain the boundary terms by the same approach described above. For the harmonic system described in Section [2.3.3]

$$\partial_t Q^{\mu\nu} = \frac{\gamma^{it}}{\gamma^{tt}} D_{i+} Q^{\mu\nu} - (\gamma^{ij} + \frac{\gamma^{it}\gamma^{jt}}{\gamma^{tt}}) H^{-1} A_{ij} \gamma^{\mu\nu} \tag{3.50}$$

with the boundaries obtained in Appendix [A.2] the full system is

$$\partial_t Q^{\mu\nu} = -\frac{\gamma^{it}}{\gamma^{tt}} D_{i+} Q^{\mu\nu} - (\gamma^{ij} + \frac{\gamma^{it}\gamma^{jt}}{\gamma^{tt}}) H^{-1} (A_{ij} + E_0 - E_N) S_i) \gamma^{\mu\nu} \tag{3.51}$$

$$+\frac{2\gamma^{ij}}{\gamma^{tt}\beta_0} H^{-1} E_{0_i} [(1 + \frac{\gamma^{it}}{\gamma^{tt}}) D_{i+} \gamma^{\mu\nu} - \frac{Q^{\mu\nu}}{\gamma^{tt}} + \frac{2x}{r^2} (\gamma^{\mu\nu} - g_0)]$$

$$+\frac{2\gamma^{ij}}{\gamma^{tt}\beta_N} H^{-1} E_{N_i} [(1 - \frac{\gamma^{it}}{\gamma^{tt}}) D_{i+} \gamma^{\mu\nu} + \frac{Q^{\mu\nu}}{\gamma^{tt}} + \frac{2x}{r^2} (\gamma^{\mu\nu} - g_N)]$$

For my secondary variable $Q^{\mu\nu}$, where $\gamma_{\mu\nu} \equiv \sqrt{-g} g^{\mu\nu}$ and $Q^{\mu\nu} = g^{t\alpha} \partial_\alpha \gamma^{\mu\nu}$.

I apply these penalty terms to my evolution equations in our harmonic formulation code (AEIHarmonic) and in the next sections, we will test these conditions with and without the addition of additional constraint preserving conditions which do not effect the energy boundedness of this system.

3.1.5 Constraint-Preservation

In ref. [40], I used a somewhat ad-hoc boundary condition, which applies a Sommerfeld-like dissipative operator to all ten components of the metric

$$\left(\partial_t + \partial_x - \frac{1}{r}\right)(g^{\mu\nu} - g_0^{\mu\nu}) = 0\,. \tag{3.52}$$

This follows the physically motivated reasoning that far away from a source, the evolution variables each satisfy a generally radial outgoing wavelike behaviour. The condition is particularly simple to apply, and has been used extensively in evolutions using a conformal-traceless formulation of the Einstein equations (see, for example, [87]), where the choice of evolution variables has so far hindered the development of a more rigorous boundary treatment. In fact, in simulations where the boundaries have been pushed to large distances (for instance through the use of mesh refinement), the condition has proven to be useful enough to allow for long-term stable evolutions. Eventually, however, boundary effects do contaminate the interior grid, and can lead to a loss of convergence or the accuracy required to resolve delicate physical features. The conditions given by Eq. (3.52) make no effort to satisfy the Einstein constraints, and thus can over time drive the solution away from a solution of the full Einstein equations.

For the Einstein equations in harmonic form, it is possible to derive consistent boundary conditions by explicitly evaluating the constraint propagation system. This has been done for the first order harmonic evolution system described by Lindblom et al. [39], who have derived consistent conditions based on limiting incoming characteristics.

Alternatively, Kreiss and Winicour [83] have demonstrated a set of Sommerfeld type boundary conditions, which are strongly well posed, as well as preserving the harmonic constraints. The well-posedness follows from results in pseudo-differential theory of strongly well-posed systems, and applies to a broad class of conditions. Here I apply their results directly to the generalized harmonic evolution system used in this section. The harmonic constraints, Eq. (2.37), provide conditions for the time components of the metric:

$$-\partial_t g^{\mu t} - \partial_x g^{\mu x} - \partial_y g^{\mu y} - \partial_z g^{\mu z} - F^\mu = 0\,. \tag{3.53}$$

The remaining metric components are determined by applying the Sommerfeld-type condition, Eq. (3.52), in a hierarchical fashion, using previously determined components as required:

$$\left(\partial_x + \partial_t + \frac{1}{r}\right)\left(g^{AB} - g_0^{AB}\right) = 0\,, \tag{3.54}$$

$$\left(\partial_x + \partial_t + \frac{1}{r}\right)\left(g^{tA} - g^{xA} - g_0^{tA} + g_0^{xA}\right) = 0\,, \tag{3.55}$$

$$\left(\partial_x + \partial_t + \frac{1}{r}\right)\left(g^{tt} - 2g^{xt} + g^{xx} - g_0^{tt} + 2g_0^{xt} - g_0^{xx}\right) = 0\,. \tag{3.56}$$

These particular conditions are chosen to ensure well-posedness of the solution, but are not unique. They lead to the following explicit conditions on the positive x boundary:

$$\begin{aligned}
(\partial_x + \partial_t)\, g^{0\mu} &= \partial_x g^{0\mu} - \partial_x g^{1\mu} - \partial_y g^{2\mu} - \partial_z g^{3\mu} - F^{\mu}\,, && (3.57)\\
(\partial_x + \partial_t)\, g^{11} &= (\partial_x + \partial_t)\left(2g^{01} - g^{00}\right) - \frac{1}{r}\left(g^{11} - 2g^{01} + g^{00}\right)\\
&\quad + \left(\partial_x + \frac{1}{r}\right)\left(g_0^{11} - 2g_0^{01} + g_0^{00}\right)\,, && (3.58)\\
(\partial_x + \partial_t)\, g^{1A} &= (\partial_x + \partial_t)\left(g^{0A} - g_0^{0A}\right)\\
&\quad - \frac{1}{r}\left(g^{1A} - g_0^{1A}\right) + \frac{1}{r}\left(g^{0A} - g_0^{0A}\right) - \partial_x g_0^{1A}\,, && (3.59)\\
(\partial_x + \partial_t)\, g^{AB} &= -\frac{1}{r}\left(g^{AB} - g_0^{AB}\right) + \partial_x g_0^{AB}\,. && (3.60)
\end{aligned}$$

The complete list of conditions can be found in Appendix [A.3].

I combine the results of the previous section (see Appendix) with these constraint preserving conditions, to arrive at expressions for the evolution equations for $Q^{\mu\nu}$ from Eq. (2.47) with the new penalties derived in the appendix and shown in Eq. (A.32),

$$\begin{aligned}
\partial_t Q^{\mu\nu} &= -\left(g^{ij} + \frac{g^{it}g^{jt}}{g^{tt}}\right) D_{i\pm} D_{j\mp} \tilde{g}^{\mu\nu} - \frac{g^{it}}{g^{tt}} D_i Q^{\mu\nu} + \tilde{S}^{\mu\nu}\\
&\quad + \frac{2g^{ij}}{g^{tt}\beta_0} H^{-1} E_{0_i}\left[\left(1 + \frac{g^{it}}{g^{tt}}\right)\tilde{g}_t^{\mu\nu} + S_{i+}\tilde{g}^{\mu\nu} - p^{\mu\nu}\right]\\
&\quad + \frac{2g^{ij}}{g^{tt}\beta_N} H^{-1} E_{N_i}\left[\left(1 - \frac{g^{it}}{g^{tt}}\right)\tilde{g}_t^{\mu\nu} + S_{i-}\tilde{g}^{\mu\nu} - p^{\mu\nu}\right]\,, && (3.61)
\end{aligned}$$

where $\tilde{g}^{\mu\nu} = \sqrt{-g}g^{\mu\nu}$. and where the $p^{\mu\nu}$ are determined by Eqs. (3.57)–(3.60). For example

$$p^{0\mu} = S_{i+}\tilde{g}^{0\mu} - \left(S_{i+}\tilde{g}^{i\mu} + D_{A+}\tilde{g}^{\mu A} + D_{B+}\tilde{g}^{\mu B} + F^{\mu}\right)\,, \qquad (3.62)$$

corresponds to the constraint conditions in Eqs. (3.57), where i is the direction outward from the boundary face, $S_{i\pm}$ is the stencil for sideways finite differencing on the boundary, and A, and B are tangent to the face.

3.1.6 Results

The boundary prescription described in the previous section has been implemented for the harmonic Einstein evolution code (presented in [40] and Section [2.3.3]). I have carried out tests comparing three boundary configurations. The first, which I refer to as "standard Sommerfeld" simply applies Eq. (3.52) to each evolution variable on each face of the cubical evolution domain, which was the boundary implementation used in [40]. The second ("SAT") applies the boundary treatment derived in Section [3.1.4], and the third ("CP-SAT") improves on this by implementing the constraint preserving conditions of Section [3.1.5]. I find that in each case, the SAT and CP-SAT boundary conditions respectively improve on the standard Sommerfeld condition in their ability to reduce boundary reflections and constraint violations over time.

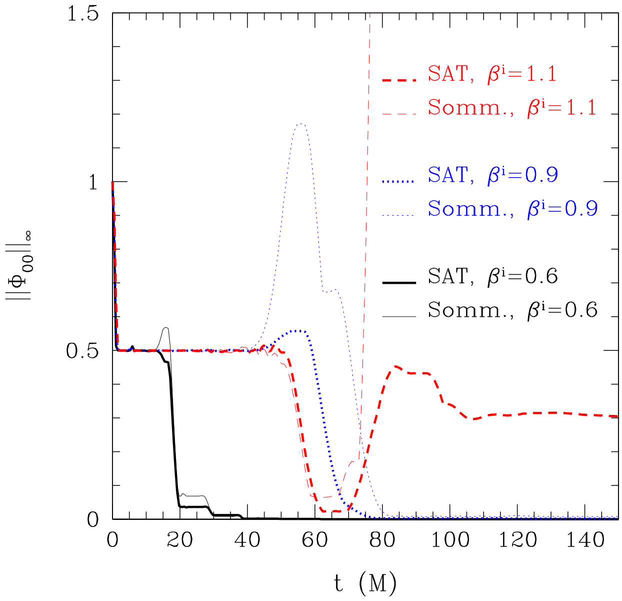

Figure 3.1: The evolution of ϕ for flat-space wave equations with a constant shift in the x-direction. As initial data I have used a spherical Gaussian pulse of amplitude 1.0 and width 1.0, on a grid 8 (121 grid points) units in size. Thin lines are the Sommerfeld-type boundary conditions without the SAT terms applied, whereas thick lines use the SAT boundary treatment given by Eq. (3.49).

Shifted waves

As a first test of the methodologies outlined in the previous section, I consider a simplified non-relativistic example problem which demonstrates the effectiveness of the SAT method. One of the challenges of designing boundary treatments that control the energy growth for black hole space-times in commonly used gauges is the problem of non-zero shift. A useful problem which has been used as a toy model for the full Einstein equations is the shifted scalar wave equation [42, 109],

$$\left(\partial_t^2 - 2\beta^i\partial_i\partial_t - \left(\delta^{ij} - \beta^i\beta^j\right)\partial_i\partial_j\right)\phi = 0\,, \tag{3.63}$$

with shift vector $\beta^i = g^{it}/g^{tt}$ (see Eq. (3.40)). In the appendix [A.1.3], I have explicitly derived the boundary treatment of this problem, which has been implemented in a 3D evolution code.

In Fig. 3.1, I display results from evolutions of a Gaussian wave packet, for various constant values of the shift. The L_∞-norm of the energy of the solution is plotted as a function of time for evolutions using standard Sommerfeld type conditions, Eq. (3.52), and compared with the SAT conditions derived in Section [3.1.4]. As the waveform impinges on the boundary, there is a certain amount of unphysical reflection, but the energy

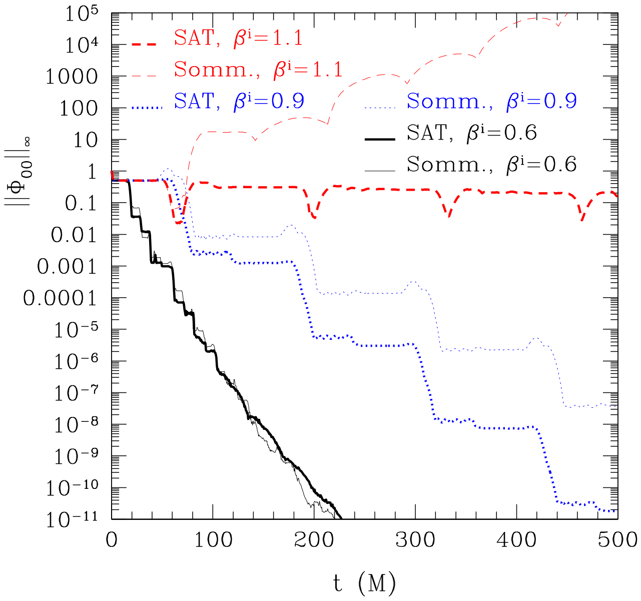

Figure 3.2: The same as in Fig. 3.1 but shown in a logarithmic scale for $||\Phi_{00}||_\infty$ and on a longer timescale. Note that standard Sommerfeld boundary conditions are unstable for $|\beta^i| > 1$.

is largely removed from the grid in steps corresponding to the crossing time, as visible in Fig. 3.2. The boundary reflections are much lower in the case of the SAT boundary conditions, and the evolution is stable even to superluminal, $|\beta^i| > 1$, shifts suggesting that these conditions are stable even for outflow boundaries.

Linear waves

As a first test of the implementation of the constraint preserving boundary conditions for the full Einstein equations, I have considered low amplitude wave solutions of the linearized Einstein system. These solutions exhibit non-trivial dynamics which exercise the boundaries, but for which the source terms of the Einstein equations are negligible. The particular initial data which I use are the quadrupole Teukolsky waves [110],

$$\begin{aligned} ds^2 &= -dt^2 + (1 + Af_{rr})dr^2 + (2Bf_{r\phi})rdrd\theta + (2Bf_{r\theta})r\sin\theta drd\phi \\ &+ (1 + Cf^{(1)}_{\theta\theta} + Af^{(2)}_{\theta\theta})r^2d\theta^2 + [2(A-2C)f_{\theta\phi}]r^2\sin\theta d\theta d\phi \\ &+ (1 + Cf^{(1)}_{\phi\phi} + Af^{(2)}_{\phi\phi})r^2\sin^2\theta d\phi^2 \,. \end{aligned} \tag{3.64}$$

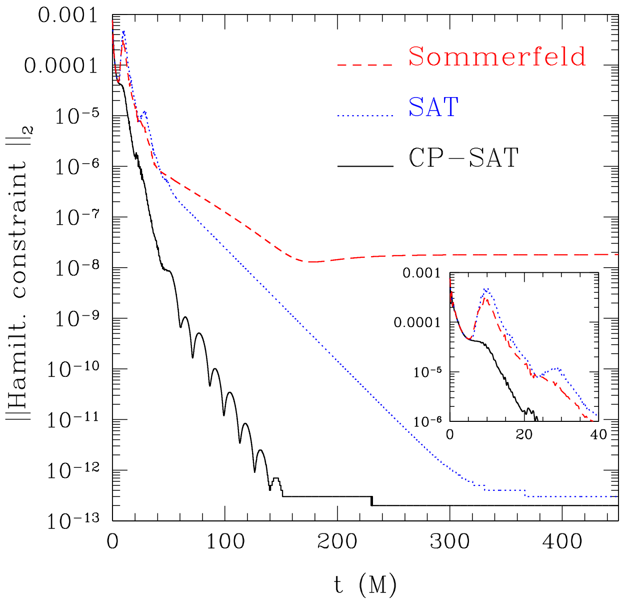

Figure 3.3: The L_2-norm of the Hamiltonian constraint for a Teukolsky wave, comparing my constraint-preserving boundary conditions with the standard non-SBP Sommerfeld conditions, as well as the purely Sommerfeld SAT algorithm to ensure well-posedness. The boundaries for this simulation are at a radius of 7M from the center of initial Gaussian pulse.

with radial dependence given by

$$\begin{aligned} A &= 3\left[\frac{F^{(2)}}{r^3}+\frac{3F^{(1)}}{r^4}+\frac{3F}{r^5}\right], && (3.65)\\ B &= -\left[\frac{F^{(3)}}{r^2}+\frac{3F^{(2)}}{r^3}+\frac{6F^{(1)}}{r^4}+\frac{6F}{r^5}\right], && (3.66)\\ C &= \frac{1}{4}\left[\frac{F^{(4)}}{r}+\frac{2F^{(3)}}{r^2}+\frac{9F^{(2)}}{r^3}+\frac{21F^{(1)}}{r^4}+\frac{21F}{r^5}\right], && (3.67)\\ F^{(n)} &\equiv \left[\frac{d^nF(x)}{dx^n}\right]_{x=t-r} && (3.68) \end{aligned}$$

where $F(x) = F(t-r)$ described the shape of the out-going wave. The functions $f_{rr}, \ldots, f^{(2)}_{\phi\phi}$ depend only on the angles (θ, ϕ) given explicitly in [110] for azimuthal quantum number $m = -2, \ldots, 2$. This initial data has been used as a testbed in a number of numerical studies [111–114]. The particular solution which I use follows Eppley [115] in combining incoming and outgoing wave packets so as to produce a solution which is regular everywhere in the space-time.

The overall behaviour of the evolutions using the three boundary conditions is summarized in Fig. 3.3, which plots the evolution of the L_2-norm of the Hamiltonian constraint as a function of coordinate time, for a wave of amplitude 0.001. In each case, there is a reduction of the constraint violation as the wave propagates off the grid. In the standard Sommerfeld case, this quickly saturates at a level of 10^{-7}, determined by the finite differencing resolution. In the case of the SAT boundary conditions, however, the constraint violation eventually reaches machine round-off due to the constraint damping in the interior of the domain. This happens at a much faster rate for the explicitly constraint preserving condition ("CP-SAT") which introduces the modification described in Section [3.1.5]. It is notable that in this case, the initial boundary reflection, which the standard Sommerfeld condition shares with the simple SAT treatment, is also absent.

Nonlinear waves

The goal of this boundary treatment is to reduce the errors introduced into the evolution domain during evolutions of strong field spacetimes involving non-linear waves, as for instance, generated during binary black hole evolutions. To model this problem in a simplified setting which does not involve complications due to excision or interior mesh-refinement boundaries, I have carried out tests using the nonlinear Brill wave solutions [116]. These solutions have been studied in a number of numerical contexts, both as testbeds, as well as exploring the onset of black hole formation [115, 117–120]. The initial spatial metric takes the form

$$ds^2 = \Psi^4[e^{2q}(d\rho^2 + dz^2) + \rho^2 d\phi^2], \tag{3.69}$$

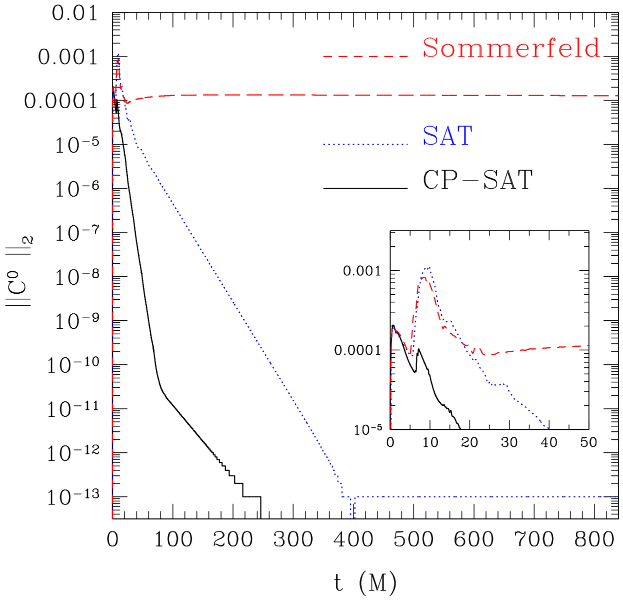

Figure 3.4: The L_2-norm of the harmonic constraints for a Brill wave of amplitude 0.5, comparing constraint-preserving boundary conditions with the standard Sommerfeld conditions, as well as the purely Sommerfeld SAT algorithm to ensure well-posedness. The boundaries in these simulations are also at a radius of 7M from the center.

in cylindrical (ρ, ϕ, z) coordinates. I choose q of the form of a Gaussian packet centered at the origin,

$$q = a\rho^2 e^{-r^2}, \tag{3.70}$$

where a is a parameter which is used to set the overall amplitude of the axisymmetric wave. Generally I choose a value of $a = 0.5$ to construct a wave which is strong, but not so as to evolve to a black hole. As a result, I expect the initially non-linear solution generates waves which propagate off the grid leaving behind a flat space-time. As the boundary data is unknown, I set the data in the boundary conditions to Minkowski space and rely on the fact that these conditions are non-reflective and constraint preserving.

In Fig. 3.5 I show a number of frames from two evolutions, displaying the metric γ^{tt} component at various time instances on a grid 7 units in size. In the right column, the standard Sommerfeld conditions have been used, whereas on the left we have used the constraint preserving SAT boundary conditions. By the second frame at $t = 8$, the wave pulse has reached the boundary, and the following frames show the reflected pulse. Qualitatively, the CP-SAT boundary conditions show a much smoother profile, with smaller amplitude features. By $t = 45$, the wave has left the grid in the CP-SAT case, to the extent that it cannot be seen on the linear scale of the figure. In the standard Sommerfeld case, however, there is still some non-trivial dynamical evolution. A more quantitative demonstration is shown in Fig. 3.4, which plots the L_2-norm of the harmonic constraint C^0 as a function of coordinate time for three situations: The standard naive Sommerfeld boundary conditions (“Sommerfeld”), the SAT boundary conditions developed in Sec. 3.1.4 (“SAT”), and the constrained version of these boundary conditions, following the prescription of Section [3.1.5] (“CP-SAT”). In the Sommerfeld case, the constraint violation is entirely reflected by the grid boundaries, and the value remains essentially constant at its initial value throughout the evolution, even though constraint damping has been used on the interior code. The SAT boundary conditions, however, do a much better job of removing constraint violation from the grid, showing the exponential decrease with time that is expected from the damped solution. The constraint preserving boundary conditions show the strongest damping, suggesting that the constraint violating modes introduced by these boundary conditions are much smaller than for the SAT case. The evolution of the other constraint components show the same behaviour.

As a final test of the stability of my boundary prescription, I have carried out evolutions of Brill waves for which I have attempted to excite high-frequency error modes along the lines of the “robust stability” test [121, 122]. This test is a means of determining whether it is possible for modes of any frequency within any of the grid variables to exhibit exponential growth during the evolution. On a numerical grid, error modes exist at fixed frequencies, set by the grid resolution, and the standard test consists of perturbing each variable at each grid point by a small amount of randomly determined amplitude ϵ. The effect of the random perturbation is to seed modes which then have the potential to grow, if the system is unstable at that frequency. Since being first used in [122] and proposed as a standard testbed in [121], the test has been used in a number of applications to demonstrate well-posedness of numerical implementations [85, 121–125]. In Fig. 3.6 I applied this test by applying some kernel of random data to all points including the boundary points. For the SAT methods the random noise gets damped and then the decay of the energy looks similar to that of the standard brill test in Fig. 3.4. For the standard

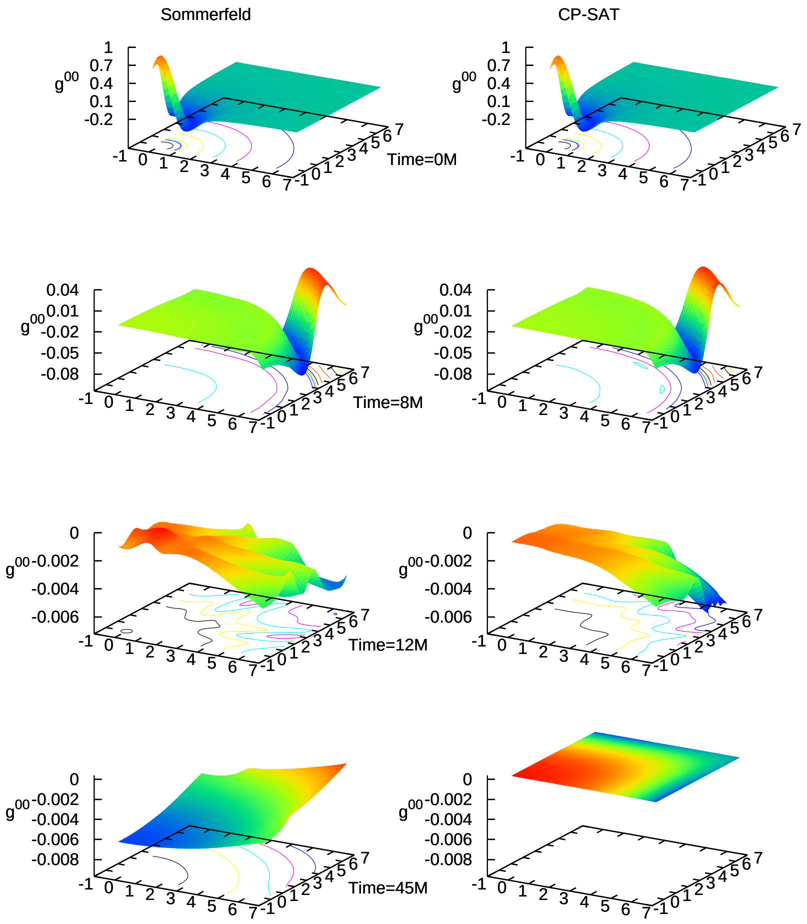

Sommerfeld

CP-SAT

Figure 3.5: The tt component of the metric for a Brill wave of amplitude $a = 0.5$, comparing constraint-preserving boundary conditions with the standard Sommerfeld conditions. The above plot shows a two-dimensional cut in the xy plane at various times. On the right is the evolution of the Brill wave with constraint-preserving SAT and on the left is the same simulation but with standard Sommerfeld type boundary conditions.

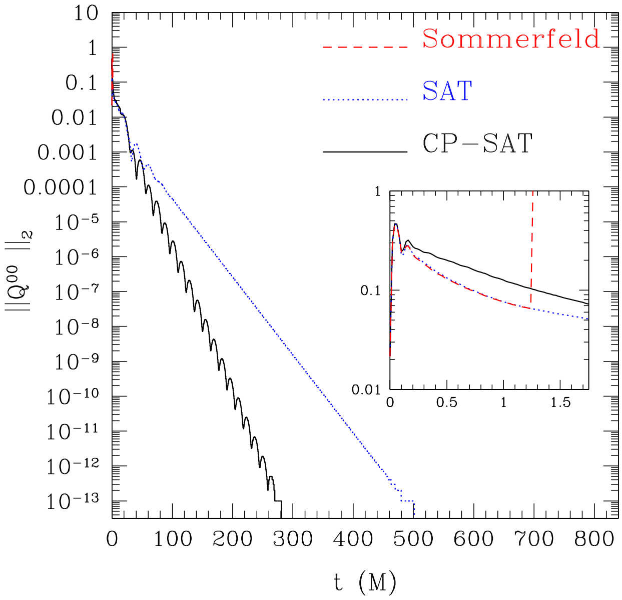

Figure 3.6: Evolution of Q^{00} component of the harmonic data for a Brill wave perturbed by random noise of a kernel amplitude of $\epsilon \pm 0.075$, over all the grid points. This is placed on top of Brill wave initial data with an amplitude of $a = 0.5$.

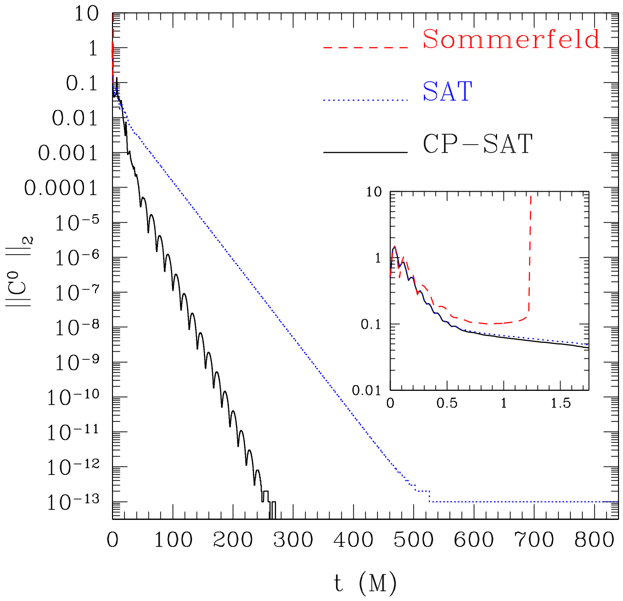

Figure 3.7: Evolution of the L_2-norm of the harmonic constraints for a Brill wave ($a = 0.5$) perturbed by a checkerboard noise pattern of amplitude $\epsilon \pm 0.1$, over all the grid points, in order to excite the highest frequency grid mode.

Sommerfeld boundary conditions the evolution becomes unstable at the boundaries.

A variant of this test recognizes that in the case of an ill-posed system, the fastest exponential growth will result from the highest frequency mode. On a finite-difference grid, the frequency of this mode is set by the grid spacing. I can excite this mode by adding perturbations to the data in a “checkerboard” pattern, where neighboring points receive an opposite perturbation of fixed amplitude ϵ. That is, I choose

$$\epsilon_{ijk} = \begin{cases} +\epsilon, & \text{for } i+j+k \text{ even}, \\ -\epsilon, & \text{for } i+j+k \text{ odd}. \end{cases} \tag{3.71}$$

In Fig. 3.7 I show the evolution of the L_2-norm of the C^0 constraint component for the evolution of an $a = 0.5$ Brill wave for which each component of the initial data has been modified according to Eq. (3.71) with $\epsilon = 0.1$. The two versions of the SAT boundary conditions prove to be rather impervious to the initial data perturbation, and display essentially the same behaviour as in the unperturbed case, Fig. 3.4. It is perhaps notable that the non-constraint-persevering boundary conditions show a slightly slower decay rate than for the non-perturbed data of Fig. 3.4, so that it takes more than 100 time units to reach the level of machine round-off, whereas the constraint preserving boundary conditions reach this level in essentially the same amount of time as in the unperturbed case (though with a somewhat different decay profile). The simple Sommerfeld boundary conditions, however, are unable to cope with the initial perturbation and lead to an instability on a very short timescale.

Shifted Gauge Waves

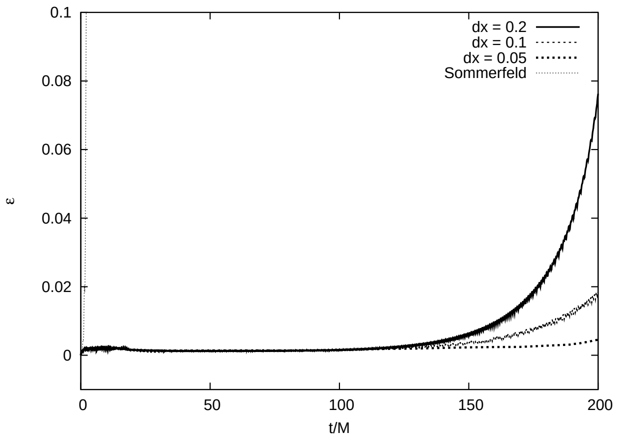

Figure 3.8: The infinity norm of the error in $\tilde{g}_{xx}$ relative to the exact solution, $\mathcal{E}$, for 2D shifted gauge wave simulations with amplitude $A = 0.01$, $d = 2$, and boundary width $x, y \in [-7, 7]$. The resolutions presented here are $dx, dy = 0.05, 0.1, 0.2$ doubled relative to the next lowest resolution. The solution with standard boundary conditions blows up at early times and is shown as the dashed line with $dx = 0.1$.

An important test of the validity and convergence of any numerical code is a comparison against an exact answer. It is important to show that our codes converge at the expected rate for the truncation error for changing grid spacing, as discussed in Section [2.5.1]. For this reason I present here the results of the simulation of a shifted gauge wave with constraint preserving SAT boundaries at three different resolutions and compare against the exact solution as proof that the harmonic code with these boundary conditions provides a stable and convergent evolution scheme.

The choice of the shifted gauge wave test is a stringent test for convergence, as even a gauge wave without shift can have a constraint preserving instability in harmonic coordinates (i.e the gauge wave metric has exponentially growing perturbations which satisfy the harmonic conditions and the Einstein equations). The addition of a shift introduces a new type of exponentially growing instability in the standard harmonic reduction of the Einstein equations. Thus the choice of a shifted gauge wave is a stringent non-linear test of our system [126]. The success of this test shows that numerical noise excites instabilities that can be cured by a combination of discrete conservation laws, well-posed and constraint preserving boundaries, and constraint adjustments.

The standard gauge wave test is based upon the flat metric

$$ds^2 = (1 - H)(-dt^2 + dx^2) + dy^2 + dz^2\,, \tag{3.72}$$

where

$$H = H(x - t) = A \sin\left(\frac{2\pi(x - t)}{d}\right)\,,\,, \tag{3.73}$$

is a sinusoidal wave of amplitude A propagating along the x-axis. In order to test 2-dimensional features, the coordinates are rotated according to

$$x = \frac{1}{sqrt2}(x' - y')\,, \qquad y = \frac{1}{sqrt2}(x' + y')\,, \tag{3.74}$$

which produces a gauge wave propagating along the diagonal with dependence

$$\sin\left(\frac{2\pi(x' - y' - t'\sqrt{2})}{d'}\right)\,, \qquad d' = d\sqrt{2}\,. \tag{3.75}$$

Adjusting d or d' to the size of the evolution domain gives periodicity in the x and y directions.

In figure (3.8) I show the error values for a 2D shifted gauge wave with amplitude $A = 0.01$, $d = 2$, and boundary width $x, y \in [-7, 7]$. The resolutions presented here are $dx, dy = 0.05, 0.1, 0.2$ doubled relative to the next lowest resolution, thus we expect, from the convergence rate at time t, with the error $\mathcal{E} = \parallel \Phi_\rho - \Phi_{exact} \parallel_\infty$

$$r(t) = \log_2\left(\frac{\parallel \Phi_{h=2\delta x} - \Phi_{exact} \parallel_\infty}{\parallel \Phi_{h=\delta x} - \Phi_{exact} \parallel_\infty}\right)\,, \tag{3.76}$$

to obtain $r(t = late) \approx 2$ and $r(t = mid) \approx 3$ for our system with fourth order convergent interior stencils, and second order at he outer boundary. Indeed, we obtain for $r(t = 10)_{(0.05.0.1)} = 4.0380$, $r(t = 30)_{(0.05.0.1)} = 3.3907$, and $r(t = 200)_{(0.1.0.2)} = 2.0457$. The standard non-SAT Sommerfeld boundary simulations were unstable for the shifted gauge wave tests.

Black Hole Space-times

The ultimate goal of this boundary treatment is to improve the accuracy and stability of binary black hole simulations. As a simple test I did simulations for constraint preserving SAT penalty boundaries and non-constraint-preserving standard Sommerfeld conditions for a head on collision of two Brill-Lindquist black holes from a small separation of $3M$ with boundaries relatively close in at $144M$. The simulations were done in a fully harmonic gauge and the interiors of the apparent horizons for each black hole was excised. I extracted waves by both methods described in Section [2.6.3] and derived the total energy of the system from the Hamiltonian and momentum constraints.

In Fig. [3.9] I show the constraint growth of the two simulations. Here you can see that the harmonic coordinate constraints are much better preserved with the constraint preserving SBP penalty boundaries than with standard Sommerfeld. This behaviour holds for all the harmonic constraints as well as for the physical constraints. The constraint violations in the constraint preserving SAT run continue to diminish smoothly down to numerical error up to $1000M$, where the run was stopped. In Fig. [3.10] we show the $l = 2, m = 0$ modes or the Zerilli scalar for waves extracted at a radius of $70M$ from the center of mass of the system. The noise from the boundary reflection is very clear to see at around $200M$ for the standard boundary simulations. For these simulations the

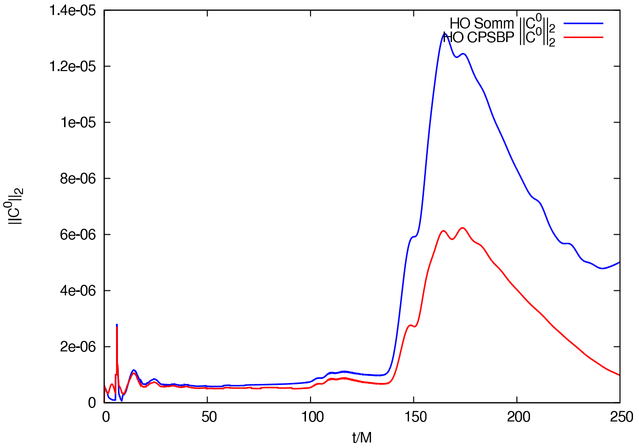

Figure 3.9: The L_2-norm of the harmonic constraints for a head-on collision of two black holes each of mass $0.5M$ starting from an initial separation of $3M$ and with boundaries at $144M$, comparing constraint-preserving boundary conditions with the standard Sommerfeld conditions.

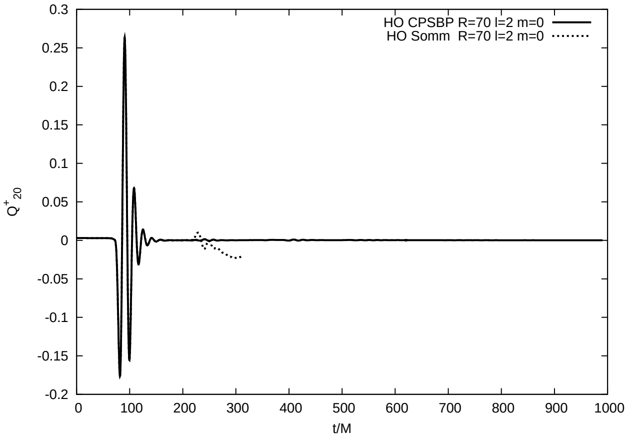

Figure 3.10: The $\ell = 2, m = 0$ component of the Zerilli scalar for the extracted gravitational radiation for a head-on collision of two black holes each of mass $0.5M$ starting from an initial separation of $3M$ and with boundaries at $144M$, comparing constraint-preserving boundary conditions with the standard Sommerfeld conditions.

standard Sommerfeld boundary condition run crashes around $300M$ due to an instability at the excision boundary cause by incoming noise reflected from the outer boundary. This is strong proof that constraint preserving penalty boundaries improve stability for binary black hole simulations, and can extend simulation runtime and improve accuracy.

3.1.7 Discussion

I have examined the initial boundary value problem for the second-order formulation of the Einstein equations in the generalized harmonic gauge. The system of evolution equations for this finite-difference harmonic code was derived in [40] where it was shown to be accurate, stable, and convergent for long-term evolutions of black hole space-times, such as head-on collisions of two black holes, isolated black holes, and binary black hole inspiral and merger. In this section I described the derivation, implementation and testing of a new boundary treatment for this system. I demonstrated that this new treatment maintained the validity and convergence (to lower order) seen with the standard boundary treatments. I additionally show that these conditions give us greater accuracy (for all reasonable resolutions), improved constraint preservation, improved boundary transparency, and greater stability in robust stability tests.

I implemented Sommerfeld-type boundary conditions as in Eq.(3.52), which are applied via the simultaneous approximation term (SAT) method to control the energy growth of the system, and are designed to be maximally dissipative. I then establish well-posedness for the semi-discrete symmetric hyperbolic evolution system via the energy method [103] by bounding the energy growth of the system under the assumption that the boundaries are in the linearized regime. I have implemented finite-differencing stencils that obey the summation by parts (SBP) rule [102] with the diagonal norm, with minimum bandwidth second-derivative SBP stencils as derived in [108]. These stencils give fourth-order accuracy in the interior, and second-order at the boundary. While the standard stencils give fourth-order everywhere, I show that the improved accuracy of the SBP conditions more than makes up for the loss of two orders of convergence.

The stability and well-posedness of the boundary conditions has been demonstrated for a number of test problems: shifted scalar waves, linearized waves, nonlinear waves, and random and high frequency stability tests. Further improved accuracy results from incorporating the constraint preservation into the conditions, following the prescription of [83, 97]. The boundary conditions are still Sommerfeld type for most metric components, but I substitute conditions gained from enforced preservation of the harmonic constraints. This gives us four conditions directly from the harmonic constraints, three from the coupling of these conditions to my outgoing Sommerfeld-type conditions, and the three components for the directions tangent to each boundary face come only from our Sommerfeld-type conditions. In Section [5.1.6] I show that, as expected, these new outgoing Sommerfeld, constraint-preserving conditions retain the robust stability and convergence properties of the purely Sommerfeld-SBP conditions. The tests also demonstrate that these new conditions lead to smaller errors in satisfying the constraints, and are more transparent to waves propagating through the boundaries. They should thus lead to more accurate evolutions than the purely Sommerfeld SAT penalty boundary conditions.

In a related study, Rinne et al. [111] have considered a number of boundary treatments for the case of a first-order in space harmonic formulation, including the Kreiss-Winicour [83] treatment adopted here for a second-order system. They find that an additional physically motivated condition, $\partial_t \Psi_0 = 0$, which aims to eliminate incoming radiation, can have important effects in reducing physical reflections. Similar modifications may also prove beneficial to the second-order system presented here, though apparent reflections from the outer boundary are rather small even in the case of non-linear waves studied in Section [3.1.6]. These physically motivated conditions will be discussed for boundary conditions for the BSSN formulation in the next section.

With binary black hole evolutions now extending over multiple orbits, and thus many crossing times on conventional computational grids, boundary effects can potentially have a non-trivial influence on the late-time dynamics and extracted gravitational wave signals from such simulations. The tests provided here, including nonlinear Brill wave and binary black hole head-on collision evolutions, suggest that these methods will also be effective for isolated strong sources, and thus will also be appropriate for black hole inspiral simulations, though these involve a number of other technical considerations (such as excision). The methods can be extended to other formulations of the Einstein equations, provided certain hyperbolicity assumptions are satisfied, and I will describe in the next section how to pursue improvements of other commonly used systems such as the conformal-traceless one employed in [87].

3.2 ADM -BSSN

> *Our firmest convictions are apt to be the most suspect, they mark our limitations and our bounds. Life is a pretty thing unless it is moved by the indomitable urge to extend its boundaries.*
>
> Jose Ortega y Gasset

The Baumgarte-Shapiro-Shibata-Nakamura (BSSN) formulation of Einstein field equations is the most common formulation used in numerical relativity simulations today. This is both because of historical reasons, and because of convenience in setting stable and intuitive evolving gauge conditions, which allow for long term stable binary black hole simulations. However, proving well-posedness in BSSN is a much more daunting problem than for the harmonic formulation of the Einstein equations, because BSSN is only a strongly hyperbolic system for certain specific gauge conditions. However, the stability of the system has been proven in [127] for a Bona-Masso type gauge condition and a fixed shift. Thus, when we have artificial boundaries, in [127] they require the normal component of the shift to be zero at the boundary, and conditions are placed on the nine incoming eigenfields to obtain well-posedness. Deriving stable and well-posed boundary conditions for the BSSN formulation has been a challenge faced by many in the field for at least the past decade of numerical relativity. Today, most numerical relativity groups still use the naive boundary conditions called “radiative” boundaries, described in Section [2.6.5] imposed to all the geometric variables, thus over-specifying the problem on the boundaries. Those conditions are very easy to implement numerically, however, they do not preserve the physical constraints and can introduce an unreasonable amount of artificial radiation into the system. In this section I construct boundary conditions which preserve the constraints and discuss the well posedness of the initial-boundary value problem (IBVP) for the BSSN system.

Beyer's work in [127] shows that the BSSN formulation for a Bona-Masso type gauge condition and a fixed shift is reducible to a first order symmetric hyperbolic system (FOSH). In that work and boundary conditions leading to a well posed system are formulated. However, the boundary conditions presented in that paper are not constraint-preserving. Thus, they may yield reflections or constraint-violating modes. The work by Gundlach and Garcia in [34], formulates constraint-preserving boundary conditions for the BSSN system but the well-posedness of the resulting IBVP has not been established. For the BSSN system I want to meet the same conditions for accuracy and validity as with boundaries for the harmonic formulation described in the previous section [3.1]. That is, it must not change the dynamical behavior of the fields reaching the boundary surface, it must not introduce any fields coming from said boundary, the fields on the boundary must be themselves be stable and bounded, and it must preserve the condition on the full system that it must also preserve the constraints for all times. In other words, the conditions must provide one with both well-posedness and constraint preservation for the full system with boundaries.

From [127] I have the requirement that nine sufficient conditions must be imposed, and it gives us:

- the time dependence of the Ψ_0 Weyl component has to be zero, or at least bounded (for binary simulations I simply require Ψ_0 to be bounded);
- the normal to the boundary component of the shift vector, as well as the derivative of the lapse in that direction have to be zero;
- finally, I get the other two conditions relating the lapse and the shift in the directions tangential to the boundary.

I present here a discussion on the well posedness of the complete system, as well as the possible numerical implementation of such conditions at the boundary.

I present a new set of boundary conditions for the BSSN system with "1+log" slicing described in Section [2.3.2] and the "Gamma driver" shift described Section [2.4.4] which is currently commonly used in numerical simulations of binary black holes today. The main properties of the boundary conditions described in this section are:

- they preserve the constraints throughout the evolution,
- they control the Weyl scalar Ψ_0 at the boundary (a condition that should yield small spurious reflections of gravitational radiation),
- they yield a well-posed IBVP for the linearized problem (a reasonable assumption if boundaries are far away), and are expected to yield a well posed problem in the nonlinear case as well.

As in [127] I have nine conditions. The boundary conditions obtained are the nine:

- for the gauge fields, I obtain the boundary condition that the normal component of the shift has to be zero, as in [127]
- the condition that the derivative of the lapse along the normal direction has to be zero at the boundary (flat)
- another two conditions for the tangential components of the shift
- and from the fields and constraints I obtain the natural condition that the momentum constraint has be satisfied boundary, leading to von Neumann type conditions for the extrinsic curvature,
- and, as in [127], I obtain that the Weyl scalar Ψ_0 at the boundary has to be bounded, leading to relations between the second spatial derivatives of the metric coefficients.

In total, these are other five constraints, giving us the nine conditions needed at the boundary.

This construction is based on the methods in [128,129] where the boundary conditions are specified in three steps. In the first step, the constraint propagation system is analyzed. This system describes the propagation of the constraint variables, and I show that it can be cast into a FOSH system. Homogeneous maximally dissipative boundary conditions are specified for this system that guarantee the propagation of the constraints. The second step consists of analyzing the propagation of the *Weyl curvature.* The BSSN evolution system implies a convenient FOSH for the electric and magnetic parts of the Weyl tensor, and the momentum constraint variable. I show that compatible boundary conditions for this system can be specified by freezing the momentum constraint variable to zero and freezing the Weyl scalar Ψ_0. Finally, the third step consists in controlling the *gauge degrees of freedom.* The gauge functions, the lapse α and the shift vector β_i are free to be chosen as best fits the problem to be evolved. This freedom, however, is limited by several pragmatic requirements. I study the system for common evolution equations where I reduce the evolution system for lapse and shift to a set of condition-dependent evolution equations and specify boundary conditions for them. I present a brief discussion of a numerical implementation of the boundary conditions that I am proposing and finish with some conclusions of the complete system of boundary conditions obtained in this work. What follows in this section is previously unpublished work and was work done with the assistance and guidance of Dario Nuñez and Olivier Sarbach.

3.2.1 Boundary Conditions for the BSSN System

The evolution equations in this section are the BSSN evolution equations with Bona-Masso slicing and hyperbolic Gamma driver shift as in Section [2.4.4] with the exception of the advection terms in the evolution equation for the shift. Using the notation from [127] the system derived and shown in Section [2.3.2] reads

$$\begin{aligned}
\hat{\partial}_0\alpha &= -\alpha^2 f(\alpha,\phi.x^\mu)(K-K_0(x^\mu))\,, && (3.77)\\
\hat{\partial}_0\beta^i &= \alpha^2 G(\alpha,\phi.x^\mu)B^i\,, && (3.78)\\
\hat{\partial}_0 B^i &= e^{-4\phi}H(\alpha,\phi,x^\mu)\hat{\partial}_0\Gamma^i - \eta^i(B^i,\alpha,x^\mu)\,, && (3.79)\\
\hat{\partial}_0\tilde{\gamma}_{ij} &= -2\alpha\tilde{A}_{ij} + 2\tilde{\gamma}_{k(i}\partial_{j)}\beta^k - \frac{2}{3}\tilde{\gamma}_{ij}\partial_k\beta^k\,, && (3.80)\\
\hat{\partial}_0\phi &= \frac{1}{6}\left(-\alpha K + \partial_k\beta^k\right)\,, && (3.81)\\
\hat{\partial}_0\tilde{A}_{ij} &= e^{-4\phi}\left[-\tilde{D}_i\tilde{D}_j\alpha + \alpha\tilde{R}_{ij} + \alpha - 4\partial_{(i}\phi\cdot\tilde{D}_{j)}\alpha\right]^{TF} && (3.82)\\
&+ \alpha\left(K\tilde{A}_{ij} - 2\tilde{A}_{ik}\tilde{A}^k_j\right) + 2\tilde{A}_{k(i}\partial_{j)}\beta^k - \frac{2}{3}A_{ij}\partial_k\beta^k - \alpha e^{-4\phi}\hat{S}_{ij}\,, \\
\hat{\partial}_0 K &= -e^{-4\phi}\left[\tilde{D}^i\tilde{D}_i\alpha - 2\partial_i\phi\cdot\tilde{D}^i\alpha\right] + \alpha\left(\tilde{A}_{ij}\tilde{A}^{ij} + \frac{1}{3}K^2\right) - \alpha S\,, && (3.83)\\
\hat{\partial}_0\tilde{\Gamma}^i &= \tilde{\gamma}^{jk}\partial_j\partial_k\beta^i + \frac{1}{3}\tilde{\gamma}^{ij}\partial_j\partial_k\beta^k + \partial_k\tilde{\gamma}^{kj}\cdot\partial_j\beta^i - \frac{2}{3}\partial_k\tilde{\gamma}^{ki}\cdot\partial_j\beta^j && (3.84)\\
&- 2\tilde{A}^{ij}\partial_j\alpha + 2\alpha\left[(m-1)\partial_k\tilde{A}^{ki} - \frac{2m}{3}\tilde{D}^i K + m\left(\tilde{\Gamma}^i_{jk}\tilde{A}^{jk} + 6\tilde{A}^{ij}\partial_j\phi\right)\right] - S^i\,,
\end{aligned}$$

where I have introduced the operator $\hat{\partial}_0 = \partial_t - \beta^j\partial_j$, and where $G(\alpha,\phi,x^\mu)$ and $H(\alpha,\phi,x^\mu)$ are smooth, strictly positive functions, and $\eta(B^i,\phi,x^\mu)$ is a smooth function and come from the 'Γ-driver' condition [33]. Here, all quantities with a tilde refer to the conformal three metric $\tilde{\gamma}_{ij}$. That is, $\tilde{D}^i$ and $\tilde{\Gamma}^k_{ij}$ refer to the covariant derivative and the Christoffel symbols, respectively, with respect to $\tilde{\gamma}_{ij}$. The expression $[\ldots]^{TF}$ denotes the trace-free part with respect to the conformal three metric, and

$$\begin{aligned}
\tilde{R}_{ij} &= -\frac{1}{2}\tilde{\gamma}^{kl}\partial_k\partial_l\tilde{\gamma}_{ij} + \tilde{\gamma}_{k(i}\partial_{j)}\tilde{\Gamma}^k - \tilde{\Gamma}_{(ij)k}\partial_j\tilde{\gamma}^{jk} && (3.85)\\
&+ \tilde{\gamma}^{ls}\left(2\tilde{\Gamma}^k_{(i}\tilde{\Gamma}_{j)ks} + \tilde{\Gamma}^k_{ls}\tilde{\Gamma}_{klj}\right)\,, \\
\tilde{R}^{\phi}_{ij} &= -2\tilde{D}_i\tilde{D}_j\phi - 2\tilde{\gamma}_{ij}\tilde{D}^k\tilde{D}_k\phi + 4\tilde{D}_i\phi\tilde{D}_j\phi - 4\tilde{\gamma}_{ij}\tilde{D}^k\phi\tilde{D}_k\phi\,, && (3.86)
\end{aligned}$$

are the conformal equations for the Ricci tensor in terms of the conformal metric and scalar. The parameter m, in the evolution equation for $\tilde{\Gamma}^i$, which was introduced in [130], controls how the momentum constraint is added to the evolution equations for the variable $\tilde{\Gamma}^i$. The system in [33] corresponds to the choice $m = 1$. f, G and H are strictly positive and smooth functions of their arguments. The source terms $\mathcal{S}, \hat{\mathcal{S}}_{ij}$ and $\mathcal{S}^i$ are defined in terms of the Ricci tensor, $R^{(4)}_{ij}$, and the constraint variables

$$\begin{aligned}
\mathcal{H} &= \frac{1}{2}\left(\gamma^{ij}R^{(3)}_{ij} + K^2 - K^{ij}K_{ij}\right)\,, && (3.87)\\
\mathcal{M}_i &= \tilde{D}^j\tilde{A}_{ij} - 2\tilde{A}_{ij}\tilde{\gamma}^{ij}(\tilde{D}_i\phi) - \frac{2}{3}\tilde{D}_i K + 6\tilde{A}_{ij}\tilde{D}^j\phi\,, && (3.88)\\
\mathcal{C}^i &= \tilde{\Gamma}^i - \partial_j\tilde{\gamma}^{ij}\,, && (3.89)\\
& && (3.90)
\end{aligned}$$

Table 3.1: Boundary conditions for the BSSN variables. Nine sufficient and necessary conditions at the boundary for the geometric variables, where x is the direction perpendicular to the boundary, and A stands for the other two directions.

Function	BC
α	$\partial_x \alpha = 0$
β^x	$\beta^x = 0$
$\dot{\beta}_A$	$\left(\partial_t - \sqrt{3\kappa_0}\partial_x\right)\beta_A = \frac{4\kappa_0}{f_0 - 4\kappa_0}\partial_A \alpha$ or $\partial_x \beta_A = 0$
$K_{,i}$	$\mathcal{M}_i = 0 \to K_{,i} = \frac{3}{2}\left(\tilde{D}^j \tilde{A}_{ij} + 6\tilde{A}_{ij}\tilde{D}^j \phi\right)$
$\dot{\tilde{A}}_{xx}, \tilde{A}_{xx,A}$	$\Psi_0 = 0 \to \mathcal{E}_{\perp\perp} = -n \wedge \mathcal{B}_{\perp\perp}$

according to

$$\mathcal{S} = \tilde{\gamma}^{ij} R^{(4)}_{ij} - 2\mathcal{H}\,, \tag{3.91}$$

$$\hat{\mathcal{S}}_{ij} = \left[R^{(4)}_{ij} + \tilde{\gamma}_{k(i}\partial_{j)} C^k\right]^{TF}\,, \tag{3.92}$$

$$\mathcal{S}^i = 2\alpha m \tilde{\gamma} \mathcal{M}_j - \hat{\partial}_0 \mathcal{C}^i\,. \tag{3.93}$$

The vacuum equations consist of the evolution equations (3.77) with $\mathcal{S} = 0$, $\hat{\mathcal{S}}_{ij} = 0$, $\mathcal{S}^i = 0$ and, of course, the requirement that the constraints satisfy $\mathcal{H} = 0, \mathcal{M}_i = 0$ and $\mathcal{C}_i = 0$.

Jumping ahead, the boundary conditions for the BSSN system, consistent with the constraint equations, conditions are shown in Table [3.1]. Here it can be seen that they are nine conditions at the boundary. Four conditions must be imposed to the gauge functions; the conditions on their behavior in the normal direction is expected, as the gauge functions should not push the boundary; the other two conditions relating their behavior in the directions tangential to the boundary, were initially surprising and add additional challenges at corners and edges of boundary planes for Cartesian coordinates. Other three conditions come from the requirement that the momentum constraints have to be satisfied at the boundary, and the following sections will explain the implementation for such a condition. These conditions describe a relation between the derivatives of the trace of the extrinsic curvature, and the divergence of its trace-free part. This condition has to be satisfied over the entirety of the initial hypersurface. I am only demanding that such relation must be preserved during the evolution. The last two conditions relate to the actual two degrees of freedom that a gravitational problem has in the gauge. For this case, I am considering a problem that is localized and isolated, that I am already in a region where the expected peeling behavior of the Weyl components can be consider valid, and Ψ_0 can be interpreted as describing the incoming gravitational radiation which is taken to be bounded and negligible for the situations considered. Thus, I obtain conditions on the electric and magnetic part the Weyl tensor at the boundary. Again, these conditions are only valid in the linearized regime, and thus only valid in a regime far from the highly non-linear and dynamic parts of the simulation domain. Furthermore, the requirements on the gauge mean that for black hole initial data, these conditions could introduce more noise and reflection than naive conditions in the regime where the difference between zero shift and flat lapse is far greater than numerical error.

3.2.2 Propagation of the Constraints

It can be shown that the evolution equations (3.77) and the Bianchi identities imply that the constraint variables $\mathcal{H}, \mathcal{M}_i$, and $\mathcal{C}^i$ satisfy the following propagation system [127]

$$
\begin{aligned}
\hat{\partial}_0\mathcal{H} &= -\frac{1}{\alpha}D^j\left(\alpha^2\mathcal{M}_j\right) - \alpha e^{-4\phi}\tilde{A}^{ij}\tilde{\gamma}_{ki}\partial_j\mathcal{C}^k + \frac{2\alpha}{3}K\mathcal{H}\,, && (3.94)\\
\hat{\partial}_0\mathcal{M}_j &= \frac{\alpha^3}{3}D^j\left(\alpha^{-2}\mathcal{H}\right) + \alpha K\mathcal{M}_j + D^i\left(\alpha\left[\tilde{\gamma}_{k(}\partial_{j)}\mathcal{C}^k\right]^{TF}\right)\,, && (3.95)\\
\hat{\partial}_0\mathcal{C}^k &= 2\alpha m\tilde{\gamma}^{kl}\mathcal{M}_l\,. && (3.96)
\end{aligned}
$$

By introducing the new constraint variable $Z_i^k = \partial_i\mathcal{C}^k$, $Z_{ij} = Z_i^k\tilde{\gamma}_{kj}$, one can reduce Eqs. (3.94) to the first order linear system

$$
\begin{aligned}
\hat{\partial}_0\mathcal{H} &= -\frac{1}{\alpha}D^j\left(\alpha^2\mathcal{M}_j\right) - \alpha e^{-4\phi}\tilde{A}^{ij}Z_{ij} + \frac{2\alpha}{3}K\mathcal{H}\,, && (3.97)\\
\hat{\partial}_0\mathcal{M}_j &= \frac{\alpha^3}{3}D^j\left(\alpha^{-2}\mathcal{H}\right) + \alpha K\mathcal{M}_j + D^i\left(\alpha Z_{(ij)}\right)^{TF} && (3.98)\\
&- \alpha\sigma\left[\partial_k Z_j^k - \partial_j Z_k^k\right]\,, &&\\
\hat{\partial}_0\mathcal{C}^k &= 2\alpha m\tilde{\gamma}^{kl}\mathcal{M}_l\,, && (3.99)\\
\hat{\partial}_0 Z_{ij} &= 2\alpha m\partial_i\mathcal{M}_j + \textsf{lower order terms.} && (3.100)
\end{aligned}
$$

Here, I have included in the right-hand side of Eq. (3.97) the term $\partial_k Z_j^k - \partial_j Z_k^k$ (which is identically zero since $Z_i^k = \partial_i\mathcal{C}^k$) with an arbitrary factor σ. As I will show, this σ helps us to obtain a FOSH system. The all equations in the system Eq. (3.97) have the form

$$\hat{\partial}_0 C = \hat{\mathbf{A}}(u)^i D_i C + \hat{\mathbf{B}}(u)C\,, \tag{3.101}$$

where C are the constraint variables, $u = (\alpha, \phi, \tilde{\gamma}_{ij}, K, \tilde{A}_{ij}, \tilde{\Gamma}^i)$ are the main variables, and $\hat{\mathbf{A}}^i$ and $\hat{\mathbf{B}}$ are matrix-valued functions of u for $i = 1, 2, 3$. Decomposing $Z_{ij} = \hat{Z}_{(ij)} + Z_{[ij]} + \frac{1}{3}\tilde{\gamma}_{ij}Z$ into its trace-free symmetric part, $\hat{Z}_{(ij)}$, its anti-symmetric part, $Z_{[ij]}$, and its trace, $Z = \tilde{\gamma}_{ij}Z_{ij}$, and representing C in terms of the variables $C = (\mathcal{C}^k, S_1 := 2m\mathcal{H} + Z, S_2 := \mathcal{H} + 2Z, Mj, Z(ij), Z[ij])^T$, the principal symbol $\hat{\mathbf{A}}(n) = \hat{\mathbf{A}}(u)^i n_i$ acting on the constraint variables is given by

$$
\hat{\mathbf{A}}(n)\begin{pmatrix}\mathcal{C}^k\\ S_1\\ S_2\\ \mathcal{M}_j\\ \hat{Z}_{(ij)}\\ Z_{[ij]}\end{pmatrix} = \alpha\begin{pmatrix}0\\ 0\\ (4m\sigma-1)n^j\mathcal{M}_j\\ \frac{1}{3}n_j S_2 + (1-\sigma)n^i\hat{Z}_{(ij)} + \sigma n^i Z_{[ij]}\\ 2m\left(n_{(i}\mathcal{M}_{j)}\right)^{TF}\\ 2mn_{[i}\mathcal{M}_{j]}\end{pmatrix}\begin{pmatrix}\mathcal{C}^k\\ S_1\\ S_2\\ \mathcal{M}_j\\ \hat{Z}_{(ij)}\\ Z_{[ij]}\end{pmatrix}\,, \tag{3.102}
$$

where $n_i \equiv \tilde{\gamma}^{ij} n_j$ and $n_i n^i = 1$ is normalized. This system is symmetric hyperbolic provided the following inequalities hold:

$$4m\sigma - 1 > 0, \qquad 2m(1-\sigma) > 0, \qquad 2m\sigma > 0\,, \tag{3.103}$$

for the free parameters. This is the case if and only if $m > 1/4$ and $1/4m < \sigma < 1$. For this case, in order to show well-posedness as in Section [2.6.4], a symmetrizer $\hat{\mathbf{H}} = \hat{\mathbf{H}}^T$ is given by

$$\begin{aligned} C^T \hat{\mathbf{H}} C = \tilde{\gamma}_{ij}\mathcal{C}^i\mathcal{C}^j + S_1^2 + \frac{1}{3(4m\sigma-1)} S_2^2 + \tilde{\gamma}^{ij}\mathcal{M}_i\mathcal{M}_j + \\ \frac{1-\sigma}{2m}\tilde{\gamma}^{ik}\tilde{\gamma}^{jl}\hat{Z}_{(ij)}\hat{Z}_{(kl)} + \frac{\sigma}{2m}\tilde{\gamma}^{ik}\tilde{\gamma}^{jl} Z_{[ij]} Z_{[kl]}\,. \end{aligned} \tag{3.104}$$

where $\hat{\mathbf{H}}$ must be positive definite and satisfies $\hat{\mathbf{H}}\hat{\mathbf{A}}(n) = \hat{\mathbf{A}}(n)^T\hat{\mathbf{H}}$ for the principal symbol. Defining the energy norm

$$\mathcal{E} = \int_\Omega C^T \hat{\mathbf{H}} C d^3x\,, \tag{3.105}$$

for the constraint variables on the domain Ω, and taking a time derivative to show boundedness, using Eq.(3.102) and Gauss' theorem, I find

$$\begin{aligned} \frac{d}{dt}\mathcal{E} &= 2\int_\Omega C^T\hat{\mathbf{H}}\left[(\hat{\mathbf{A}}^i + \beta)\partial_i C + \hat{\mathbf{B}}C\right] d^3x + \int_\Omega C^T(\partial_t \hat{\mathbf{H}} C) d^3x \\ &= \int_\Omega \Big[\partial_i\left(C^T\hat{\mathbf{H}}\hat{\mathbf{A}}^i C + C^T\hat{\mathbf{H}}\beta^i C\right) \\ &+ C^T\left(\hat{\mathbf{H}}\hat{\mathbf{B}} + \hat{\mathbf{B}}^T\hat{\mathbf{H}} - \partial_i(\hat{\mathbf{H}}\hat{\mathbf{A}}^i + \hat{\mathbf{H}}\beta^i) + \partial_t\hat{\mathbf{H}}\right)C\Big] d^3x \\ &\leq \int_{\partial\Omega} C^T\hat{\mathbf{H}}\hat{\mathbf{A}}(n) C d^2x + \kappa\mathcal{E}\,, \end{aligned} \tag{3.106}$$

where I have assumed that the shift is tangential to the boundary at the boundary and where κ is a constant that depends only on bounds for the symmetric parts of the matrix-valued functions $\hat{\mathbf{B}}$, $\hat{\mathbf{H}}^{-1}\partial_i(\hat{\mathbf{H}}\hat{\mathbf{A}}^i + \hat{\mathbf{H}}\beta^i)$, and $\hat{\mathbf{H}}^{-1}\partial_t\hat{\mathbf{H}}$. Therefore, if boundary conditions on the constraints C can be imposed such that $C^T\hat{\mathbf{H}}\hat{\mathbf{A}}(n)C|_{\partial\Omega} \leq 0$, the estimate (3.106) implies that $\mathcal{E}(t) \geq e^{\kappa t}\mathcal{E}(0)$.

In particular, this guarantees that zero initial data for C yields $C = 0$ for all $t \geq 0$. Explicitly,

$$C^T\hat{\mathbf{H}}\hat{\mathbf{A}}(n)C = 2n^i\mathcal{M}^j\left[\frac{1}{3}\delta_{ij}S_2 + (1+\sigma)\hat{Z}_{(ij)} + \sigma Z_{[ij]}\right]\,, \tag{3.107}$$

gives us the first restriction for the physical constraints to provide constraint preservation for the whole system with artificial boundaries for this constraint propagation system. One possibility to meet this requirement is to require that the momentum constraint variable vanishes at the boundary, $M_j|_{\partial\Omega} = 0$. One way to enforce this is to code this requirement into the evolution equation for the curvature scalar K at the boundary.

More generally, I can look at the characteristic fields which are defined as the projections of C onto the eigenspaces of $\mathbf{A}(\mathbf{n})$ as in (3.104). The characteristic speeds and corresponding fields are

$$\begin{aligned}
\mu &= 0\,, \qquad \Big(C^k\,, \qquad S_1\,, \qquad \frac{4m}{3}S_2 - (4m\sigma - 1)n^i n^j \hat{Z}_{ij}\ , \\
&\qquad h_i^k Z_{kj} n^j\,, \qquad h_{[i}^k h^l_{\ j]} Z_{kl}\,, \qquad \left(h_{(i}^k h^l_{\ j)} - \frac{1}{2}h_{ij}h^{kl}\right) Z_{kl}\Big)\ , \\
\mu &= \pm\alpha\sqrt{\frac{4m-1}{3}}\,, \qquad V^{(\pm)} = n^j \mathcal{M}_j \pm \sqrt{\frac{3}{4m-1}}\left[\frac{1}{3}S_2 + (1-\sigma)n^i n^j \hat{Z}_{ij}\right]\ , \\
\mu &= \pm\alpha\sqrt{m}\,, \qquad \bar{V}_j^{(\pm)} = h^j \mathcal{M}_k \pm \frac{1}{\sqrt{m}} n^i h_j^k \left[(1-\sigma)\hat{Z}_{(ik)} + \sigma Z_{[ik]}\right]\ ,
\end{aligned} \tag{3.108}$$

where $h_j = \delta_j^k n_j n^k$ denotes the orthogonal projector onto the space tangent orthogonal to n_i. In terms of these fields, I have

$$\begin{aligned}
C^T \hat{\mathbf{H}}\hat{\mathbf{A}}(n) C &= \frac{1}{2}\sqrt{\frac{4m-1}{3}}\left[\left(V^{(+)}\right)^2 - \left(V^{(-)}\right)^2\right] \\
&+ \frac{\sqrt{m}}{2}\tilde{\gamma}^{ij}\left[V_i^{(+)}V_j^{(-)} - V_i^{(-)}V_j^{(+)}\right]\ ,
\end{aligned} \tag{3.109}$$

Giving us the rest of the conditions for constraint preservation on the boundaries for this constraint propagation system. Therefore, I may also impose the boundary conditions

$$\left[V^{(+)} + c_1 V^{(-)}\right]_{\partial\Omega} = 0\,, \qquad \left[\bar{V}_j^{(+)} + c_2 \bar{V}_j^{(-)}\right]_{\partial\Omega} = 0\,, \tag{3.110}$$

where c_1 and c_2 are two functions on the boundary with magnitude smaller or equal than one. The particular case $c_1 = c_2 = 1$ corresponds to imposing the momentum constraint on the boundary.

3.2.3 Propagation of the Weyl Curvature

For the following section, I restrict my analysis to the case $m = 1$. Furthermore, I consider only small amplitude, high frequency perturbations of smooth solutions. In this limit only the principal part of the equations matters and the coefficient appearing in front of the derivative operators can be frozen to the value of the smooth solution at an arbitrary point p. By rescaling and rotating the coordinates as necessary, one can achieve a space-time metric that has the Minkowski form at point p. This means that the coefficients in front of the derivative operators in the evolution equations can be frozen to the values

$$\alpha = 1\,, \qquad \phi = 0\,, \qquad \tilde{\gamma}_{ij} = \delta_{ij}\,, \tag{3.111}$$

for a conformally flat system far away from the highly nonlinear and highly dynamic region of the simulation domain. In this way, the evolution equations simplify to linear equations with constant coefficients as I did in the previous section [3.1]. Furthermore, the domain $\Omega = \{(x, y, z) \in \Re^3 : x > 0\}$ can be considered to be a half-plane with boundary at $x = 0$. Intuitively, the high-frequency limit is the relevant limit for analyzing that the system is well posed and stable in a numerical (discrete) regime.

For the following, I use the standard operators from vector calculus $\mathbf{grad}$, $\mathbf{curl}$, $\mathbf{div}$ defined by

$$(\mathbf{grad}\phi)_i = \partial_i \phi\,, \qquad (\mathbf{curl}X)_i = \varepsilon_{ikl}\partial^k X^l\,, \qquad \mathbf{div}X = \partial^k X_k\,, \tag{3.112}$$

for scalar and vector fields ϕ and X, respectively. They satisfy the identities

$$\begin{aligned} \mathbf{curl}\,\mathbf{grad}\phi &= 0\,, \qquad \mathbf{div}\,\mathbf{curl}X = 0\,, \qquad \mathbf{div}\,\mathbf{grad}\phi = \Delta\phi\,, \\ \mathbf{curl}\,\mathbf{curl}X &= -\Delta X + \mathbf{grad}\,\mathbf{div}X\,, \end{aligned} \tag{3.113}$$

where $\Delta = \partial^k\partial_k$ denotes the standard Laplacian. I consider the following generalization from tensor calculus:

$$\begin{aligned} (\mathbf{grad}X)_{ij} &:= \partial_{(i}X_{j)} - \frac{1}{3}\delta_{ij}\partial^k X_k\,, \qquad (\mathbf{curl}T)_{ij} := \varepsilon_{kl(i}\partial^k T^l_{\;j)}\,, \\ (\mathbf{div}T)_j &:= \partial^i T_{ij}\,, \end{aligned} \tag{3.114}$$

where T is a symmetric, traceless tensor field. By definition, $\mathbf{grad}X$ and $\mathbf{curl}T$ are symmetric, traceless tensor fields. The following identities generalize the previous ones from vector calculus:

$$\mathbf{curl}\,\mathbf{grad}X = \frac{1}{2}\mathbf{grad}\,\mathbf{curl}X\,, \tag{3.115}$$

$$\mathbf{div}\,\mathbf{curl}T = \frac{1}{2}\mathbf{curl}\,\mathbf{div}T\,, \tag{3.116}$$

$$\mathbf{div}\,\mathbf{grad}X = \frac{1}{2}\Delta X + \frac{1}{6}\mathbf{grad}\,\mathbf{div}X\,, \tag{3.117}$$

$$\mathbf{curl}\,\mathbf{curl}T = -\Delta T + \frac{3}{2}\mathbf{grad}\,\mathbf{div}T\,, \tag{3.118}$$

Notice that the identities (3.115, 3.117) imply that $\mathbf{curl}\,\mathbf{grad}\,\mathbf{grad}\phi = 0$ and $\mathbf{div}\,\mathbf{grad}\,\mathbf{grad}\phi = 2\mathbf{grad}\Delta\Phi/3$. With this notation, the evolution equations (3.77) in the high-frequency limit are

$$\dot\alpha = -f_0 K\,, \tag{3.119}$$

$$\dot\beta^i = G_0 B^i\,, \tag{3.120}$$

$$\dot B = H_0\left(\Delta\beta + \frac{1}{3}\mathbf{grad}\,\mathbf{div}\beta - \frac{4}{3}\mathbf{grad}K\right)\,, \tag{3.121}$$

$$\dot\gamma = -2A + 2\mathbf{grad}\beta\,, \tag{3.122}$$

$$\dot\phi = \frac{1}{6}\left(K + \mathbf{div}\beta\right)\,, \tag{3.123}$$

$$\dot A = \frac{1}{2}\Delta\gamma + \mathbf{grad}\Gamma - 2\mathbf{grad}\,\mathbf{grad}\phi - \mathbf{grad}\,\mathbf{grad}\alpha\,, \tag{3.124}$$

$$\dot K = -\Delta\alpha\,, \tag{3.125}$$

$$\dot\Gamma = \Delta\beta + \frac{1}{3}\mathbf{grad}\,\mathbf{div}\beta - \frac{4}{3}\mathbf{grad}K\,, \tag{3.126}$$

where f_0, G_0 and H_0 are the values of f, G and H frozen at the point p, and where for notational simplicity I omit the tildes over $\tilde{\gamma}$, $\tilde{A}$, and $\tilde{\Gamma}$ and continue to do so in what follows. The linearized constraints are

$$\begin{aligned} \mathcal{H} &\equiv \frac{1}{2}\mathbf{div}\Gamma - 4\Delta\phi = 0\,, && (3.127)\\ \mathcal{M} &\equiv \mathbf{div}A - \frac{2}{3}\mathbf{grad}K = 0\,, && (3.128)\\ \mathcal{C} &\equiv \Gamma - \mathbf{div}\gamma = 0\,. && (3.129) \end{aligned}$$

To establish a stable system in the high-frequency domain, I focus my attention to the linearized electric and magnetic parts of the Weyl curvature tensor. In terms of the BSSN variables, these symmetric traceless tensors can be defined as

$$\begin{aligned} \mathcal{E} &= \dot{A} + \mathbf{grad}\,\mathbf{grad}\mathcal{M}\,, && (3.130)\\ \mathcal{B} &= \mathbf{curl}A\,. && (3.131) \end{aligned}$$

Using the evolution equations (3.119) and the above identities (3.115-3.118) I find that these quantities obey the FOSH system

$$\begin{aligned} \dot{\mathcal{E}} &= -\mathbf{curl}\mathcal{B} + \frac{3}{2}\mathbf{grad}\mathcal{M}\,, && (3.132)\\ \dot{\mathcal{B}} &= +\mathbf{curl}\mathcal{E}\,, && (3.133)\\ \dot{\mathcal{M}} &= \mathbf{div}\mathcal{E}\,. && (3.134) \end{aligned}$$

which is subject to the constraint $2\mathbf{div}B = 2\mathbf{div}\,\mathbf{curl}A = \mathbf{curl}\,\mathbf{div}A = \mathbf{curl}M$. The corresponding symbol with respect to the one-form n is

$$\begin{aligned} \dot{\mathcal{E}} &= -n \wedge \mathcal{B} + \frac{3}{2} n \otimes \mathcal{M}\,, && (3.135)\\ \dot{\mathcal{B}} &= +n \wedge \mathcal{E}\,, && (3.136)\\ \dot{\mathcal{M}} &= n \cdot \mathcal{E}\,. && (3.137) \end{aligned}$$

where I use the notation $(n \wedge \mathcal{B})_{ij} := \varepsilon_{kl(i} n^k \mathcal{B}^l_{j)}$, $(n \otimes \mathcal{M})_{ij} := n_{(i}\mathcal{M}_{j)} \frac{1}{3}\delta_{ij} n^k \mathcal{M}_k$, $(n \cdot \mathcal{E})_j = n^i \mathcal{E}_{ij}$. Decomposing, I obtain

$$\begin{aligned} \mathcal{M} &= \mathcal{M}_{\|} n + \mathcal{M}_{\perp}\,,\\ \mathcal{E} &= \frac{3}{2}\mathcal{E}_{\|\|} n \otimes n + 2n \otimes \mathcal{E}_{\|\perp} + \mathcal{E}_{\perp\perp}\,, \end{aligned}$$

into pieces parallel and orthogonal to n, this implies

$$\begin{gathered} \dot{\mathcal{E}}_{\|\|} = \mathcal{M}_{\|}\,, \qquad \dot{\mathcal{B}}_{\|\|} = 0\,, \qquad \dot{\mathcal{M}}_{\|} = \mathcal{E}_{\|\|}\,,\\ \dot{\mathcal{E}}_{\|\perp} = -\frac{1}{2} n \wedge \mathcal{B}_{\|\perp} + \frac{3}{4}\mathcal{M}_{\perp}\,, \qquad \dot{\mathcal{B}}_{\|\perp} = \frac{1}{2} n \wedge \mathcal{E}_{\|\perp}\,,\\ \dot{\mathcal{E}}_{\perp\perp} = -n \wedge \mathcal{B}_{\perp\perp}\,, \qquad \dot{\mathcal{B}}_{\perp\perp} = n \wedge \mathcal{E}_{\perp\perp}\,, \end{gathered}$$

from which I obtain the characteristic fields

$$\begin{aligned}
V^{(\pm 1)} &= \mathcal{E}_{\|\|} \pm \mathcal{M}_{\|}\,, \\
V_{\perp}^{(\pm 1)} &= 4\mathcal{E}_{\|\perp} \mp 2n \wedge \mathcal{B}_{\|\perp} \pm 3\mathcal{M}\,, \\
Z_{\perp}^{(0)} &= \mathcal{B}_{\|\perp} - \frac{1}{2} n \wedge \mathcal{M}_{\perp}\,, \\
V_{\perp\perp}^{(\pm 1)} &= \mathcal{E}_{\perp\perp} \mp n \wedge \mathcal{B}_{\perp\perp}\,,
\end{aligned}$$

with corresponding speeds indicated by the superscripts (± 1) and (0). Maximally dissipative boundary conditions allow a coupling between the in- and outgoing fields of the form $V^{(+1)} = cV^{(1)} + G$, where c is a constant which is smaller than or equal to one in magnitude, n is the unit outward normal to the boundary and G is boundary data. The fields $V_{\perp\perp}^{(\pm 1)}$ are related to the (linearized) Weyl scalars Ψ_0 and Ψ_4 constructed from a null tetrad $l, k, m, \bar{m}$ with $l = \partial_t + n$, $k = \partial_t n$ through

$$V_{\perp\perp}^{(+1)} = (\Psi_0 \bar{m} \otimes \bar{m} + \Psi_0 m \otimes m)\,, \qquad V_{\perp\perp}^{(-1)} = (\Psi_4 \bar{m} \otimes \bar{m} + \Psi_4 m \otimes m)\,.$$

In particular, the allowed class of boundary conditions makes it possible to freeze the Weyl scalar Ψ_0 at the boundary to its initial value by imposing

$$V_{\perp\perp}^{(+1)} = V_{\perp\perp}^{(+1)}|_{t=0}\,. \tag{3.138}$$

This condition has been shown to yield a reflection coefficient that decays as fast as $(kR)^4$ for monochromatic gravitational radiation with wave number k and a spherical outer boundary of radius R [84, 131]. It has also been tested numerically in [111] and shown to out-perform other currently used boundary conditions. By imposing $V^{(+1)} = V^{(-1)}$, it is also possible to set the constraint $\mathcal{M}_{\|\|}$ to zero at the boundary. On the other hand, the form of $V_{\perp}^{(\pm 1)}$ does not allow us to set the orthogonal component, $\mathcal{M}_{\perp}$, of the momentum constraint variable to zero.

For this reason, I perform a slight modification to the propagation system (3.132) by using the constraint $2\mathbf{div}\mathcal{B}\mathbf{curl}\mathcal{M} = 0$. For this, let $n := \partial_x$. n is a unit vector field, which, at the boundary, coincides with the unit outward normal to $\partial\Omega$. Then, replace Eq. (3.132) with

$$\dot{\mathcal{E}} = -\mathbf{curl}\mathcal{B} + \frac{3}{2}\mathbf{grad}\mathcal{M} + n \otimes \left[n \wedge \left(\mathbf{div}\mathcal{B} - \frac{1}{2}\mathbf{curl}\mathcal{M} \right) \right]\,. \tag{3.139}$$

With this modification I have $\dot{\mathcal{E}}_{\|\perp} = M_{\perp}$. The time-derivative of the other fields remain unchanged. The characteristic fields with respect to n are the same as before except for $V_{\perp}^{(\pm 1)}$ which has to be replaced by

$$V_{\perp}^{(\pm)} = \mathcal{E}_{\|\perp} \pm \mathcal{M}_{\perp}\,. \tag{3.140}$$

Therefore, it is now possible to impose the momentum constraint at the boundary: $M = 0$ by requiring $V^{(+1)} = V^{(-1)}$ and $V_{\perp}^{(+1)} = V_{\perp}^{(-1)}$. In order to show that this leads to a well-posed system I prove that these boundary conditions, together with the Ψ_0-freezing boundary condition (3.138) are maximally dissipative conditions and that the modified evolution system (3.132, 3.139) is still symmetric hyperbolic. For this, it is convenient to replace $\mathcal{B}$ by the new variable $\mathcal{K}$ defined by

$$\mathcal{K} := \mathcal{B} - n \otimes (n \wedge \mathcal{M}) \,. \tag{3.141}$$

In order to write down the principal symbol of the resulting evolution equations, I choose standard Cartesian coordinates $x\,, y\,, z$ on Ω such that $n = \partial_x$. The principal symbol with respect to an arbitrary one-form m then reads

$$\begin{aligned}
\dot{\mathcal{E}}_{xx} &= -\varepsilon^{AB} m_A \mathcal{K}_{Bx} + m_x \mathcal{M}_x - m^A \mathcal{M}_A \,, && (3.142)\\
\dot{\mathcal{K}}_{xx} &= -\varepsilon^{AB} m_A \mathcal{E}_{Bx} \,, && (3.143)\\
\dot{\mathcal{M}}_x &= m_x \mathcal{M}_x + m^A \mathcal{E}_{Ax} \,, && (3.144)\\
\dot{\mathcal{E}}_{xB} &= -\varepsilon^{CD} m_C \hat{\mathcal{K}}_{DB} - \frac{1}{2} \varepsilon^{C}_{B} m_C m_C \mathcal{K}_{xx} + m_x \mathcal{M}_B + \frac{1}{2} m_B \mathcal{M}_x \,, && (3.145)\\
\dot{\mathcal{K}}_{xB} &= +\varepsilon^{CD} m_C \hat{\mathcal{E}}_{DB} + \frac{1}{2} \varepsilon^{C}_{B} m_C \mathcal{E}_{xx} \,, && (3.146)\\
\dot{\mathcal{M}}_B &= m_x \mathcal{E}_{xB} + m^A \hat{\mathcal{E}}_{AB} - \frac{1}{2} m_B \mathcal{E}_{xx} \,, && (3.147)\\
\dot{\mathcal{E}}_{AB} &= -m_x \varepsilon_{C(A} \hat{\mathcal{K}}^{C}_{B)} + \varepsilon_{C(A} m^C \mathcal{K}_{B)x} - \frac{1}{2} \delta_{AB} \varepsilon^{CD} m_C \mathcal{K}_{Dx} && (3.148)\\
&+ m_{(A} \mathcal{M}_{B)} - \frac{1}{2} \delta_{AB} m^C \mathcal{M}_C \,, &&\\
\dot{\mathcal{K}}_{AB} &= +m_x \varepsilon_{C(A} \hat{\mathcal{E}}^{C}_{B)} - \varepsilon_{C(A} m^C \mathcal{E}_{B)x} + \frac{1}{2} \delta_{AB} \varepsilon^{CD} m_C \mathcal{E}_{Dx} \,, && (3.149)\\
& && (3.150)
\end{aligned}$$

where the indices A, B, C, D refer to the coordinates y and z, and I have defined $\hat{\mathcal{E}}_{AB} := \mathcal{E}_{AB} \frac{1}{2} \delta_{AB} \delta^{CD} \mathcal{E}_{CD}$ and an analogous relation for $\hat{\mathcal{K}}_{AB}$. It is straightforward to verify that this symbol is symmetric with respect to the symmetrizer $\mathbf{H}$ defined by

$$\begin{aligned}
U^T \mathbf{H} U &= \mathcal{E}_{xx}^2 + \mathcal{K}_{xx}^2 + \mathcal{M}_x^2 + 2\delta^{AB} \left(\mathcal{E}_{xA} \mathcal{E}_{xB} + \mathcal{K}_{xA} \mathcal{K}_{xB} + \mathcal{M}_A \mathcal{M}_B \right) && (3.151)\\
&+ 2\delta^{AC} \delta^{BD} \left(\hat{\mathcal{E}}_{AB} \hat{\mathcal{E}}_{CD} + \hat{\mathcal{K}}_{AB} \hat{\mathcal{K}}_{CD} \right) \,, &&
\end{aligned}$$

where $U = (\mathcal{E},\, \mathcal{K},\, \mathcal{M})^T$. In a coordinate-independent notation, I may also write

$$U^T \mathbf{H} U = |\mathcal{E}_{\|\|}|^2 + |\mathcal{K}_{\|\|}|^2 + |\mathcal{M}_{\|}|^2 + 2|\mathcal{E}_{\|\perp}|^2 + 2|\mathcal{K}_{\|\perp}|^2 + 2|\mathcal{M}_{\perp}|^2 + |\mathcal{E}_{\perp\perp}|^2 + |\mathcal{K}_{\perp\perp}|^2 \,. \tag{3.152}$$

As I did for the harmonic system, in order to demonstrate well-posedness mathematically, I want to obtain a bound on the time dependence of the energy of the system. To do this I define the energy norm, as before

$$N := \int_{\Omega} U^T \mathbf{H} U d^3x \tag{3.153}$$

and take the time derivative to obtain the estimate

$$\begin{aligned}\frac{d}{dt}N &= -\int_{\partial\Omega}\left[2\mathcal{E}_{xx}\mathcal{M}_x + 4\mathcal{E}_{xA}\mathcal{M}^A + 4\hat{\mathcal{E}}^{AB}\varepsilon_{AC}\hat{\mathcal{K}}^C_B\right] d^2x \\ &= \int_{x=0}\left[\frac{1}{2}\left(|V^{(+1)}|^2 - |V^{(-1)}|^2\right) + \left(|V_\perp^{(+1)}|^2 - |V_\perp^{(-1)}|^2\right)\right. \\ &+ \left.\left(|V_{\perp\perp}^{(+1)}|^2 - |V_{\perp\perp}^{(-1)}|^2\right)\right] dydz \\ &= -\int_{x=0}|V_{\perp\perp}^{(-1)}|^2_{t=0}dydz + \int_{x=0}|V_{\perp\perp}^{(+1)}|^2_{t=0}dydz \\ &\leq 2\int_{x=0}|\Psi_0|^2_{t=0}dydz\end{aligned} \tag{3.154}$$

if the boundary conditions $\mathcal{M}_x = 0$ and (3.138) are imposed. Therefore, I obtain an L^2-estimate for the curvature variables $\mathcal{E}$, $\mathcal{B}$, $\mathcal{M}$. In view of Eqs. (3.130, 3.131, 3.129) this yields L^2-estimates for $\dot{A}$, $\mathbf{curl}A$ and $\mathbf{div}A$ provided I have appropriate estimates for the lapse, α, and the trace of the extrinsic curvature, K. As for the harmonic system, by integrating the evolution equations in time one obtains L^2-estimates for ϕ, $\mathbf{grad}\phi$, γ, $\mathbf{curl}\gamma$, $\mathbf{div}\gamma$ provided suitable estimates are available for α, K and β. This will be shown in the next section.

These estimates are sufficient to bound the L^2 norm of the full gradient of A. On $\Re^3$, it can be proven that an L^2 bound on $\mathbf{curl}A$ and $\mathbf{div}A$ imply an L^2-bound on $\mathbf{grad}A$. However, this is not true in general on the half-plane Ω: For example, let χ be an arbitrary harmonic function on which decays exponentially to zero as $|x| \to \inf$ and let $A := \mathbf{grad}\,\mathbf{grad}\chi$. Then, $\mathbf{curl}A = 0$ and $\mathbf{div}A = 2\mathbf{grad}\Delta\chi/3 = 0$, but $A \neq 0$ unless boundary conditions at $x = 0$ force χ to be linear. Thus conditions need to be specified on all boundary planes for well-posedness to hold.

3.2.4 Propagation of Lapse and Shift

In this section I analyze the "gauge sector", that is the propagation of lapse and shift. I continue to work with the assumptions of the last section: $m = 1$, and small amplitude, high frequency perturbations to smooth solutions so that the evolution equations for the lapse and shift are given by Eqs. (3.119, 3.120). I will also use the corresponding evolution equation for the trace of the extrinsic curvature, Eq. (3.125). It is useful to define the quantities: $a := f_0^{-1}\mathbf{grad}\alpha$, $D := G^{-1}\mathbf{div}\beta$, $R := G^{-1}\mathbf{curl}\beta$. Thus from these definitions and Eqs.(3.119-3.125) I obtain the following first-order system

$$
\begin{aligned}
\dot{\alpha} &= -f_0 K\,, && (3.155)\\
\dot{\beta} &= G_0 B\,, && (3.156)\\
\dot{B} &= \kappa_0\left(-3\mathbf{curl}R + 4\mathbf{grad}D - \frac{4}{G_0}\mathbf{grad}K\right)\,, && (3.157)\\
\dot{R} &= \mathbf{curl}B\,, && (3.158)\\
\dot{D} &= \mathbf{div}B\,, && (3.159)\\
\dot{K} &= f_0\mathbf{div}a\,, && (3.160)\\
\dot{a} &= \mathbf{grad}K\,, && (3.161)
\end{aligned}
$$

where $\kappa_0 := G_0 H_0/3$ and where I have used the identity (3.113). This system is almost in symmetric hyperbolic form– only the last term on the right-hand side of the evolution equation for B is an exception. However, if I assume that $4\kappa_0 \neq f_0$ and replace D and B by the new fields

$$
F := D + \frac{4H_0 K}{3(f_0 - 4\kappa_0)}\,, \qquad C := B + \frac{4H_0 f_0 a}{3(f_0 - 4\kappa_0)}\,, \tag{3.162}
$$

and use the constraint $f_0\mathbf{curl}a = \mathbf{curl}\,\mathbf{grad}\alpha = 0$, I can rewrite the system in the form

$$
\begin{aligned}
\dot{K} &= f_0\mathbf{div}a\,, && (3.163)\\
\dot{a} &= \mathbf{grad}K\,, && (3.164)\\
\dot{C} &= \kappa_0\left(-3\mathbf{curl}R + 4\mathbf{grad}F\right)\,, && (3.165)\\
\dot{R} &= \mathbf{curl}C\,, && (3.166)\\
\dot{F} &= \mathbf{div}C\,, && (3.167)
\end{aligned}
$$

which is now manifestly symmetrizable hyperbolic. If I introduce the energy norm as in the previous sections

$$
E := \frac{1}{2}\int_\Omega \left(K^2 + f_0|a|^2 + C^2 + 3\kappa_0|R|^2 + 4\kappa_0 F^2\right) d^3x\,, \tag{3.168}
$$

the evolution equations then imply that

$$
\begin{aligned}
\frac{d}{dt}E &= \int_\Omega \mathbf{div}\left(f_0 K a + 4\kappa_0 F C + 3\kappa_0 C\wedge R\right) d^3x && (3.169)\\
&= -\int_{x=0} \left(f_0 K a_x + 4\kappa_0 F C_x + 3\kappa_0 (C\wedge R)_x\right) dydz\,.
\end{aligned}
$$

In terms of the characteristic fields this becomes

$$
Y^{(\pm)} := K + \sqrt{f_0}a_\parallel\,, \qquad W_\parallel^{(\pm)} := C_\parallel \pm 2\sqrt{\kappa_0}F\,, \qquad W_\perp^{(\pm)} := C_\perp \mp \sqrt{3\kappa_0}n\wedge R\,, \tag{3.170}
$$

where again $n = \partial_x$, so the time derivative of the energy norm becomes

$$\begin{aligned} \frac{d}{dt}E &= \frac{1}{4}\int_{x=0} \Big(\sqrt{f_0}\left[|Y^{(+)}|^2 - |Y^{(-)}|^2\right] \qquad (3.171) \\ &+ 2\sqrt{\kappa_0}\left[|W_{\|}^{(+)}|^2 - |W_{\|}^{(-)}|^2\right] + \sqrt{3\kappa_0}\left[|W_{\perp}^{(+)}|^2 - |W_{\perp}^{(-)}|^2\right]\Big)\, dydz\,. \end{aligned}$$

An interesting possibility to bound this solution then consists of the following boundary conditions

$$\partial_x\alpha = 0\,, \qquad \beta_x = 0\,, \qquad (\partial_t - \sqrt{3\kappa_0}\partial_x)\beta_A = \frac{4\kappa_0}{f_0 - 4\kappa_0}\partial_A\alpha\,, \qquad A = y, z\,. \tag{3.172}$$

Thus implying that $Y^{(+)} = Y^{(-)}$, $W_{\|}^{(+)} = W_{\|}^{(-)}$and $W_{\perp}^{(+)} = 0$, which makes the boundary term negative definite. Furthermore, these conditions allow for the control the normal component of the shift, which is what is wanted. However, an alternative choice for gauge conditions at the boundary could consist of

$$\partial_x\alpha = 0\,, \qquad \beta_x = 0\,, \qquad (\partial_t - \sqrt{3\kappa_0}\partial_x)\beta_A = 0\,, \qquad A = y, z\,. \tag{3.173}$$

which implies $Y^{(+)} = Y^{(-)}$, $W_{\|}^{(+)} = W_{\|}^{(-)}$ and $W_{\perp}^{(+)} = W_{\perp}^{(-)}$ and makes the boundary term zero.

In this way, I obtain an L^2-estimate for the fields $K = -f_0^{-1}\dot{\alpha}$, $\mathbf{grad}\alpha$, $B = G_0^{-1}\dot{\beta}$, $\mathbf{curl}\beta$ and $\mathbf{div}\beta$. With the boundary condition $x = 0$ this implies an L^2-estimate for the symmetric and traceless gradient, $\mathbf{grad}$, of the shift β. This follows from the integral identity

$$\begin{aligned} \int_\Omega |\mathbf{grad}\beta|^2 d^3x &= \int_\Omega \left(\frac{1}{2}|\mathbf{curl}\beta|^2 + \frac{2}{3}|\mathbf{div}\beta|^2\right) d^3x \qquad (3.174) \\ &- \int_{x=0} \left(\beta^A\partial_A\beta_x - \beta_x\partial_A\beta^A\right) dydz\,, \end{aligned}$$

which follows using twice integration by parts. Therefore, I obtain an estimate for the H^1-norms of lapse and shift. The second derivatives of α and β can be estimated by first taking time and tangential derivatives of the evolution equations and boundary conditions, and repeating the above analysis to obtain an L^2 bound for $\ddot{\alpha}$ and $\ddot{\beta}$ and an H^1 bound for $\partial_A\alpha$ and $\partial_A\beta$ and then using the evolution equations $\ddot{\alpha} = f_0\Delta\alpha$ and $\ddot{\beta} = \kappa_0(3\Delta\beta + \mathbf{grad}\,\mathbf{div}\beta - 4\mathbf{grad}K)$ in order to estimate the second normal derivatives $\partial_x\partial_x\alpha$ and $\partial_x\partial_x\beta$. In this way, one arrives at an H^2-bound for α and β^i. In the fully-discrete system, this of course, only holds if you have finite differencing stencils whose operators obey SBP as described in the previous section, and, of course, only in the linearized regime, where an assumption of flat lapse and negligible shift is valid within numerical error.

3.2.5 Numerical Implementation

I have derived boundary conditions involving the geometric fields and their derivatives evaluated at the boundary. Those conditions coming from the fact that the momentum constraint has to be preserved at the boundary, $M_j|_{\partial\Omega} = 0$, should not be difficult to implement numerically, as long as these conditions are already satisfied for the initial hypersurface, so one must be careful to see that it is also initially satisfied at the boundaries. Once this is done, the condition must hold through out the evolution. But this is usually checked at every few steps, as a measure that the constraints are being preserved, so it is only needed to see that this is so at the boundaries as well. Simply put, from the momentum constraint, I have obtained the right-hand-side conditions

$$\begin{aligned} \dot{K} &= K_{,r} - \frac{1}{r}K = \frac{3}{2}\left(\tilde{D}^j \tilde{A}_{rj} + 6\tilde{A}_{rj} + 6\tilde{A}_{rj}\tilde{D}^j\phi\right) && (3.175) \\ \dot{A}_{xx} &= -(\mathbf{curl}A)_{xx} && (3.176) \end{aligned}$$

With respect to the gauge conditions, the ones referring to the direction normal to the hypersurface, $\beta_x = \partial_x\alpha = 0$, should not present any implementation problem. If one starts with initial conditions considering that the lapse is approximately one and shift is vanishing at the boundary and the normal component of the lapse should remain zero. However, for boundaries in the simulation domain in the region where the lapse is different from one by much more than numerical error, and the lapse or the shift is rapidly evolving, these boundaries will perform much worse than standard radiative conditions.

With respect to the other two conditions, if I consider that $\partial_x\beta_A = 0$, and that initially the shift was zero, one has to implement that it remains so at the boundary. If I chose the other two conditions: $(\partial_t - \sqrt{3\kappa_0}\partial_x)\beta_A = \frac{4\kappa_0}{f_0 - 4\kappa_0}\partial_A\alpha$, they are more robust and, by construction, they are consistent with the evolution equation for the shift, but their numerical implementation is more challenging. However, where $\partial_x\beta_A = 0$ is not consistent with the shift conditions for the system, this choice is not stable. Thus a more freely evolving condition such as $(\partial_t - \sqrt{3\kappa_0}\partial_x)\beta_A = \frac{4\kappa_0}{f_0 - 4\kappa_0}\partial_A\alpha$ is the better choice for most simulations using a Gamma-driver shift.

It is of course the final test of this proposal, to show that it is not only a theoretical discussion, which is in itself valid and important to know that one works with a clean problem, but also it is has to be seen directly during the actual numerical evolutions.

3.2.6 Discussion

Besides the importance of having a well-posed system, there is a practical consequence of defining correct conditions at the boundary. This is the fact that this choice allows one to place the boundary conditions, in principle, in any place where the linearized assumptions hold, thus reducing the need for making large numerical grids with the consequence of savings in computational resource requirements needed to simulate a given problem.

The question is not how to avoid the problem of artificial outer boundary well-posedness by creative ways, for instance adding numerical dissipation so that almost nothing arrives at the boundary, but the purpose should rather be to directly face the problem and having, at least in the theoretical level, a set of equations that are well defined. It took some time for the numerical community to get convinced of the practical advantages of having a well-posed system of equations, and for a time a great deal of attention was focused on the developing powerful codes. During this time several mathematical aspects were neglected. Learning from that experience, it seems reasonable to insist on the need for evolving with a clean and properly posed system of equations.

In the present work I have derived for the BSSN formulation the necessary boundary conditions which preserve the constraints and lead to a stable initial-boundary value problem in the linear limit for spacetimes which are the conformally flat. These conditions are given in terms of the variable fields and its derivatives at the boundary, and I have shown that the final system is indeed symmetric hyperbolic and preserves the constraints. Notice that the needed conditions at the boundary do not involve all the geometric quantities nor their derivatives, only the normal component of the shift, β^x, the derivative of the lapse in the normal direction, $\partial_x \alpha$, a relation between the advection derivative of the tangential components of the shift and the the derivative of the lapse in these directions; three relations among the derivative of the trace of extrinsic curvature, the gradient of the symmetric traceless tensor $\tilde{A}_{ij}$, and the conformal function, ϕ; and two relations between the temporal and spatial derivative of the normal component of the symmetric traceless tensor $\tilde{A}_{xx}$. Thus, unlike standard methods, one does not over-specify the conditions on the boundary surface.

For sufficiently distant boundaries in the linearized regime, the boundary conditions described in the present work will help to make the numerical evolutions of relativistic spacetimes more robust. In terms of practical gain, there is still much work to be done in order to quantify the importance of using adequate boundary conditions. However, any improvement in accuracy and efficiency is a valuable contribution for the current state of the field of numerical relativity.

Chapter 4

Physics from Numerical Simulations

Binary black hole systems are expected to be one of the strongest sources of gravitational waves and are therefore the subject of intense investigation. With earth-based gravitational-wave detectors now working at design-sensitivity and a space-borne detector in planning stages, the need for reliable templates to be used by detectors in matched filtering techniques has made the need for numerical analysis more urgent. Using numerical methods developed in the past four years [19, 20, 132] there has been an explosion of results (see, *e.g.*, refs. [9, 59, 133–143]). These developments are important for at least three different reasons. First, they allow for improved templates to be used in the analysis of the data coming from the detectors. Second, they allow probes of General Relativity in regimes that have previously been inaccessible. Lastly,– and the topic of this chapter – they can provide important astrophysical information.

Recent progress in numerical relativity has solved the problem of stably evolving black hole initial data for useful timescales. This has opened the door to studies of physical phenomena resulting from strong-field gravitational interactions and to extended and systematic studies of these systems. A result of particular interest to astrophysics is an accurate calculation of the recoil velocity and spin of the final merged black hole generated during an asymmetric collision of a black-hole binary. It is well known that a binary with unequal masses or spins of the individual bodies will radiate gravitational energy asymmetrically. This results in an uneven flux, which gives a net linear momentum to the final black hole, often called a “kick” [144, 145]. While estimations of kick velocities have been available for some time [146–148], the largest part of the system’s acceleration is generated in the final orbits of the binary system, and as such requires fully relativistic calculations to be determined accurately. General relativity also predicts that black hole spins and their angular momenta interact due to frame dragging and cause ‘spin-up’ and ‘spin-down’ effects, not predicted by classical gravity. The knowledge of both the ‘kick’ velocity and of the final spin could have a direct impact on studies of the evolution of supermassive black holes and on statistical studies on the dynamics of compact objects in dense stellar systems, as well as significant effect on the waveform and impact on parameter estimation for gravitational wave detectors, which will be discussed in the next chapter.

It can be convenient to think of the inspiral and merger of two black holes (BHs) as a mechanism which takes, as input, two BHs of initial masses M_1, M_2 and spin vectors $\boldsymbol{S}_1$, $\boldsymbol{S}_2$ and produces, as output, a third BH of mass $M_{\rm fin}$ and spin $\boldsymbol{S}_{\rm fin}$. Since most or all of the eccentricity is removed quickly by the gravitational radiation reaction during the inspiral [149], in conditions of particular astrophysical interest, the inspiral takes place through quasi-circular orbits. Furthermore, for nonspinning equal mass BHs, the final spin does not depend on the value of the eccentricity as long as it is not too large [150]. The determination of $M_{\rm fin}$ and $\boldsymbol{S}_{\rm fin}$ from the knowledge of $M_{1,2}$ and $\boldsymbol{S}_{1,2}$, is of great importance in several fields. In astrophysics, it provides information on the properties of isolated stellar mass BHs produced at the end of the evolution of a binary system of massive stars. In cosmology, it can be used to model the distribution of masses and spins of the supermassive BHs produced through the merger of galaxies. In addition, in gravitational wave astronomy, the *a priori* knowledge of the final spin can help the detection of the ringdown. What makes this a difficult problem is clear: the space of initial parameters for the final spin has seven dimensions (*i.e.*, the mass ratio $q \equiv M_2/M_1$ and the six components of the two spin vectors). A number of analytical approaches have been developed over the years to determine the final spin, either exploiting the dynamics of point-particles [4, 151] or using more sophisticated approaches such as the effective one body (EOB) approximation [152]. Ultimately, however, computing $\boldsymbol{a}_{\rm fin} \equiv \boldsymbol{S}_{\rm fin}/M_{\rm fin}^2$ accurately requires the solution of the full Einstein equations and thus the use of numerical relativity simulations. Several groups have investigated this problem over the last couple of years [1, 8, 9, 87, 153].

In this section I will discuss work done in collaboration with Luciano Rezzolla, Enrico Barausse, Ernst Nils Dorband, Denis Pollney, Christian Reisswig, Sascha Husa, Peter Diener, and Erik Schnetter to study the parameter space of binary black hole collisions in vacuum. I will discuss the simulations done to cover this seven-dimensional parameter space, done with the code described in Section [2.7]. I will then discuss how we derived phenomenological formulae for the prediction of final recoil velocity and spin of a merged black hole from physical assumptions and fits to our numerically generated results. This section is based upon papers written with the aforementioned people and myself. The spin results may be found in the works [8, 154]. The kick results may be obtained from [87, 155].

4.1 Simulations

Over the past few years, a number of simulations have been carried out to determine the recoil velocities for a variety of binary black-hole systems. Non-spinning but unequal-mass binaries were the first systems to be studied and several works have now provided an accurate mapping of the unequal mass space of parameters [136, 139, 156]. More recently, the recoils from binaries with spinning black holes have also been considered by investigating equal-mass binaries in which the spins of the black holes are either aligned with the orbital angular momentum [155, 157], or anti-aligned (i.e. S_1 is parallel to L and $S_1 = -S_2$). In the first case, a systematic investigation has shown that the largest recoil possible from such systems is on the order of $450\,{\rm km/s}$ [87]. In the second case, instead, specific configurations with spins orthogonal to the orbital one have been shown to lead to recoils as high as $2500\,\mathrm{km/s}$ [158, 159], suggesting a maximum kick of about $4000\,\mathrm{km/s}$ for maximally-spinning black holes [160]. Recoil velocities of this magnitude could lead to the ejection of massive black holes from the hosting galaxies, with important consequences on their cosmological evolution. Beyond that, studies have been, and are still being performed to cover the space of misaligned (not aligned or anti-aligned) and unequal spins, and unequal masses with spins. Challenges still remain to extend to extremal spins ($S_i \approx 0.9$) and low mass ratios ($q \approx 0.1$) for numerical simulations. However, by fitting to the results for the range and dimensions of the parameter space we are able to cover, and by matching to the extreme mass ratio inspiral case (EMRI) for which we may use a point particle solution, we can fairly accurately predict final spin and recoil velocity for the entire space of parameters (a_{1i}, a_{2i}, and q).

The numerical simulations have been carried out using the CCATIE code described in Section [2.7], a three-dimensional finite-differences code using the Cactus Computational Toolkit [91] and Carpet mesh refinement infrastructure [93]. The main features of the code have been recently reviewed in [87], where the code has been employed using the "moving-punctures" technique [20, 59] described in Section [2.4.4]. For aligned and anti-aligned spins, initial data consists of five sequences with constant orbital angular momentum, which is different from sequence to sequence. In the r and ra-sequences, the initial spin of one of the black holes $\mathbf{S}_2$ is held fixed along the z-axis and the spin of the other black hole is varied so that the spin ratio a_1/a_2 takes the values between -1 and $+1$, with $a_i \equiv \mathbf{S}_i/M_i^2$. In the t-sequence, instead, the spin with a negative z-component is held fixed, while in the s and u-sequences $a_1/a_2 = 1$ and -1, respectively. In all those cases, the masses are $M_i = M/2 = 1/2$. I performed further simulations for unequal masses with aligned spins, and two simulations with misaligned spins and equal masses, and two simulations with spins selected to merge near Schwarzschild ($\mathbf{S}_{fin} = 0$) as predicted by our formula.

For r, ra, s, t, and u sequences defined in Table (4.2) the orbital initial data parameters we use the effective-potential method, which allows one to choose the initial data parameters such that the resulting physical parameters (*e.g.,* masses and spins) describe a binary black-hole system on a quasi-circular orbit. For the misaligned and unequal mass runs higher accuracy was required and I generated the initial data by integrating post-Newtonian equations to obtain the inspiral parameters. The free parameters are: the coordinate locations $\mathbf{C}_i$, the mass parameters m_i, the linear momenta $\mathbf{p}_i$, and the spins $\mathbf{S}_i$. For the aligned and anti-aligned runs quasi-circular orbits were then selected by setting $\mathbf{p}_1 = -\mathbf{p}_2$ to be orthogonal to $\mathbf{C}_2 - \mathbf{C}_1$, so that $\mathbf{L} \equiv \mathbf{C}_1 \times \mathbf{p}_1 + \mathbf{C}_2 \times \mathbf{p}_2$ is the orbital angular momentum. The initial parameters for the aligned and misaligned spin simulations are collected in the left part of Table 4.2, while the right part reports the results of simulations. For all simulations herein, we have employed 8 levels of refinement and a minimum resolution $0.024\,M$, which has been reduced to $0.018\,M$ for binaries $r5$, $r6$. Our results for the u-sequence differ slightly from those reported by [157], probably because of our accounting of the integration constant in $|v_{\rm kick}|$ [87].

We evolve a conformal-traceless "$3+1$" formulation of the Einstein equations [27–29, 95] described in Section [2.3.2], in which the spacetime is decomposed into three-dimensional spacelike slices, described by a metric γ_{ij}, its embedding in the full spacetime, specified by the extrinsic curvature K_{ij}, and the gauge functions α (lapse) and β^i

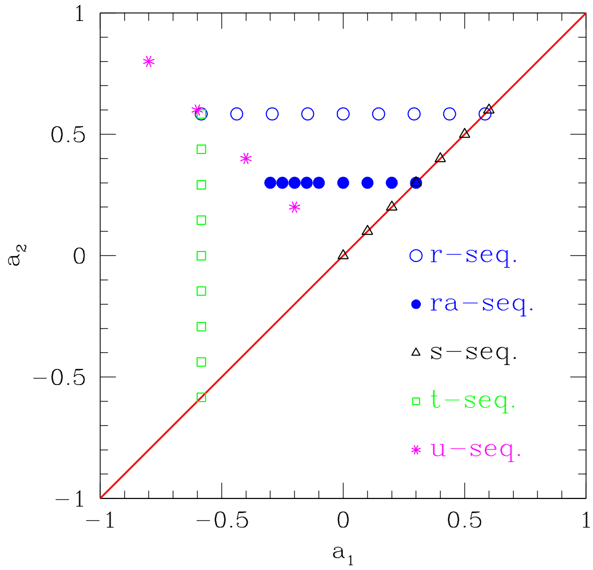

Figure 4.1: Position in the (a_1, a_2) space of the five sequences r, ra, s, t, and u for which the inspiral and merger has been computed.

(shift) that specify a coordinate frame. The particular system which we evolve transforms the standard ADM variables as follows. The 3-metric γ_{ij} is conformally transformed via

$$\phi = \frac{1}{12} \ln \det \gamma_{ij}, \qquad \tilde{\gamma}_{ij} = e^{-4\phi} \gamma_{ij}, \tag{4.1}$$

and the conformal factor ϕ evolved as an independent variable, whereas $\tilde{\gamma}_{ij}$ is subject to the constraint $\det \tilde{\gamma}_{ij} = 1$. The extrinsic curvature is subjected to the same conformal transformation, and its trace $\operatorname{tr} K_{ij}$ evolved as an independent variable. That is, in place of K_{ij} we evolve:

$$K \equiv \operatorname{tr} K_{ij} = g^{ij} K_{ij}, \qquad \tilde{A}_{ij} = e^{-4\phi}(K_{ij} - \frac{1}{3}\gamma_{ij} K), \tag{4.2}$$

with $\operatorname{tr} \tilde{A}_{ij} = 0$. Finally, new evolution variables

$$\tilde{\Gamma}^i = \tilde{\gamma}^{jk} \tilde{\Gamma}^i_{jk} \tag{4.3}$$

are introduced, defined in terms of the Christoffel symbols of the conformal 3-metric.

The Einstein equations specify a well known set of evolution equations for the listed variables and are given by

$$(\partial_t - \mathcal{L}_\beta)\,\tilde{\gamma}_{ij} = -2\alpha\tilde{A}_{ij}, \tag{4.4}$$

$$(\partial_t - \mathcal{L}_\beta)\,\phi = -\frac{1}{6}\alpha K, \tag{4.5}$$

$$(\partial_t - \mathcal{L}_\beta)\,\tilde{A}_{ij} = e^{-4\phi}[-D_iD_j\alpha + \alpha R_{ij}]^{TF} + \alpha(K\tilde{A}_{ij} - 2\tilde{A}_{ik}\tilde{A}^k{}_j), \tag{4.6}$$

$$(\partial_t - \mathcal{L}_\beta)\,K = -D^iD_i\alpha + \alpha(\tilde{A}_{ij}\tilde{A}^{ij} + \frac{1}{3}K^2), \tag{4.7}$$

$$\begin{aligned}\partial_t\tilde{\Gamma}^i &= \tilde{\gamma}^{jk}\partial_j\partial_k\beta^i + \frac{1}{3}\tilde{\gamma}^{ij}\partial_j\partial_k\beta^k + \beta^j\partial_j\tilde{\Gamma}^i - \tilde{\Gamma}^j\partial_j\beta^i + \frac{2}{3}\tilde{\Gamma}^i\partial_j\beta^j \\ &- 2\tilde{A}^{ij}\partial_j\alpha + 2\alpha(\tilde{\Gamma}^i{}_{jk}\tilde{A}^{jk} + 6\tilde{A}^{ij}\partial_j\phi - \frac{2}{3}\tilde{\gamma}^{ij}\partial_jK),\end{aligned} \tag{4.8}$$

where R_{ij} is the three-dimensional Ricci tensor, D_i the covariant derivative associated with the three metric γ_{ij} and "TF" indicates the trace-free part of tensor objects. The Einstein equations also lead to a set of physical constraint equations that are satisfied within each spacelike slice,

$$\mathcal{H} \equiv R^{(3)} + K^2 - K_{ij}K^{ij} = 0, \tag{4.9}$$

$$\mathcal{M}^i \equiv D_j(K^{ij} - \gamma^{ij}K) = 0, \tag{4.10}$$

which are usually referred to as Hamiltonian and momentum constraints. Here $R^{(3)} = R_{ij}\gamma^{ij}$ is the Ricci scalar on a three-dimensional time slice. Our specific choice of evolution variables introduces five additional constraints,

$$\det\tilde{\gamma}_{ij} = 1, \tag{4.11}$$

$$\operatorname{tr}\tilde{A}_{ij} = 0, \tag{4.12}$$

$$\tilde{\Gamma}^i = \tilde{\gamma}^{jk}\tilde{\Gamma}^i_{jk}. \tag{4.13}$$

Our code actively enforces the algebraic constraints (4.11) and (4.12). The remaining constraints, $\mathcal{H}$, $\mathcal{M}^i$, and (4.13), are not actively enforced, and can be used as monitors of the accuracy of our numerical solution. See [33] for a more comprehensive discussion of the these points.

We specify the gauge in terms of the standard ADM lapse function, α, and shift vector, β^a [161]. We evolve the lapse according to the "$1+\log$" slicing condition:

$$\partial_t\alpha - \beta^i\partial_i\alpha = -2\alpha(K - K_0), \tag{4.14}$$

where K_0 is the initial value of the trace of the extrinsic curvature, and equals zero for the maximally sliced initial data we consider here. The shift is evolved using the hyperbolic $\tilde{\Gamma}$-driver condition [33],

$$\partial_t\beta^i - \beta^j\partial_j\beta^i = \frac{3}{4}\alpha B^i\,, \tag{4.15}$$

$$\partial_tB^i - \beta^j\partial_jB^i = \partial_t\tilde{\Gamma}^i - \beta^j\partial_j\tilde{\Gamma}^i - \eta B^i\,, \tag{4.16}$$

where η is a parameter which acts as a damping coefficient. The advection terms on the right-hand-sides of these equations were not present in the original definitions of [33], where co-moving coordinates were used, but have been added following the experience of [60, 132], and are required for correct advection of the puncture in "moving-puncture" evolutions.

Spatial differentiation of the evolution variables is performed via straightforward finite-differencing using fourth-order accurate centered stencils for all but the advection terms for each variable, which are upwinded in the direction of the shift. Vertex-centered adaptive mesh-refinement (AMR) is employed using nested grids [92, 93] with a $2:1$ refinement for successive grid levels, and the highest resolution concentrated in the neighborhood of the individual horizons as described in Section [2.7]. Individual apparent horizons are located every few time steps during the evolution [70, 162] by the method described in Section [2.6.1].

The time steps on each grid are set by the Courant condition and thus the spatial grid resolution for that level, with the time evolution being carried out using fourth-order accurate Runge-Kutta integration steps as in Section [2.5.2]. Boundary data for finer grids are calculated with spatial prolongation operators employing 5th-order polynomials, and prolongation in time employing 2nd-order polynomials. The latter allows a significant memory saving, requiring only three time levels to be stored, with little loss of accuracy due to the long dynamical timescale relative to the typical grid time step.

4.1.1 Initial data

The initial data are constructed applying the "puncture" method [49], which uses Bowen-York extrinsic curvature and solves the Hamiltonian constraint equation numerically as in [52]as discussed in Section [2.4].

We have considered a sequence of binaries for which the initial spin of one of the black holes is held fixed at $\boldsymbol{S}_2/M^2 = 0.146\,\boldsymbol{e}_z$, and the spin of the other black hole is $\boldsymbol{S}_1/M^2 = (a_1/a_2)\boldsymbol{S}_2/M^2$, where the spin ratio a_1/a_2 takes the values $-1,\ -3/4, \ldots, 3/4, 1$, and M is the sum of the black hole masses, $M = M_1 + M_2$. Thus the black hole spins are anti-aligned when a_1/a_2 is negative and aligned when it is positive. In all cases the initial data parameters are chosen such that the black hole masses are

$$M_i = \sqrt{\frac{A_i}{16\pi} + \frac{4\pi S_i^2}{A_i}} = \frac{1}{2}, \tag{4.17}$$

[163, 164] where A_i is the area of the i-th apparent horizon as derived in Section [2.6.2].

For the orbital initial data parameters I use the effective potential method introduced in [165] and extended to spinning configurations in [166]. The effective potential method is a way of choosing the initial data parameters such that the required physical parameters (e.g. masses and spins) are obtained to describe a binary black-hole system on a quasi-circular orbit.

The free parameters to be chosen for the puncture initial data are: the puncture coordinate locations $\boldsymbol{C}_i$, the puncture mass parameters m_i, the linear momenta $\boldsymbol{p}_i$, and the

Table 4.1: The puncture initial data parameters defining the binaries: location $\pm x/M$, linear momenta $\pm p/M$, mass parameters m_i/M, spins S_i/M^2, dimensionless spins a_i, ADM mass M_{ADM} measured at infinity, and ADM angular momentum J_{ADM} computed from Eq. (4.48). Note that we set $M_1 = M_2 = 1/2$ [*cf.*, Eq. (4.17)].

Model	$\pm x/M$	$\pm p/M$	m_1/M	m_2/M	S_1/M^2	S_2/M^2	a_1	a_2	M_{ADM}/M	J_{ADM}/M^2
$r0$	3.0205	0.1366	0.4011	0.4009	-0.1460	0.1460	-0.5840	0.5840	0.9856	0.8252
$r1$	3.1264	0.1319	0.4380	0.4016	-0.1095	0.1460	-0.4380	0.5840	0.9855	0.8612
$r2$	3.2198	0.1281	0.4615	0.4022	-0.0730	0.1460	-0.2920	0.5840	0.9856	0.8979
$r3$	3.3190	0.1243	0.4749	0.4028	-0.0365	0.1460	-0.1460	0.5840	0.9857	0.9346
$r4$	3.4100	0.1210	0.4796	0.4034	0.0000	0.1460	0.0000	0.5840	0.9859	0.9712
$r5$	3.5063	0.1176	0.4761	0.4040	0.0365	0.1460	0.1460	0.5840	0.9862	1.007
$r6$	3.5988	0.1146	0.4638	0.4044	0.0730	0.1460	0.2920	0.5840	0.9864	1.044
$r7$	3.6841	0.1120	0.4412	0.4048	0.1095	0.1460	0.4380	0.5840	0.9867	1.081
$r8$	3.7705	0.1094	0.4052	0.4052	0.1460	0.1460	0.5840	0.5840	0.9872	1.117
$r0l$	4.1924	0.1073	0.4066	0.4065	-0.1460	0.1460	-0.5840	0.5840	0.9889	0.8997
$r0s$	2.8186	0.1441	0.3997	0.3994	-0.1460	0.1460	-0.5840	0.5840	0.9849	0.8123

individual spins $\boldsymbol{S}_i$. Since I am interested in quasi-circular orbits we work in the zero momentum frame and choose $\boldsymbol{p}_1 = -\boldsymbol{p}_2$ to be orthogonal to $\boldsymbol{C}_2 - \boldsymbol{C}_1$. The physical parameters we want to control are: the black hole mass ratio M_1/M_2, the orbital angular momentum $\boldsymbol{L} = \boldsymbol{C}_1 \times \boldsymbol{p}_1 + \boldsymbol{C}_2 \times \boldsymbol{p}_2$ (see for example [165–167]) and the dimensionless spin parameters $a_i = \boldsymbol{S}_i/M_i^2$. In order to choose the input parameters that correspond to the desired physical parameters I have to use a non-linear root finding procedure, since the physical parameters depend non-linearly on the input parameters and it is not possible to invert the problem analytically.

As detailed in [166], when the black-hole spins are taken as parameters, it is possible to reduce the number of independent input variables, so that at a given separation $\bar{\mathbf{C}} \equiv |\mathbf{C_2} - \mathbf{C_1}|/\mathbf{m_1}$, the independent input parameters are: $\bar{q} \equiv m_1/m_2$ and the dimensionless magnitude of the linear momentum p/m_1. Using a Newton-Raphson method, I solve for $\bar{q}$ and p/m_1 so that $M_1/M_2 = 1$ and the system has a given dimensionless orbital angular momentum, $L/(\mu M)$ where $\mu = m_1 m_2/M^2$ is the reduced mass. For such a configuration the initial data solver [52] returns a very accurate value for M_{ADM}, which together with the accurate irreducible mass calculated by the apparent horizon finder [70, 162] makes it possible to calculate an accurate value of the dimensionless binding energy

$$E_b/\mu = (M_{\mathrm{ADM}} - M_1 - M_2)/\mu. \tag{4.18}$$

The quasi-circular initial data parameters are then obtained by finding the minimum in E_b/μ for varying values of $\bar{\boldsymbol{C}}$ while keeping the required orbital angular momentum $L/(\mu M)$ constant.

I chose a fixed orbital angular momentum $L/(\mu M) = 3.3$ for the quasi-circular orbit initial data parameters. This value was chosen to ensure that model $r0$ would have enough evolution time for an accurate kick measurement, while at the same time model $r8$ would not require too much evolution time due to orbital ‘hang-up’ effects for aligned spins. In order to check the influence of the evolution time before plunge on the kick measurements of the $r0$ model, we also calculated initial data for a $r0$ configuration at larger initial separation $r0l$ and at smaller initial separation $r0s$. The parameters for all the initial data sets are shown in Table 4.1.

Note that the physical mass M_i of a single puncture black hole increases when the spin parameter is increased if the mass parameter m_i is kept constant. For that reason obtaining $M_1 = M_2$ in general requires that $m_1 \neq m_2$. Even in the case where the spins have the same magnitude but different directions, the two black holes will have different spin-orbit interactions leading to slightly different physical masses if $m_1 = m_2$. For this reason, the initial data for $r0$ in Table 4.1 has slightly different puncture mass parameters $m_1 \neq m_2$. In contrast, in model $r8$ the black holes have identical spin parameters and thus also the same spin-orbit interaction, resulting in identical mass parameters $m_1 = m_2$. For this reason I wrote a Newton-Raphson solver to iterate with the quasi-circular puncture initial data solver to solve for the puncture masses to converge to the desired ADM masses with spin accounted for.

4.1.2 Convergence tests

As discussed in section [2.5.1] the finite difference error of the derivative stencils used in the numerical algorithm is $O(h^4)$, while the error in the time-interpolation stencils used for mesh refinement boundary points is $O(\Delta t^3)$. Thus the expected theoretical convergence rate is three. However, it is only time-related operations which are at third order, and since the time step which we use is smaller than the grid spacing and much smaller than the dynamical timescales, we can expect that the error coefficient of the leading order term is quite small. Third order convergence is expected during time-periods when the system goes through rapid dynamical changes, such as the plunge or merger, and fourth-order is expected at early times in the simulation.

The proper convergence of the code was established using the binary system $r0$, for which we have carried out evolutions using 8 levels of mesh refinement with fine grid-spacings of $h/M = 0.024$, 0.018, and 0.012 (*i.e.*, resolutions “medium”, “high”, and “very-high”, respectively, where “low” refers to $h = 0.030$ which was deemed to be of insufficient accuracy). Other refinement levels have resolutions that are half of the next finest grid. The refinement levels on the initial slice are set up to be identical for the three resolutions and their locations and sizes evolve according to the same algorithm in each case.

We focus on the convergence of a number of different aspects of the code. The first of these is the degree of satisfaction of the Einstein equations, which can be partially determined by examining the Hamiltonian and momentum constraints (4.9)–(4.10). A more stringent requirement is to evaluate how well the Einstein tensor satisfies the vacuum condition, $G_{\alpha\beta} = 0$. For this we define the positive definite quantity

$$\boldsymbol{G} \equiv \begin{cases} \sqrt{G_{00}^2 + G_{01}^2 + \cdots + G_{33}^2} & \text{outside appar. horizons} \\ 0 & \text{inside appar. horizons .} \end{cases} \tag{4.19}$$

In computing norms over the entire grid, we find it useful to mask out the interiors of the horizons, where the error at the puncture locations – which is not expected to converge – can dominate over more relevant errors in the physically observable domain. In order to compute $G_{\alpha\beta}$ we compute the 4-derivatives of the ADM metric, lapse and shift, then construct the 4-derivatives of the 4-metric from which we can compute the Riemann tensor and then finally obtain $G_{\alpha\beta}$. Time-derivatives are taken using three time-levels, centered around the past time-level. Spatial derivatives are taken using fourth-order accurate centered stencils. Thus the finite-difference error in computing $G_{\alpha\beta}$ is $\mathcal{O}(\Delta t^2)$ in time and $\mathcal{O}(h^4)$ in the space dimensions. Effectively we see a minimum of third order accuracy for this quantity, indicating that the coefficient of the $\mathcal{O}(\Delta t^2)$ error term is small compared to the higher-order terms.

Since the metric gradients and hence the truncation errors are the largest near the black-holes, through the L_∞ norm of (4.19) we effectively monitor that the Einstein tensor converges near the horizons for the duration of the evolution. This is a strong test in comparison with the common use of the L_2 norm, as the latter tends to dilute errors in small regions or 2D surfaces such as grid boundaries, as they are normalized over the entire grid volume. By contrast, the L_∞ norm measures the worst error on the grid, which by propagation of error will also suffer if there are any non-convergent regions on the grid.

This convergence of $\boldsymbol{G}$ is summarized in Fig. 4.2, which reports the time evolution of the L_∞ norm of (4.19) at the medium and very-high resolutions. Also indicated with dashed and dotted lines are the expression for the L_∞ norm of (4.19) at the very-high resolution when rescaled for third (dotted line) and fourth-order convergence (dashed line).

There is a period at the beginning of the evolutions where the initial data construction prevents fourth-order convergence. This is due to the fact that the initial data is computed by an interpolation of the results of a spectral solver onto the finite difference grid which is used for evolution. An error is introduced because we keep fixed the number of spectral coefficients and because the Cartesian grid points do not coincide with the spectral collocation points of the Chebyshev polynomials, resulting in a certain amount of high-frequency noise that spoils the convergence for some time at the beginning of the simulation. Numerical dissipation and the constraint damping built into the evolution system implies that the evolution quickly adjusts itself to actually solving the Einstein equations to a good accuracy. The effects of these initial transient modes can last for different amounts of time for the different resolutions, *e.g.*, $\sim 10\,M$ for the medium resolution and $\sim 30\,M$ for the very-high resolution.

Soon after this transient has disappeared, the code shows the expected fourth-order convergence, with the largest values of the violation found in the vicinity of the apparent horizons, where the gradients in the metric are the steepest. The violations grow rapidly with time as the binary inspirals and the largest values of the violation of the Einstein tensor are seen at the time of the merger, $t \approx 109\,M$, with values as large as $\mathcal{O}(300)$. Such violations are essentially confined to a *single* grid point on the trailing edge of the apparent horizon and are produced by the very steep gradients in the shift. Clearly, violations of this magnitude would not be revealed when looking at the L_2 norms and are a source of concern. However, as we will show later, such violations do not propagate away from the horizon to affect the fourth-order convergence of the waveforms in the interior and sliding to thrid order near the boundaries.

At the time of the merger the excision of a common apparent horizon from the calculation of the L_∞ norm is responsible for the decrease by about four orders of the violation. After this, the L_∞ do not grow further in time for the very-high resolution simulation, while a modest increase is seen in the simulation run at medium resolution. During this time the code shows a convergence which is between third-order (right after the merger) and fourth-order (during the ringdown).

In addition to convergence in the Einstein tensor, we also validate the correctness of the physically relevant information contained in the waveforms. We do this by computing convergence rate of the waveforms Q^{+}_{22}, Q^{+}_{33}, and $Q^{\times}_{21}$ using the ratio of the integrated differences between the medium and high resolutions, and the high and very-high resolutions

$$\rho(Q) \equiv \frac{\sqrt{\int_{u_1}^{u_2} |Q_{0.024} - Q_{0.018}|^2 du}}{\sqrt{\int_{u_1}^{u_2} |Q_{0.018} - Q_{0.012}|^2 du}}\,, \tag{4.20}$$

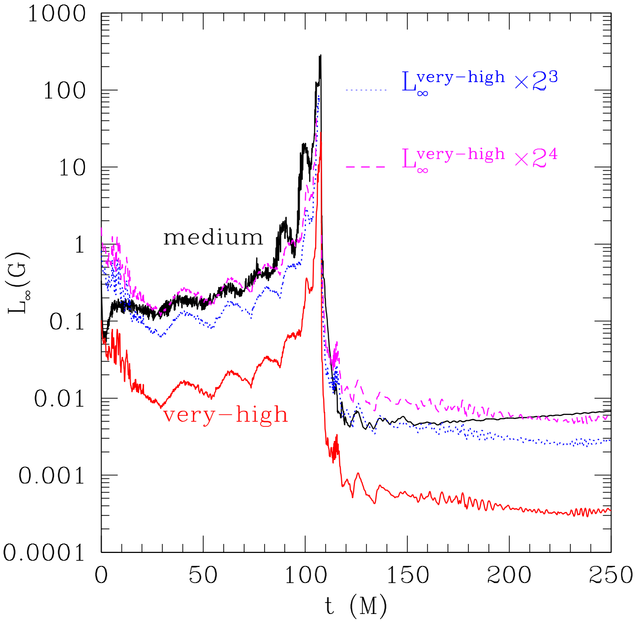

Figure 4.2: The L_∞ norm of the Einstein tensor Eq. (4.19) as a function of time. During the periods of strong dynamics (*i.e.*, when the time derivatives of the evolution variables are large) the convergence order is dominated by the accuracy of the time-interpolation algorithm used at mesh refinement boundaries, thus yielding third-order accuracy. At the times when these time-derivatives are small, the fourth-order finite-differencing algorithm becomes the dominant source of the error. Note that the very large violations (of $\mathcal{O}(300)$ at the medium resolution) are confined to a *single* grid point on the trailing edge of the apparent horizon and are produced by the very steep gradients in the shift. As discussed later, this does not affect the fourth-order convergence of the waveforms. At the time of the merger a common apparent horizon forms and its excision from the calculation of the L_∞ norm is responsible for the drop in the violation.

where $u \equiv t - r_{\rm E}$ is the retarded time at a given detector, Q stands for either Q^+_{22}, Q^+_{33} or $Q^\times_{21}$ and refers to either its amplitude or the phase. As indicated in Eq. (4.20), the integrals are evaluated over the retarded interval $[u_1, u_2]$ which does not include the initial spurious burst of radiation (which we do not expect to converge) but contains otherwise the complete waveform including the ringdown.

Assuming a truncation error $\mathcal{O}(h^p)$ and that the coefficient of this error does not depend on resolution, the function ρ becomes to leading order

$$\rho = \frac{(h_{0.024})^p - (h_{0.018})^p}{(h_{0.018})^p - (h_{0.012})^p}\,, \tag{4.21}$$

where $h_{0.024} = 0.024\,M$ and I underline the importance of having used a full doubling of the resolution between the smallest and largest resolution to improve the accuracy of this estimate over more narrowly spaced resolution steps. In practice, we measure ρ and then solve for the *"effective"* convergence order p using Eq. (4.21). A discussion of the details in this procedure are presented in Appendix A.4 alongside with the computed convergence rates for the amplitudes and phases of Q which are found to between two ($\ell = 3$) and four ($\ell = 2$) (*cf.*, Table A.1).

The above definition of convergence rate results in non-integer values for the exponent ρ, even though our methods are explicitly polynomial. This is because the derivation of (4.21) assumes a coefficient of one in the leading order error term that extrapolates between resolutions. If the coefficient is in practice different for a given set of resolutions, then a non-integer value is larger if the coefficient is smaller. As such, values obtained in this way should not be considered literal polynomial extrapolation orders. By "convergence order 3.8" we rather mean that our results are consistent with third-order finite differencing where the leading third-order error coefficient is quite small so that at the given resolutions the convergence appears to be closer to a fourth-order approximation. Very high convergence exponents are a likely indication that the lowest resolution is not in the convergent regime for the measured quantity. Non-integer convergence orders obtained in this way are resolution dependent, and should themselves converge to the lowest order finite difference approximation used in the code in the limit of infinite resolution.

An important property of the waveforms which has emerged when performing these convergence tests is that the dominant source of error is a de-phasing which causes the lower resolution evolutions to "lag" behind the higher resolution. This delay is usually rather small and between $0.1\,M$ and $0.5\,M$, but it is visible when comparing the total amplitude of Q as a function of time. The most important consequence of this error is that it can spoil the convergence tests if not properly taken into account: the residuals errors seem, in fact, to indicate over-convergence. This is shown in the upper panel of Fig. 4.3, which reports the differences between Q^{+}_{22} when computed at different resolutions scaled for fourth-order convergence. The overlap is rather poor and even indicating that the truncation error is smaller than expected. This is an artifact of the near cancellation of the lowest-order terms in the truncation error and induced by the small time-differences at different resolutions.

We remove this effect by shifting the time coordinate of the medium and high resolution runs by the time interval needed to produce an alignment of the maxima of the emitted radiation. Details on how to do this are discussed in Appendix A.4, and we report in the lower panel of Fig. 4.3 the same data shown in the upper panel, but after the time-shifting. Clearly, the overlap is now extremely good suggesting that the time-shifting is essential for obtaining the expected fourth-order convergence in the waveforms. In accord with the convergence in the waveforms we also see fourth order convergence in the final kick value, and spins.

As a final note we remark that besides validating a proper convergence of the code, it is also important to assess the accuracy of any measurable quantity at the relevant resolutions considered here. As a representative and physically meaningful quantity we have

Table 4.2: Binary sequences for which numerical simulations have been carried out, with different columns referring to the puncture initial location $\pm x/M$, the linear momenta $\pm p/M$, the mass parameters m_i/M, the dimensionless spins a_i, the normalized ADM mass $\widetilde{M}_{\rm ADM} \equiv M_{\rm ADM}/M$ measured at infinity, and the normalized ADM angular momentum $\widetilde{J}_{\rm ADM} \equiv J_{\rm ADM}/M^2$. Finally, the last six columns contain the numerical and fitted values for $|v_{\rm kick}|$ (in $\rm km/s$), $a_{\rm fin}$ and the corresponding errors.

	$\pm x/M$	$\pm p/M$	m_1/M	m_2/M	a_1	a_2	$\widetilde{M}_{\rm ADM}$	$\widetilde{J}_{\rm ADM}$	$\lvert v_{\rm kick}\rvert$	$\lvert v^{\rm fit}_{\rm kick}\rvert$	err. (%)	$a_{\rm fin}$	$a^{\rm fit}_{\rm fin}$	err. (%)
$r0$	3.0205	0.1366	0.4011	0.4009	-0.584	0.584	0.9856	0.825	261.75	258.09	1.40	0.6891	0.6883	0.12
$r1$	3.1264	0.1319	0.4380	0.4016	-0.438	0.584	0.9855	0.861	221.38	219.04	1.06	0.7109	0.7105	0.06
$r2$	3.2198	0.1281	0.4615	0.4022	-0.292	0.584	0.9856	0.898	186.18	181.93	2.28	0.7314	0.7322	0.11
$r3$	3.3190	0.1243	0.4749	0.4028	-0.146	0.584	0.9857	0.935	144.02	146.75	1.90	0.7516	0.7536	0.27
$r4$	3.4100	0.1210	0.4796	0.4034	0.000	0.584	0.9859	0.971	106.11	113.52	6.98	0.7740	0.7747	0.08
$r5$	3.5063	0.1176	0.4761	0.4040	0.146	0.584	0.9862	1.007	81.42	82.23	1.00	0.7948	0.7953	0.06
$r6$	3.5988	0.1146	0.4638	0.4044	0.292	0.584	0.9864	1.044	45.90	52.88	15.21	0.8150	0.8156	0.07
$r7$	3.6841	0.1120	0.4412	0.4048	0.438	0.584	0.9867	1.081	20.59	25.47	23.70	0.8364	0.8355	0.11
$r8$	3.7705	0.1094	0.4052	0.4052	0.584	0.584	0.9872	1.117	0.00	0.00	0.00	0.8550	0.855	0.00
$ra0$	2.9654	0.1391	0.4585	0.4584	-0.300	0.300	0.9845	0.8250	131.34	132.58	0.95	0.6894	0.6883	0.16
$ra1$	3.0046	0.1373	0.4645	0.4587	-0.250	0.300	0.9846	0.8376	118.10	120.28	1.85	0.6971	0.6959	0.17
$ra2$	3.0438	0.1355	0.4692	0.4591	-0.200	0.300	0.9847	0.8499	106.33	108.21	1.77	0.7047	0.7035	0.17
$ra3$	3.0816	0.1339	0.4730	0.4594	-0.150	0.300	0.9848	0.8628	94.98	96.36	1.46	0.7120	0.7111	0.13
$ra4$	3.1215	0.1321	0.4757	0.4597	-0.100	0.300	0.9849	0.8747	84.74	84.75	0.01	0.7192	0.7185	0.09
$ra6$	3.1988	0.1290	0.4782	0.4602	0.000	0.300	0.9850	0.9003	63.43	62.19	1.95	0.7331	0.7334	0.04
$ra8$	3.2705	0.1261	0.4768	0.4608	0.100	0.300	0.9852	0.9248	41.29	40.55	1.79	0.7471	0.7481	0.13
$s0$	2.9447	0.1401	0.4761	0.4761	0.000	0.000	0.9844	0.8251	0.00	0.00	0.00	0.6892	0.6883	0.13
$s1$	3.1106	0.1326	0.4756	0.4756	0.100	0.100	0.9848	0.8749	0.00	0.00	0.00	0.7192	0.7185	0.09
$s2$	3.2718	0.1261	0.4709	0.4709	0.200	0.200	0.9851	0.9251	0.00	0.00	0.00	0.7471	0.7481	0.13
$s3$	3.4098	0.1210	0.4617	0.4617	0.300	0.300	0.9855	0.9751	0.00	0.00	0.00	0.7772	0.7769	0.03
$s4$	3.5521	0.1161	0.4476	0.4476	0.400	0.400	0.9859	1.0250	0.00	0.00	0.00	0.8077	0.8051	0.33
$s5$	3.6721	0.1123	0.4276	0.4276	0.500	0.500	0.9865	1.0748	0.00	0.00	0.00	0.8340	0.8325	0.18
$s6$	3.7896	0.1088	0.4002	0.4002	0.600	0.600	0.9874	1.1246	0.00	0.00	0.00	0.8583	0.8592	0.11
$t1$	4.0812	0.1103	0.4062	0.4426	-0.584	0.438	0.9884	0.8638	238.37	232.62	2.41	0.6640	0.6658	0.27
$t2$	3.9767	0.1131	0.4057	0.4652	-0.584	0.292	0.9881	0.8265	200.25	205.21	2.48	0.6400	0.6429	0.45
$t3$	3.8632	0.1165	0.4053	0.4775	-0.584	0.146	0.9879	0.7906	174.58	175.86	0.73	0.6180	0.6196	0.26
$t4$	3.7387	0.1204	0.4047	0.4810	-0.584	0.000	0.9878	0.7543	142.62	144.57	1.37	0.5965	0.5959	0.09
$t5$	3.6102	0.1246	0.4041	0.4761	-0.584	-0.146	0.9876	0.7172	106.36	111.34	4.68	0.5738	0.5719	0.33
$t6$	3.4765	0.1294	0.4033	0.4625	-0.584	-0.292	0.9874	0.6807	71.35	76.17	6.75	0.5493	0.5475	0.32
$t7$	3.3391	0.1348	0.4025	0.4387	-0.584	-0.438	0.9873	0.6447	35.36	39.05	10.45	0.5233	0.5227	0.11
$t8$	3.1712	0.1419	0.4015	0.4015	-0.584	-0.584	0.9875	0.6080	0.00	0.00	0.00	0.4955	0.4976	0.42
$u1$	2.9500	0.1398	0.4683	0.4685	-0.200	0.200	0.9845	0.8248	87.34	88.39	1.20	0.6893	0.6883	0.15
$u2$	2.9800	0.1384	0.4436	0.4438	-0.400	0.400	0.9846	0.8249	175.39	176.78	0.79	0.6895	0.6883	0.17
$u3$	3.0500	0.1355	0.3951	0.3953	-0.600	0.600	0.9847	0.8266	266.39	265.16	0.46	0.6884	0.6883	0.01
$u4$	3.1500	0.1310	0.2968	0.2970	-0.800	0.800	0.9850	0.8253	356.87	353.55	0.93	0.6884	0.6883	0.01

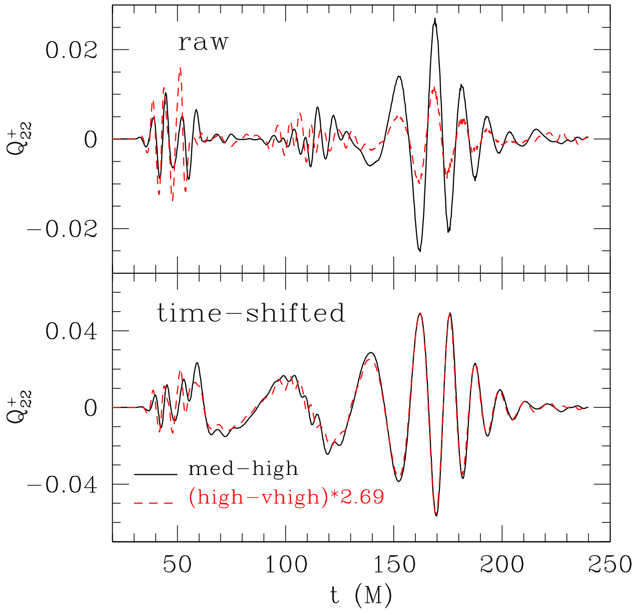

Figure 4.3: Convergence of the fiducial waveform Q^+_{22} for the binary system $r0$ before and after the time-shift defined in Eqs. (A.38)–(A.40). In the upper graph we show the difference between Q^+_{22} when computed at different resolutions, scaled for fourth-order convergence and using raw data (*i.e.*, without time-shifting). The overlap between the curves is rather poor indicating an over-convergence (*i.e.*, the truncation error appears to be smaller than expected). In the lower panel we show the same data but after time-shifting. The very good overlap of the scaled curves on the indicates that the time-shifting is essential for obtaining properly scaling differences between runs of various resolutions.

considered the accuracy of the fiducial waveform Q^+_{22} for the binary system $r0$. This is shown in Fig. 4.4, where in the upper graph we report the waveforms at the three different resolutions: very-high (continuous line), high (dashed line) and medium (dotted line). Already with the lowest of these resolutions the accuracy is sufficiently high so that the curves are essentially indistinguishable from each other by eye. The lower panels show magnifications of the relevant portions of the waveform, with the lower-left panel concentrating on the initial transient radiation produced by the truncation error. The latter clearly is rather large at the medium resolution, but it converges away smoothly when the grid spacing is decreased. The lower-right panel, on the other hand, refers to the quasi-normal ringing and shows that it is well-captured at all resolutions.

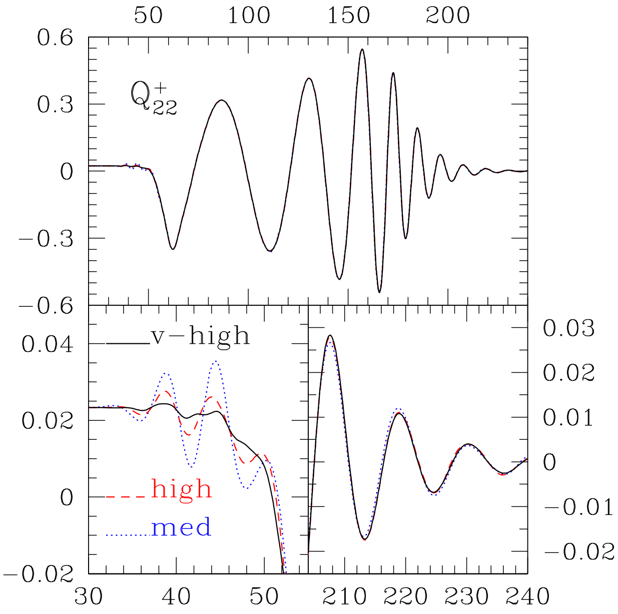

Figure 4.4: Accuracy of the fiducial waveform Q^{+}_{22} for the binary system $r0$. In the upper graph we show the waveforms at the three different resolutions: very-high (continuous line), high (dashed line), medium (dotted line). The accuracy is very good already with the lowest resolution and the curves cannot be distinguished. The lower panels show magnifications of some relevant portions of the waveform, with the lower-left panel concentrating on the initial transient radiation produced by the truncation error. The lower-right panel, on the other hand, refers to the quasi-normal ringing and shows that it is well-captured at all resolutions.

4.2 Kicks

Together with energy and angular momentum, gravitational radiation also carries away linear momentum. In the case of a binary system of non-spinning black holes, a physical intuition of this loss of linear momentum can be built rather easily. As the two bodies orbit around the common center of mass, each will emit radiation which is longitudinally-beamed. Unless the two black holes have exactly the same mass, their motion will be different, with the smaller black hole moving more rapidly and, hence, being more efficient in beaming its emission. The net momentum gained over an orbit is negligible if the orbit is almost circular (the momentum loss in any direction is essentially balanced by an equal loss in the diametrically opposite direction), but it can become large when integrated over many orbits, leading to a recoil that is a fraction ($\lesssim 10^{-2}$) of the speed of light during the last portion of the orbit prior to the merger.

A number of PN/perturbative analyses (see, *e.g.*, [148, 168]) have provided estimates of this recoil velocity, while numerical-relativity simulations [136, 139] have recently measured it to rather high precision, predicting a maximal kick of 175 km/s for a binary system of nonspinning black holes with a mass ratio $q \equiv M_1/M_2 \simeq 0.36$, where M_1 and M_2 are the masses of the two black holes. Such a recoil has indeed quite important astrophysical consequences, since it could, provided it is large enough, kick the binary out of its host environment. Clearly, a replaced or an even missing central black hole would have dramatic consequences for the further development of the host. Determining accurately what are the expected escape velocities for the most typical environments hosting a binary black hole system is rather difficult, but the estimates made in refs. [169, 170], for instance, predict that the escape velocities for dwarf galaxies and globular clusters are $\lesssim 100$ km/s, but for giant galaxies these can be ~ 1000 km/s.

When adopting a purely geometrical viewpoint, it is obvious that a kick velocity should be expected in any binary system which is not perfectly symmetric. A difference in the masses is a simple way of producing such an asymmetry but surely not the only one. Indeed, even an equal-mass system can be made asymmetric if the two black holes have unequal spins [171]. Also in this case, a simple physical intuition can be constructed. Consider, for simplicity an equal-mass binary in which only one member is spinning parallel to the orbital angular momentum. As a result of the spin-induced frame dragging, the speed of the nonspinning body will be increased and its radiation further beamed. Using PN theory at the 2.5 order, Kidder [172] has treated this spin-orbit interaction concluding that in the case of a circular, non-precessing orbit, the total kick for a binary system of arbitrary mass and spin ratio can be expressed as [148]

$$|v|_{\text{kick}} = c_1 \frac{q^2(1-q)}{(1+q)^5} + c_2 \frac{a_2 q^2 (1 - q a_1/a_2)}{(1+q)^5} \ , \tag{4.22}$$

where $a_{1,2} \equiv S_{1,2}/M_{1,2}^2$ are the dimensionless spins of the two black holes and these are aligned with the total orbital angular momentum, *i.e.*, $\boldsymbol{S}_{1,2} = a_{1,2} M_{1,2}^2 \boldsymbol{e}_z$ for an orbital motion in the (x, y) plane. Here, c_1 and c_2 are factors depending on the total mass of the system and on the orbital separation at which the system stops radiating. This radius is difficult to determine precisely as it lies in a region where the PN approximation is not very accurate and is, in practice, not even a constant but, rather, depends on both the mass and the spin ratio. Assuming for simplicity $c_1 \simeq c_2$, expression (4.41) reveals that a substantial contribution to the recoil velocity comes from the spins alone. In addition, for any given q, it predicts a linear growth of the recoil velocity with increasing difference in spins, yielding a kick which is comparable with the one coming from the asymmetry in the mass. Stated differently, when it comes to recoil velocities, the spin contributions may be the dominant ones.

Apart from finding the maximal possible value for the recoil velocity it has been tried to develop a semi-analytic description fitting the data available so far [173, 174]. In this section I want to draw the attention to the techniques of extracting the waves and thus the recoil velocity. It is, for example, not clear how sensitive the methods used are to gauge effects such as the motion of the black hole on the grid. During the time it takes to extract the information, the system will have moved significantly when its speed is $\sim 1\%$ of the speed of light.

4.2.1 Kick measurements via Ψ_4

In radiating spacetimes where the radiation is emitted asymmetrically, there will be a net linear momentum imparted to the system. In particular, in the case of a binary black hole merger, the final black hole receives a "kick" which causes it to move off at a given velocity. This velocity can be determined by an analysis of the emitted radiation. In ADM-type numerical simulations, this is typically done by evaluating some scalar quantity which can be associated with the wave energy at some large radius within the computational domain. The chosen radius needs to be large enough that it is in the "wave zone", where non-linear self-interaction of the gravitational field is negligible and the waves can be picked out as perturbations of a background.

Two methods have become commonplace to determine the emitted wave energy. The first uses the Newman-Penrose curvature scalar Ψ_4, which can be identified with the gravitational radiation if a suitable frame is chosen at the extraction radius. An alternative method measures the metric of the numerically generated spacetime against a fixed background at the extraction radius, and determines the Zerilli-Moncrief perturbation modes. Both methods yield data for the gravitational wave energy which can be integrated to determine a net linear momentum. Both of these methods are described in detail in Section [2.6.3].

The Newman-Penrose formalism provides a convenient representation for a number of radiation related quantities as spin-weighted scalars. In particular, the curvature component

$$\Psi_4 \equiv -C_{\alpha\beta\gamma\delta} n^\alpha \bar{m}^\beta n^\gamma \bar{m}^\delta , \tag{4.23}$$

is defined as a particular component of the Weyl curvature, $C_{\alpha\beta\gamma\delta}$, projected onto a given null frame, $\{\boldsymbol{l}, \boldsymbol{n}, \boldsymbol{m}, \bar{\boldsymbol{m}}\}$. In practice, we define an orthonormal basis in the three space $(\hat{\boldsymbol{r}}, \hat{\boldsymbol{\theta}}, \hat{\boldsymbol{\phi}})$, centered on the Cartesian grid center and oriented with poles along $\hat{\boldsymbol{z}}$. The normal to the slice defines a time-like vector $\hat{\boldsymbol{t}}$, from which we construct the null frame

$$\boldsymbol{l} = \frac{1}{\sqrt{2}}(\hat{\boldsymbol{t}} - \hat{\boldsymbol{r}}), \quad \boldsymbol{n} = \frac{1}{\sqrt{2}}(\hat{\boldsymbol{t}} + \hat{\boldsymbol{r}}), \quad \boldsymbol{m} = \frac{1}{\sqrt{2}}(\hat{\boldsymbol{\theta}} - \mathrm{i}\hat{\boldsymbol{\phi}}) \, . \tag{4.24}$$

We then calculate Ψ_4 via a reformulation of (4.23) in terms of ADM variables on the slice [175],

$$\Psi_4 = C_{ij} \bar{m}^i \bar{m}^j , \tag{4.25}$$

where

$$C_{ij} \equiv R_{ij} - K K_{ij} + K_i{}^k K_{kj} - \mathrm{i}\epsilon_i{}^{kl} \nabla_l K_{jk} . \tag{4.26}$$

The identification of the Newman-Penrose Ψ_4 with the gravitational radiation content of the spacetime is a result of the peeling theorem, which states that in an appropriate frame the Ψ_4 component of the curvature has the slowest falloff with radius, $\mathcal{O}(1/r)$. The conditions of this theorem are not satisfied exactly at a small radius and in the chosen frame. While there are proposals for how this situation can be improved [176], we find that beyond $r_{\mathrm{E}} \geq 30\,M$ in fact our measure of Ψ_4 scales extremely well with the different extraction radii r_{E}, suggesting that the peeling property is satisfied to a reasonable approximation (see Fig. 4.5).

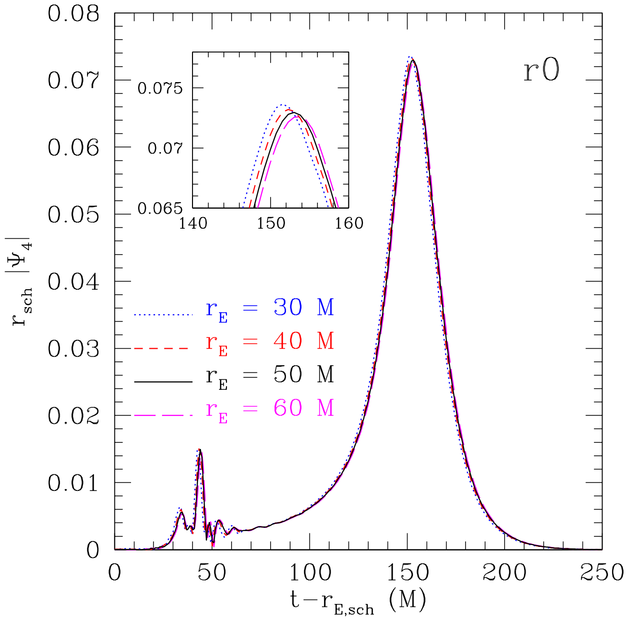

Figure 4.5: Amplitude of $r_{\rm E,sch}|\Psi_4|$ for extraction spheres at $r_{\rm E} = 30\,M$, $40\,M$, $50\,M$ and $60\,M$, demonstrating that Ψ_4 does indeed fall off as required by the peeling property. There is a slight decrease in amplitude with larger radius, suggesting that dissipative effects may become important at larger radii. Results in this paper use waveforms from the $r_{\rm E} = 50\,M$ extraction sphere, unless indicated otherwise.

The gravitational wave polarization amplitudes h_+ and $h_\times$ are related to Ψ_4 by [77]

$$\ddot{h}_+ - {\rm i}\ddot{h}_\times = \Psi_4\,, \tag{4.27}$$

where the double over-dot stands for second-order time derivative. The flux of linear momentum emitted in gravitational waves in the i-direction can be computed from the Isaacson's energy-momentum tensor and can be written in terms of the two polarization amplitudes as [148]

$$\mathcal{F}_i \equiv \dot{P}_i = \frac{r^2}{16\pi}\int d\Omega\; n_i\left(\dot{h}_+^2 + \dot{h}_\times^2\right)\,, \tag{4.28}$$

where $n_i = x_i/r$ is the unit radial vector that points from the source to the observer and $d\Omega = \sin\theta d\phi d\theta$ is the line element of our extraction 2-sphere S^2. Using Eq. (4.27), this leads to an expression for the momentum flux in terms of Ψ_4 as it is commonly used in recent numerical relativity calculations [136, 139, 155, 157, 159, 160, 177]:

$$\mathcal{F}_i = \lim_{r_{\rm sch}\to\infty}\left\{\frac{r_{\rm sch}^2}{16\pi}\int d\Omega\; n_i\left|\int_{-\infty}^{t} dt\Psi_4\right|^2\right\}\,. \tag{4.29}$$

The Schwarzschild radius, $r_{\rm sch}$, is derived from the coordinate (isotropic) radius via the standard formula

$$r_{\rm sch} = r_{\rm iso}\left(1 - \frac{M}{2r_{\rm iso}}\right)^2 . \tag{4.30}$$

assuming a constant ADM mass $M = M_{_{\rm ADM}}$ throughout the simulation. With this choice of radial coordinate, expression (4.29) has been shown to provide recoil velocities which are in better agreement with those obtained through gauge-invariant perturbations than with the alternative coordinate radius, (*cf.* Sect. 4.2.2) and reported in the literature (Additional details on the numerical measurement of Ψ_4 are presented in Appendix A.5.)

4.2.2 Kick measurements via gauge-invariant perturbations

An independent method to compute the linear momentum carried away by gravitational radiation is based on the measurements of the non-spherical gauge-invariant perturbations of a Schwarzschild black hole (see Refs. [178–180] for applications to Cartesian coordinates grids). In practice, a set of "observers" is placed on 2-spheres of fixed coordinate radius $r_{_{\rm E}}$, where they extract the gauge-invariant, odd-parity (or *axial*) current multipoles $Q^{\times}_{\ell m}$ and even-parity (or *polar*) mass multipoles $Q^{+}_{\ell m}$ of the metric perturbation [76]. The numerical implementations of the gauge-invariant variables is done by following the multi-polar analysis outlined by Abrahams and Price [181]. The $Q^{+}_{\ell m}$ and $Q^{\times}_{\ell m}$ variables are related to h_+ and $h_\times$ as [182]

$$\begin{aligned} h_+ - {\rm i}h_\times = \frac{1}{\sqrt{2}r}\sum_{\ell=2}^{\infty}\sum_{m=-\ell}^{\ell}\Bigg(&Q^{+}_{\ell m} \\ &-{\rm i}\int_{-\infty}^{t} Q^{\times}_{\ell m}(t')dt'\Bigg)\, {}_{-2}Y^{\ell m} . \end{aligned} \tag{4.31}$$

Here ${}_{-2}Y^{\ell m}$ are the $s = -2$ spin-weighted spherical harmonics and (ℓ, m) are the indices of the angular decomposition. Validations of this approach in 3D vacuum spacetimes can be found in Refs. [114, 180, 183], while its use with matter sources has first been reported in [184].

We note that the notation introduced in Eq. (4.31) could be misleading as it seems to suggest that $h_\times$ is always of odd-parity and h_+ is always of even-parity. In the absence of axisymmetry, *i.e.*, when $m \neq 0$, both $h_\times$ and h_+ are a superposition of odd and even parity modes. It is only for axisymmetric systems, for which only $m = 0$ modes are present, that $Q^{\times}_{\ell m}$ and $Q^{+}_{\ell m}$ are *real* numbers, that h_+ is *only* even-parity and $h_\times$ is *only* odd-parity. Despite this possible confusion, we here prefer to maintain the notation of Eq. (4.31) which is the most common in the literature [182].

The flux of linear momentum emitted in gravitational waves in terms of $Q^{+}_{\ell m}$ and $Q^{\times}_{\ell m}$ can be computed by inserting Eq. (4.31) in Eq. (4.28), then decomposing n_i in spherical harmonics and performing the angular integral. This procedure goes along the lines discussed by Thorne in Ref. [185], where all the relevant formulae are already present, and which we here simply rewrite adopting the gauge-invariant quantities.

In Ref. [185] the even-parity (or *electric*) multipoles are indicated with $I_{\ell m}$ and the odd-parity (or *magnetic*) ones with $S_{\ell m}$. They are related to our notation by

$$ {}^{(\ell)}I_{\ell m} = Q^{+}_{\ell m} \; , \tag{4.32} $$

$$ {}^{(\ell+1)}S_{\ell m} = Q^{\times}_{\ell m} \; , \tag{4.33} $$

where ${}^{(\ell)}f_{\ell m} \equiv d^{\ell} f_{\ell m}/dt^{\ell}$. From the well known property $(Q^{+,\times}_{\ell m})^{*} = (-1)^{m} Q^{+,\times}_{\ell\, -m}$, where the asterisk indicates complex conjugation, one can rewrite Eq. (4.20) of Ref. [185] in a more compact form. Following Ref. [168] where the lowest multi-polar contribution was explicitly computed in this way, it is convenient to combine the components of the linear momentum flux in the equatorial plane in a complex number as $\mathcal{F}_x + \mathrm{i}\mathcal{F}_y$. The multi-polar expansion of the flux vector can be written as

$$ \mathcal{F}_x + \mathrm{i}\mathcal{F}_y = \sum_{\ell=2}^{\infty} \sum_{m=0}^{\ell} \delta_m \left(\mathcal{F}^{\ell m}_x + \mathrm{i}\mathcal{F}^{\ell m}_y \right) \; , \tag{4.34} $$

$$ \mathcal{F}_z = \sum_{\ell=2}^{\infty} \sum_{m=0}^{\ell} \delta_m \mathcal{F}^{\ell m}_z \; , \tag{4.35} $$

where $\delta_m = 1$ if $m \neq 0$ and $\delta_m = 1/2$ if $m = 0$. Each multipole reads

$$ \begin{aligned} \mathcal{F}^{\ell m}_x + \mathrm{i}\mathcal{F}^{\ell m}_y \equiv{}& \frac{(-1)^m}{16\pi\ell(\ell+1)} \Bigg\{ -2\mathrm{i} \left[a^{+}_{\ell m} \dot{Q}^{+}_{\ell -m} Q^{\times}_{\ell\, m-1} + a^{-}_{\ell m} \dot{Q}^{+}_{\ell m} Q^{\times}_{\ell\, -(m+1)} \right] \\ & + \sqrt{\frac{\ell^2(\ell-1)(\ell+3)}{(2\ell+1)(2\ell+3)}} \Bigg[b^{-}_{\ell m} \left(\dot{Q}^{+}_{\ell\, -m} \dot{Q}^{+}_{\ell+1\; m-1} + Q^{\times}_{\ell\, -m} \dot{Q}^{\times}_{\ell+1\; m-1} \right) \\ & + b^{+}_{\ell m} \left(\dot{Q}^{+}_{\ell m} \dot{Q}^{+}_{\ell+1\; -(m+1)} + Q^{\times}_{\ell m} \dot{Q}^{\times}_{\ell+1\; -(m+1)} \right) \Bigg] \Bigg\} \; , \end{aligned} \tag{4.36} $$

$$ \begin{aligned} \mathcal{F}^{\ell m}_z \equiv{}& \frac{(-1)^m}{8\pi\ell(\ell+1)} \Bigg\{ 2m \, \mathrm{Im} \left[\dot{Q}^{+}_{\ell\, -m} Q^{\times}_{\ell m} \right] + c_{\ell m} \sqrt{\frac{\ell^2(\ell-1)(\ell+3)}{(2\ell+1)(2\ell+3)}} \\ & \mathrm{Re} \left[\dot{Q}^{+}_{\ell\, -m} Q^{+}_{\ell+1\, m} + Q^{\times}_{\ell\, -m} \dot{Q}^{\times}_{\ell+1\, m} \right] \Bigg\} \; , \end{aligned} \tag{4.37} $$

and

$$ a^{\pm}_{\ell m} \equiv \sqrt{(\ell \pm m)(\ell \mp m + 1)} \; , \tag{4.38} $$

$$ b^{\pm}_{\ell m} \equiv \sqrt{(\ell \pm m + 1)(\ell \pm m + 2)} \; , \tag{4.39} $$

$$ c_{\ell m} \equiv \sqrt{(\ell - m + 1)(\ell - m + 1)} \; . \tag{4.40} $$

Note that here both $\mathcal{F}^{\ell m}_x$ and $\mathcal{F}^{\ell m}_y$ are *real* numbers and are obtained as the real and imaginary part of the right-hand-side of Eq. (4.36). For a general system without symmetries one is expecting $\mathcal{F}^{\ell m}_z$ to be nonzero. However, our initial data set-up, an inspiralling binary with spins anti-aligned and parallel to the orbital angular momentum, implies that the linear momentum flux vector is completely contained in the equatorial plane of the system and so that $\mathcal{F}_z^{\ell m} = 0$ by construction. Since I am imposing equatorial symmetry (*i.e.,* invariance for $\theta \to \pi - \theta$) we have that multipoles with $\ell + m = even$ are purely even-parity (*i.e.,* $Q^{+}_{\ell m} \neq 0$ and $Q^{\times}_{\ell m} = 0$) and those with $\ell + m = odd$ are purely odd-parity (*i.e.,* $Q^{+}_{\ell m} = 0$ and $Q^{\times}_{\ell m} \neq 0$).

We have validated both methods by measuring the recoil velocity for a binary system of nonspinning black holes having a mass ratio of $2/3$ at an initial separation of $4.1\,M$. The results of this calibration extracted at $r = 50\,M$ are shown in Fig. 4.6, which reports the evolution of the kick velocity using Ψ_4 (solid lines), and the gauge-invariant quantities when the summation in (4.36) is truncated to the first 6 multipoles (dashed lines), which we have found to be sufficient to show convergence. Indicated with symbols are the estimates and relative error bars obtained by [136] (circle) and by [139] (star).

We note that because the binary system starts evolving at a finite separation, it will have already gained a net linear momentum that can influence the value of the final kick. Computing this initial linear momentum amounts to selecting a proper constant in the integration of (4.29) or (4.36). Fortunately, this is rather straightforward to do and amounts to determining the direction in 3-space in which the center of mass of the system is moving initially. In practice, we plot the evolution of the x and y-components of the kick velocity (the z-component is zero because of symmetry) and calculate the vector to the center of the spiral generated as the evolution proceeds. This vector is then composed with the final one, yielding the final kick; note that being a vector this integration constant is not simply an additive constant for the kick velocity $|v|_{\rm kick}$. In Fig. 4.6, we have plotted the effect of including this constant, comparing the case where it is set to zero [set of curves *(a)*], with a value set by extrapolating the recoil backwards to compensate for the small but nonzero initial linear momentum [set of curves *(b)*]. In the first case we find agreement with [139], while in the second case the good agreement is with [136].

A validation of this procedure is also rather straightforward: only an accurate estimate of the initial momentum yields a monotonic evolution of the kick velocity (or, in the case of very close binaries, reduces the oscillations considerably); any different choice would yield the oscillations seen in curves *(a)* (*cf.,* Fig. 1 of ref. [136] or Fig. 3 of ref. [139]). Selecting the correct integration constant becomes less important as the separation of the binary is increased (see also the discussion below), but it can easily lead to errors of 10% or more for the rather close binaries considered here.

4.2.3 Results

This section collects the results of our analysis of the recoil velocity of spin-aligned binaries and discusses the different aspects of the study which combined provide a consistent and accurate picture of this process. We will first concentrate on the systematic error introduced by the use of initial data with zero linear momentum and on the techniques we have developed to remove it. We will then discuss the actual computation of the recoil velocities and their dependence on the spin ratio, highlighting the modes of the radiation which are largely responsible for the asymmetric emission. Finally, we will discuss the accuracy of our measurements and our ability to preserve mass and angular momentum to below 1%.

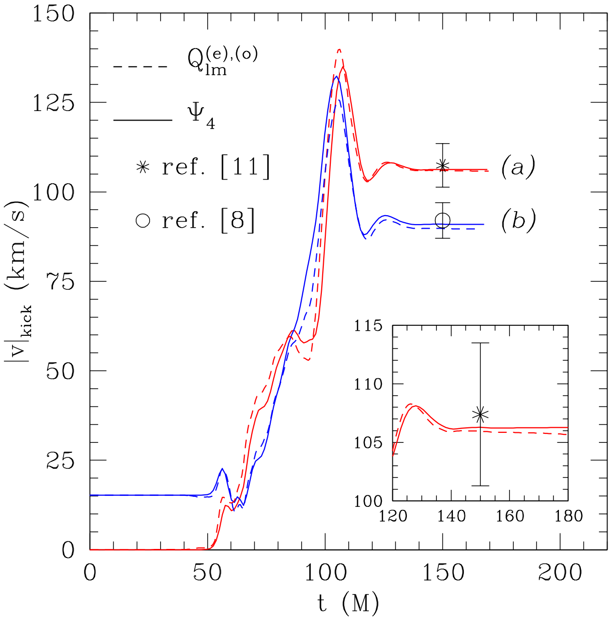

Figure 4.6: Recoil velocity as function of time for a binary system of nonspinning black holes with a mass ratio of $2/3$ at an initial separation $4.1\,M$. The set of curves *(a)* and *(b)* differ in the choice of the integration constant, while the solid and dashed lines show the two independent computations of the momentum flux [eqs. (4.29) and (4.36)].

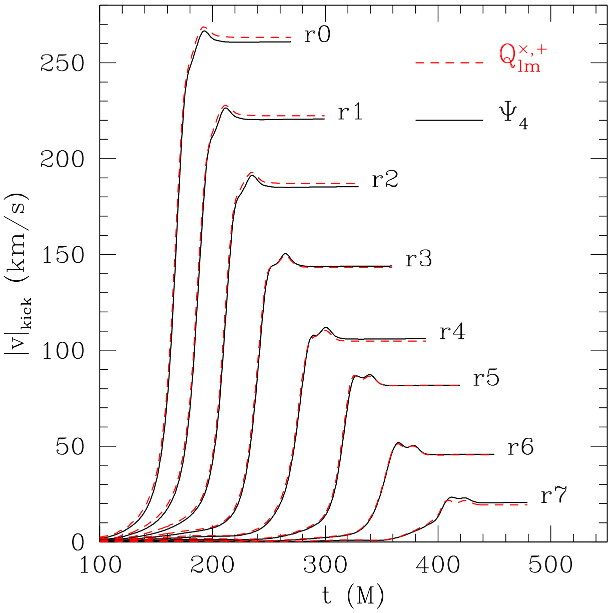

Figure 4.7: Recoil velocity as function of time for the sequence of runs *i.e.,* from $r0$ with $-a_1 = a_2 = 0.586$, to r4 with $a_1 = 0, a_2 = 0.586$). Note that the merger is delayed for smaller values of $|a_1|$.

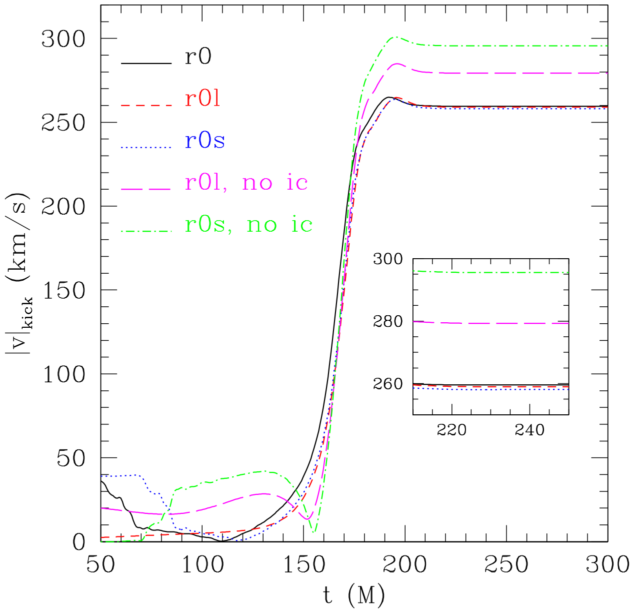

Figure 4.8: The recoil velocity of the binary $r0$ is compared to those of the same system but with either a larger or a smaller initial separation (*i.e.*, $r0l$ and $r0s$, respectively). Note the same recoil velocity is obtained when the integration constant is properly taken into account, while an error as large as $\sim 13\%$ is made otherwise.

A number of interesting features are worth remarking. Firstly, all of the curves show a monotonic growth as a result of a suitable choice for the integration constant. Secondly, the two types of measurements agree to very good precision. Thirdly, binaries that have a spin ratio closer to zero merge progressively later. It is apparent that the growth rate of the kick velocity (and hence the rapidity of the inspiral), increases with the asymmetry in the spins. Fourthly, increasing the initial separation for a binary with $a_1/a_2 = -1$ does not change significantly the integration constant chosen for $r0$, thus indicating that the kick estimate for the latter is robust. Finally, as in unequal-mass binaries, the largest contribution to the kick comes from the final parts of the inspiral and is dominated by the last orbit. However, unlike equal-mass binaries, the post-merger evolution of the kick velocity is not modified substantially by the quasi-normal mode ringing (*cf.*, Figs. 4.7 and 4.6), with the final kick velocity being only slightly smaller than the maximum one reached during the evolution.

As predicted by the PN expression (4.41), the final velocities shown in Fig. 4.7 exhibit a linear dependence with the spin ratio, and this is shown in Fig. 4.9, which reports the asymptotic kick velocities when measured with Ψ_4 (open circles) or with the gauge-invariant perturbations (stars). Also indicated are the error bars which include errors from the determination of the integration constants, from the dependence of the waveforms on the extraction radii, and from the truncation error.

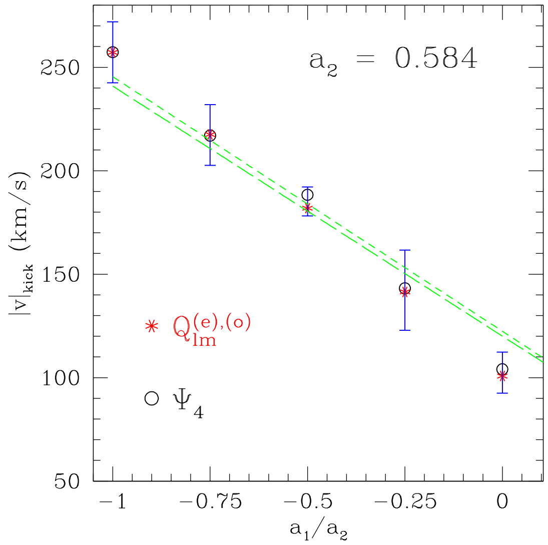

Figure 4.9: Kick velocities and error bars for different spin ratios; the dashed lines show a linear fit of all the data when the point at $a_1/a_2 = 1$ is given an infinite weight since $|v|_{\rm kick} = 0$ for $a_1 = a_2$.

The data points in Fig. 4.9 are not the only ones available and indeed a binary system with $a_1/a_2 = 1$ is bound to produce a zero kick velocity. The dashed lines in Fig. 4.9 represent a linear fit of all the data when the point at $a_1/a_2 = 1$ is given an infinite weight to account for $|v|_{\rm kick} = 0$ when $a_1 = a_2$ (short-dashed line for Ψ_4 and long-dashed for $Q_{\ell m}^{\rm (e,o)}$). These lines are only illustrative and bear a physical significance only if the linear dependence should hold for all the possible values of the spin-ratio.

4.2.4 Initial transients in the waveforms

Both Eqs. (4.29) and (4.36) provide an expression of the recoil velocity in terms of the radiated (linear) momentum per (infinitesimal) time interval. A time-integration of those equations is needed in order to compute the recoil and this obviously opens the question of determining an integration constant which is in practice a vector. Fortunately, this integration constant has here a clear physical meaning and it is therefore easy to compute. In essence it reflects the fact that at the time the simulation is started, the binary system has already accumulated a non-vanishing net momentum as a result of the slow inspiral from an infinite separation.

Since the initial data is constructed so as to have a vanishing linear momentum, there will be a inconsistency between this assumption and the actual evolution of the initial data. Stated differently, the numerical evolution of the Einstein equations will soon tend to a spacetime which is different from the initial one and which corresponds to one with a net linear momentum. This momentum is the one that the binary has gained when inspiralling from $t = -\infty$ till $t = 0$. Calculating the integration constant amounts therefore to computing the vector accounting for this mismatch and is essential for a correct measurement of the recoil velocity. The error made when neglecting this constant, as routinely done in numerical-relativity calculations, inevitably produces a systematic deviation from the correct answer and, as we will show in the next section, it can altogether prevent from having the correct qualitative behavior.

The relevance of this integration constant depends on the initial separation and it is more important for binaries that start their evolution initially quite close. The tighter the binary is, the larger the emitted momentum per unit time and the more important it is to evaluate the initial mismatch. Fig. 4.8 helps to illustrate this point. The figure shows the time evolution of the recoil velocity $|v|_{\rm kick} \equiv \sqrt{v_x^2 + v_y^2}$ for the same binary system having spin ratio $a_1/a_2 = -1$ but with increasing initial separation. More precisely, we consider systems $r0l$, $r0$ and $r0s$ which differ only in the initial separation, which is about $8.4,\ 6.0$ and $5.6\,M$, respectively. The data Fig. 4.8 is properly shifted in time so as to have the curves overlap and shows that *only* when the integration constant is properly taken into account, do the three simulations yield the same recoil velocity (*cf.*, solid, dashed, and dotted lines). On the other hand, when the integration constant is not included in the calculation, different evolutions will yield different estimates, with a systematic error that can be as large as 13% (*cf.*, long-dashed and dot-dashed lines) and is clearly unacceptable given that the overall precision of the simulations is below 1% (*cf.*, Figs. 4.15–4.16 and the discussion in Sect. 4.2.7).

Besides providing the right answer, the calculation of the integration constant also results in a considerable saving in computational costs. The complete dynamics of the binary $r0l$ including the merger and ringdown, in fact, requires simulations for about $600\,M$; the same answer in terms of recoil velocity can be obtained with the system $r0s$, whose dynamics is fully accounted for with a simulation lasting only for $340\,M$.

To compute the integration constant it is sufficient to look carefully at the evolution in the velocity-space of the two components v_x and v_y of the recoil velocity (because of the symmetry the z-component is zero but the method described here can be easily extended to the case in which $v^z \neq 0$). This is shown in the left panel of Fig. 4.10, which reports the track of the "center of mass" for system $r0$ in such a space. Different types of line refer to different intervals in time during the evolution and, for an observer at $r_{\rm E} = 50\,M$, the dotted one refers to $t \lesssim 50\,M$, the dashed one to $50\,M \lesssim t \lesssim 75\,M$, the continuous one to $75\,M \lesssim t \lesssim 183\,M$, and finally the long-dashed one to $t \gtrsim 183\,M$.

For $t \lesssim 50\,M$ the system undergoes very little evolution in velocity-space (*cf.*, dotted line in the inset within the inset of the left panel) but a rapid change, lasting for about $25\,M$, takes place as the radiation reaches the observer. The radiation received has information about the "correct" linear momentum of the spacetime which is a solution of the Einstein equations for system $r0$ as if it had inspiraled from infinity, and thus rapidly moves the center of mass to a net nonzero recoil velocity (*cf.*, almost-straight dashed line in the inset in the left panel). Once the system has adjusted for the proper linear momentum, the evolution proceeds as expected, with the recoil velocity vector slowly tracking a spiral in velocity space. This is an important point which we prefer to underline: the rate of change of linear momentum is very large only initially and this is because as the binary migrates from the initial non-radiating state (the data is conformally flat) to the consistent radiating state, it will emit the amount of linear momentum it would have emitted when inspiralling from infinite separation. After this burst of linear momentum, the evolution of the recoil velocity is minute, essentially until it grows very rapidly during the last orbit.

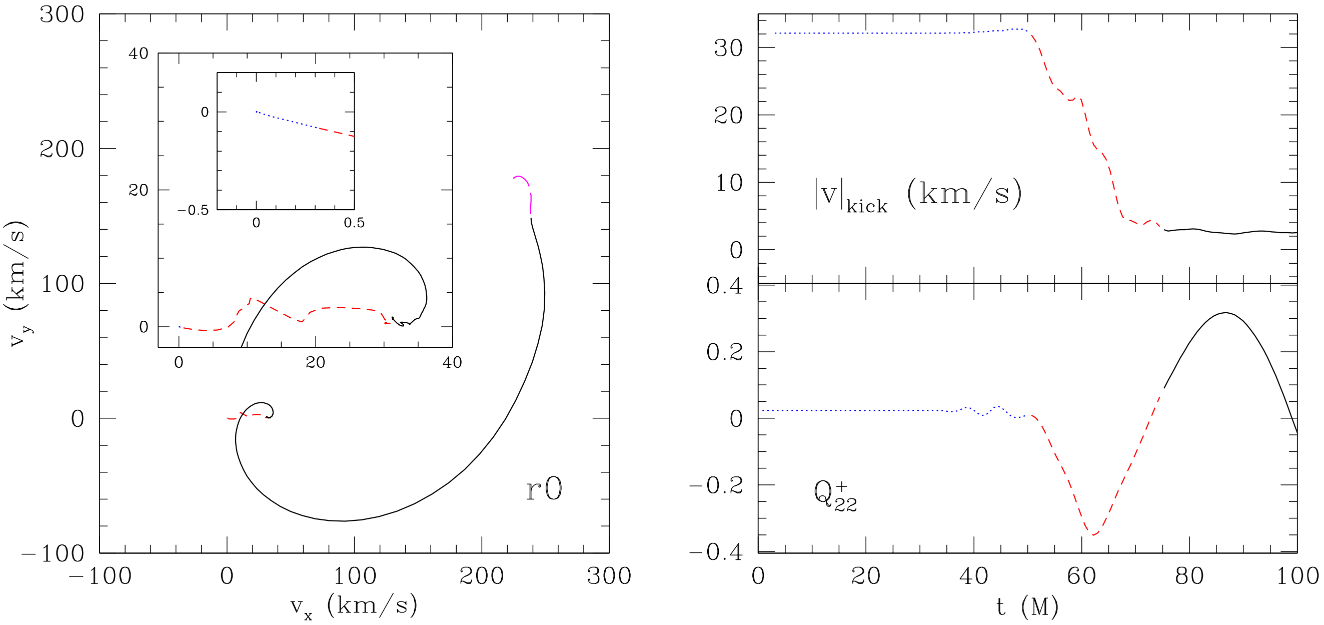

Figure 4.10: *Left panel:* Evolution in velocity space of the recoil-velocity vector. Very little variation is recorded before the radiation reaches the observer at $r_{\rm E} = 50\,M$ (dotted lines in the two insets). The absence of the proper linear momentum in the initial data triggers a rapid and an almost straight-line motion (dashed line) of the center of the spiral away from the origin of coordinates during the initial stages of the evolution. After this transient motion, the evolution is slower, with the spiral progressively opening up (solid line). The vector to the center of the spiral corresponds to the initial linear momentum of the spacetime and is used as integration constant for Eqs. (4.29) and (4.36). The final part of the evolution is characterized by a change in the spiral pattern (long-dashed line) as a result of the interaction of different modes in the ringdown of the final black hole. Note that the figure has been rotated clockwise of about 30° to allow for the two insets. *Right panel:* Initial behavior of the recoil velocity (upper graph) and of the waveform (Q^+_{22}) for model $r0$ (lower graph). This figure should be compared with the initial vector evolution of the recoil velocity shown in the left panel where the same types of lines have been used for the different stages of the evolution.

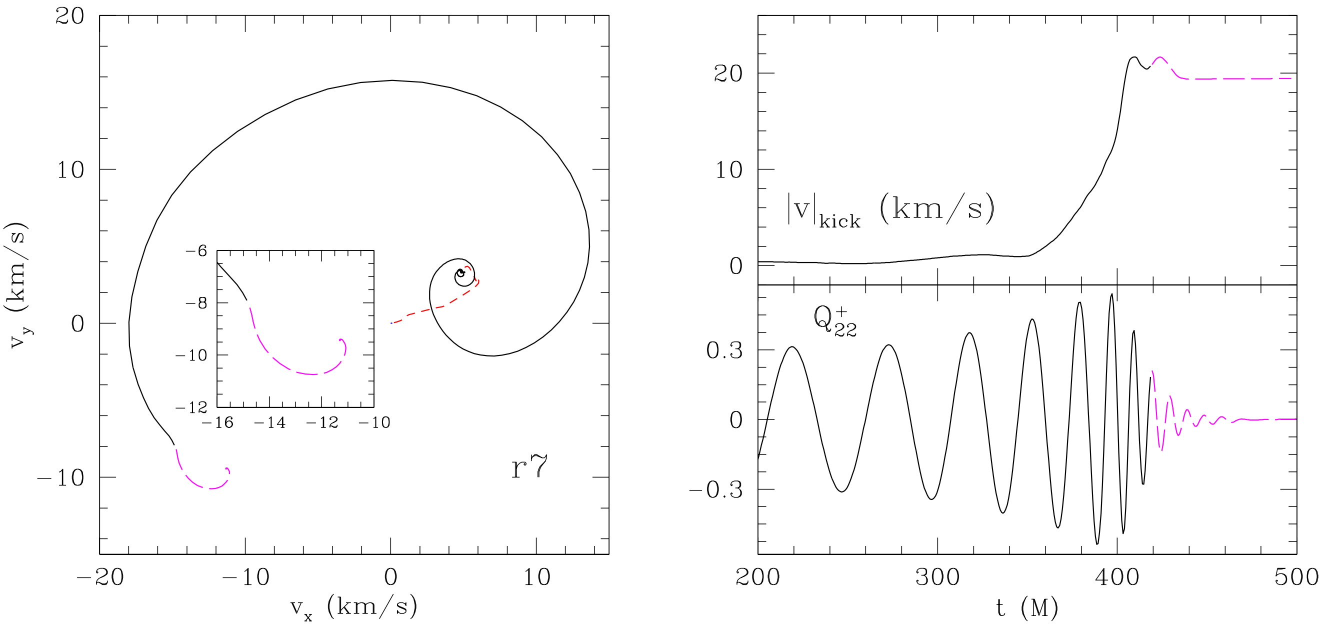

Figure 4.11: *Left panel:* The same as in the left panel of Fig. 4.10 but for system $r7$. Shown in the inset is the sudden re-orientation of the recoil velocity vector during ringdown and corresponding to a new spiral with different aperture (long-dashed line). Although more pronounced in $r7$, the appearance of this "hook" at ringdown is seen all the members of the sequence. *Right panel:* The same as in the left panel of Fig. 4.10 but for system $r7$. The upper graph concentrates on the final stages of the evolution in of the recoil velocity and on the appearance of a second peak during ringdown (long-dashed curve). The lower graph shows the same but in terms of the Q^+_{22} waveform. A discussion of these final stages of the evolution is made in Sect. 4.2.6.

Computing the integration constant consists then in calculating the position of the center of the spiral and this can be done either by a simple inspection of a graph in the velocity-space, from which one computes the center of the spiral or, equivalently, by searching for the initial vector that would lead to an essentially *monotonic* in time growth of the recoil velocity. The latter procedure does not require a human judgment it yields the same answer (to less than $1\,\mathrm{km/s}$) as the one guessed by looking at the velocity space.

The right panel of Fig. 4.10 shows the same evolution as the left one, but through different quantities. The upper panel, in particular, shows the time evolution of the recoil velocity and the rapid changes it undergoes initially when the radiation first invests the observer. The lower panel, on the other hand, shows the Q^{+}_{22} amplitude and highlights that, while the initial burst of radiation stops after $t \sim 50\,M$ (*cf.*, dotted line), the waveform is still not fully consistent until $t \sim 75\,M$ (*cf.*, dashed line).

It is worth remarking that the evolution of the recoil vector in the velocity-space has another interesting feature during the final stages of the evolution and when the final black hole is ringing down. This is marked as a long-dashed line in the left panel of of Fig. 4.10 and shows a break in the building of the spiral and the appearance of a new spiral with a different aperture (we refer to this feature as “the hook”). This is more evident in the left panel of Fig. 4.11, which shows the evolution of the recoil vector for the binary system $r7$ and offers a magnification of the hook in the inset. The hook accounts for a rapid change in the recoil velocity and it is due to the interplay of different modes during the ringdown. This is clearly illustrated in the right panel of Fig. 4.11 which similarly reports the time evolution of the recoil velocity and the final stages of the Q^{+}_{22} waveform.

4.2.5 Recoil velocities

The recoil velocity has been calculated for the sequence of models listed in Table 4.1. As mentioned in Sect. 4.1.1, this sequence corresponds to equal-mass black holes, whose initial spins are unequal, though always aligned with the z-axis. The $r0$ model has equal but opposite spins, while the $r8$ model has equal and aligned spins on the black holes, with other models corresponding to intermediate values, as outlined in Section 4.1.1. Since the total initial orbital angular momentum $\boldsymbol{L}$ of the system is chosen to be constant over the sequence, the initial separations of the black holes increases in the sequence, as well as the time to merger due to spin-spin effects which contribute to an orbital “hang-up” in the aligned case.

I extract gravitational waves by both the gauge-invariant and the Ψ_4 methods described in the previous section and by interpolating the radiation-related quantities onto 2-spheres at coordinate radii $r_{\rm E} = 30\,M$, $40\,M$, $50\,M$, and $60\,M$. The use of multiple extraction radii is made to check the consistency of the measurement and the precise value of the extraction radius has little influence on the actual kick calculation. In the case of the binary system $r0$ we have verified that the recoil velocity yields the same value with differences that are smaller than $2\,\mathrm{km/s}$ for extraction 2-spheres at distances larger than $30\,M$. As a result, we have used $r_{\rm E} = 50\,M$ as the fiducial distance for an observer in the wave-zone and all of the results presented hereafter will be made at this extraction 2-sphere. A validation that the gauge-invariant quantities have the proper scaling with

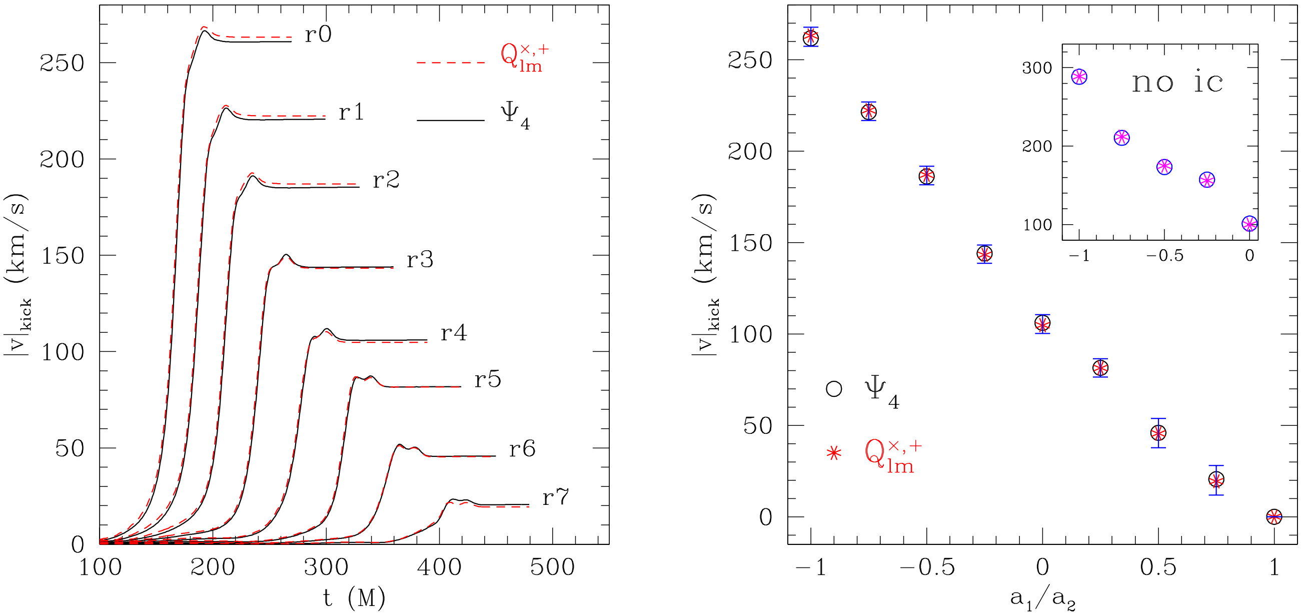

Figure 4.12: *Left panel:* Recoil velocity as a function of the spin asymmetry parameter a_1/a_2 for the models listed in Table 4.1. Indicated with a continuous lines are the results obtained via Ψ_4, while a dashed line is used for the gauge-invariant quantities $Q^{+,\times}_{\ell m}$. *Right panel:* Final recoil velocity calculated with both the use Ψ_4 (empty circles) and the gauge-invariant quantities (stars). Shown in the inset is the incorrect scaling obtained when the correction for the integration constant is not made.

radius is presented in Appendix A.6.

The evolution of the recoil velocity for the entire sequence listed in Table 4.1 is displayed in the left panel of Fig. 4.12. It is apparent that the suitable choice of the integration constant discussed in the previous section yields early evolutions that are always monotonic in time and that, as expected, the largest recoil velocity is generated for the case in which the asymmetry is the largest, namely for the binary $r0$. The left panel Fig. 4.12 also shows that the profile for each case is rather similar, with the largest contribution to the kick velocity being generated in a period of about $80\,M$, corresponding roughly to the timescale of the last orbit and merger.

It is worth noting that during the final stages of the evolution, the recoil velocity is not monotonic but shows at least two peaks, whose relative amplitude depends on the spin ratio. For spin ratios ~ -1 the first peak is hardly visible, while the second one is the most pronounced one. As the spin ratio increases, however, the first peak becomes more prominent and for spin ratios ~ 1 it becomes comparable with the second one or even larger for binaries $r6$ and $r7$. As mentioned in the previous Section and further discussed in the following one, the appearance of these peaks is related to the interplay of different mode-contributions during the ringdown. The second peak, in particular, can be associated to a rapid change in the recoil-velocity vector and is behind the characteristic "hook"

Table 4.3: Final kick velocities in units of $\mathrm{km/s}$ for the models listed in Tab. 4.1. Columns two and three show the values obtained using the gauge-invariant quantities $Q^{\times,+}_{\ell m}$ and Ψ_4 respectively and taking into account the integration constant. Columns four and five, on the other hand, show the results obtained when ignoring the integration constant. The same data are shown in the right panel of Fig. 4.12.

Model	$Q^{\times,+}_{\ell m}$	Ψ_4	$Q^{\times,+}_{\ell m}$, no ic	Ψ_4, no ic
$r0$	263.2	261.8	288.9	288.4
$r1$	222.4	221.4	211.9	210.6
$r2$	187.1	186.2	174.8	173.3
$r3$	143.3	144.0	155.9	157.3
$r4$	104.8	106.1	100.0	101.3
$r5$	81.4	81.5	76.9	77.0
$r6$	45.6	45.9	55.4	56.2
$r7$	19.4	20.6	13.8	14.8
$r8$	0.0	0.0	0.0	0.0

discussed in the left panels of Figs. 4.10 and 4.11. As a representative measure of the accuracy in determining these recoil velocities, we have carried out simulations also for the binary system $r8$, in which the black holes have identical spin and thus from which no kick should result. The computed recoil velocity has been found to be $10^{-4}\ \mathrm{km/s}$, clearly indicating that our evolutions do an excellent job in preserving the orbital symmetry of these binaries.

The recoil velocities attained by the final black holes and shown for in the left panel of Fig 4.12 can be studied in terms of their dependence on the spin ratio a_1/a_2, which can also be regarded as the "asymmetry" parameter of the system, being the largest for $a_1/a_2 = -1$ and zero for $a_1/a_2 = 1$. These velocities are collected in Table 4.3 and are shown as a function of a_1/a_2 in the right panel of Fig 4.12, where I have indicated with open circles the values obtained using Ψ_4 and with stars those obtained using the gauge-invariant perturbations.

The data in the right panel of Fig 4.12 is shown together with its error-bars, which include errors from the determination of the integration constants, from the truncation error and from the amount of ellipticity contained in the initial data. We have estimated these errors to be of $5\ \mathrm{km/s}$ for binaries $r0$–$r5$ and of $8\ \mathrm{km/s}$ for binaries $r6$ and $r7$. Shown also in the inset is the recoil data obtained when ignoring the integration constant. When the proper evaluation of the initial transient is not made, the data does not show the correlation with the spin ratio which is instead shown by the corrected data. The correlation found the one predicted by PN studies. Recall that using PN theory at the 2.5 order, Kidder [172] has concluded that in the case of a circular, non-precessing orbit, the

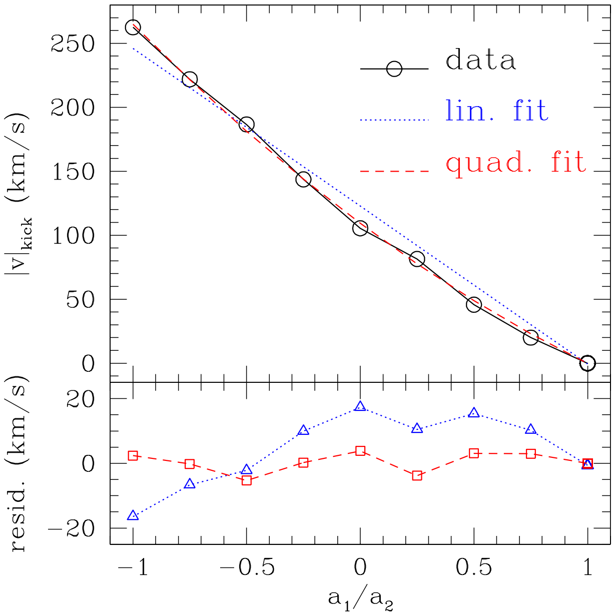

Figure 4.13: *Upper panel:* Comparison of the computed data for the recoil velocity (open circles) with the least-squares fits using either a linear (dotted line) or a quadratic dependence (dashed line). *Lower panel:* Point-wise residuals computed with the linear (dotted line) or a quadratic fit (dashed line).

total kick for a binary system of arbitrary mass and spin ratio can be expressed as [148]

$$\begin{aligned} |v|_{\rm kick} &= c_1 \frac{q^2(1-q)}{(1+q)^5} + c_2 \frac{a_2 q^2(1-q a_1/a_2)}{(1+q)^5} \\ &= \tilde{c}_2 a_2 \left(1 - \frac{a_1}{a_2}\right) , \end{aligned} \qquad (4.41)$$

where $q \equiv M_1/M_2$ is the mass ratio and is equal to one for the binaries considered here, thus leading to the second form of Eq. (4.41). The coefficients c_1 and $\tilde{c}_2 \equiv c_2/32$ depend on the total mass of the system and on the orbital separation at which the system stops radiating, which is intrinsically difficult to determine with precision since it lies in a region where the PN approximation is not very accurate. Indeed, we find that the coefficient c_2 is not really a constant in the case of equal-mass binaries but, rather, it can be seen to depend at least linearly on the spin ratio.

This is shown in Fig. 4.13, whose upper panel offers a comparison among the computed data for the recoil velocity (open circles) with the least-squares fits using either a linear (dotted line) or a quadratic dependence (dashed line). It is quite apparent that a linear dependence on a_1/a_2, such as the one expected in Eq. (4.41) for $c_2 = {\rm const.}$ does not reproduce well the numerical data and yields point-wise residuals of the order of $20\,{\rm km/s}$. These are shown with a dotted line in the lower panel of Fig. 4.13. A quadratic dependence on a_1/a_2, on the other hand, reproduces the numerical data very nicely, with

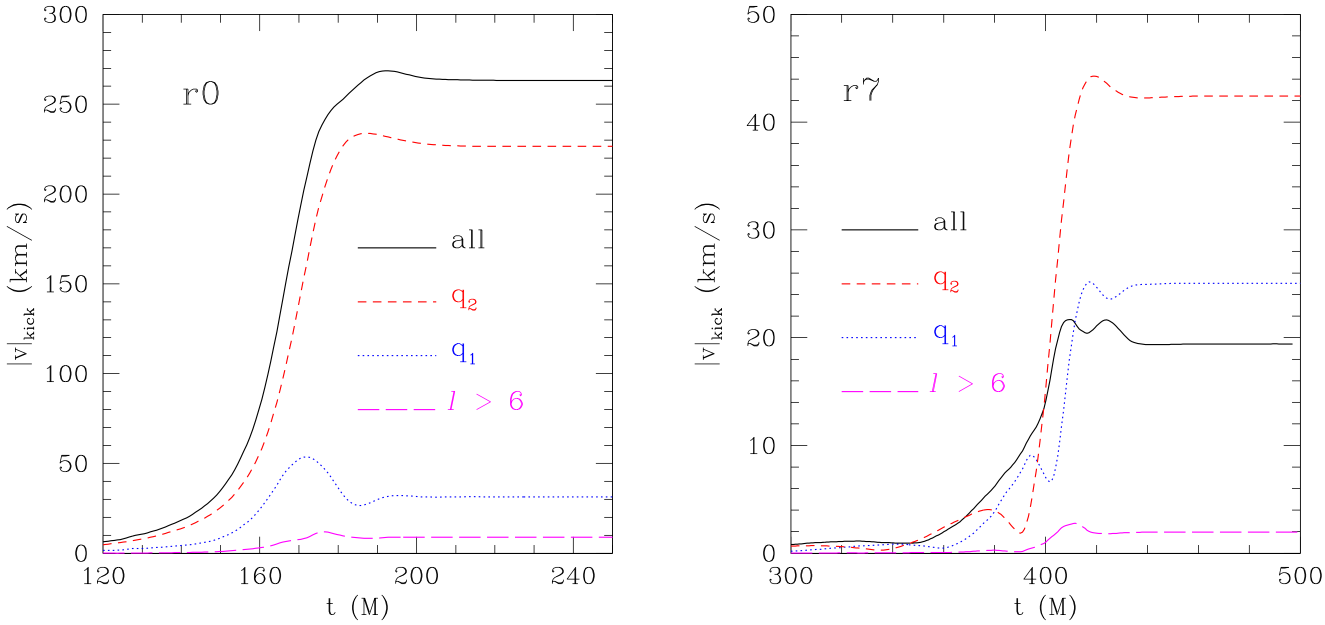

Figure 4.14: The total kick calculated via Eq. (4.36) up to $\ell = 7$ is compared to the contributions of individual terms q_1 and q_2, as well as the sum of term excluding these. In the case of the $r0$ system (left panel) the spins are anti-aligned and the q_2 term is dominant and the q_1 term does not provide a significant contribution. In the case of the $r7$ system (right panel), on the other hand, the spins are essentially aligned and the while the q_2 term is still dominant, the q_1 term also makes a significant contribution.

residuals that are of the order of $5\,\mathrm{km/s}$, as shown with a dashed line in the lower panel of the same figure, and thus compatible with the reported error-bars.

We can re-express Eq. (4.41) in the more generic form

$$|v|_{\rm kick}\left(a_2, \frac{a_1}{a_2}\right) = |a_2| f\left(\frac{a_1}{a_2}\right) \tag{4.42}$$

where a_2 plays here the role of a "scale-factor". The function $f(a_1/a_2)$ with $a_1/a_2 \in [-1,\, 1]$ and maximum at $a_1/a_2 = -1$ can then be seen from numerical-relativity calculations (or higher-order PN approximations) and our least-squares fit suggests the expression

$$f_{\rm quad.} = 109.3 - 132.5\left(\frac{a_1}{a_2}\right) + 23.1\left(\frac{a_1}{a_2}\right)^2\ \mathrm{km/s}\,. \tag{4.43}$$

The maximum kick velocity for a given a_2 is then readily calculated even without a detailed knowledge of the function $f(a_1/a_2)$ as

$$(|v|_{\rm kick})^{\rm max}(a_2) = |a_2| f(-1)\,. \tag{4.44}$$

Using the data reported in Table 4.3 for $a_2 = -0.584$ we obtain for $|a_2| = 1$ that the maximum recoil velocity attainable from a binary system of equal-mass black holes with spins aligned to the orbital angular momentum is $448 \pm 5\,{\rm km/s}$. This is in very good agreement with our previous estimate made in Ref. [155] with a smaller sequence and in equally good agreement with the results reported in Ref. [157].

4.2.6 Mode contributions to the recoil velocity

For the models studied in the previous section we have evaluated Eq. (4.36) including modes up to $\ell = 7$. In practice, however, the recoil is strongly determined by the lower-mode contributions. In particular, the two terms

$$q_1 \equiv \frac{1}{48\pi}\sqrt{\frac{30}{7}}\dot{Q}^{+}_{22}\,Q^{+}_{3-3}, \tag{4.45}$$

$$q_2 \equiv -\frac{\rm i}{48\pi}\dot{Q}^{+}_{2-2}\,Q^{\times}_{2\,1} \tag{4.46}$$

are the dominant ones. This can be seen in Fig. 4.14, where the time evolutions of the terms q_1 and q_2 are plotted (dotted and dashed lines, respectively) together with the total kick calculated via Eq. (4.36) (solid line), and with the contributions from all other terms up to $\ell = 7$ excluding q_1 and q_2 (long-dashed line). A rapid inspection of the figure reveals that the kick is dominated in particular by the q_2 term, whereas the q_1 term has a magnitude of the order of all the other modes combined. A similar result holds for each member of the sequence, so that the two contributions determine the final kick to more that 95%. The mode contributions are vector quantities, just as the kick velocity itself, and are not always aligned.

This coupling also goes some way to explain some features of the recoil velocity profiles displayed in Fig. 4.12. As mentioned in the previous section, the binaries $r4$ to $r8$ show a double peak in the evolution of the kick velocity before it settles down to the final value. The same feature can be seen in the more asymmetric $r0$ to $r3$ binaries, where it appears as a flattening of the slope near the maximum. Since the two peaks are shown both by the gauge-invariant and by the Ψ_4-based techniques we do not believe them to be a simple numerical artifact. Overall, the properties of the recoil velocity near its maximum, and before it settles to the final value, are determined by the relative phases of the two contributions identified above. An analysis of the terms q_1 and q_2 in vector-space reveals that when they are relatively aligned at the peak of the acceleration, there is a clear single peak in the evolution.

4.2.7 Angular Momentum and Mass Conservation

In this section we discuss the radiated angular momentum and energy during the evolution of the different initial-data sets. I compute the radiated angular momentum and mass by calculating the difference between the initial data and that of the final black hole, and then compare these quantities with the corresponding ones measured in terms of the emitted gravitational radiation. The differences in the two independent estimates serve as indicators of the conservative properties of the code.

The radiated angular momentum can be simply written as the difference between the initial and final values

$$\boldsymbol{J}_{\rm rad} = \boldsymbol{J}_{\rm fin} - \boldsymbol{J}_{\rm ini}\,, \tag{4.47}$$

where, as a result of the conformal flatness of the initial-data slice, $\boldsymbol{J}_{\rm ini}$ is given by the simple expression (see for example [165–167])

$$\boldsymbol{J}_{\rm ini} \equiv \boldsymbol{J}_{\rm ADM} = \boldsymbol{C}_1 \times \boldsymbol{p}_1 + \boldsymbol{C}_2 \times \boldsymbol{p}_2 + \boldsymbol{S}_1 + \boldsymbol{S}_2\,. \tag{4.48}$$

Here $\boldsymbol{C}_i$, $\boldsymbol{p}_i$ and $\boldsymbol{S}_i$ are the position, the linear momentum and the spin of the i-th black hole. The final angular momentum $\boldsymbol{J}_{\rm fin}$, on the other hand, is set to be equal to the spin of the final black hole after all the radiation has left the computational domain. Two different methods are used to obtain this measure, both of which are based on properties of the apparent horizon of the final hole.

The first method employs the isolated/dynamical horizon formalism and searches for a rotational Killing vector ϕ^a on the final apparent horizon so as to measure the spin of the final black hole as [186–188]

$$J = -\frac{1}{8\pi}\oint_S K_{ab}\phi^a\hat{r}^b d^2V\,. \tag{4.49}$$

This expression (4.49) is valid on any sphere where a Killing vector ϕ^a can be found, and is therefore a quasi-local measure of the angular momentum. In particular, at large distances where the spacetime is close to axisymmetric, there is a good approximation to an angular Killing vector, and we can apply this expression to determine the angular momentum of the spacetime. Note also that Eq. (4.49) is identical to the ADM angular momentum when evaluated at spacelike infinity [187, 188].

The second method, assumes that the final black hole has settled to a Kerr one and uses the rotational-induced distortion of the apparent horizon of the final black hole to estimate its spin. Defining C_p and C_e to be respectively the apparent horizon's polar and equatorial proper circumferences, their ratio $C_r \equiv C_p/C_e$ will undergo damped oscillations as the perturbed black hole settles to a Kerr state through the quasi-normal ringing. The final value of C_r can be expressed as a nonlinear function of the dimensionless spin parameter $a = J/M^2$ as [189–191]

$$C_r(a) = \frac{1+\sqrt{1-a^2}}{\pi}E\left(-\frac{a^2}{(1+\sqrt{1-a^2})^2}\right)\,, \tag{4.50}$$

where $E(k)$ is the complete elliptic integral of the second kind

$$E(k) = \int_0^{\pi/2}\sqrt{1-k\sin^2\theta}d\theta\,. \tag{4.51}$$

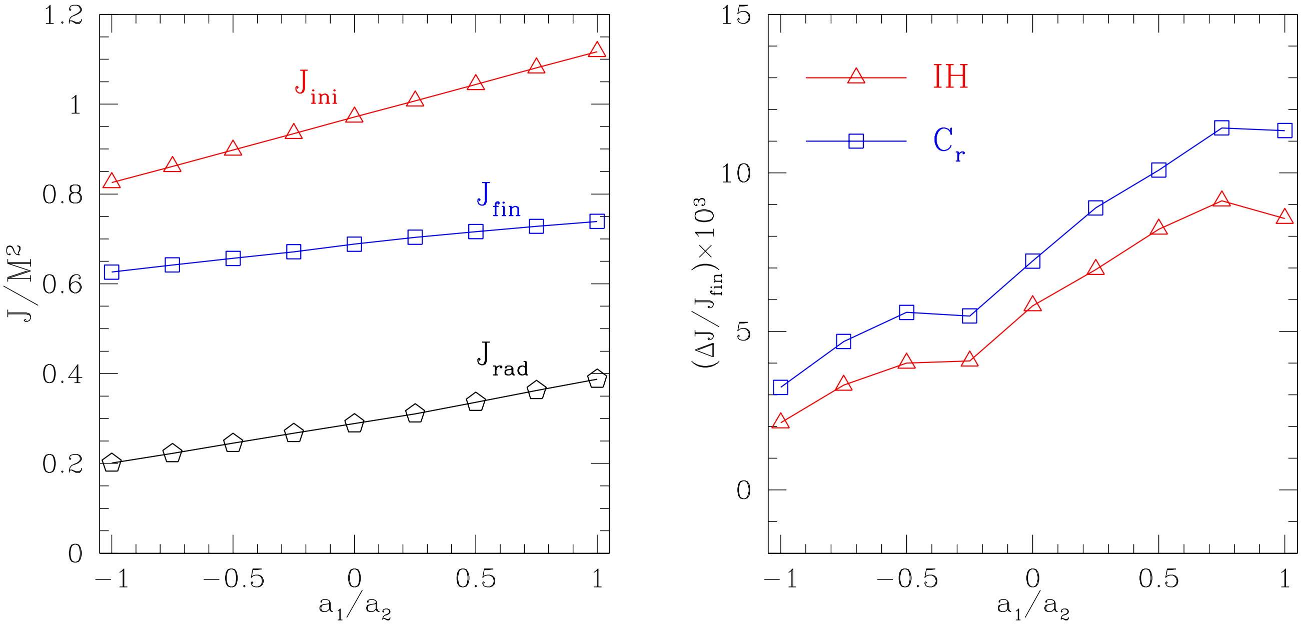

Figure 4.15: *Left panel:* Dependence on the spin ratio of the initial total angular momentum $J_{\rm ini}$ [as computed from Eq. (4.48)], of the radiated angular momentum $J_{\rm rad}$ [as computed through the gauge-invariant waveforms], and of the final spin of the black hole $J_{\rm fin}$. All quantities show a linear behavior, whose coefficient are collected in Table 4.4. *Right panel:* Relative error $\Delta J/J_{\rm ini}$ in the conservation of the angular momentum [*cf.*, Eq. (4.55)]. Different curves refer to whether the final spin of the black hole is computed using the isolated/dynamical horizon formalism (triangles) or the distortion of the apparent horizon (squares). In both cases the error is of about 1% at most for simulations at the medium resolution.

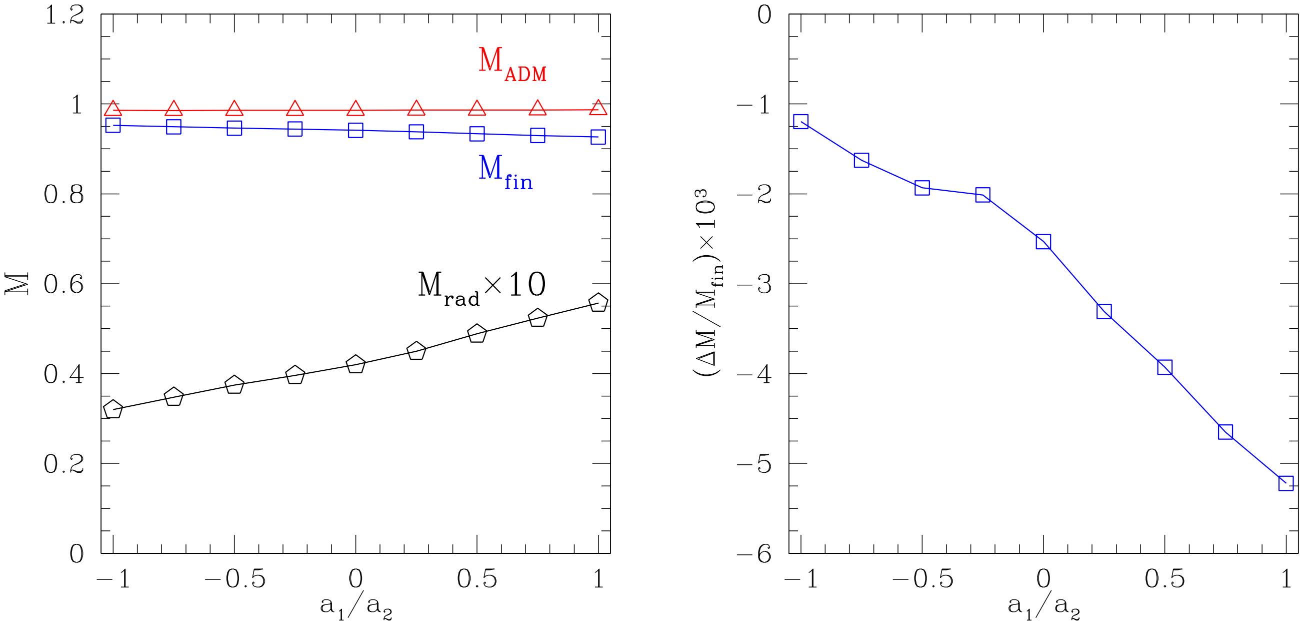

Figure 4.16: *Left panel:* Dependence on the spin ratio of the ADM mass $M_{\rm ADM}$, of the scaled radiated energy $M_{\rm rad}$ [as computed through the gauge-invariant waveforms and scaled by a factor of 10 to make it visible], and of the final mass of the black hole $M_{\rm fin}$. All quantities show linear behaviors, whose coefficients are collected in Table 4.4. *Right panel:* Relative error $\Delta M/M_{\rm ini}$ in the conservation of the energy [*cf.*, Eq. (4.57)]. Note that the error is of about 0.5% at most for simulations at the medium resolution.

By inverting numerically Eq. (4.50) we obtain a from the late time C_r that is measured from the apparent horizon shape. For computing J one multiplies a by the square of the final mass, which we take to be $M_{\rm ADM} - M_{\rm rad}$. An alternative choice involving the total mass Eq. (4.17) as measured from the apparent horizon would lead to essentially the same results.

As mentioned at the beginning of this section, the determination of the radiated angular momentum can also be done using directly the asymptotic waveform amplitudes h_+ and $h_\times$ as [182, 192, 193]

$$\frac{d^2 J}{dt\, d\Omega} = -\frac{r^2}{16\pi}\left(\partial_t h_+ \partial_\phi h_+^* + \partial_t h_\times \partial_\phi h_\times^*\right) , \tag{4.52}$$

where the amplitude h_+ and $h_\times$ themselves can be expressed either in terms of the Zerilli-Moncrief gauge-invariant variables $Q^+_{\ell m}$, $Q^\times_{\ell m}$ or, alternatively, in terms of the Newman-Penrose scalar Ψ_4. A comparison between the two approaches is presented in Appendix A.6, where it is shown that the differences are minute. Because of this, hereafter we will refer to asymptotic amplitudes measured in terms of the gauge-invariant variables only. Additional details on the resolution of the extraction 2-sphere are also presented in Appendix A.5.

The left panel of Fig. 4.15 summarizes this comparison by showing, as functions of the spin ratio a_1/a_2, $J_{\rm fin}$ from Eq. (4.49), $J_{\rm rad}$ from Eq. (4.52) both adding nicely to yield $J_{\rm ini}$. Note that $J_{\rm ini}$ is growing linearly as it is obvious from Eq. (4.48), but also that that a similar behavior is shown by the radiated angular momentum (and hence by the final spin of the black hole). Using a linear fitting we can derive phenomenological expressions for the relative losses of angular momentum

$$\frac{J_{\rm rad}}{J_{\rm ini}} = \xi^J_{\rm rad}\left(\frac{a_1}{a_2}\right) + \chi^J_{\rm rad} , \tag{4.53}$$

and the relative spin-up of the final black hole

$$\frac{J_{\rm fin}}{J_{\rm ini}} = \xi^J_{\rm fin}\left(\frac{a_1}{a_2}\right) + \chi^J_{\rm fin} . \tag{4.54}$$

The fitted values for $\xi^J_{\rm rad,\,fin}$ and $\chi^J_{\rm rad,\,fin}$ are presented in Table 4.4 and readily indicate that the system looses 24% of its initial orbital angular momentum in the case of anti-aligned spins and up to 34% for aligned spins.

Expressions (4.53) and (4.54) do not have a PN counterpart and yet, since they depend only on the spin-ratio, they represent simple and powerful ways of estimating both the efficiency in the extraction of angular momentum and the spin of the final black in a binary merger when the spins are orthogonal to the orbital plane. This information could be easily injected in those N-body simulations in which the interaction of binary black holes is taken into account [194] and thus yield accurate estimates on final distribution of black-hole spins.

Since we have two independent and different ways of computing $J_{\rm rad}$ [*i.e.*, either from Eq. (4.52) or from Eq. (4.47)] we can quantify our ability to conserve angular momentum

Table 4.4: Coefficients for the phenomenological expressions (4.53) and (4.54) (and the corresponding coefficients for $\Delta M_{\rm rad,\,fin}/M$) by means of which it is possible to compute the relative losses of energy and angular momentum, as well as the final mass and spin of the black hole in binary mergers in which the spins are orthogonal to the orbital plane.

$\xi^J_{\rm rad}$	0.0513	$\xi^M_{\rm rad}$	0.0118
$\chi^J_{\rm rad}$	0.2967	$\chi^M_{\rm rad}$	0.0437
$\xi^J_{\rm fin}$	-0.0513	$\xi^M_{\rm fin}$	-0.0118
$\chi^J_{\rm fin}$	0.7033	$\chi^M_{\rm fin}$	0.9563

Table 4.5: Final and radiated angular momenta and masses, computed from the gauge-invariant waveforms. Shown is also the radiated spin and mass relative to their initial values, which are listed in Tab. 4.1.

	a_1/a_2	$J_{\rm fin}$	$J_{\rm rad}$	$J_{\rm rad}/J_{\rm ADM}$	$M_{\rm fin}$	$M_{\rm rad}$	$M_{\rm rad}/M_{\rm ADM}$
$r0$	-1.00	0.6244	0.2008	0.2434	0.9536	0.0320	0.0325
$r1$	-0.75	0.6391	0.2222	0.2580	0.9507	0.0348	0.0353
$r2$	-0.50	0.6530	0.2449	0.2727	0.9482	0.0374	0.0380
$r3$	-0.25	0.6676	0.2670	0.2857	0.9461	0.0396	0.0402
$r4$	0.00	0.6827	0.2886	0.2971	0.9439	0.0420	0.0426
$r5$	0.25	0.6966	0.3106	0.3084	0.9412	0.0450	0.0456
$r6$	0.50	0.7075	0.3363	0.3222	0.9376	0.0488	0.0495
$r7$	0.75	0.7181	0.3626	0.3355	0.9344	0.0523	0.0530
$r8$	1.00	0.7292	0.3878	0.3471	0.9315	0.0557	0.0564

by measuring the normalized residual

$$\frac{\Delta J}{J_{\rm ini}} \equiv \frac{J_{\rm fin}+J_{\rm rad}-J_{\rm ini}}{J_{\rm ini}}\,. \tag{4.55}$$

This is shown in the right panel of Fig. 4.15 and the two different lines refer to the two measures of the final spin of the black hole, *i.e.*, either via the isolated-horizon formalism (triangles) or via the distortion of the apparent horizon (squares). In both cases the error is extremely small, ranging between 1.1% and 0.2% for simulations at the medium resolution, and thus providing convincing evidence of our accuracy in the preservation of angular momentum. It should be noted that while there seems to be a small advantage in using the isolated horizon measure, the differences are too small to be significant. A small change in the procedure, such as the use of the mass measured via the apparent horizon via Eq. (4.50) in place of $M_{\rm ini}-M_{\rm fin}$ (as we are doing in this figure), would counter the advantage.

We proceed to a similar analysis for the conservation of the mass/energy of the system by considering the difference between the the initial mass and final plus the radiated masses. As for the initial mass we obviously consider the ADM mass of the system $M_{\rm ADM}$, while the radiated energy $M_{\rm rad}$ is computed through the gravitational waveforms [182, 195, 196]

$$\frac{d^2E}{dtd\Omega} = \frac{r^2}{16\pi}\left(\left|\dot{h}_+\right|^2 + \left|\dot{h}_\times\right|^2\right) . \tag{4.56}$$

As for the angular momenta, we have chosen to express the right hand side of Eq. (4.56) in terms of the Zerilli-Moncrief functions and to use as final mass of the black hole $M_{\rm fin}$, the one given by Eq. (4.17) and measured via the apparent horizon.

The left panel of Fig. 4.16 shows $M_{\rm ADM}$, $M_{\rm fin}$ and $M_{\rm rad}$, with the latter rescaled the radiated by a factor of ten to make it more visible. Also in this case there is a clear linear behavior of both the radiated energy and of the final mass of the black hole in terms of the spin ratio. As a result, phenomenological expressions of the type (4.53) and (4.54) are possible also for $M_{\rm fin}$ and $M_{\rm rad}$. The corresponding values of the coefficients $\xi^M_{\rm rad,\,fin}$ and $\chi^M_{\rm rad,\,fin}$ are also presented in Table 4.4.

Finally, to check the precision at which the energy is conserved, and in analogy to Eq. (4.55), we have computed the relative error

$$\frac{\Delta M}{M_{\rm ADM}} \equiv \frac{M_{\rm fin} + M_{\rm rad} - M_{\rm ADM}}{M_{\rm ADM}} , \tag{4.57}$$

and plotted this as a function of the spin ratio in the right panel of Fig. 4.16. Clearly, also the energy losses are extremely small and for all the binaries in the sequence, the error in the energy balance is below 0.52% at the medium resolution. Table 4.5 summarizes the numerical results for the radiated energy and angular momentum for the members of the sequence.

4.3 Spins

While the recent possibility of measuring accurately the final spin through numerical-relativity calculations represents an enormous progress, the complete coverage of the full parameter space uniquely through simulations is not a viable option. As a consequence, work has been done to derive analytic expressions for the final spin which models the numerical relativity data but also exploit as much information as possible from perturbative studies, and from the symmetries of the system [1, 8, 87, 197]. In this sense, these approaches do not amount to a blind fitting of the numerical-relativity data, but, rather, use the data to construct a physically consistent and mathematically accurate modelling of the final spin. Despite a concentrated effort in this direction, the analytic expressions for the final spin could, at most, cover 3 of the 7 dimensions of the space of parameters [8]. Here, I show that without additional fits and with a minimal set of assumptions it is possible to obtain the extension to the complete space of parameters and reproduce all of the available numerical-relativity data.

A number of analytical approaches have been developed over the years to determine the final spin of a binary coalescence [5, 152, 197–199]. Very recently, a method, inspired by the dynamics of a test particle around a Kerr BH, has been proposed for generic binaries ([4], BKL hereafter). The approach assumes that the angular momentum of the final BH is the sum of the individual spins and of the orbital angular momentum of a test particle on the last-stable orbit of a Kerr BH with the same spin parameter as that of the final BH.

Here, we combine this with the data obtained in recent simulations to provide a phenomenological but analytic estimate for the final spin in a binary BH system with arbitrary mass ratio and spin ratio, but in which the spins are constrained to be parallel to the orbital angular momentum. In addition to the data presented in [1], I add three simulations of equal-mass, high-spin binaries and three simulations of unequal-mass, spinning binaries (see Table 4.6). Other data is taken from unequal-mass, nonspinning binaries [3, 7, 139], and of equal-mass, spinning binaries [1, 2]; all of the AEI data is summarized in Table 4.2.

4.3.1 Methods and Results

Analytic fitting expressions for $\boldsymbol{a}_{\rm fin}$ have so far been built using binaries having spins that are either *aligned* or *antialigned* with the initial orbital angular momentum. This is because in this case both the initial and final spins can be projected in the direction of the orbital angular momentum and it is possible to deal simply with the (pseudo)-scalar quantities a_1, a_2 and $a_{\rm fin}$ ranging between -1 and $+1$. If the BHs have *equal mass* but *unequal* spins that are either *parallel* or *antiparallel*, then the spin of the final BH has been shown to be accurately described by the simple analytic fit [1]

$$a_{\rm fin}(a_1, a_2) = p_0 + p_1(a_1 + a_2) + p_2(a_1 + a_2)^2 \,. \tag{4.58}$$

When seen as a power series of the initial spins, expression (4.58) suggests an interesting physical interpretation. Its zeroth-order term, in fact, can be associated with the (dimensionless) orbital angular momentum not radiated in gravitational waves and amounting to $\sim 70\%$ of the final spin at most. The first-order term, on the other hand, can be seen as the contributions from the initial spins and from the spin-orbit coupling, amounting to $\sim 30\%$ at most. Finally, the second-order term, can be associated with the spin-spin coupling, with a contribution to the final spin which is of $\sim 4\%$ at most.

If the BHs have *unequal mass* but spins that are *equal* and *parallel*, the final spin is instead given by the analytic fit [8] as a function of the two free variables in the problem: the symmetric mass ratio $\nu \equiv M_1 M_2/(M_1 + M_2)^2$ and the spin of the initial BHs $a \equiv J/M^2$, *i.e.*, $a_{\rm fin} \equiv J_{\rm fin}/M^2_{\rm fin} = a_{\rm fin}(a, \nu)$. By construction $a_1 = a_2 = a$, and $\vec{a}/|\vec{a}| = \pm\vec{L}/|\vec{L}|$, where $\vec{L}$ is the orbital angular momentum. We next express $a_{\rm fin}$ as a third-order polynomial of ν and a

$$\begin{aligned} a_{\rm fin} = \quad & s_0 + s_1 a + s_2 a^2 + s_3 a^3 + s_4 a^2 \nu + s_5 a \nu^2 + \\ & t_0 a \nu + t_1 \nu + t_2 \nu^2 + t_3 \nu^3 \,. \end{aligned} \tag{4.59}$$

Expression (6.9) is a lowest-order *ansatz*. It intends to capture the behaviour of a function known exactly only in the extreme mass-ratio limit (EMRL) and which has support from numerical simulations in two restricted regimes: *i.e.*, $\nu = 1/4;\ 0 \leq |a| \lesssim 0.75$ and $0.16 \lesssim \nu \leq 1/4;\ a = 0$. A-priori there is no reason to believe expectation that $a_{\rm fin}(\nu, a)$ from the proposed fit will capture the general behaviour well, but it does.

Table 4.6: Initial parameters of the new binaries computed at the AEI. The different columns contain the initial spin a, the symmetric mass ratio ν, half of the initial separation $x/M = \frac{1}{2}(x_1 - x_2)$, the dimensionless initial angular momentum $\tilde{J} = J/(\mu M)$, the numerical and fitted values for $a_{\rm fin}$ and the corresponding relative error.

	a	ν	x/M	$\tilde{J}$	$a_{\rm fin}$	$a_{\rm fin}^{\rm fit}$	|err.| (%)
$t8$	-0.5840	0.2500	3.1712	2.432	0.4955	0.4981	0.53
$ta8$	-0.3000	0.2500	3.7078	3.000	0.5941	0.5927	0.23
$tb8$	-0.8000	0.2500	3.8082	2.200	0.4224	0.4227	0.08
$tb8\ell$	-0.8000	0.2500	4.8600	2.400	0.4266	0.4227	0.92
$p1$	-0.8000	0.1580	3.2733	0.336	0.0050	0.0046	9.89
$p2$	-0.5330	0.1875	3.3606	1.872	0.2778	0.2794	0.57
$p3$	-0.2667	0.2222	3.4835	2.883	0.5228	0.5216	0.23

Given the available numerical estimates, it is possible to calculate the coefficients s_0–s_5, and t_0–t_3 by simply performing a two-dimensional (2D) least-square fit of the data. This, however, would require a lot of care and is likely to lead to inaccurate estimates for the coefficients. This is due mostly to the fact that the space of parameters presently accessible to numerical simulations is rather small. Reliable results are in fact available only for spins $|a| \lesssim 0.8$ and mass ratios $q \equiv M_2/M_1 \gtrsim 0.25$ and thus corresponding to $\nu \gtrsim 0.16$. However, it is possible to exploit *exact* results which hold in the EMRL, *i.e.*, for $\nu = 0$, to constrain the coefficients in expression (6.9). It is worth emphasizing that the EMRL results are not only exact, but also in regimes that numerical relativity simulations cannot probe. More specifically, we can exploit that in the EMRL the final spin cannot be affected by the infinitesimally small BH. In practice, this amounts to requiring that

$$a_{\rm fin}(a, \nu = 0) = a\,, \tag{4.60}$$

which constrains four of the six coefficients

$$s_0 = s_2 = s_3 = 0\,, \qquad s_1 = 1\,. \tag{4.61}$$

Additional but non-exact constraints on the coefficients can also be applied by exploiting the knowledge, near the EMRL, of the functional dependence of $a_{\rm fin}$ on the mass ratio. A convenient way of doing this is suggested by BKL, and within this approach it is possible to perform a Taylor expansion of $a_{\rm fin}$ for $\nu \ll 1$ and determine that

$$\begin{aligned} a'_{\rm fin}\big|_{(a=1,\nu=0)} &= 2(\sqrt{3}/3 - 1)\,, \quad a'_{\rm fin}\big|_{(a=0,\nu=0)} = 2\sqrt{3}\,, \\ a'_{\rm fin}\big|_{(a=-1,\nu=0)} &= 2(1 + 19\sqrt{15}/45)\,, \end{aligned} \tag{4.62}$$

where $a'_{\rm fin} \equiv \partial a_{\rm fin}/\partial \nu$. The coefficients in (6.9) are then $s_4 = \sqrt{3}(19\sqrt{5} - 75)/45$,

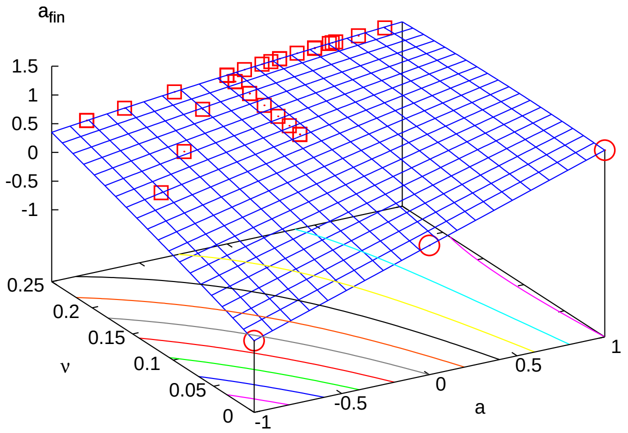

Figure 4.17: Global dependence of the final spin on the symmetric mass ratio and on the initial spins as predicted by expression (4.63). Squares refer to numerical estimates while circles to the EMRL constraints.

$t_1 = 2\sqrt{3}$, $t_0 = [\sqrt{3}(15 - 19\sqrt{5}) - 90]/45$. While this may seem a good idea, it leads to bad fits of the data. We believe this is due to two distinct reasons: *(i)* the lack of accurate numerical data for near-extreme BHs, *i.e.*, $|a| \approx 1$, and which therefore leads to incorrect estimates of the coefficients; *(ii)* expressions (4.62) are analytic but not exact and should be used with caution. There are, in fact, deviations from analyticity in ν as $\nu \rightarrow 0$, and as revealed by the presence of integer powers of $\nu^{1/5}$ during the transition between the last stable orbit and the plunge (see [199]). In the case of non-spinning binaries ($a = 0$), it is now possible to verify that the deviations are indeed very small [200], but this check is not possible for very large spins. In view of this and to make the minimal number of assumptions, we retain the analytic estimate only for the coefficient t_1, so that (6.9) has five out of ten coefficients constrained analytically

$$a_{\rm fin} = a + s_4 a^2 \nu + s_5 a \nu^2 + t_0 a \nu + 2\sqrt{3}\nu + t_2 \nu^2 + t_3 \nu^3\,. \tag{4.63}$$

Determining the remaining five coefficients from a least-square fit of the available data yields

$$\begin{aligned} s_4 &= -0.129 \pm 0.012\,, & s_5 &= -0.384 \pm 0.261\,, \\ t_0 &= -2.686 \pm 0.065\,, & t_2 &= -3.454 \pm 0.132\,, \\ t_3 &= 2.353 \pm 0.548\,, \end{aligned} \tag{4.64}$$

with surprisingly small residuals and large error-bars only for s_5. The functional behaviour of expression (4.63) and the position of the numerical data points are shown in Fig. 4.17.

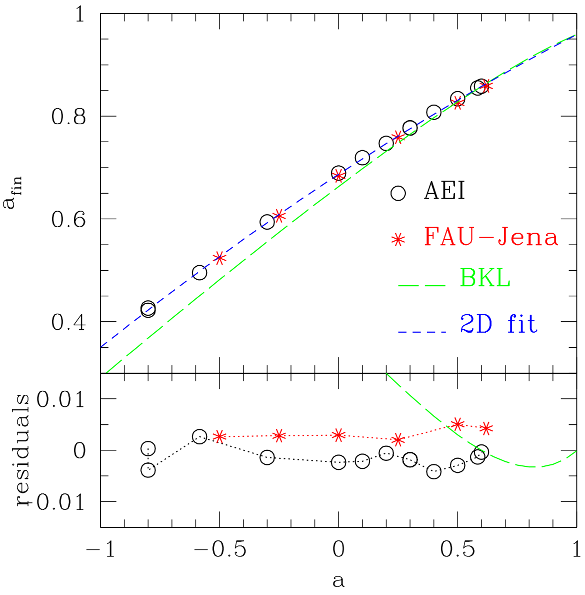

Figure 4.18: *Upper panel:* Comparison of the numerical data with the 2D fit through (4.63) in the case of equal-mass binaries, ($\nu = 1/4$). Empty circles indicate the AEI data [1], stars the FAU-Jena data [2]], a long-dashed line the BKL, and a short-dashed one the fit. *Lower panel:* residuals between the different estimates and the fit.

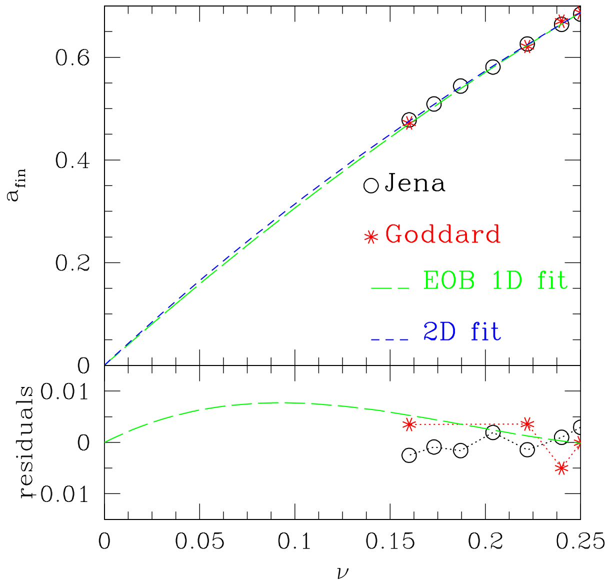

Figure 4.19: *Upper panel:* Comparison of the numerical data with the 2D fit through (4.63) in the case of nonspinning binaries. Empty circles indicate the Jena data [3], stars the Goddard data [4]], a long-dashed line the quadratic EOB fit [5] and a short-dashed line our 2D fit. *Lower panel:* residuals between the different estimates and the 2D fit.

4.3.2 Results

The estimate for the final spin in the case of equal masses and the comparison with available data and estimates is made in Fig. 4.18. The upper panel shows the numerical estimates, [circles for the AEI data [1] and stars for the FAU-Jena data [2]], the BKL estimate and our 2D fit through (4.63). The lower panel shows the residuals between the different estimates and the 2D fit; these are always of a few percent only and become larger for the BKL estimate when $a \lesssim 0$.

Despite the fact that the cubic dependence assumed in (6.9), expression (4.63) is only *quadratic* with a. When $\nu = 1/4$, it confirms what was obtained [1], indicating that, for equal-mass binaries, the next order will be four. Using (4.63) and (6.10) we estimate that the minimum and maximum final spins for an equal-mass binary are $a_{\rm fin} = 0.3502 \pm 0.03$ and $a_{\rm fin} = 0.9590 \pm 0.03$, respectively.

For nonspinning binaries, expression (4.63) is cubic in ν and a comparison with the available data and the estimate from the EOB approach combined with test-mass limit predictions for the ringdown [5] is shown in Fig. 4.25. In particular, the upper panel shows the numerical values, [empty circles for the Jena data [3] and stars for the Goddard data [4]], a long-dashed line for the quadratic EOB 1D fit [5] and a short-dashed line for our 2D fit. The residuals in are shown in the lower panel.

A physically useful condition that can be deduced from the 2D fit are the values of the initial spin and mass ratio that will lead to a final *Schwarzschild* BH [4, 151]. In practice this amounts to requiring $a_{\rm fin}(a,\nu) = 0$ in (4.63) and this curve in the $(a,\,\nu)$ plane is shown in the upper panel of Fig. 4.20. Binaries on the curve produce Schwarzschild BHs, while binaries above the curve start with a positive total angular momentum and end with a positive one; binaries below the curve, on the other hand, start with a positive total angular momentum and end with a negative one, *i.e.*, with a global *flip*. Also shown in the upper panel of Fig. 4.20 is the prediction from BKL: $a_{\rm Schw.}|_{\rm BKL} = 2\nu\sqrt{3}/(2\nu-1)$. The two estimates are very similar for all values of ν and small differences appear for $\nu \gtrsim 0.15$, where the BKL estimate is less accurate. Shown with a cross is the binary p_1 (*cf.*, Table 4.6) which yields a final BH with spin $a_{\rm fin} = 0.005$. The numerical value is between the BKL prediction and the 2D fit.

The BKL is expected to be particularly accurate for $\nu \ll 1$ and its prediction in this regime is captured very well by the 2D fit (of course the two predictions are identical for $\nu = 0$). This is shown in the lower panel of Fig. 4.20 with different curves referring to $\nu = 0.001\,, 0.01$ and 0.1; interestingly, the differences are small even for $\nu = 0.1$. It is simple to derive the value of a which will produce a final BH with the *same* spin as the initial ones. This amounts to requiring that $a_{\rm fin}(a,\nu) = a$ in (4.63) and the resulting solution is shown in Fig. 4.21; the axis $\nu = 0$ is a trivial solution and a magnification of the behaviour away from the EMRL is shown in the inset. For equal-mass binaries the critical value is $a_{\rm crit} = 0.9460$, in good agreement with the BKL estimate $a_{\rm crit} \gtrsim 0.948$ [4]. The minuteness of the region for which $a_{\rm fin} < a$ (dashed region) suggests that BHs from aligned-spins binaries are typically spun-up by mergers.

By setting $\nu = 1/4$ and $2a = a_1 + a_2$ in (4.63), we verify that the coefficients s_1–s_5 and t_0–t_3 coincide, within the error-bars, with the coefficients p_0, p_1 and p_2 reported in [1] for equal-mass, unequal-spin binaries. The fact that the fit here is equivalent to, but has been independently derived from, the one for the equal-mass, unequal-spin binaries, is an indication of its robustness. Indeed, it is possible to extend (4.63) to the whole (a_1, a_2, ν) space *i.e.*, to describe the final spin of generic aligned, unequal-spin, unequal-mass BH binaries, by replacing a with $(a_1 + a_2 q^2)/(1+q^2)$. The resulting expression reduces to (4.63) for unequal-mass, equal-spin binaries, and to the one in [1] for equal-mass, unequal-spin binaries. Our suggested extension of (4.63) to the (a_1, a_2, ν) space is the simplest one which recovers, for aligned spins, the well-tested limits of equal-mass, unequal-spins and unequal-mass, equal-spins.

The dependence of the final spin on the mass ratio in the case of extreme aligned BHs is particularly challenging to calculate and not yet investigated accurately by numerical calculations. The predictions of expression (4.63) in this limit amount to mere extrapolations and are therefore accurate to a few percent at most. As an example, when $a = 1$, the fit (4.63) is a non-monotonic function with maximum $a_{\rm fin} \simeq 1.029$ for $\nu \simeq 0.093$; this clearly is an artifact of the extrapolation.

$$\begin{aligned} a_{\rm fin}(a,\nu) = a + s_4 a^2 \nu + s_5 a \nu^2 + t_0 a \nu + \\ 2\sqrt{3}\nu + t_2 \nu^2 + t_3 \nu^3\,, \end{aligned} \tag{4.65}$$

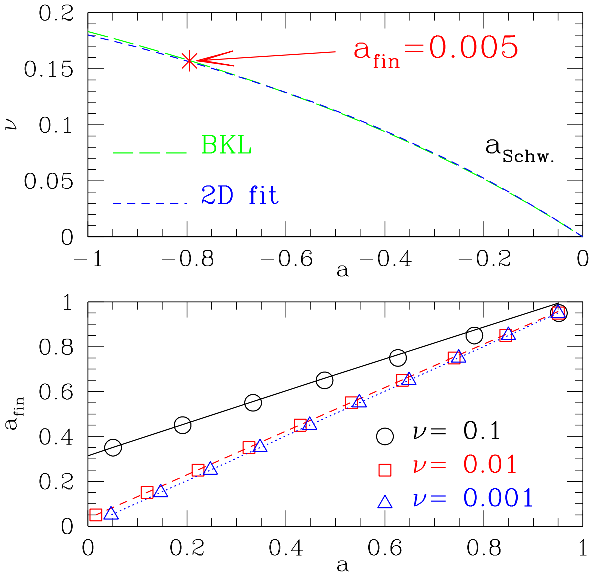

Figure 4.20: *Upper panel:* Set of initial spins and mass ratios leading to a final Schwarzschild BH: *i.e.*, $a_{\rm fin}(a, \nu) = 0$. The two curves refer to the BKL estimate (long dashed) and to the 2D fit (short dashed), respectively. Indicated with a star is a numerical example leading to $a_{\rm fin} = 0.005$. *Lower panel:* Comparison between the BKL prediction (symbols) and the 2D fit (solid, dashed and long-dashed lines) near the EMRL. Different curves refer to different values of ν and the match is complete for $\nu = 0$.

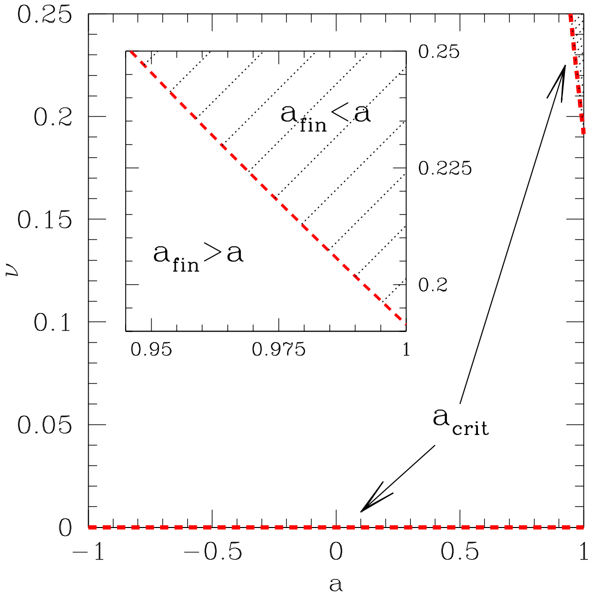

Figure 4.21: Critical values of the initial spin and mass ratio leading to a final BH having the same spin as the initial ones *i.e.*, $a_{\rm fin}(a,\nu)=a$. A magnification is shown in the inset, where the dashed/non-dashed region refers to binaries *spun-down/up* by the merger.

where ν is the symmetric mass ratio $\nu\equiv M_1M_2/(M_1+M_2)^2$. Although obtained independently in [1] and [8], expressions (4.58) and (4.65) are compatible as can be seen by considering (4.65) for equal-mass binaries ($\nu=1/4$) and verifying that the following relations hold within the computed error-bars

$$p_0=\frac{\sqrt{3}}{2}+\frac{t_2}{16}+\frac{t_3}{64}\,,\qquad p_1=\frac{1}{2}+\frac{s_5}{32}+\frac{t_0}{8}\,,\qquad p_2=\frac{s_4}{16}. \tag{4.66}$$

As long as the initial spins are aligned (or antialigned) with the orbital angular momentum, expression (4.65) can be extended to *unequal-spin, unequal-mass* binaries through the substitution

$$a\ \longrightarrow\ \tilde{a}\equiv\frac{a_1+a_2q^2}{1+q^2}\,. \tag{4.67}$$

To obtain this result, it is sufficient to consider (4.58) and (4.65) as polynomial expressions of the generic quantity

$$\tilde{a}\equiv a_{\rm tot}\frac{(1+q)^2}{1+q^2}\,. \tag{4.68}$$

where $a_{\rm tot}\equiv(a_1+a_2q^2)/(1+q)^2$ is the total dimensionless spin for generic aligned binaries. In this way, expressions (4.58) and (4.65) are naturally compatible, since $\tilde{a}=(a_1+a_2)/2$ for equal-mass unequal-spin binaries, and $\tilde{a}=a$ for unequal-mass equal-spin binaries. Furthermore, the extreme mass-ratio limit (EMRL) of expression (4.65) with the substitution (4.67) yields the expected result: $a_{\rm fin}(a_1, a_2, \nu = 0) = a_1$.

As already commented above, the predictions of expressions (4.65) and (4.67) cover 3 of the 7 dimensions of the space of parameters; we next show how to to cover the remaining 4 dimensions and derive an analytic expression for the magnitude of the dimensionless spin vector $|\boldsymbol{a}_{\rm fin}|$ of the BH produced by the coalescence of two generic BHs in terms of the mass ratio q and of the initial dimensionless spin vectors $\boldsymbol{a}_{1,2}$. To make the problem tractable analytically, 4 assumptions are needed. While some of these are very natural, others can be relaxed if additional accuracy in the estimate of $|\boldsymbol{a}_{\rm fin}|$ is necessary. Removing any of these assumptions inevitably complicates the picture, introducing additional dimensions, such as the initial separation in the binary or the radiated mass, in the space of parameters.

As a result, in the simplest description the required assumptions are as follows:

(i) The mass radiated to gravitational waves $M_{\rm rad}$ can be neglected i.e., $M_{\rm fin} = M \equiv M_1 + M_2$. We note that $M_{\rm rad}/M = 1 - M_{\rm fin}/M \approx 5 - 7 \times 10^{-2}$ for most of the binaries evolved numerically. The same assumption was applied in the analyses of [1, 8], as well as in [4]. Relaxing this assumption would introduce a dependence on $M_{\rm fin}$ which can only be measured through a numerical simulation.

(ii) At a sufficiently large but finite initial separation the final spin vector $\boldsymbol{S}_{\rm fin}$ can be well approximated as the sum of the two initial spin vectors and of a third vector $\tilde{\boldsymbol{\ell}}$

$$\boldsymbol{S}_{\rm fin} = \boldsymbol{S}_1 + \boldsymbol{S}_2 + \tilde{\boldsymbol{\ell}}\,, \tag{4.69}$$

Differently from refs. [151] and [4], where a definition similar to (4.69) was also introduced, here we will constrain $\tilde{\boldsymbol{\ell}}$ by exploiting the results of numerical-relativity calculations rather than by relating it to the orbital angular momentum of a test particle at the innermost stable circular orbit (ISCO). When viewed as expressing the conservation of the total angular momentum, eq. (4.69) also defines the vector $\tilde{\boldsymbol{\ell}}$ as the difference between the orbital angular momentum when the binary is widely separated $\boldsymbol{L}$, and the angular momentum radiated until the merger $\boldsymbol{J}_{\rm rad}$, *i.e.*, $\tilde{\boldsymbol{\ell}} = \boldsymbol{L} - \boldsymbol{J}_{\rm rad}$.

(iii) The vector $\tilde{\boldsymbol{\ell}}$ is parallel to $\boldsymbol{L}$. This assumption is correct when $\boldsymbol{S}_1 = -\boldsymbol{S}_2$ and $q = 1$ [this can be seen from the post-Newtonian (PN) equations at 2.5 order], or by equatorial symmetry when the spins are aligned with $\boldsymbol{L}$ or when $\boldsymbol{S}_1 = \boldsymbol{S}_2 = 0$ (also these cases can be seen from the PN equations). For more general configurations one expects that $\tilde{\boldsymbol{\ell}}$ will also have a component orthogonal to $\boldsymbol{L}$ as a result, for instance, of spin-orbit or spin-spin couplings, which will produce in general a precession of $\tilde{\boldsymbol{\ell}}$. In practice, the component of $\tilde{\boldsymbol{\ell}}$ orthogonal to $\boldsymbol{L}$ will correspond to the angular momentum $\boldsymbol{J}^{\perp}_{\rm rad}$ radiated in a plane orthogonal to $\boldsymbol{L}$, with a resulting error in the estimate of $|\tilde{\boldsymbol{\ell}}|$ which is $\sim |\boldsymbol{J}^{\perp}_{\rm rad}|^2/|\tilde{\boldsymbol{\ell}}|^2 \sim |\boldsymbol{J}^{\perp}_{\rm rad}|^2/(2\sqrt{3}M_1M_2)^2$. Measuring $\boldsymbol{J}^{\perp}_{\rm rad}$ via numerical-relativity simulations, or estimating it via high-order PN equations, is an obvious way to improve our approach. A similar assumption was also made in ref. [4]. It is astrophysically reasonable, , however, given that spins should tend to align during early inspiral [201–203].

(iv) When the initial spin vectors are equal and opposite ($\boldsymbol{S}_1 = -\boldsymbol{S}_2$) and the masses are equal ($q = 1$), the spin of the final BH is the same as for the nonspinning binaries.

Stated differently, equal-mass binaries with equal and opposite-spins behave as nonspinning binaries, at least when it comes down to the properties of the final black hole. While this result cannot be derived from first principles, it reflects the expectation that if the spins are the same and opposite, their contributions to the final spin cancel exactly for equal-mass binaries. Besides being physically reasonable, this expectation is met by all of the simulations performed to date, both for spins aligned with $\boldsymbol{L}$ [1, 8] and orthogonal to $\boldsymbol{L}$ [153]. In addition, this expectation is met by the easily leading-order contributions to the spin-orbit and spin-spin point-particle Hamiltonians and spin-induced radiation flux [152, 204]. A similar assumption is also made, although not explicitly, in ref. [4] which, for $\boldsymbol{S}_{\rm tot} = 0$, predicts $\iota = 0$ and $|\boldsymbol{a}_{\rm fin}| = L_{\rm orb}(\iota = 0, |\boldsymbol{a}_{\rm fin}|)/M =$const. [*cf.* eqs. (12)–(13) in ref. [4]].

Using these assumptions we can now derive the analytic expression for the final spin. We start by expressing the vector relation (4.69) as

$$\boldsymbol{a}_{\rm fin} = \frac{1}{(1+q)^2}\left(\boldsymbol{a}_1 + \boldsymbol{a}_2 q^2 + \boldsymbol{\ell} q\right) , \tag{4.70}$$

where $\boldsymbol{a}_{\rm fin} = \boldsymbol{S}_{\rm fin}/M^2$ [*cf.* assumption *(i)*], $\boldsymbol{\ell} \equiv \tilde{\boldsymbol{\ell}}/(M_1 M_2)$, $\boldsymbol{a}_{1,2} \equiv \boldsymbol{S}_{1,2}/M_{1,2}^2$, and its norm is then given by

$$\begin{aligned}|\boldsymbol{a}_{\rm fin}| = \frac{1}{(1+q)^2}\Big[&|\boldsymbol{a}_1|^2 + |\boldsymbol{a}_2|^2 q^4 + 2|\boldsymbol{a}_2||\boldsymbol{a}_1| q^2 \cos\alpha + \\ &2\left(|\boldsymbol{a}_1|\cos\beta + |\boldsymbol{a}_2| q^2 \cos\gamma\right)|\boldsymbol{\ell}| q + |\boldsymbol{\ell}|^2 q^2\Big]^{1/2} ,\end{aligned} \tag{4.71}$$

where the three (cosine) angles α, β and γ are defined by

$$\cos\alpha \equiv \hat{\boldsymbol{a}}_1 \cdot \hat{\boldsymbol{a}}_2 , \quad \cos\beta \equiv \hat{\boldsymbol{a}}_1 \cdot \hat{\boldsymbol{\ell}} , \quad \cos\gamma \equiv \hat{\boldsymbol{a}}_2 \cdot \hat{\boldsymbol{\ell}} . \tag{4.72}$$

Because $\boldsymbol{a}_{1,2} \parallel \boldsymbol{S}_{1,2}$ and $\boldsymbol{\ell} \parallel \boldsymbol{L}$ [*cf.* assumption *(iii)*], the angles α, β and γ are also those between the initial spin vectors and the initial orbital angular momentum, so that it is possible to replace $\hat{\boldsymbol{a}}_{1,2}$ with $\hat{\boldsymbol{S}}_{1,2}$ and $\hat{\boldsymbol{\ell}}$ with $\hat{\boldsymbol{L}}$ in (4.72). α, β and γ are well-defined if the initial separation of the two BHs is sufficiently large [*cf.* assumption *(ii)*] and that the error introduced by assumption *(iii)* in the measure of $\cos\alpha, \cos\beta$ and $\cos\gamma$ is also of the order of $|\boldsymbol{J}^{\perp}_{\rm rad}|/|\tilde{\boldsymbol{\ell}}|$.

The angle $\theta_{\rm fin}$ between the final spin vector and the initial orbital angular momentum can be calculated from $|\boldsymbol{a}_{\rm fin}|$. Because of assumption *(iii)*, the component of the final spin in the direction of $\boldsymbol{L}$ is [*cf.* eq. (4.70)]

$$a^{\parallel}_{\rm fin} \equiv \boldsymbol{a}_{\rm fin} \cdot \hat{\boldsymbol{\ell}} = \frac{|\boldsymbol{a}_1|\cos\beta + |\boldsymbol{a}_2| q^2 \cos\gamma + |\boldsymbol{\ell}| q}{(1+q)^2} , \tag{4.73}$$

so that $\cos\theta_{\rm fin} = a^{\parallel}_{\rm fin}/|\boldsymbol{a}_{\rm fin}|$, and the component orthogonal to the initial orbital angular momentum is $a^{\perp}_{\rm fin} = |\boldsymbol{a}_{\rm fin}|\sin\theta_{\rm fin}$.

In essence, therefore, our approach consists of considering the dimensionless spin vector of the final BH as the sum of the two initial spins and of a third vector parallel to the initial orbital angular momentum when the binaries are widely separated. Implicit in the assumptions made, and in the logic of mapping an initial-state of the binary into a final one, is the expectation that the length of this vector is an intrinsic “property” of the binary, depending on the initial spin vectors and mass ratio, but not on the initial separation. This is a consequence of assumption *(ii)*: because the vector $\tilde{\boldsymbol{\ell}}$ measures the orbital angular momentum that cannot be radiated, it can be thought of as the angular momentum of the binary at the “effective” ISCO and, as such, it cannot be dependent on the initial separation.

A consequence of our assumptions is that $\boldsymbol{a}_{\rm fin}$ for a BH-binary is already fully determined by the set of coefficients s_4, s_5, t_0, t_2, t_3 computed to derive expression (4.65). The latter, in fact, is simply the final spin for a special set of values for the cosine angles; since the fitting coefficients are constant, they must hold also for generic binaries.

In view of this, all that is needed is to measure $|\boldsymbol{\ell}|$ in terms of the fitting coefficients computed in refs. [1,8]. This can be done by matching expression (4.73) with (4.65) [with the condition (4.67)] for parallel and aligned spins ($\alpha = \beta = \gamma = 0$), for parallel and antialigned spins ($\alpha = 0$, $\beta = \gamma = \pi$), and for antiparallel spins which are aligned or antialigned ($\alpha = \beta = \pi$, $\gamma = 0$ or $\alpha = \gamma = \pi$, $\beta = 0$). This matching is not unique, but the degeneracy can be broken by exploiting assumption *(iv)* and by requiring that $|\boldsymbol{\ell}|$ depends linearly on $\cos\alpha$, $\cos\beta$ and $\cos\gamma$. We therefore obtain

$$\begin{aligned}|\boldsymbol{\ell}| = {} & \frac{s_4}{(1+q^2)^2}\left(|\boldsymbol{a}_1|^2 + |\boldsymbol{a}_2|^2 q^4 + 2|\boldsymbol{a}_1||\boldsymbol{a}_2| q^2 \cos\alpha\right) + \\ & \left(\frac{s_5\nu + t_0 + 2}{1+q^2}\right)\left(|\boldsymbol{a}_1|\cos\beta + |\boldsymbol{a}_2| q^2 \cos\gamma\right) + \\ & 2\sqrt{3} + t_2\nu + t_3\nu^2\,. \end{aligned} \tag{4.74}$$

We now consider some limits of expressions (4.71) and (4.74). First of all, when $q \to 0$, (4.71) and (4.74) yield the correct EMRL, *i.e.*, $|\boldsymbol{a}_{\rm fin}| = |\boldsymbol{a}_1|$. Secondly, for equal-mass binaries having spins that are equal and antiparallel, (4.71) and (4.74) reduce to

$$|\boldsymbol{a}_{\rm fin}| = \frac{|\boldsymbol{\ell}|}{4} = \frac{\sqrt{3}}{2} + \frac{t_2}{16} + \frac{t_3}{64} = p_0 \simeq 0.688\,. \tag{4.75}$$

This result allows us to qualify more precisely a comment made before: because for equal-mass BHs which are either nonspinning or have equal and opposite spins, the vector $|\boldsymbol{\ell}|$ does not depend on the initial spins, expression (4.75) states that $|\boldsymbol{\ell}| M_{\rm fin}^2/4 = |\boldsymbol{\ell}| M^2/4 = |\boldsymbol{\ell}| M_1 M_2$ is, for such systems, the orbital angular momentum at the effective ISCO. We can take this a step further and conjecture that $|\boldsymbol{\ell}| M_1 M_2 = |\tilde{\boldsymbol{\ell}}|$ is the series expansion of the dimensionless orbital angular momentum at the ISCO also for *unequal-mass* binaries which are either nonspinning or with equal and opposite spins. The zeroth-order term of this series (namely, the term $2\sqrt{3} M_1 M_2$) is exactly the one predicted from the EMRL.

Finally, we consider the case of equal, parallel and aligned/antialigned spins ($|\boldsymbol{a}_2| =$

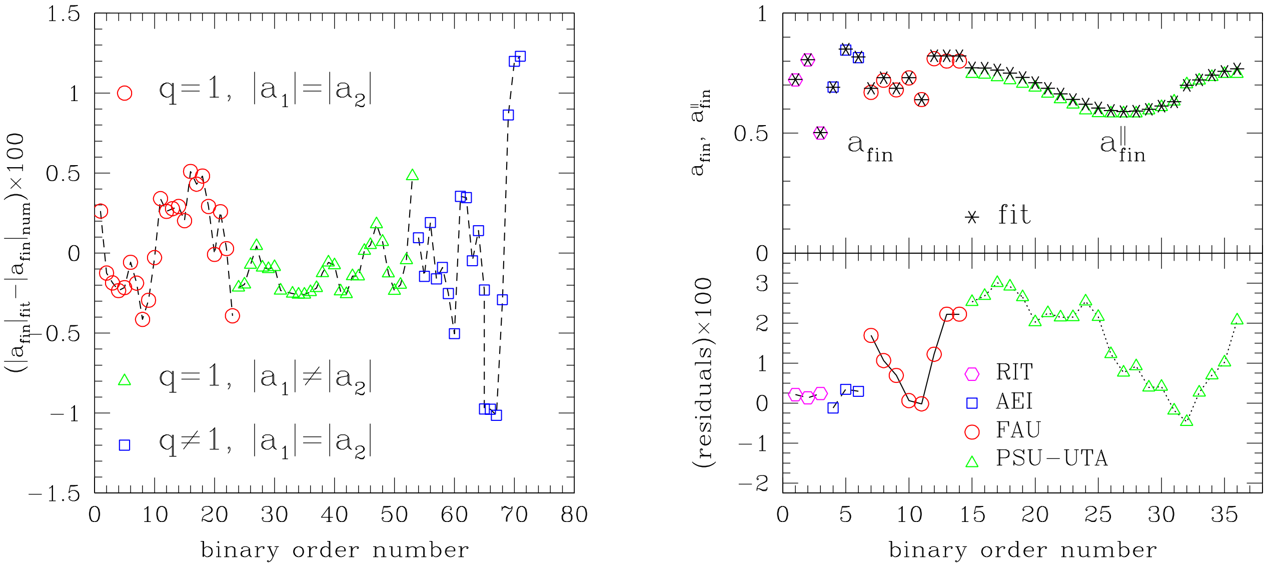

Figure 4.22: *Left panel:* Rescaled residual for aligned binaries. The circles refer to equal-mass, equal-spin binaries presented in refs. [1–3, 6–8], triangles to equal-mass, unequal-spin binaries presented in ref. [1, 6], and squares to unequal-mass, equal-spin binaries presented in refs. [3, 6–8]. Here and in the right panel the "binary order number" is just a dummy index labelling the different configurations. *Right panel:* The top part reports the final spin computed for misaligned binaries. Hexagons refer to data from [9] (labelled "RIT"), squares to the data Table 4.7 (labelled "AEI"), circles to data from [10] (labelled "FAU"), and triangles to data from [11] (labelled "PSU-UTA"). Note that these latter data points refer to the aligned component $a^{\parallel}_{\rm fin}$ since this is the only component available from ref. [11]. The bottom part of this panel shows instead the rescaled residuals for these misaligned binaries.

a_1^x	a_1^y	a_1^z	a_2^x	a_2^y	a_2^z	ν	$\lvert\boldsymbol{a}_{\rm fin}\rvert$	$\theta_{\rm fin}(^\circ)$
0.151	0.000	-0.563	0.000	0.000	0.583	0.250	0.692	2.29
0.151	0.000	0.564	0.000	0.151	0.564	0.250	0.846	3.97
0.413	0.000	0.413	0.000	0.413	0.413	0.250	0.815	7.86

Table 4.7: Initial parameters of the new misaligned AEI binaries.

$|\boldsymbol{a}_1|$, $\alpha = 0$, $\beta = \gamma = 0,\ \pi$), for which expressions (4.73) and (4.74) become

$$\begin{aligned} a_{\rm fin} \;=\; & |\boldsymbol{a}_1| \cos\beta \left[1 + \nu(s_4|\boldsymbol{a}_1|\cos\beta + t_0 + s_5\nu)\right] + \\ & \nu(2\sqrt{3} + t_2\nu + t_3\nu^2)\,, \end{aligned} \tag{4.76}$$

where $\cos\beta = \pm 1$ for aligned/antialigned spins. As expected, expression (4.76) coincides with (4.65) when $|\boldsymbol{a}_1|\cos\beta = a$ and with (4.58) [through the coefficients (4.66)] when $q = 1$ and $2|\boldsymbol{a}_1|\cos\beta = a_1 + a_2$. Similarly, (4.73) and (4.74) reduce to (4.65) for equal, antiparallel and aligned/antialigned spins ($|\boldsymbol{a}_2| = |\boldsymbol{a}_1|$, $\alpha = 0$, $\beta = 0, \gamma = \pi$, or $\beta = \pi, \gamma = 0$).

The only way to assess the validity of expressions (4.71) and (4.74) is to compare their predictions with the numerical-relativity data. This is done in Figs. 4.22 and 4.23, which collect all of the published data, together with the three additional binaries computed with the `CCATIE` code [87] and reported in Table 4.7. In these plots, the "binary order number" is just a dummy index labelling the different configurations. The left panel of Fig. 4.22, in particular, shows the rescaled residual, *i.e.*, $(|\boldsymbol{a}_{\rm fin}|_{\rm fit} - |\boldsymbol{a}_{\rm fin}|_{\rm num.}) \times 100$, for aligned binaries. The plot shows the numerical-relativity data with circles referring to equal-mass, equal-spin binaries from refs. [1–3, 6–8], triangles to equal-mass, unequal-spin binaries from refs. [1, 6], and squares to unequal-mass, equal-spin binaries from refs. [3, 6–8]. Although the data is from simulations with different truncation errors, the residuals are all very small and with a scatter of $\sim 1\%$.

A more stringent test is shown in the right panel of Fig. 4.22, which refers to misaligned binaries. In the top part, hexagons indicate the numerical values for $|\boldsymbol{a}_{\rm fin}|$ from ref. [9], squares the ones in Table 4.7, circles those from ref. [10] and triangles those from ref. [11]; note that these latter data points refer to the aligned component $a_{\rm fin}^{\|}$ since this is the only component available from ref. [11]. The agreement is again very good, with errors of a couple of percent (see bottom part of the same panel), even if the binaries are generic and for some the initial and final spins differ by almost 180° [9].

Finally, Fig. 4.23 reports the angle between the final spin vector and the initial orbital angular momentum $\theta_{\rm fin}$ using the same data (and convention for the symbols) as in the right panel of Fig. 4.22. Measuring the final angle accurately is not trivial, particularly due to the fact that the numerical evolutions start at a finite separation which does not account for earlier evolution. The values reported in [9] (and the relative error-bars) are shown with hexagons, while the squares refer to the binaries in Table 4.7, and have been computed using a new approach for the calculation of the Ricci scalar on the AH [205]. Shown with asterisks and circles are instead the values predicted for the data from [10,11] by our analytic fit (asterisks) and by the point-particle approach suggested in ref. [4] (circles).

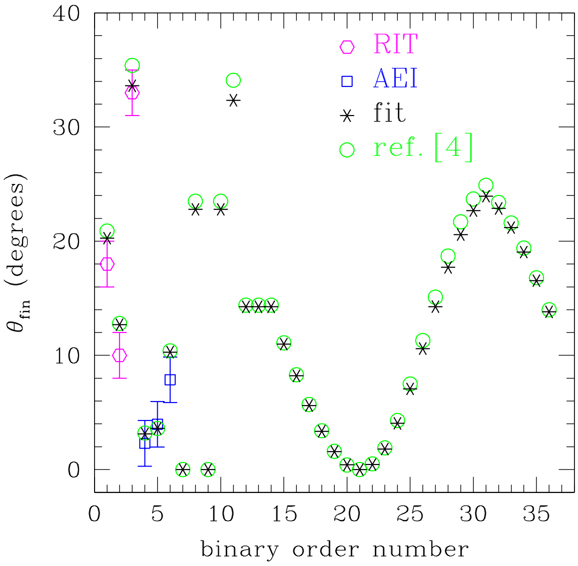

Figure 4.23: Using the same data (and convention for the symbols) as in the right panel of Fig. 4.22, we here report the angle between the final spin vector and the initial orbital angular momentum $\theta_{\rm fin}$. Shown instead with asterisks and circles are the values predicted for the data from refs [10, 11] by our analytic fit (asterisks) and by the point-particle approach suggested in ref. [4] (circles).

Clearly, when a comparison with numerical data is possible, the estimates of the fit are in reasonable agreement and with the smallest residuals. However, for two of the three binaries from [9] the estimates are slightly outside the error-bars. Note that the reported angles are relative to the orbital plane at a small initial binary-separation, and thus are likely to be underestimates as they do not take into account the evolution from asymptotic distances; work is in progress to clarify this. When the comparison with the numerical data is not possible because $\theta_{\rm fin}$ is not reported (as for the data in ref. [11]), our approach and the one in ref. [4] yield very similar estimates.

4.3.3 Discussion

We have considered the spin vector of the BH produced by a BH binary merger as the sum of the two initial spins and of a third vector, parallel to the initial orbital angular momentum, whose norm depends only on the initial spin vectors and mass ratio, and measures the orbital angular momentum not radiated. Without other fits than those already available to model aligned/antialigned binaries, we have measured the unknown vector and derived a formula that accounts therefore for all of the 7 parameters describing a BH binary inspiralling in quasi-circular orbits. The equations (4.71) and (4.74), encapsulate the near-zone physics to provide a convenient, as well as robust and accurate prediction over a wide range of parameters, determination of the merger product of rather generic BH binaries.

Testing the formula against all of the available numerical data from recent publications and from our own simulations has revealed differences between the predicted and the simulated values of a few percent at most. This approach is intrinsically approximate and it has been validated on a small set of configurations. It can be improved: by reducing the χ^2 of the fitting coefficients as new simulations are carried out; by using fitting functions that are of higher-order than those in expressions (4.58) and (4.65); by estimating $\boldsymbol{J}^{\perp}_{\rm rad}$ through PN expressions or by measuring it via numerical simulations.

Overall, the data sample computed numerically consists of 38 values for $|v_{\rm kick}|$ and for $a_{\rm fin}$ which, for simplicity, we have considered to have constant error-bars of $8\ {\rm km/s}$ and 0.01, which represent, respectively, the largest errors reported in [87]. In both cases we have modelled the data with generic quadratic functions in a_1 and a_2 so that, in the case of the recoil velocity, the fitting function is

$$|v_{\rm kick}| = |c_0 + c_1 a_1 + c_2 a_1^2 + d_0 a_1 a_2 + d_1 a_2 + d_2 a_2^2|\,. \tag{4.77}$$

The fitting function on the right-hand-side of (6.1) is smooth everywhere but that its absolute value is not smooth along the diagonal $a_1 = a_2$. Using (6.1) and a blind least-square fit of the data, we obtained the coefficients (in ${\rm km/s}$)

$$\begin{aligned} c_0 &= 0.67 \pm 1.12\,, & d_0 &= -18.56 \pm 5.34\,, \\ c_1 &= -212.85 \pm 2.96\,, & d_1 &= 213.69 \pm 3.57\,, \\ c_2 &= 50.85 \pm 3.48\,, & d_2 &= -40.99 \pm 4.25\,, \end{aligned} \tag{4.78}$$

with a reduced-$\chi^2 = 0.09$. Clearly, the errors in the coefficients can be extremely large and this is simply the result of small-number statistics. However, the fit can be improved by exploiting some knowledge about the physics of the process to simplify the fitting expressions. In particular, we can use the constraint that no recoil velocity should be produced for binaries having the same spin, *i.e.*, that $|v_{\rm kick}| = 0$ for $a_1 = a_2$, or the symmetry condition across the line $a_1 = a_2$. Enforcing both constraints yields

$$c_0 = 0\,, \quad c_1 = -d_1\,, \quad c_2 = -d_2\,, \quad d_0 = 0\,, \tag{4.79}$$

thus reducing the fitting function (6.1) to the simpler expression

$$|v_{\rm kick}| = |c_1(a_1 - a_2) + c_2(a_1^2 - a_2^2)|\,. \tag{4.80}$$

Performing a least-square fit using (6.3) we then obtain

$$c_1 = -220.97 \pm 0.78\,, \qquad c_2 = 45.52 \pm 2.99\,, \tag{4.81}$$

with a comparable reduced-$\chi^2 = 0.14$, but with error-bars that are much smaller on average. Because of this, we consider expression (6.3) as the best description of the data at second-order in the spin parameters. Using (6.3) and (6.4), we have built the contour plots shown in Fig. 4.24.

A few remarks are worth making. Firstly, we recall that post-Newtonian calculations have so far derived only the linear contribution in the spin to the recoil velocity (see [148] and references therein). However, the size of the quadratic coefficient (6.4) is not small when compared to the linear one and it can lead to rather sizeable correc-

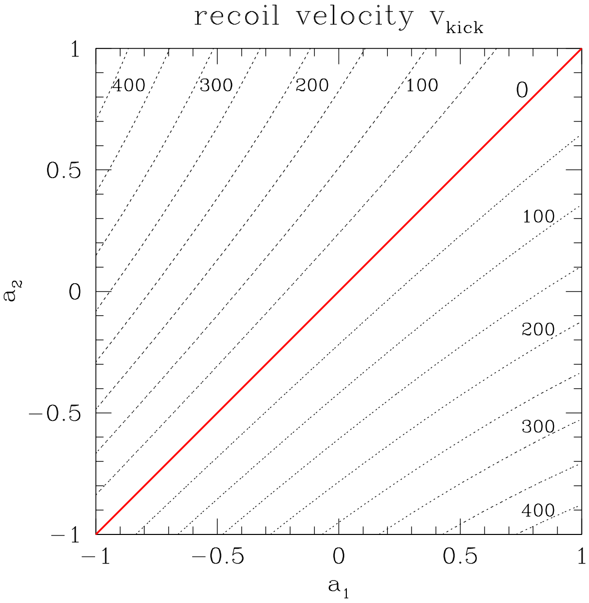

Figure 4.24: Contour plots of $|v_{\rm kick}|$ as a function of the spin parameters a_1 and a_2. The diagram has been computed using expressions (6.3) and (6.4).

tions. These are maximized when $a_1 = 0$ and $a_2 = \pm 1$, or when $a_1 = \pm 1$ and $a_2 = 0$, and can be as large as $\sim 20\%$; while these corrections are smaller than those induced by asymmetries in the mass, they are instructive in pointing out the relative importance of spin-spin and spin-orbit effects during the merger and can be used as a guide in further refinements of the post-Newtonian treatments. Secondly, expression (6.3) clearly suggests that the maximum recoil velocity should be found when the asymmetry is the largest and the spins are antiparallel, *i.e.*, $a_1 = -a_2$. Thirdly, when $a_2 = {\rm const.}$, expression (6.3) confirms the quadratic scaling proposed in [87] with a smaller data set [*cf.*, eq. (42) there]. Fourthly, for $a_1 = -a_2$, expression (6.3) is only linear and reproduces the scaling suggested by [157]. Finally, using (6.3) the maximum recoil velocity is found to be $|v_{\rm kick}| = 441.94 \pm 1.56\ {\rm km/s}$, in very good agreement with the results of [157] and [87].

In the same way we have first fitted the data for $a_{\rm fin}$, with a function

$$a_{\rm fin} = p_0 + p_1 a_1 + p_2 a_1^2 + q_0 a_1 a_2 + q_1 a_2 + q_2 a_2^2\,, \tag{4.82}$$

and found coefficients with very large error-bars. As a result, also for $a_{\rm fin}$ we resort to physical considerations to constrain the coefficients $p_0 \ldots q_2$. More specifically, at least at lowest order, binaries with equal and opposite spins will not contribute to the final spin and thus behave essentially as nonspinning binaries. Stated differently, we assume that $a_{\rm fin} = p_0$ for binaries with $a_1 = -a_2$. In addition, enforcing the symmetry condition across the line $a_1 = a_2$ we obtain

$$p_1 = q_1\,, \quad p_2 = q_2 = q_0/2\,, \tag{4.83}$$

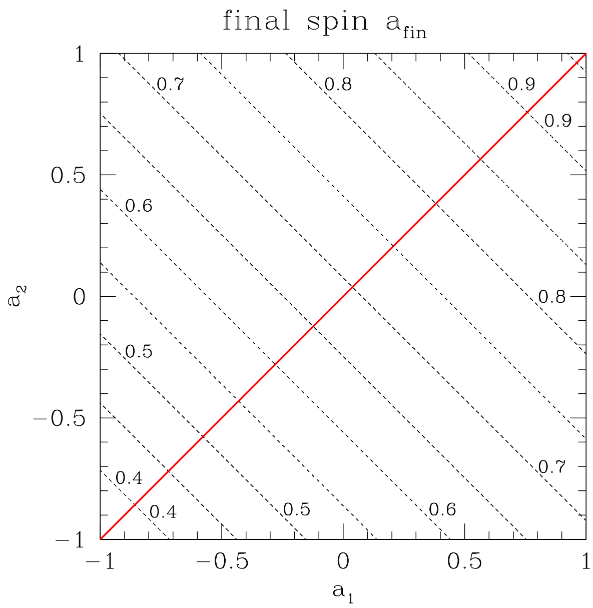

Figure 4.25: Contour plots of $a_{\rm fin}$ as a function of the spin parameters a_1 and a_2. The diagram has been computed using expressions (6.7) and (6.8).

so that the fitting function (6.5) effectively reduces to

$$a_{\rm fin} = p_0 + p_1(a_1 + a_2) + p_2(a_1 + a_2)^2 \,. \tag{4.84}$$

Performing a least-square fit using (6.7) we then obtain

$$\begin{aligned} p_0 &= 0.6883 \pm 0.0003\,, \qquad p_1 = 0.1530 \pm 0.0004\,, \\ p_2 &= -0.0088 \pm 0.0005\,, \end{aligned} \tag{4.85}$$

with a reduced-$\chi^2 = 0.02$.

It should be noted that the coefficient of the quadratic term in (6.8) is much smaller then the linear one and with much larger error-bars. Given the small statistics it is hard to assess whether a quadratic dependence is necessary or if a linear one is the correct one (however, see also the comment below on a possible interpretation of expression (6.7)). In view of this, we have repeated the least-square fit of the data enforcing the conditions (6.6) together with $p_2 = 0$ (*i.e.*, adopting a linear fitting function) and obtained $p_0 = 0.6855 \pm 0.0007$ and $p_1 = 0.1518 \pm 0.0012$, with a worse reduced-$\chi^2 = 0.16$. Because the coefficients of the lowest-order terms are so similar, both the linear and the quadratic fits are well within the error-bars of the numerical simulations. Nevertheless, since a quadratic scaling yields smaller residuals, we consider it to be the best representation of the data and have therefore computed the contour plots in Fig. 4.25 using (6.7) and (6.8).

Here too, a few remarks are worth making: Firstly, the fitted value for the coefficient p_0 agrees very well with the values reported by several groups [3, 139] when studying the inspiral of unequal-mass nonspinning binaries. Secondly, expression (6.7) has maximum values for $a_1 = a_2$, suggesting that the maximum and minimum spins are $a_{\rm fin} = 0.9591 \pm 0.0022$ and $a_{\rm fin} = 0.3471 \pm 0.0224$, respectively. Thirdly, the quadratic scaling for $a_{\rm fin}$ substantially confirms the suggestions of [134] but provides more accurate coefficients. Expression (6.8) lends itself to an interesting interpretation. Being effectively a power series in terms of the initial spins of the two black holes, its zeroth-order term can be seen as the orbital angular momentum not radiated in gravitational waves and which amounts, at most, to $\sim 70\%$ of the final spin. The first-order term, on the other hand, can be seen as the contribution to the final spin coming from the initial spins of the two black holes and this contribution, together with the one coming from the spin-orbit coupling, amounts at most to $\sim 30\%$ of the final spin. Finally, the second-order term, which is natural to expect as nonzero in this view, can then be related to the spin-spin coupling, with a contribution to the final spin which is of $\sim 4\%$ at most.

The monotonic behaviour expressed by (6.8) does not show the presence of a local maximum of $a_{\rm fin} \simeq 0.87$ for $a_1 = a_2 \sim 0.34$ as suggested by [198] in the effective one-body (EOB) approximation. Because the latter has been shown to be in good agreement with numerical-relativity simulations of nonspinning black holes [5, 206], additional simulations will be necessary to refute these results or to improve the EOB approximation for spinning black holes.

Reported in the right part of Table 4.2 are also the fitted values for $a_{\rm fin}$ and $|v_{\rm kick}|$ obtained through the fitting functions (6.3) and (6.7), and the corresponding errors. The latter are of few percent for most of the cases and increase up to $\sim 20\%$ only for those binaries with very small kicks and which are intrinsically more difficult to calculate. As a concluding remark we note that the fitting coefficients computed here have been constructed using overall moderate values of the initial spin; the only exception is the binary $u4$ which has the largest spin and which is nevertheless fitted with very small errors (*cf.* Table 4.2). In addition, since the submission of this work, another group has reported results from equal-mass binaries with spins as high as $a_1 = a_2 = \pm 0.9$ [2]. Although also for these very high-spin binaries the error in the predicted values is of 1% at most, a larger sample of high-spin binaries is necessary to validate that the fitting expressions (6.3) and (6.7) are robust also at very large spins.

We further performed simulations with an unequal masses and aligned spins (see Table 4.6) and obtained a third order polynomial fit for $|a_{\rm fin}|$ from arbitrary symmetric mass ratio $\nu \equiv M_1 M_2/(M_1+M_2)^2$ and the aligned equal spins of the initial BHs $a \equiv J/M^2$, *i.e.*, $a_{\rm fin} \equiv J_{\rm fin}/M_{\rm fin}^2 = a_{\rm fin}(a,\, \nu)$

$$\begin{aligned} a_{\rm fin} = \quad & s_0 + s_1 a + s_2 a^2 + s_3 a^3 + s_4 a^2 \nu + s_5 a \nu^2 + \\ & t_0 a \nu + t_1 \nu + t_2 \nu^2 + t_3 \nu^3 \,. \end{aligned} \tag{4.86}$$

as shown in figure 4.17. Determining the remaining five coefficients from a least-square fit of the available data yielded

$$\begin{aligned} s_4 &= -0.129 \pm 0.012\,, \qquad & s_5 &= -0.384 \pm 0.261\,, \\ t_0 &= -2.686 \pm 0.065\,, \qquad & t_2 &= -3.454 \pm 0.132\,, \\ t_3 &= 2.353 \pm 0.548\,, \end{aligned} \tag{4.87}$$

we then ran simulations for misaligned spins (see table 4.7) and obtained a fit for arbitrary initial spins and mass ratio $q \equiv M_1/M_2$

$$\begin{aligned}|\boldsymbol{a}_{\text{fin}}| = {} & \frac{1}{(1+q)^2}\Big[|\boldsymbol{a}_1|^2 + |\boldsymbol{a}_2|^2 q^4 + 2|\boldsymbol{a}_2||\boldsymbol{a}_1|q^2\cos\alpha + \\ & 2\left(|\boldsymbol{a}_1|\cos\beta + |\boldsymbol{a}_2|q^2\cos\gamma\right)|\boldsymbol{\ell}|q + |\boldsymbol{\ell}|^2 q^2\Big]^{1/2}\,,\end{aligned} \tag{4.88}$$

where

$$\begin{aligned}|\boldsymbol{\ell}| = {} & \frac{s_4}{(1+q^2)^2}\left(|\boldsymbol{a}_1|^2 + |\boldsymbol{a}_2|^2 q^4 + 2|\boldsymbol{a}_1||\boldsymbol{a}_2|q^2\cos\alpha\right) + \\ & \left(\frac{s_5\nu + t_0 + 2}{1+q^2}\right)\left(|\boldsymbol{a}_1|\cos\beta + |\boldsymbol{a}_2|q^2\cos\gamma\right) + \\ & 2\sqrt{3} + t_2\nu + t_3\nu^2\,.\end{aligned} \tag{4.89}$$

These formulae give fairly accurate predictions for the final spin and kick of a merged black hole and will be useful for studies of the evolution of supermassive black holes and on statistical studies on the dynamics of compact objects in dense stellar systems, as well as significant effect on the waveform and impact on parameter estimation for gravitational wave detectors.

Chapter 5

Gravitational Wave Detector Data Analysis

Binary black-hole systems with spins aligned or anti-aligned to the orbital angular momentum, and which therefore do not exhibit precession effects, provide the natural ground to start detailed studies of the influence of strong-field spin effects on gravitational wave observations of coalescing binaries. Furthermore, such systems may be the preferred end-state of the inspiral of generic supermassive binary black-hole systems [201–203]. In view of this, we have computed the inspiral and merger of a large set of binary systems of equal-mass black holes with spins parallel to the orbital angular momentum but otherwise arbitrary (see Table 4.2). Attention is particularly focused on the gravitational-wave emission so as to quantify how much spin effects contribute to the signal-to-noise ratio (SNR), to the horizon distances, and to the relative event rates for representative ranges in masses and detectors, as well as for the formulation of a generic phenomenological waveform for aligned spin binary black hole inspiral configurations for detector pipeline templates. As expected, the SNR increases with the projection of the total black hole spin in the direction of the orbital momentum. We find that equal-spin binaries with maximum spin aligned with the orbital angular momentum are more than "three times as loud" as the corresponding binaries with anti-aligned spins, thus corresponding to event rates up to 27 times larger. We also consider the waveform mismatch between the different spinning configurations and find that, within our numerical accuracy, binaries with opposite spins $\boldsymbol{S}_1 = -\boldsymbol{S}_2$ cannot be distinguished whereas binaries with spin $\boldsymbol{S}_1 = \boldsymbol{S}_2$ have clearly distinct gravitational-wave emissions. We derive a simple expression for the energy radiated in gravitational waves and find that the binaries always have efficiencies $E_{\mathrm{rad}}/M \gtrsim 3.6\%$, which can become as large as $E_{\mathrm{rad}}/M \simeq 10\%$ for maximally spinning binaries with spins aligned with the orbital angular momentum.

Finally, in Section [5.2] I show the derivation of an analytical inspiral-merger-ringdown gravitational waveforms from the black-hole binaries with non-precessing spins presented in Table 4.2. By matching a post-Newtonian description of the inspiral to a set of numerical calculations performed in full general relativity, I obtain a waveform family with a conveniently small number of physical parameters. These waveforms will allow us to detect a larger parameter space of BH binary coalescence, to explore various scientific questions related to GW astronomy, and could dramatically improve the expected detection rates of GW detectors as I will show in the next section.

The work presented in this chapter is presented in the papers [207, 208] and was done in collaboration with Ajith Parameshwaran, Christian Reisswig, Mark Hannam, Sascha Husa, Yanbei Chen, Bernd Brügmann, Nils Dorband, Doreen Müller,Frank Ohme, Denis Pollney, Lucia Santamaría, and Luciano Rezzolla.

5.1 Detectability

It has been a long-standing goal of the field of numerical relativity to provide results for gravitational-wave data analysis in order to enhance the capabilities of current and future gravitational wave detectors, especially regarding the observation of compact binary coalescence. With a series of breakthroughs in 2005 [19, 20, 132], this long-term goal has become reality. However, further work is required to actually understand the practical implications of numerical solutions of the full Einstein equations for gravitational-wave data analysis. Some early studies suggest that template banks that use numerical information can increase the reach of detectors [14, 15, 209], aid the calibration of search pipelines [210–212], and improve the estimation of parameters, such as *e.g.,* sky location [213].

Here I present the use of gravitational waveforms from numerical-relativity (NR) calculations for a number of sequences of equal-mass spinning black hole binaries whose spins are aligned or anti-aligned with the orbital angular momentum as shown in Table 5.1, and consider the detectability of these binaries for the ground-based gravitational wave-detectors as well as for the planned space-based LISA interferometer.

Interest in this type of binary stems from the fact that there are strong physical indications they represent preferred configurations in nature, at least if the black holes are supermassive. It has been shown, in fact, that when the binary is surrounded by a massive circumbinary disc, as the one expected by the merger of two galaxies, the dissipative dynamics of the matter produces a torque with the effect of aligning the spins to the orbital angular momentum [203]. In addition, the merger of binaries with aligned spins yields recoil velocities which are sufficiently small (*i.e.,* $\lesssim 450\,\mathrm{km/s}$ [11, 155, 157]) to prevent the final black hole from being expelled from the host galaxy. This would then be compatible with the overwhelming astronomical evidence that massive black holes reside at the centers of most galaxies.

The parameter space is therefore 2-dimensional (rather than 6 dimensional) parametrized by the projections a_1, a_2 of the dimensionless spins $\boldsymbol{a}_i \equiv \boldsymbol{S}_i/M_i^2$ of the individual black holes on to direction of the angular momentum (chosen as the z-axis). As a result, spins that are aligned with the orbital angular momentum are characterized by positive values of a_1, a_2, while anti-aligned spins have negative values. Previous studies of this parameter space [1, 8, 87, 154, 155, 214], have considered the recoil velocity and final spin of the merger remnant, and have constructed phenomenological formulas for these quantities given the initial spins a_1 and a_2 of the binary.

The focus of this Section is on the detectability of a given set of binaries in the parameter sub-space of (anti-) aligned spins, *i.e.,* for each of these binaries and across a set of different masses we calculate the signal-to-noise ratio (SNR) for the LIGO [215, 216], enhanced LIGO (eLIGO) [217], advanced LIGO (AdLIGO) [14, 218], Virgo [219], advanced Virgo (AdVirgo) [220], and LISA [221, 222] detectors.

In this way I attempt to address the following questions:

> *(i)* Which among the aligned-spin configurations is the "loudest" and which one is the "quietest"?
>
> *(ii)* How large is the difference in signal-to-noise ratio between the loudest and the quietest?
>
> *(iii)* How do these considerations depend on the detector used, the mass of the binary, and the number of harmonics?
>
> *(iv)* Are there configurations whose waveforms are difficult to distinguish and are hence degenerate in the space of templates?

Overall, I find that equal-spinning, maximally anti-aligned binaries generally produce the lowest SNR while equal-spinning, maximally aligned binaries (the orbital 'hang-up' case) produce the highest SNR. For any mass, the SNR can be described with a low-order polynomial of the initial spins $\rho = \rho(a_1, a_2)$ and generally it increases with the total dimensionless spin along the angular momentum direction, $a \equiv \frac{1}{2}(\boldsymbol{a}_1 + \boldsymbol{a}_2) \cdot \hat{\boldsymbol{L}}$. The possibility of describing the whole behaviour of the waveforms from equal-mass, aligned/antialigned binaries in terms of a single scalar quantity, namely a, provides a certain amount of optimism that also more complex spin configurations can, ultimately, be described in terms of only a few parameters.

I show the impact that higher-order contributions in the waveforms with $\ell \leq 4$ have on the maximum SNR and show that for low masses $M \in [20, 100]$ they contribute, say for the LIGO detector, $\approx 2.5\%$, whereas for intermediate masses $M > 100\ M_{\odot}$ they contribute $\approx 8\%$. I calculate the mismatch between the waveforms from different binaries across our spin-diagram and find that binaries along the diagonal $a_1 = -a_2$ (the u sequence) cannot be distinguished within our given numerical accuracy, whereas configurations along the diagonal $a_1 = a_2$ (the s sequence) are clearly different (*cf.* Fig 5.7 and 5.8, as well as Table 5.4). Finally, I show the derivation of a simple expression for the energy radiated in gravitational waves and find that this is bounded between $\simeq 3.6\%$ and $\simeq 10\%$ for maximally spinning binaries with spins anti-aligned or aligned with the orbital angular momentum, respectively.

The plan of this section is as follows: in Section [5.1.1], I recall very briefly the numerical set up and illustrate the properties of the initial data used in the simulations. Section [5.1.2] is dedicated to the discussion of the gravitational-wave observables used for the subsequent analysis, while Section [5.1.6] presents the results in terms of the SNR and how this is influenced by higher-order modes. This Section also contains a discussion of the match between the waveforms from different binaries and an assessment of the accuracy of our results. Section [5.1.10], provides a brief discussion of the analytic expressions we have found representing either the SNR or the energy radiated in gravitational waves. Finally, conclusions are summarized in Section [5.1.12].

Table 5.1: Binary sequences for which numerical simulations have been carried out, with various columns referring to the puncture initial location $\pm x/M$, the mass parameters m_i/M, the dimensionless spins a_i, and the normalized ADM mass $\widetilde{M}_{\rm ADM} \equiv M_{\rm ADM}/M$ measured at infinity. Finally, the last four columns contain the numerical values of the energy radiated during the simulation using the two methods described in the text and the corresponding errors between them, as well as the error to the fitted values.

	$\pm x/M$	m_1/M	m_2/M	a_1	a_2	$(p_x,\ p_y)_1 = -(p_x,\ p_y)_2$	$\widetilde{M}_{\rm ADM}$	$E^{\rm NR}_{\rm rad}$	$E^{Q^{\times,+}}_{\rm rad}$	err. (%)	fit err. (%)
r_0	4.0000	0.3997	0.3998	-0.600	0.600	$(0.002103, -0.112457)$	0.9880	0.0366	0.0356	2.8	1.6
r_2	4.0000	0.3997	0.4645	-0.300	0.600	$(0.002024, -0.111106)$	0.9878	0.0407	0.0394	3.3	0.6
r_4	4.0000	0.3998	0.4825	0.000	0.600	$(0.001958,\ \ 0.001958)$	0.9876	0.0459	0.0445	3.1	1.9
r_6	4.0000	0.3999	0.4645	0.300	0.600	$(0.001901, -0.108648)$	0.9876	0.0523	0.0504	3.8	2.2
s_{-8}	5.0000	0.3000	0.3000	-0.800	-0.800	$(0.001300, -0.101736)$	0.9894	0.0240	0.0231	3.8	3.0
s_0	4.0000	0.4824	0.4824	0.000	0.000	$(0.002088, -0.112349)$	0.9877	0.0360	0.0354	1.7	0.2
s_2	4.0000	0.4746	0.4746	0.200	0.200	$(0.001994, -0.110624)$	0.9877	0.0421	0.0410	2.7	1.7
s_4	4.0000	0.4494	0.4494	0.400	0.400	$(0.001917, -0.109022)$	0.9876	0.0499	0.0480	4.0	2.5
s_6	4.0000	0.4000	0.4000	0.600	0.600	$(0.001860, -0.107537)$	0.9876	0.0609	0.0590	3.2	0.2
s_8	4.0000	0.4000	0.4000	0.800	0.800	$(0.001816, -0.106162)$	0.9877	0.0740	0.0744	0.5	2.2
t_0	4.0000	0.3995	0.3995	-0.600	-0.600	$(-0.002595,\ 0.118379)$	0.9886	0.0249	0.0243	2.5	1.1
t_1	4.0000	0.3996	0.4641	-0.600	-0.300	$(-0.002431,\ 0.116748)$	0.9883	0.0271	0.0264	2.7	1.8
t_2	4.0000	0.3997	0.4822	-0.600	0.000	$(-0.002298,\ 0.115219)$	0.9881	0.0295	0.0289	2.1	2.2
t_3	4.0000	0.3998	0.4642	-0.600	0.300	$(-0.002189,\ 0.113790)$	0.9880	0.0326	0.0317	2.8	1.8
u_2	4.0000	0.4745	0.4745	-0.200	0.200	$(\ 0.002090, -0.112361)$	0.9878	0.0361	0.0354	2.0	0.2
u_4	4.0000	0.4492	0.4494	-0.400	0.400	$(\ 0.002095, -0.112398)$	0.9879	0.0363	0.0355	2.3	0.7
u_8	4.0000	0.2999	0.2999	-0.800	0.800	$(\ 0.002114, -0.112539)$	0.9883	0.0374	0.0363	3.0	3.7

5.1.1 Numerical Setup and Initial Data

The numerical simulations have been carried out using the `CCATIE` code, a three-dimensional finite-differencing code using the `Cactus` Computational Toolkit [91] and the `Carpet` [93] adaptive mesh-refinement driver. The code implements the "moving-punctures" technique to represent dynamical black holes following [20, 59] (see Section [2.4.4]).

In the results presented below we have used 9 levels of mesh refinement with a fine-grid resolution of $\Delta x/M = 0.02$ and fourth-order finite differencing. The wave-zone grid has a resolution of $\Delta x/M = 0.128$ and extends from $r = 24\,M$ to $r = 180\,M$, in which our wave extraction is carried out. The outer (coarsest) grid extends to a spatial position which is $819.2\,M$ in each coordinate direction. Note that, because these are higher resolution and longer numerical inspiral than the sequences presented in Table 4.2 we have much higher accuracy and more overlap with the post-Newtonian curves. Because the black holes spins are all directed along the z-axis of our Cartesian grids, it is possible to use a reflection symmetry condition across the $z = 0$ plane as described in Section [2.6.5].

The initial data are constructed applying the "puncture" method [49, 51, 223, 224] as described in Section [2.4.4]. We have considered four different sequences labelled as "*r*", "*s*," "*t*", and "*u*" along straight lines in the (a_1, a_2) parameter space, also referred to as the "spin diagram". As shown in Fig. 5.1, these sequences cover the most important portions of the space of parameters, which, is symmetric with respect to the $a_1 = a_2$ diagonal.

Similar sequences have also been considered in [1, 8, 87, 154, 155] but have here been recalculated both using a higher resolution and with improved initial orbital parameters. Post-Newtonian (PN) evolutions following the scheme outlined in [88], which provides a straightforward prescription for initial-data parameters with small initial eccentricity, and which can be interpreted as part of the process of matching our numerical calculations to the inspiral described by the PN approximations were used. The free parameters to be chosen for the puncture initial data are therefore: the puncture coordinate locations $\boldsymbol{C}_i$, the puncture bare mass parameters m_i, the linear momenta $\boldsymbol{p}_i$, and the individual spins $\boldsymbol{S}_i$. The initial parameters for all of the binaries considered are collected in the left part of Table 5.1. The initial separations are fixed at $D = 8\,M$, where M is the total initial black hole mass, chosen as $M = 1$ (note that the initial ADM mass of the spacetime is not exactly 1 due to the binding energy of the black holes), while the individual asymptotic initial black hole masses are therefore $M_i = 1/2$. The only exception is for the binary s_{-8}, for which $D = 10\,M$, because the plunge happens too quickly to fit in a comparable waveform for a comparable number of wave cycles.

5.1.2 NR waveforms

The analysis carried hereafter will be made in terms of gauge-invariant metric perturbations on a Schwarzschild background, rather than via the Newman-Penrose curvature scalar Ψ_4 (both methods are described in Section [2.6.3]. While the two prescriptions

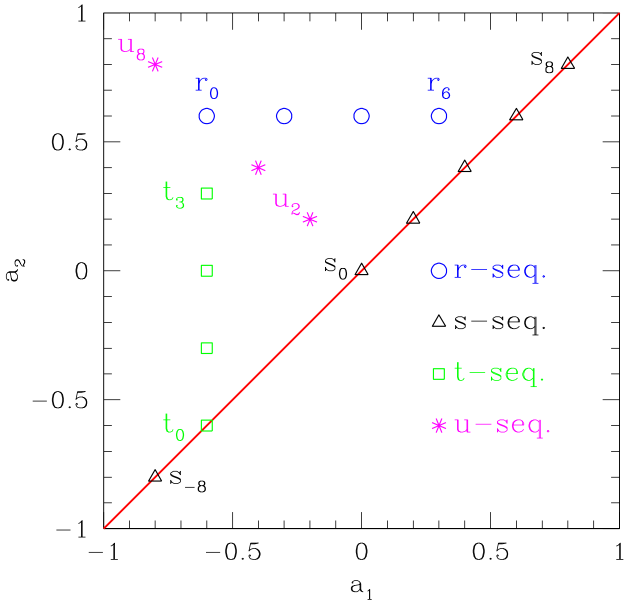

Figure 5.1: Schematic representation in the $(a_1,\ a_2)$ plane, also referred to as the "spin diagram", of the initial data collected in Table 5.1. These sequences cover most important portions of the space of parameters which is symmetric with respect to the $a_1 = a_2$ diagonal.

yield estimates that are in very good agreement with each other and with differences below 2%, we have found that the results obtained using gauge-invariant quantities have a smaller numerical error, and are thus preferable.

More specifically, we compute the gravitational-wave amplitudes $h^{+}_{\ell m}$ and $h^{\times}_{\ell m}$ in terms of the even and odd master functions $Q^{+}_{\ell m}$ and $Q^{\times}_{\ell m}$ via the relations [182]

$$h_{\ell m}(t) = h^{+}_{\ell m}(t) - \mathrm{i} h^{\times}_{\ell m}(t) = Q^{+}_{\ell m}(t) - \mathrm{i} \int_{-\infty}^{t} dt' Q^{\times}_{\ell m}(t') \, , \tag{5.1}$$

where the gauge-invariant perturbations are typically extracted at a radius of $r_{\rm E} = 160M$ (see Section [5.1.9] for a discussion of the accuracy of our measurements).

As mentioned before, all our binaries [but s_{-8}] have initial separations of $D = 8.0M$ [$D = 10.0M$], which, in the parameter space that we have considered, leads to a maximum initial frequency of the numerical waveforms, that is $\omega_{\rm ini} = 0.084/M$. Depending therefore on the mass M, such an initial frequency can be greater than the lower cut-off frequency of the detector for a given source at an arbitrary distance. Because for most masses, a "real" waveform will be "longer" than the one computed here, we need to account for the missing frequency band between the lower cut-off and the initial frequency of the wave. This can be accomplished by attaching to the NR wave the PN part of the wave and will be discussed in the next Section.

The values of the initial frequencies and of the associated minimum masses $M_{\rm min}$ for each of the detectors considered are reported in Table 5.2.

5.1.3 Matching PN and NR waveform amplitudes

The existence of a cut-off mass set by the initial frequency of the NR simulations would clearly restrict the validity of our considerations to large masses only. To counter this and thus include also binaries with smaller masses, we account for the early inspiral phase by describing it via PN approximations. To produce the PN waveforms, and the PN energy that we are using directly in Section [5.1.11], we have used the spinning TaylorT1 approximant used in Hannam et al. [225], and which is based on the PN expressions described in [172, 226–232]. The choice of TaylorT1 is motivated by that fact, that in [225] it is found to be more robust in the spinning case than the TaylorT4 approximant, which was previously found to yield excellent results in the nonspinning case [233] (see [233] for a comparison of different techniques to obtain the gravitational-wave phase information for quasi-circular inspiral). These waveforms are 3.5 PN accurate in the nonspinning phase, and 2.5 PN accurate in the spin-dependent terms entering the phasing. The gravitational-wave amplitudes, on the other hand, have been computed according to ref. [234] to the highest PN order that is currently known for each of the spherical harmonic modes we use.

A phase-coherent construction of hybrid PN-NR waveforms is rather delicate, and has not yet been achieved for the higher spherical harmonic modes we use here. However, for the present purpose of computing the SNR and the radiated energies, such a construction in the time domain is not necessary and all of the relevant work can be done more simply

Table 5.2: Initial instantaneous frequencies $M\omega_{\mathrm{ini}}$ and associated minimum masses M_{min} of the NR waveforms for the different models and for each detector according to the corresponding lower cut-off frequency (*i.e.,* at 30 Hz for Virgo, at 40 Hz for eLIGO, at 10 Hz for AdLIGO/AdVirgo, and at 10^{-4} Hz for LISA). All the values for the masses are in units of solar masses.

	$M\omega_{\mathrm{ini}}$	M_{min} Virgo	M_{min} eLIGO	M_{min} AdLIGO/AdVirgo	M_{min} LISA
r_0	0.080	86.2	64.6	258.5	2.58×10^7
r_2	0.078	84.0	63.0	252.0	2.52×10^7
r_4	0.077	82.9	62.2	248.8	2.49×10^7
r_6	0.076	81.8	61.4	245.5	2.46×10^7
s_{-8}	0.060	64.6	48.4	193.8	1.93×10^7
s_0	0.080	86.2	64.6	258.5	2.58×10^7
s_2	0.078	84.0	63.0	252.0	2.52×10^7
s_4	0.076	81.8	61.4	245.5	2.46×10^7
s_6	0.075	80.8	60.6	242.3	2.42×10^7
s_8	0.073	78.6	59.0	235.8	2.36×10^7
t_0	0.084	90.5	67.8	271.4	2.71×10^7
t_1	0.083	89.4	67.0	268.2	2.68×10^7
t_2	0.082	88.3	66.2	264.9	2.65×10^7
t_3	0.081	87.2	65.4	261.7	2.62×10^7
u_2	0.080	86.2	64.6	258.5	2.58×10^7
u_4	0.080	86.2	64.6	258.5	2.58×10^7
u_8	0.080	86.2	64.6	258.5	2.58×10^7

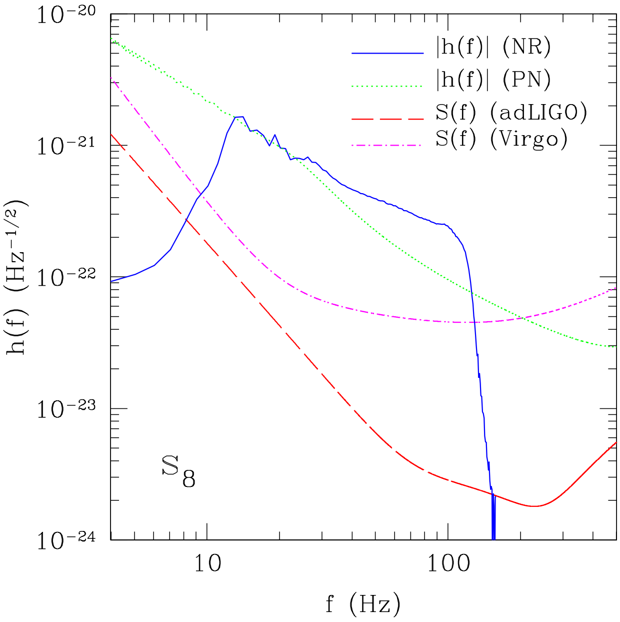

Figure 5.2: Noise strain for the Advanced LIGO and Virgo detectors and the Fourier-transformed amplitude of the PN and NR waveform at $\theta = 0, \phi = 0$ for a total mass $M = 200\,M_{\odot}$ at a distance $d = 100\,\mathrm{Mpc}$ for the maximally spinning model s_8. The glueing frequency is at $f_{\rm glue} = 27.14$ Hz.

in the frequency domain. In practice, we Fourier transform the PN and NR waveforms and "glue" them together at a suitable "glueing" frequency $\omega_{\rm glue}$. Since the SNR depends only on the amplitude of the waveform, [eq. (5.5)], it is not necessary to match the PN-waveform in the phase. This simplifies the process of waveform matching and basically reduces to a simple check of the amplitude matching to address the error of the mismatch. Without any parameter adjustment, the PN-waveform amplitudes match well with the inspiral part of the NR-waveforms, and result in an error which is usually $\approx 1.5\%$ and in the worst case $\approx 4.0\%$ for the binary configuration t_0. It is important to pay attention in the time-domain analysis in order to limit the noise artifacts in the Fourier-transformed amplitudes, is the use of a windowing function (*e.g.*, a hyperbolic tangent) to smoothly blend the waveform to zero before the initial burst of spurious radiation, as well as after the ringdown, in order to limit spurious oscillations in the Fourier-transformed waveform. A representative example is shown in Fig. 5.2, where the noise strain for the Virgo and Advanced LIGO detectors is reported, together with the Fourier-transformed amplitude of the PN and NR waveform for the maximally spinning model s_8. The waveform is assumed to be observed at $\theta = 0, \phi = 0$ for a total mass $M = 200\,M_{\odot}$ and from a distance $d = 100\,\mathrm{Mpc}$. The glueing frequency in this case is at $f_{\rm glue} = \omega_{\rm glue}/(2\pi) = 27.14$ Hz.

Since each ℓ, m mode of the gravitational-wave field will have a different initial frequency, we need to make sure that they are all properly taken into account when determining the glueing frequency, so that

$$\omega_{\rm glue} \geq \max_{\ell,m}(\omega_{\rm ini})_{\ell m} \,. \tag{5.2}$$

In practice, the initial frequency of our highest mode, $\ell = 4, m = 4$, has an initial frequency $(\omega_{\rm ini})_{44} = 2(\omega_{\rm ini})_{22}$. As a result, we select the glueing frequency according to the binary configuration with the largest initial frequency, the binary t_0, and take $\omega_{\rm glue} = 2(\omega_{\rm ini})_{22} = 0.168/M$. We also measure how sensitive this choice is, by considering how the results are affected when choosing instead $\omega_{\rm glue} \pm \Delta\omega$, with $\Delta\omega \ll \omega_{\rm glue}$. For $\Delta\omega = 0.01/M$ we find a maximal difference in the computed SNR of $\sim 2.0\%$ over all configurations and all masses. Such a difference affects equally the maximum and averaged SNRs (see Section [5.1.5] for a discussion on these two different measures of the SNR). A change of $\Delta\omega$ in $\omega_{\rm glue}$ affects only marginally the relative difference between SNRs computed by including modes up to $\ell = 2$ and $\ell = 4$, and in this case the differences are $\sim 2.0\%$. Overall, the uncertainties introduced by the choice of $\omega_{\rm glue}$ are much smaller than the typical error at which we report the SNRs.

5.1.4 Radiated Energy

Since the total energy must be conserved, we can use the radiated energy as an important tool to verify the accuracy of the gravitational-wave amplitude and thus the overall precision of our calculations. More specifically, because it is straightforward to determine the initial and the final total mass, it is also straightforward to compare the difference in the two with the radiated energy. In practice, we compute the initial mass of the system as $M_{\rm ini} = \widetilde{M}_{\rm ADM}$, while the final mass of the merger remnant $M_{\rm fin}$ is deduced from the properties of the apparent horizon within the isolated-horizon formalism as discussed in Section [2.6.2]. The radiated energy is then given by the difference

$$E^{\rm NR}_{\rm rad} = M_{\rm ADM} - M_{\rm fin} \,, \tag{5.3}$$

and should be equal to the energy that has been radiated through gravitational waves during the simulation [182]

$$E^{Q^{\times,+}}_{\rm rad} = \frac{1}{32\pi}\sum_{\ell,m}\int_0^t dt' \left(\left| \frac{dQ^{+}_{\ell m}}{dt} \right|^2 + \left| Q^{\times}_{\ell m} \right|^2 \right) \,. \tag{5.4}$$

For all binaries the difference between $E_{\rm rad}$ and $E^{Q^{\times,+}}_{\rm rad}$ is between $\sim 0.5\%$ and $\sim 4.0\%$ and a detailed comparison of the numerical values is reported in Table 5.1. In Section [5.1.11] I will discuss an analytic fit to the computed data that provides a measure of the amount of mass radiated during the inspiral, merger and ringdown as a function of the initial spins.

5.1.5 SNR, Horizon Distances and Event Rates

Following ref. [235], we define the SNR, ρ, for matched-filtering searches as

$$\rho^2 \equiv \left(\frac{S}{N}\right)^2_{\text{matched}} = 4\int_0^\infty \frac{|\tilde{h}(f)|^2}{S_h(f)}df \tag{5.5}$$

where $\tilde{h}(f)$ is the Fourier transform of the time domain gravitational-wave signal $h(t)$, defined in the continuum as

$$\tilde{h}(f) = \int_{-\infty}^{\infty} h(t)e^{-2\pi i f t}dt\,, \tag{5.6}$$

and $S_h(f)$ is the noise power spectral density for a given detector. Hereafter we will consider the $S_h(f)$ for the ground-based detectors LIGO, enhanced LIGO, advanced LIGO and Virgo, as well as the space-bound LISA interferometer. The associated noise power spectral densities are reported in Appendix A.8.

Since the SNR (5.5) depends on the angle from the source to the detector, it is useful to introduce the angle-averaged SNR $\langle\rho^2\rangle$, which can be computed after decomposing the gravitational-wave signal in terms of spherical harmonic modes. Using the orthonormality of the spin-weighted spherical harmonic basis ${}_sY_{\ell m}$, the *"angle-averaged"* SNR

$$\rho_{\text{avg}} \equiv \langle\rho^2\rangle \equiv \frac{1}{\pi}\int d\Omega \int df \frac{\left|\sum_{\ell m}\tilde{h}_{\ell m}(f)\,{}_{-2}Y_{\ell m}(\Omega)\right|^2}{S_h(f)}\,, \tag{5.7}$$

can be written as a sum of integrals of the absolute squares of the Fourier-transformed modes $\tilde{h}_{\ell m}(f)$

$$\rho_{\text{avg}} = \frac{1}{\pi}\sum_{\ell m}\int df \frac{|\tilde{h}_{\ell m}(f)|^2}{S_h(f)}\,. \tag{5.8}$$

For each binary, distance and mass, we have calculated both the *"maximum"* SNR ρ_{max} for an optimally oriented detector, *i.e.*, the SNR for a detector oriented such that it measures only the $+$ polarization of the gravitational-wave signal, and the averaged SNR. Here the mass is always meant to be the *redshifted* total mass, $(1+z)M_{\text{source}}$, where z is the redshift and M_{source} is the mass at the source. For sources at small distances, *i.e.*, less than $100\,\text{Mpc}$, then $z \lesssim 0.024$ and hence $M \simeq M_{\text{source}}$ to within a few percent. Identical results would have been obtained if we had considered the $\times$ polarization.

If the gravitational-wave signal is modeled through the dominant $\ell = 2 = m$ mode only (or in our case via a superposition $\ell = 2 = \pm m$), the maximum SNR can be deduced from the average SNR after exploiting the properties of the spin-weighted spherical harmonic ${}_{-2}Y_{22}$ and ${}_{-2}Y_{2-2}$, namely

$$\rho_{\text{max}} = \sqrt{5\rho^2_{\text{avg}}(\ell=2, m=2)} \tag{5.9}$$

$$= \sqrt{\frac{5}{2}\rho^2_{\text{avg}}(\ell=2, m=\pm 2)}\,, \tag{5.10}$$

but such a relation is no longer true when including modes with $\ell > 2$. The relation between the maximum and the averaged value of the SNR can only be determined numerically.

When computing the SNR, a reference distance needs to be fixed. In this case, I set the reference distance to be $d_\rho = 100\,\mathrm{Mpc}$. The results of the SNR at d_ρ across the spin diagram can then be recast in terms of an *"horizon distance"*, namely the distance at which a given binary system with redshifted mass M has an SNR equal to a threshold for detectability and which we chose to be $\rho = 8$, as customary for ground-based detectors. The horizon distance is then simply defined as

$$d_H = d_\rho \left(\frac{\rho(d = d_\rho)}{8} \right) \mathrm{Mpc}\,. \tag{5.11}$$

The quantity d_H is equivalent to the SNR but has the advantage to provide, at least for detectors not operating at large SNRs, a estimate of the increase in the relative event rate R as

$$R \sim \left(\frac{d_H}{d_{H,a=-1}} \right)^3 , \tag{5.12}$$

where $d_{H,a=-1}$ is the horizon distance of the configuration with lowest SNR, belonging to the extrapolated case $a = -1$. Expression (5.12) is valid as an equality only for small horizon distances, namely those for which the redshift is negligible. At large redshifts the observed masses would differ considerably from the masses at the source. In other words, at large redshifts the horizon distances would be different not only because of the spin, but also because the masses at the sources would be intrinsically different. This impacts the deduced event rate as defined in (5.12), which considers only the contributions coming from the spin. Hence, for large redshifts the event rate R defined here serves only as a lower limit for masses larger than the optimal one and as an upper bound for masses smaller than the optimal.

As a concrete example, let us assume that we have calculated the horizon distance for a binary with $a = -1$ which, as can be deduced from Fig. 5.4, will lead to the smallest SNR for a given detector. We also assume that this binary has a mass which is smaller than the optimal one. Let us now consider a binary with the same mass at the detector but with $a > -1$; this binary will clearly lead to a larger SNR but because the masses at the detector are the same, the mass of the binary with $a > -1$ will be (because of the redshift) smaller at the source. As a result, its horizon distance will be overestimated, and hence the event rate coming from (5.12) only an upper bound. A similar argument for masses larger than the optimal one would instead lead to the conclusion that the event rate R is only a lower bound.

5.1.6 Results

The results of the analysis discussed above are summarized in Fig. 5.3, which shows the averaged and maximum horizon distance $d_H = d_H(a, M)$ for some of the detectors considered. As mentioned above, the horizon distance has been computed at a reference SNR $\rho = 8.0$, and is parametrized in terms of the total mass of the system (in solar

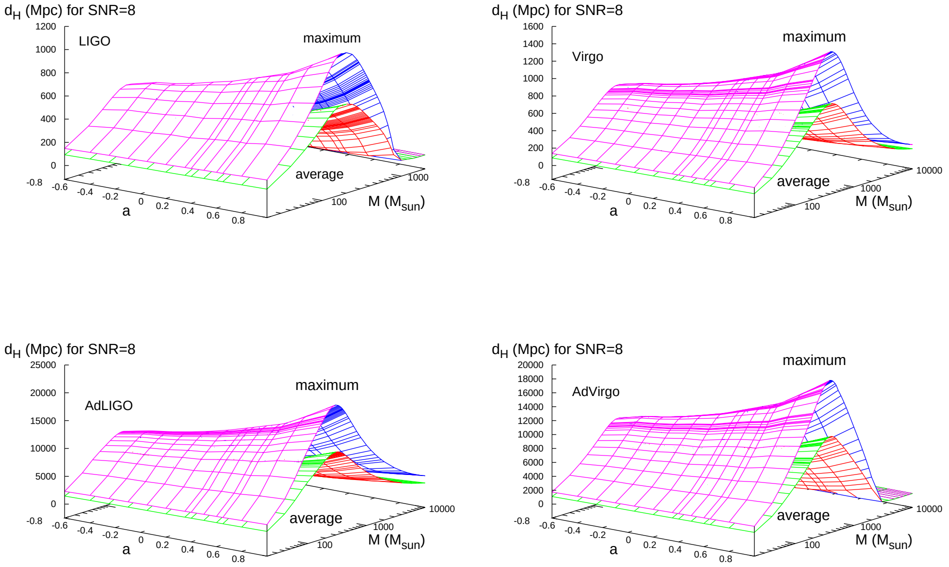

Figure 5.3: Averaged and maximum horizon distance $d_H = d_H(a, M)$ for the LIGO detector (top left panel), for the Virgo detector (top right panel), and for the advanced versions of both detectors (bottom left and right panels, respectively). The horizon distance has been computed at a reference SNR $\rho = 8.0$.

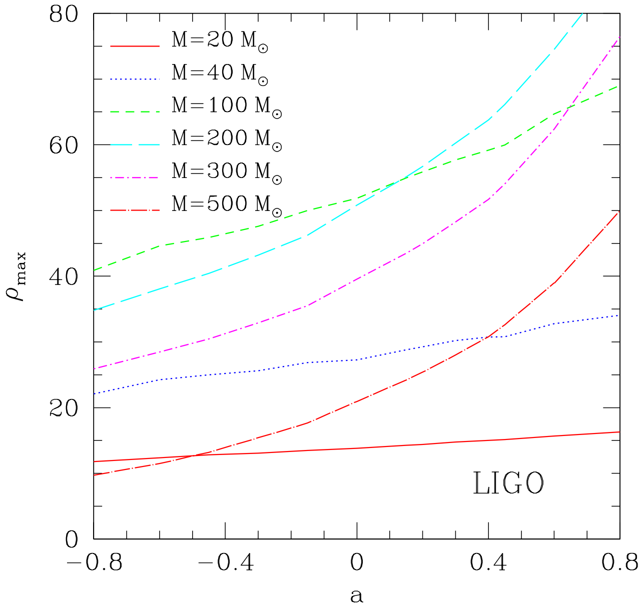

Figure 5.4: Maximum SNR $\rho_{\rm max} = \rho(a,\, M)$ for the LIGO detector for a given set of masses at a distance $d = 100\,{\rm Mpc}$. Note that the growth of $\rho_{\rm max}$ with a is very well described with a low-order polynomial which is of 4th order for the optimal mass (*cf.* discussion in Sect. 5.1.10). Note also that the dependence on a becomes stronger for masses $M > 200\,M_\odot$, for which the NR-part of the waveform and hence the plunge and ringdown phase dominate. In these cases, the SNR is more then doubled between $a = -1$ and $a = +1$.

masses) and of the average dimensionless spin "a" as projected along the orbital angular momentum $\boldsymbol{L}$

$$a \equiv \frac{1}{2}(\boldsymbol{a}_1 + \boldsymbol{a}_2) \cdot \hat{\boldsymbol{L}} = \frac{1}{2}(\boldsymbol{a}_1 + \boldsymbol{a}_2) \cdot \boldsymbol{e}_z \,, \tag{5.13}$$

where $\hat{\boldsymbol{L}} \equiv \boldsymbol{L}/|\boldsymbol{L}|$, and the orbital plane has been chosen to coincide with the $(x,\, y)$ plane of our Cartesian coordinate system. The top left panel of Fig. 5.3 refers to the LIGO detector, the top right panel to the Virgo detector, while the lower left and right panels refer to the advanced versions of both detectors, respectively.

These panels deserve some comments:

- The maximum SNR is always larger than the average one but the difference between the two is not constant, changing both with the total dimensionless spin a and with the total mass M.
- For any fixed value of a, the horizon distance (and hence the SNR) grows steeply to a maximum mass and then rapidly decreases to very small values of $\sim \mathcal{O}(1)$.
- For any value of a, the maximum horizon distance/SNR also marks the "optimal

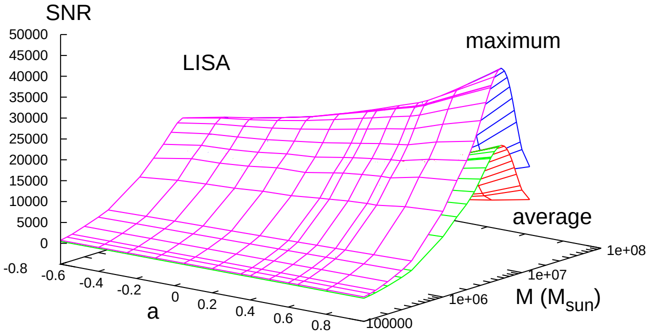

Figure 5.5: Averaged and maximum SNR $\rho = \rho(a, M)$ for the planned LISA mission and for sources at $d = 6.4\,\mathrm{Gpc}$ $(z = 1)$.

mass" for the binary $M_{\rm opt}$, the mass of the binary whose inspiral and merger is optimally tuned with the given detector and hence can be seen from further away. The differences between the maximum and average SNR are largest in the neighborhood of the optimal mass.

- The configuration with spins parallel and aligned to the orbital angular momentum are generically "louder" than those with spins parallel but antialigned with the orbital angular momentum, with the binaries having $a = \pm 1$ being the "loudest" and "quietest", respectively.

- In the cases of the LIGO and advanced Virgo detectors the horizon distance is essentially zero at cut-off masses which are $\sim 900\, M_{\odot}$ and $\sim 3000\, M_{\odot}$, respectively.

- For any fixed value of the total mass, the SNR grows with a and, as we will discuss later on, this growth is very well described with a polynomial of 4th order. This is shown more clearly in Fig. 5.4, which reports the maximum SNR $\rho_{\rm max}$ for the LIGO detector and for a given set of masses at a distance $d = 100\,\mathrm{Mpc}$. The growth of $\rho_{\rm max}$ with a becomes steeper for masses $M > 200\, M_{\odot}$, for which the NR-part of the waveform and hence the plunge and ringdown phase dominates. In these cases, the SNR is more then doubled between $a = -1$ and $a = +1$.

- When going from the present LIGO/Virgo detectors to their advanced versions, the average horizon distances go from $\sim 600/800\,\mathrm{Mpc}$ to $\sim 10^4/1.2 \times 10^4\,\mathrm{Mpc}$, thus with an observational *volume* of the Universe that is increased by a factor of $\sim 5000/3000$, respectively.

Figure 5.5 shows similar information but for the planned LISA mission. Since the horizon distance can exceed the whole Hubble horizon, the figure reports the averaged and maximum SNR $\rho = \rho(a, M)$ for sources at $d = 6.4\,\mathrm{Gpc}$ $(z = 1)$. Many of the considerations made above hold also for the LISA detector, and for sufficiently high and aligned spins ($a \gtrsim 0.8$), the SNR is $\gtrsim \mathcal{O}(10)$ with binaries having masses $\gtrsim$ few $\times\, 10^3\, M_\odot$.

The most salient information of Figs. 5.3 and 5.5 is collected in Table 5.3 which reports the properties of the "optimal" aligned binaries for the different detectors. More specifically, the Table reports in its different rows the optimal total aligned spin a, the optimal total mass in solar masses, the optimal maximum ρ and average $\rho_{\rm avg}$ SNRs, the optimal horizon distance d_H (expressed in Mpc and with H^{-1} being the Hubble radius), the optimal relative event rate R, and the glueing frequency $f_{\rm glue}$ for the optimal binary. The masses have been sampled with an accuracy of $2.5\, M_\odot$ for the ground-based detectors and of $2.5 \times 10^4\, M_\odot$ for LISA.

Table 5.3: Properties of the "optimal" aligned binaries for the different detectors. Shown in the different rows are the optimal total aligned spin a, the optimal total mass in solar masses, the optimal maximum $\rho_{\rm max}$ and average $\rho_{\rm avg}$ SNRs, the optimal horizon distance d_H (expressed in Mpc and where cH^{-1} is the Hubble radius), the lower bound for the optimal relative event rate R, and the glueing frequency $f_{\rm glue}$ for the optimal binary. The masses have been sampled with an accuracy of $2.5\, M_\odot$ for the ground-based detectors and of $2.5 \times 10^4\, M_\odot$ for LISA.

	LIGO	eLIGO	AdLIGO	Virgo	AdVirgo	LISA
a	0.8	0.8	0.8	0.8	0.8	0.8
$M_{\rm opt}$ $(M_\odot)$	197	180	290	395	390	5.35×10^6
$\rho_{\rm max}$	87	175	1667	118	1591	2.91×10^6
$\rho_{\rm avg}$	52	104	991	70	944	1.77×10^6
d_H (Mpc)	1091	2190	$> cH^{-1}$	1476	$> cH^{-1}$	$> cH^{-1}$
R	18	17	16	16	17	26
$f_{\rm glue}$ (Hz)	27.48	30.51	18.71	13.74	13.91	1.0×10^{-3}

5.1.7 Influence of higher ℓ-modes

It is important to at least consider the impact that higher-order modes have on the SNR of equal-mass aligned binaries. Some representative examples of this impact is shown in Fig. 5.6. The left panel of this figure, in particular shows the maximum SNR $\rho_{\rm max}$ as a function of the mass for the highly spinning model s_8 and for the present detectors LIGO and Virgo. Different lines refer to the SNRs computed using only the $\ell = 2$ multipoles (continuous line), or up to the $\ell = 4$ multipoles (dashed line). The contribution of the higher modes is most important near the optimal mass ($M \sim 200\, M_\odot$ for LIGO and $M \sim 400\, M_\odot$ for Virgo) but this is also non-negligible for larger masses, where it can produce an increase of $\sim 8\%$ in SNR in a detector such as Virgo.

The right panel of Fig. 5.6, shows the ratio between maximum and averaged SNR as a function of the total projected spin a for a binary of $M = 200\, M_\odot$ $(5.35 \times 10^6\, M_\odot)$ and the LIGO (LISA) detector. As mentioned in Sect. 5.1.5, this ratio is not expressed

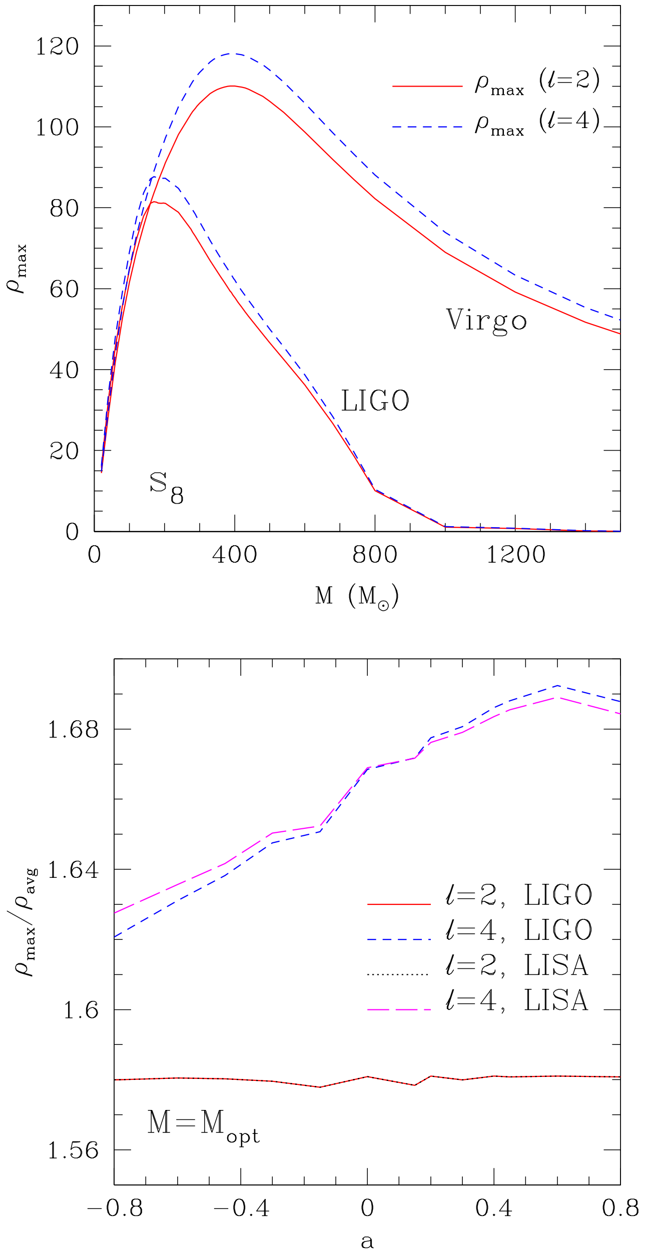

Figure 5.6: *Left panel:* maximum SNR $\rho_{\rm max}$ as a function of the mass for the highly spinning model s_8 and for the present detectors LIGO and Virgo. Different lines refer to the SNRs computed using only the $\ell = 2$ multipoles (continuous line), or up to the $\ell = 4$ multipoles (dashed line). *Right panel:* ratio between maximum and averaged SNR ρ as a function of the spins $a_1 = a_2$ for $M = 200\,M_\odot$ ($M = 3.53 \times 10^6\,M_\odot$) by including modes up to $\ell = 2$ and $\ell = 4$ for LIGO (LISA). In contrast to the case $\ell = 2$, the $\ell = 4$-curve is not constant but depends on the initial spins a_1, a_2

by a simple algebraic expression [Eq. (5.9)], but needs to be determined numerically. Interestingly, this ratio is not constant but increases by $\sim 10\%$ for larger total projected spins, underlining the importance of higher-order contributions as the initial spin increase.

5.1.8 Match between different models

An extremely useful quantity to analyze is the match between the amplitudes of the waveforms from two different binaries. This will quantify the differences in the gravitational-wave signal relative to some reference models. The match between two waveforms $h_1(t)$ and $h_2(t)$ (or a template and a waveform) can be calculated via the weighted scalar product in frequency space between two given waveforms

$$\langle h_1|h_2\rangle = 4\Re\int_0^\infty df\frac{\tilde{h}_1(f)\tilde{h}_2^*(f)}{S_h(f)}\,, \tag{5.14}$$

where $\tilde{h}_1(f)$ is the power spectral density of $h_1(t)$, the asterisk indicates a complex conjugate, and $S_h(f)$ is the noise power spectral density of a given detector. The overlap is then given by the normalized scalar product

$$\mathcal{O}[h_1, h_2] = \frac{\langle h_1|h_2\rangle}{\sqrt{\langle h_1|h_1\rangle\langle h_2|h_2\rangle}}. \tag{5.15}$$

Two parameters must be taken into account when computing the overlap. The first is the “time of arrival” $t_{\rm A}$ corresponding to an offset in the Fourier-transform of the signal $\exp[{\rm i}\omega(t - t_{\rm A})]$. The second is the “initial phase” Φ of the orbital motion when it enters the detector band.

For both of these parameters the overlap should be maximized. There are two possible ways of doing this. The first approach involves the *best* match, which gives an upper bound by maximizing over both of the phases of each waveform

$$\mathcal{M}_{\rm best} \equiv \max_{t_{\rm A}}\max_{\Phi_1}\max_{\Phi_2}\{\mathcal{O}[h_1, h_2]\}\,. \tag{5.16}$$

The second way involves the *minimax* match, and is obtained by maximizing over the phase of one waveform but minimizing over the phase of the other

$$\mathcal{M}_{\rm minimax} \equiv \max_{t_{\rm A}}\min_{\Phi_2}\max_{\Phi_1}\{\mathcal{O}[h_1, h_2]\}\,, \tag{5.17}$$

and thus represents a “worst-case” scenario since it gives lower matches although one is maximizing over the template phase. More details on the maximization procedure can be found in [236, 237]. Note that all the matches computed hereafter refer to the numerical-relativity part of the waveform only.

A sensible method to evaluate expressions (5.16) and (5.17) uses the binary s_0, the nonspinning binary, as a reference and computes the overlap with the binaries at representative locations in the spin diagram, at the corners for $s_0 - s_8$, $s_0 - u_8$, $s_0 - s_{-8}$, or along the main diagonal, $s_{-8} - s_8$. In this way we assess whether the waveform produced

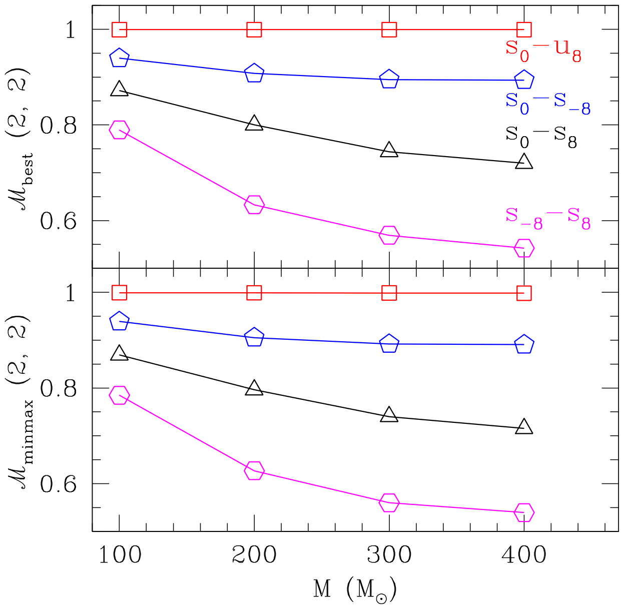

Figure 5.7: Best and minmax match as a function of mass for a waveform containing only the $\ell = 2, m = 2$ contribution and referring to the LIGO detector. Very similar behaviors can be shown also for the other detectors.

by a nonspinning binary can be used to detect also spinning binaries and how much the overlap is decreased in this case.

This is shown in Fig. 5.7, which reports the best and minmax matches as a function of mass for a waveform containing only the $\ell = 2, m = 2$ contribution for the LIGO detector. Different lines show the match computed between s_0 and other representative binaries. This shows the remarkable similarity between the waveforms of binaries having a zero total spin. This is shown by the $s_0 - u_8$ match, which is essentially very close to 1 for all the masses considered (Table 5.4). This result extends to all the other measured quantities, such as the radiated energy or angular momentum. The equivalence between nonspinning binaries and binaries with equal and opposite spins has been exploited in the derivation of expressions for the final spin presented in Chapter [4]. The results of Fig. 5.7 and Table 5.4 are therefore a simple example, although probably not the only possible one, of a well defined region of the space of initial configurations which can be mapped to an almost degenerate region (essentially to a single point) in the space of templates. This represents a serious obstacle towards a proper estimate of physical parameters of the binaries that may be removed, at least in part, only if the waveform is measured with a sufficiently high SNR.

An equally interesting result, presented in Fig. 5.7, is that the overlap is also very high between the nonspinning binary and the binary with equal and antialigned spins, $s_0 - s_{-8}$; also in this case the best match is $\mathcal{M}_{\rm best} \gtrsim 0.9$ for the range of masses that is relevant here. Slightly smaller and decreasing with increasing masses are the best matches

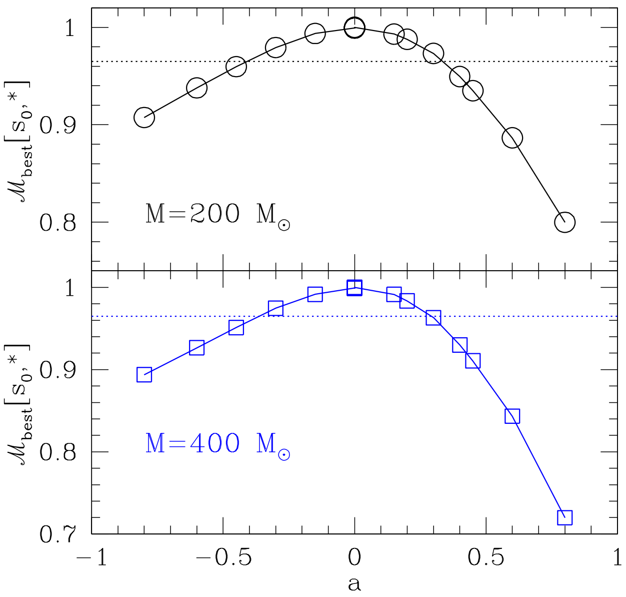

Figure 5.8: Best match as a function of the total projected spin a for a waveform containing only the $\ell = 2, m = 2$ contribution. The top/lower panels refers to binary with a total mass ($200/400\,M_\odot$) which are close to the optimal ones for the LIGO/Virgo or advanced detectors, respectively. In both panels the dotted line shows the minimum best match (0.965) needed for a detection. While the data have been computed for the LIGO detector, very similar behaviors can be shown also for the other detectors.

computed when comparing the nonspinning binary with the binary of parallel and aligned spins, so that $\mathcal{M}_{\rm best} \sim 0.8$, but only for very large masses. The waveforms appear clearly different (with $\mathcal{M}_{\rm best} \lesssim 0.6$) only when comparing the binaries along the main diagonal of the spin diagram, for $s_8 - s_{-8}$. Even in this rather extreme case the differences tend to become smaller for smaller masses. Overall, this result underlines that even simple waveforms, such as those relative to nonspinning binaries, will be effective enough to provide a detection for most configurations of equal-mass and aligned/antialigned binaries.

A different way to assess "how different" the waveforms are across all of the equal-mass aligned/antialigned spins configurations considered here is summarized in Fig. 5.8, which shows the best match as a function of the total projected spin a for waveforms containing only the $\ell = 2, m = 2$ contribution and referring to the LIGO detector. The top panel, in particular, refers to binary with a total mass of $200\,M_\odot$ (close to the optimal mass for the LIGO/Virgo detectors), while the bottom panel refers to a binary with mass $400\,M_\odot$ (close to the optimal mass for the advanced LIGO/Virgo detectors), as shown in Table 5.4. Besides the smooth behaviour of $\mathcal{M}_{\rm best}$ across all the values of a considered, it is clear that the waveform from a nonspinning binary can be extremely useful across the *whole* spin diagram and yield very large overlaps even for binaries with very high spins. In both panels, in fact, the dotted line shows the minimum best match ($\mathcal{M}_{\rm best} = 0.965$)

needed for a detection [238]. This result is reassuring in light of the fact that most of the searches in the detector data are made using phenomenological waveforms based on nonspinning binaries. This result is exploited for the template development in Section [5.2].

For completeness, the results presented in Fig. 5.7 (as well as those in Fig. 5.9) are also reported in Table 5.4, where the columns show $\mathcal{M}_{\rm best}$ and $\mathcal{M}_{\rm minmax}$ and for waveforms computed either using only the $\ell = 2, m = 2$ contribution (third and fourth columns), only the $\ell = 3, m = 2$ contribution (fifth and sixth columns), or all contributions up to $\ell = 4$ (last two columns). The matches among the high-order modes, *e.g.,* $(s_0)_{\ell=3,m=2} - (u_8)_{\ell=3,m=2}$, is higher than those of the lower ones and remains true even for higher modes beyond $\ell = 3, m = 2$. This indicates that in order to do high-precision parameter estimation by including higher modes it is also important that these modes are accurately resolved, so that they can be clearly distinguished from one another.

We generally expect the match to degrade when the waveforms are computed by including higher-order modes (up to $\ell = 4$) and that this degradation will become larger with increasing inclination θ. The most notable example is for the degeneracy along the diagonal $a_1 = -a_2$, which should be broken by the inclusion of higher-order modes. For this reason we have computed the sky-averaged match of waveforms including modes up to $\ell = 4$ (*i.e.,* the "complete" waveforms) and the corresponding matches are reported in the last two columns of Table 5.4. We measure a marked decreased in the minmax match, but a much smaller decrease in the best match. Although our resolution should be marginally enough for us to detect such a difference in the best match, we also believe that a much higher accuracy is required to determine this with certainty. The matches with complete waveforms along other directions, *e.g.,* $s_0 - s_8$ or $s_0 - s_{-8}$, do not decrease and this is due to the very large mismatch we already have with the $\ell = 2 = m$ waveforms.

Figs 5.7 and 5.8 show data computed for the LIGO detector only, however, very similar behaviors can be shown also for the other detectors.

5.1.9 Accuracy of NR waveform amplitudes

A reasonable concern that can be raised when looking the very high matches between the waveforms in the u-sequence is that these are the result of insufficient resolution. In other words, the waveforms may appear similar simply because our resolution is not sufficient to pick-up the differences. To address this concern we have computed the overlap among the waveforms obtained at three different resolutions and for a representative binary with nonzero spins, r_0. Clearly, a low match in this case would be an indication that our results are very sensitive to the numerical resolution.

The results of this validation are presented in Fig. 5.9 and are reported in the last eight rows of Table 5.4. Shown with different lines in Fig. 5.9 are the matches obtained when comparing the numerical waveforms of the binary r_0 computed at low resolution ($\Delta x/M = 0.024$) and medium resolution ($\Delta x/M = 0.020$, as well as at a medium and high resolution ($\Delta x/M = 0.018$). The matches are computed considering only the $\ell = 2, m = 2$ mode and for the LIGO detector, but very similar behaviors can be shown also for higher modes or for the other detectors.

Table 5.4: Best and minmax matches as computed for the LIGO detector for binaries with different spins in the spin diagram. Different columns show $\mathcal{M}_{\rm best}$ and $\mathcal{M}_{\rm minmax}$ for waveforms computed either using only the $\ell = 2, m = 2$ contribution (third and fourth columns), only the $\ell = 3, m = 2$ contribution (fifth and sixth columns), or the sky-averaged contributions of all modes up to $\ell = 4$ (last two columns). Finally the last eight rows show the matches at different resolutions (*i.e.,* $\Delta x/M = 0.024, 0.020, 0.018$ or low, medium and high, respectively) for the binary r_0.

	$M/M_\odot$	$\mathcal{M}_{\rm best}$ $\ell = 2, m = 2$	$\mathcal{M}_{\rm minmax}$ $\ell = 2, m = 2$	$\mathcal{M}_{\rm best}$ $\ell = 3, m = 2$	$\mathcal{M}_{\rm minmax}$ $\ell = 3, m = 2$	$\mathcal{M}_{\rm best}$ up to $\ell = 4$	$\mathcal{M}_{\rm minmax}$ up to $\ell = 4$
$s_0 - s_8$	100	0.87182	0.86914	0.87802	0.85061	0.86337	0.83272
	200	0.79987	0.79642	0.82533	0.80236	0.80070	0.75679
	300	0.74394	0.74026	0.82570	0.78819	0.74785	0.71139
	400	0.71981	0.71568	0.84074	0.81285	0.72345	0.69019
$s_0 - u_8$	100	0.99926	0.99914	0.99497	0.97411	0.99673	0.95443
	200	0.99928	0.99906	0.99372	0.95193	0.99483	0.95919
	300	0.99923	0.99870	0.99189	0.93888	0.99251	0.96105
	400	0.99919	0.99822	0.99147	0.93493	0.99110	0.96054
$s_0 - s_{-8}$	100	0.93942	0.93907	0.95717	0.94843	0.93695	0.92143
	200	0.90746	0.90536	0.95647	0.94521	0.89646	0.88041
	300	0.89491	0.89197	0.95015	0.93814	0.87303	0.84960
	400	0.89369	0.89065	0.94806	0.93550	0.85492	0.82103
$s_{-8} - s_8$	100	0.78948	0.78493	0.87041	0.85222	0.78310	0.74895
	200	0.63309	0.62703	0.90722	0.88543	0.63456	0.59426
	300	0.56934	0.56008	0.90322	0.88869	0.56941	0.52170
	400	0.54235	0.53960	0.91199	0.89848	0.55470	0.49338
$s_{-8} - u_8$	100	0.94250	0.94187	0.96299	0.94669	0.93897	0.89017
	200	0.91444	0.91229	0.96316	0.93068	0.90315	0.85958
	300	0.90188	0.89885	0.95486	0.91256	0.87846	0.83428
	400	0.89772	0.89492	0.95132	0.90583	0.85870	0.80907
$s_8 - u_8$	100	0.87127	0.86817	0.87656	0.84229	0.85866	0.80969
	200	0.79750	0.79477	0.83582	0.81476	0.79074	0.73526
	300	0.74063	0.73884	0.83897	0.80378	0.73616	0.68774
	400	0.71798	0.71343	0.84955	0.81925	0.71203	0.66611
r_0 $(0.024, 0.020)$	100	0.99979	0.99970	0.99495	0.98812	0.99855	0.99463
	200	0.99963	0.99929	0.99133	0.97100	0.99633	0.98800
	300	0.99943	0.99894	0.98752	0.95775	0.99379	0.98152
	400	0.99924	0.99868	0.98630	0.95317	0.99209	0.97683
r_0 $(0.020, 0.018)$	100	0.99990	0.99989	0.99873	0.99299	0.99881	0.99639
	200	0.99980	0.99970	0.99806	0.98074	0.99705	0.98952
	300	0.99956	0.99924	0.99707	0.97238	0.99497	0.98070
	400	0.99935	0.99866	0.99666	0.97017	0.99320	0.97429

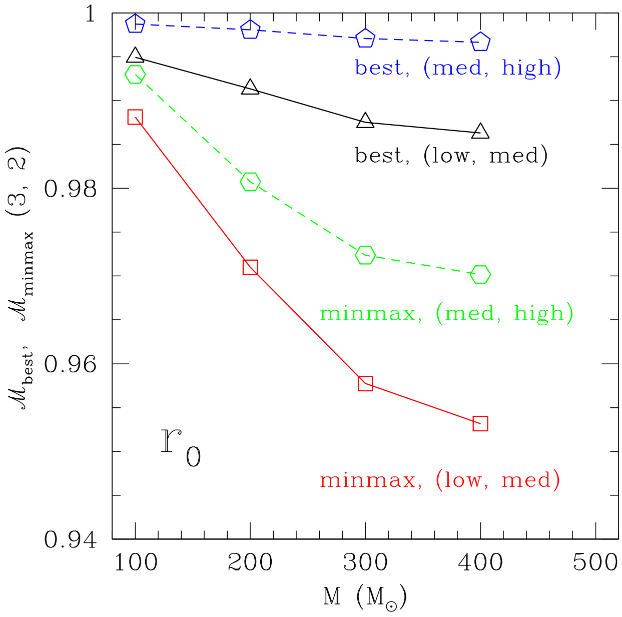

Figure 5.9: As in Fig. 5.8 but now different lines represent the matches obtained when comparing the numerical waveforms of the binary r_0 computed at different resolutions. The matches are computed for the LIGO detector, but very similar behaviors can be shown also for the other detectors.

The results reported in Fig. 5.9 and in Table 5.4 show that $\mathcal{M}_{\rm best,minmax}[\Delta x_1, \Delta x_2] > \mathcal{M}_{\rm best,minmax}[h_1, h_2]$, thus that the differences we measure in the overlaps among two different waveforms h_1 and h_2 are always larger than the differences we are able to measure at two different resolutions Δx_1 and Δx_2. In other words, the differences in the waveforms across the spin diagram are always larger than our numerical errors, even along the degenerate u-sequence (of course, as we have a convergent numerical code, the match between medium and low resolution is worse than the match between medium and high resolution). As long as the dominant $\ell = 2, m = 2$ mode is considered, the differences in the matches are well within the margin of error for numerical relativity simulations of black hole binaries throughout the field. A recent work has in fact estimated that the differences in the waveforms produced by distinct codes is $\mathcal{M}_{\rm mismatch} = 1 - \mathcal{M} \approx 10^{-4}$ for the last $\approx 1000M$ of the dominant mode of non-spinning equal mass coalescence [239]. Since the next higher mode $\ell = 3, m = 2$ starts to suffer from numerical noise, it does not yield the same high agreement, and the differences between best and minimax match show a larger deviation.

As a final comment on the accuracy of our waveforms, we note that the error made by using waveforms extracted at a finite radius, and not extrapolated at spatial infinity is well within the error budget of our estimates. We have validated this by comparing the waveforms extracted at a finite radius against the waveforms computed at future null infinity, via a newly developed Cauchy-characteristic code [240]. In the case of the nonspinning configuration s_0 we have found an error in the calculated SNR of less than 1.0%.

5.1.10 SNR Fits

As discussed in Sect. 5.1.5, the maximum SNR depends on several factors, most notably on the two initial spins, the total mass of the system and, although more weakly, on the number of multipoles included in the waveforms. The resulting functional dependencies when one degree of freedom is suppressed and the SNRs are presented in terms of the total projected spin are shown in Figs. 5.3, 5.5 and are too cumbersome to be described analytically. However, most of the complex functional dependence can still be captured when concentrating on the best case scenario, and hence on the SNRs relative to the optimal mass $M_{\rm opt}$. The behaviour of the SNR in this case is shown in Fig. 5.10, where the different symbols show the numerically computed values of $\rho_{\rm max}(a, M_{\rm opt})$ for the different detectors. Fig. 5.10 represents the cross section along the optimal mass of Figs. 5.3 and 5.5 (note that the SNR for the advanced detectors have been divided by 7 to make them fit onto the same scale).

The behaviour of the SNR in this case is sufficiently simple that it can be represented with a simple quartic polynomial of the type

$$\rho_{\rm max}(a;\, \ell \leq 4, M = M_{\rm opt}) = \sum_{n=0}^{4} k_n a^n\,, \tag{5.18}$$

whose coefficients k_n are reported in Table 5.5 for the five detectors considered.

When considering the optimal mass, the ratio of the SNRs for maximally an-

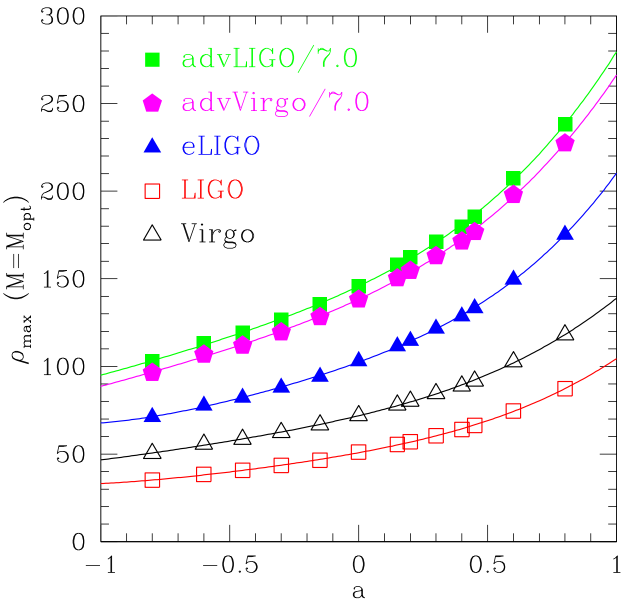

Figure 5.10: Different symbols show the numerically computed values of $\rho_{\max}(a, M_{\rm opt})$ for the different detectors and represent therefore the cross section along the optimal mass of Figs. 5.3 and 5.5. Note that the SNR for the advanced detectors have been divided by 7 to make them fit onto the same scale.

tialigned spinning binaries to maximally and aligned spinning binaries, *i.e.*, $\rho_{\max}(a = 1)/\rho_{\max}(a = -1)$ is ~ 3 for both the LIGO and Virgo detectors. This ratio is also preserved when considering the advanced LIGO and Virgo detectors. Because the event rate scales like the cube of the SNR [*cf.* expressions (5.9)-(5.12)], an increase of a factor ~ 3 in the SNR of binaries with $a = -1$ and $a = 1$ will translate into an increase of a factor ~ 27 in the event rate. It is therefore likely that many of the binaries observed will have high spins and aligned with the orbital angular momentum. This will be particularly true in the case of LISA if the prediction that the spins of supermassive black holes are aligned with the orbital angular momentum will hold [203].

5.1.11 Radiated Energy Fits

While the SNR is effectively a measure of the amount of energy released during the inspiral, it also incorporates information on the properties of the detectors and is not therefore an absolute measure of the efficiency of the gravitational-wave emission process. This information can have a number of important astrophysical applications. In particular, it can be used to study the effect the merger has on the dynamics of the circumbinary disk accreting onto the binary when this is massive [241, 242].

Table 5.5: Fitting coefficients for the maximum SNR computed for the optimal mass [Eq. (6.5)]. The different rows refer to the various detectors and have been computed including all modes up to $\ell = 4$.

detector	k_0	k_1	k_2	k_3	k_4
LIGO	50.76	27.11	13.43	8.58	4.63
eLIGO	102.45	53.63	25.33	17.67	11.26
AdLIGO	1020.42	492.25	243.60	153.84	46.99
Virgo	71.86	35.23	17.140	10.92	3.789
AdVirgo	968.08	481.52	236.45	140.69	37.91

In this Section I present a simple formula to compute the amount of energy released and express it only in terms of the initial spins. Our formula is restricted to aligned binaries. In practice, the expression for the radiated energy $E_{\rm rad}$ is derived by combining a fit to the numerical data for the binaries at an initial and finite separation $D = 8\,M$ (we refer to this energy as to $E^{\rm NR}_{\rm rad}$), with the estimate of the energy released from the binary when it goes from an infinite separation down to D (we refer to this energy as $E^{\rm PN}_{\rm rad}$), *i.e.*,

$$E_{\rm rad} = E^{\rm NR}_{\rm rad} + E^{\rm PN}_{\rm rad} = M_{\rm ADM} - M_{\rm fin} + E^{\rm PN}_{\rm rad} \tag{5.19}$$

where $M_{\rm ADM}$ is the initial ADM mass as measured at spatial infinity of the binary with separation D, and $M_{\rm fin}$ the Christodoulou mass of the final black hole. For the fit of the radiated energy during the numerical evolution, $E^{\rm NR}_{\rm rad}$, we use the same symmetry arguments first made in Chapter [4] to write a simple expression which is a Taylor expansion in terms of the initial spins

$$\frac{E^{\rm NR}_{\rm rad}(q=1,a_1,a_2)}{M} = p_0 + p_1(a_1+a_2) + p_2(a_1+a_2)^2 \, . \tag{5.20}$$

Fitting then the numerical data as in Chapter [4] we obtain the following values for the coefficients

$$\begin{aligned} p_0 &= \frac{3.606 \pm 0.0271}{100} \, , \qquad p_1 = \frac{1.493 \pm 0.0260}{100} \, , \\ p_2 &= \frac{0.489 \pm 0.0254}{100} \, . \end{aligned} \tag{5.21}$$

where the reduced chi-squared is $\chi^2_{\rm red} = 0.008$, and where the largest error is in the 2nd-order coefficient but this is only $\sim 5\%$. Expressed in this way, the different coefficients (5.21) can then be interpreted as the nonspinning orbital contribution to the energy loss (p_0, which is the largest and of $\sim 3.6\%$), the spin-orbit contribution (p_1, which is $\lesssim 3.0\%$), and the spin-spin contribution (p_2, which is $\lesssim 2.0\%$). The relative error between the numerically computed value of $E^{\rm NR}_{\rm rad}$ and the fitted one is reported in the last column of Table 5.1.

The PN expression for the energy radiated by the binary when going from an infinite separation down to a finite one $r = d$, depends on the total mass of the binary, the mass ratio and the spin components, *i.e.*, $E^{\rm PN}_{\rm rad} = E^{\rm PN}_{\rm rad}(r, M, \nu, a_1, a_2)$. Exploiting the fact that, for equal-mass binaries, the PN radiated energy $E^{\rm PN}_{\rm rad}$ follows the same series expansion used for $E^{\rm NR}_{\rm rad}$, namely a polynomial of the total spin, in this case, setting $M = 1 = q$ we obtain

$$\begin{aligned} \frac{E^{\rm PN}_{\rm rad}(a_1,a_2)}{M} &= E^{\rm PN}_{\rm rad,0} \\ &\quad + E^{\rm PN}_{\rm rad,1}(a_1+a_2) + E^{\rm PN}_{\rm rad,2}(a_1+a_2)^2 \, , \end{aligned} \tag{5.22}$$

where the coefficients for $D = 8\,M$ are given by

$$\begin{aligned} E^{\rm PN}_{\rm rad,0} &= \frac{6401}{524288} \simeq \frac{1.220}{100} \, , \\ E^{\rm PN}_{\rm rad,1} &= \frac{985}{1048576\sqrt{2}} \simeq \frac{0.0664}{100} \, , \\ E^{\rm PN}_{\rm rad,2} &= -\frac{1}{32768} \simeq -\frac{0.00305}{100} \, . \end{aligned} \tag{5.23}$$

Inspection of the coefficients (5.23) reveals that the PN orbital contribution is only $\sim 33\%$, the one of the strong-field regime, but also that the spin-related PN contributions are mostly negligible, being at most of $\sim 4\%$ of those produced in the last orbits.

We can now combine expressions (5.20)-(5.21) with expressions (5.22)-(5.23) and estimate that for equal-mass binaries with aligned spins the energy radiated via gravitational waves from infinity

$$\frac{E_{\rm rad}(a_1,a_2)}{M} = \tilde{p}_0 + \tilde{p}_1(a_1+a_2) + \tilde{p}_2(a_1+a_2)^2\,, \tag{5.24}$$

where

$$\tilde{p}_0 = \frac{4.826}{100}\,, \qquad \tilde{p}_1 = \frac{1.559}{100}\,, \qquad \tilde{p}_2 = \frac{0.485}{100}\,. \tag{5.25}$$

These numbers are specific to equal-mass binaries and refer to a situation in which the match between the PN evolution and the one in the strong-field regime is made at a specific separation of $D = 8\,M$. However, we expect the results to depend only weakly on this matching separation (as long as it is within a PN regime) and hence that expressions (5.24) and (5.25) are generically valid at the precision we are considering them here, namely $\sim 5\%$.

Using expression (5.24) a number of quantitative considerations are possible. Firstly, the largest energy is emitted by equal-mass, maximally spinning binaries with spins parallel and aligned with the orbital angular momentum at is $E_{\rm rad}(a=1)/M = 9.9\%$. Secondly, equal-mass nonspinning binaries lose a considerable fraction of their mass via radiation, with $E_{\rm rad}(a=0)/M = 4.8\%$, while maximally spinning binaries with spins parallel and antialigned with the orbital angular momentum have $E_{\rm rad}(a=-1)/M = 3.7\%$.

Expression (5.24) is not a strictly monotonic function of the total spin and has a local minimum at $a_1 = a_2 = -\tilde{p}_1/(4\tilde{p}_2) \simeq -0.8$ rather than at $a_1 = a_2 = -1$, and yields $E_{\rm rad}(a = -0.79)/M = 3.6\%$ (Fig. 5.11). Although rather shallow, we do not expect such a local minimum. We therefore interpret it as an artifact of the numerical error of our calculations (the difference between the energy radiated at $a_1 = a_2 = -1$ and that at $a_1 = a_2 = -0.8$ is $\sim 2\%$ and hence compatible with our overall error). Such a local minimum can be removed by adding higher-order terms in expression (5.20) (up to 4th order in $a_1 + a_2$) but these improvements are so small that they do not justify the use of a more cumbersome expression. A comparison between the numerical values and the fitting expression 5.24 is shown in Fig. 5.11, where crosses and squares represent the $E^{\rm NR}_{\rm rad}$ and $E_{\rm rad}$ respectively, along the diagonal of the spin-diagram (*i.e.*, for $a_1 = a_2$), while the continuous line refers to our fitting expression. Note that such a line is a 1-dimensional cut of a 2-dimensional surface and hence it is not expected to exactly fit all points.

Lousto and collaborators have recently proposed a more general formula that should account for the radiated energy in all of the relevant space of parameters, namely for binaries with arbitrary mass ratio, spin orientation and size [12]. Restricting their expression to the specific subset of binaries considered here corresponds to setting in their expression (2): $E_B = E_E = 0$, $\nu = 1/4$ and $q = 1$. The resulting expression is

$$\begin{aligned}\frac{E^{\rm RIT}_{\rm rad}}{M} &= \frac{1}{4}E_{\rm ISCO} + \frac{1}{16}E_2 + \frac{1}{64}E_3 \\ &+ \frac{1}{64}\left[E_S(a_1+a_2) + E_A(a_1+a_2)^2\right. \\ &+ \left. E_D(a_1-a_2)^2\right]\,,\end{aligned} \tag{5.26}$$

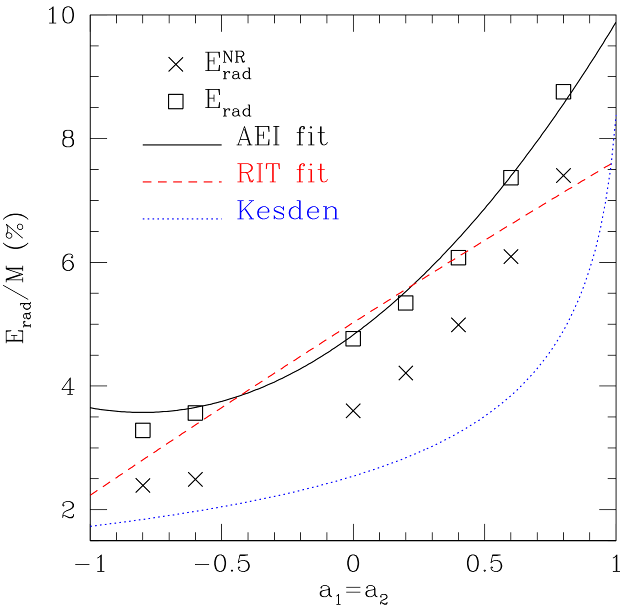

Figure 5.11: Energy radiated during the numerical calculation $E_{\rm rad}^{\rm NR}$ (crosses), the total radiated energy $E_{\rm rad} = E_{\rm rad}^{\rm NR} + E_{\rm rad}^{\rm PN}$ (squares) along the diagonal of the spin diagram, *i.e.*, for $a_1 = a_2$. Shown as a continuous line is the analytic expressions given here (AEI fit), while the dashed line is the one suggested in ref. [12] (RIT fit). Note that the lines represent 1-dimensional cuts of 2-dimensional surfaces and hence are not expected to fit well all points. Finally, indicated with a dotted line is the prediction for the radiated energy coming from the point-particle approach of [4] and refined in [13].

where the fitting coefficients have been determined to be $E_2 = 0.341 \pm 0.014$, $E_3 = 0.522 \pm 0.062$, $E_S = 0.673 \pm 0.035$, $E_A = -0.014 \pm 0.021$, $E_D = -0.26 \pm 0.44$ [12], and where

$$E_{\rm ISCO} = \left(1 - \frac{\sqrt{8}}{3}\right) + \frac{0.103803}{4} + \frac{1}{48\sqrt{3}}(a_1 + a_2) + \frac{5}{648\sqrt{2}}(a_1 - a_2)^2 \,. \tag{5.27}$$

After a bit of algebra we can rewrite (5.27) as

$$\frac{E_{\rm rad}^{\rm RIT}(a_1, a_2)}{M} = \tilde{q}_0 + \tilde{q}_1(a_1 + a_2) + \tilde{q}_2(a_1 + a_2)^2 + \tilde{q}_3(a_1 - a_2)^2 \,, \tag{5.28}$$

where now

$$\begin{aligned}
\tilde{q}_0 &= \frac{1}{4}\left(1 - \frac{\sqrt{8}}{3} + \frac{0.103803}{4}\right) + \frac{E_2}{16} + \frac{E_3}{64} \simeq \frac{5.025}{100}\,, \\
\tilde{q}_1 &= \frac{1}{192\sqrt{3}} + \frac{E_S}{64} \simeq \frac{1.352}{100}\,, \\
\tilde{q}_2 &= \frac{E_A}{64} \simeq -\frac{0.0219}{100}\,, \\
\tilde{q}_3 &= \frac{5}{2592\sqrt{2}} + \frac{E_D}{64} \simeq -\frac{0.270}{100}\,.
\end{aligned} \tag{5.29}$$

Comparing (5.24)-(5.25) with (5.28)-(5.29) shows that the reduced expression from [12] has a second order contribution $\sim (a_1 - a_2)^2$, which is absent in our expression. The remaining coefficients are rather similar but not identical. This comparison is summarized in Fig. 5.11, where the dashed line corresponds to the fitting proposed in ref. [12]. The maximum efficiency for maximally spinning black holes predicted by expression (5.28) is $\sim 8\%$, but our estimate is larger and $\sim 10\%$.

While the two expressions provide very similar estimates for $-0.5 \lesssim a_1 = a_2 \lesssim 0.4$, they also have predictions differing by more than $\sim 20\%$ for highly spinning binaries. Expressions (5.28)-(5.29) have error-bars that are as high as 100%. In view of this, and of the fact that the coefficients are constant, the simulations carried out here could be used for a new estimate of the free coefficients E_2, E_3, E_S, and E_A in (5.28). Finally, indicated with a dotted line in Fig. 5.11 is the prediction for the radiated energy coming from the point-particle approach of [4] and refined in [13].

5.1.12 Discussion

We have considered in detail the issue of the detectability of binary system of black holes having equal masses and spins that are aligned with the orbital angular momentum. Because these configurations do not exhibit precession effects, they represent a natural ground to start detailed studies of the influence of strong-field spin effects on gravitational wave observations of coalescing binaries. Furthermore, such systems may be the preferred end-state of the inspiral of generic supermassive binary black-hole systems [201–203]. In view of this, we have computed the inspiral and merger of a large set of binary systems of equal-mass black holes with spins parallel to the orbital angular momentum but otherwise arbitrary. Attention is, thus, focused on the gravitational-wave emission so as to provide answers to questions such as what are the "loudest" and "quietest" configurations and what is the difference in SNR between the two.

Overall we find that the SNR ratio increases with the projection of the total black hole spin in the direction of the orbital momentum. In addition, equal-spin binaries with maximum spin aligned with the orbital angular momentum are more than "three times as loud" as the corresponding binaries with anti-aligned spins, thus corresponding to event rates up to 27 times larger. On average these considerations are only weakly dependent on the detectors, or on the number of harmonics considered in constructing the signal.

We have also investigated whether these binaries can lead to a degenerate patch in the space of templates. We do this by computing the mismatch between the different spinning configurations. Within our numerical accuracy we have found that binaries with opposite spins $\boldsymbol{S}_1 = -\boldsymbol{S}_2$ cannot be distinguished, whereas binaries with spin $\boldsymbol{S}_1 = \boldsymbol{S}_2$ have clearly distinct gravitational-wave emissions. This result may represent a serious obstacle towards a proper estimate of the physical parameters of binaries and will probably be removed only if the SNR is sufficiently high.

Finally, we have derived a simple expression for the energy radiated in gravitational waves, and find that the binaries always have efficiencies $E_{\rm rad}/M \gtrsim 3.6\%$. This can become as large as $E_{\rm rad}/M \simeq 10\%$ for maximally spinning binaries with spins aligned to the orbital angular momentum.

5.2 Spin Templates

Building on the simulations and analysis preformed in Chapter [4] and on the analysis performed in the previous section, we present the first analytical inspiral-merger-ringdown gravitational waveforms from black-hole (BH) binaries with non-precessing spins. By matching a post-Newtonian description of the inspiral to a set of numerical calculations performed in full general relativity, we obtain a waveform family with a conveniently small number of physical parameters. The physical content of these waveforms includes the "orbital hang-up" effect, when BHs are spinning rapidly along the direction of the orbital angular momentum. These waveforms will allow us to detect a larger parameter space of BH binary coalescence, to explore various scientific questions related to GW astronomy, and could dramatically improve the expected detection rates of GW detectors.

As discussed in Section [2.2], while the *inspiral* and *ring-down* stages of the BH coalescence are well-modeled by perturbative techniques, an accurate description of the *merger* requires numerical solutions of Einstein's equations. Although performing numerical simulations over the entire parameter space of BH coalescence is computationally prohibitive, waveform templates modeling all three stages of BH coalescence can be constructed from existing simulation and PN data by combining those

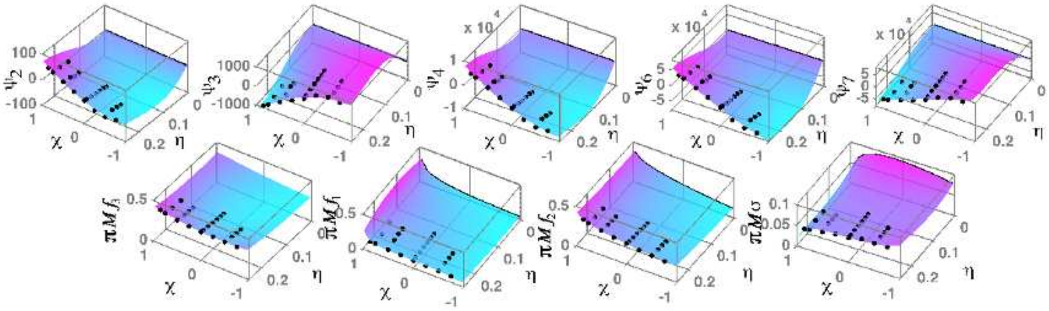

Figure 5.12: Phenomenological parameters ψ_k, f_1, f_2, f_3 and σ computed from the *equal-spin* hybrid waveforms (dots), and the analytical fits given by Eq. (5.32) (surfaces). Test-mass limit is indicated by black traces. η is the symmetric mass ratio and χ is the spin parameter.

analytical- and numerical-relativity results. Thus dramatically improving the sensitivity of searches for GWs from BH binaries, and the accuracy of estimating the source parameters [7, 14, 243, 244]. To date, "complete" inspiral-merger-ringdown (IMR) templates have been computed only for nonspinning BH binaries [7, 14, 15, 209, 244], which are effectively employed in GW searches, and in a number of astrophysical studies [245–247]. However, nonspinning BHs are expected to be astrophysically rare, and most BHs in nature may be highly spinning [248–250]. This necessitates the inclusion of spinning-binary waveforms in detector searches.

In this section, I present an inspiral-merger-ringdown (IMR) waveform family modelling the dominant harmonic of binaries with non-precessing spins (i.e., spins parallel/anti-parallel to the orbital angular momentum). These waveforms will significantly improve the "distance reach" of present and future GW detectors and will facilitate various astrophysical studies. Aligned-spin binaries are an astrophysically interesting population as such systems are expected from isolated binary evolution and in gas-rich galactic mergers [201–203]. Such systems also exhibit important strong-gravity effects like the "orbital hang-up". We make use of the degeneracies in the physical parameters to parametrize our waveform family by only the total mass $M \equiv m_1 + m_2$ of the binary, the symmetric mass ratio $\eta \equiv m_1 m_2/M^2$, and a *single* spin parameter $\chi \equiv (1+\delta)\,\chi_1/2 + (1-\delta)\,\chi_2/2$, where $\delta \equiv (m_1 - m_2)/M$ and $\chi_i \equiv S_i/m_i^2$, S_i being the spin angular momentum of the ith BH. The last feature is motivated by the observation (see e.g., [251]) that the leading spin-orbit-coupling term in post-Newtonian waveforms is dominated by this parameter.

5.2.1 Numerical simulations

Binary BH (BBH) waveforms covering at least eight cycles before merger were produced by solving the full Einstein equations numerically, as written in the "moving-puncture" 3+1 formulation described in Section [2.4.4]. The numerical solutions were calculated with the `BAM` [153, 252] and `Cactus` described in Section [2.7] codes, starting with initial data that model BHs with conformally flat punctures [49, 61]. Initial momenta were chosen to give low-eccentricity inspiral, using either an extension of the method described in [88], or the quasicircular formula used in [253]. GWs were extracted at $R_{ex} = 90M$ with `BAM` and $R_{ex} = 160M$ with `Cactus`, using the procedures discussed in Section [2.6.3]. In all simulations the GW amplitude is accurate to within at least 10% and the phase accurate to within at least 1 radian over the duration of the simulation. Studies in the equal-mass nonspinning case suggest that these waveforms are within the accuracy requirements for both GW detection and source parameter estimation with the current LIGO and Virgo detectors as shown in Section [5.1].

Five sets of simulations were used in this paper:

1. Equal-mass binaries with spins equal and parallel to the binary's orbital angular momentum, with $\chi_i = \pm\{0.25, 0.5, 0.75, 0.85\}$.
2. The same general non-precessing spin configuration, but using *unequal-mass* binaries with $q \equiv m_1/m_2 = \{2, 2.5, 3\}$ and $\chi_i = \{\pm 0.5, 0.75\}$.
3. Nonspinning binaries with $q = \{1, 1.5, 2, 2.5, 3, 3.5, 4\}$.
4. Unequal-mass, unequal-spin binaries with $q = \{2, 3\}$ and $(\chi_1, \chi_2) = (-0.75, 0.75)$.
5. Equal-mass, unequal-spin binaries with $\chi_i = \pm\{0.2, 0.3, 0.4, 0.6\}$.

The simulation sets (1)–(4) were performed with the `BAM` code, while set (5) was performed with the `Cactus` code. The analytical waveform family is constructed *only* employing the equal-spin simulation sets (1)–(3), while sets (4) and (5) were used to test the efficacy of the template family to model the expected signals from more general spin/mass configurations.

5.2.2 Constructing hybrid waveforms

Following [14, 209], we produce a set of "hybrid waveforms" by matching post-Newtonian (PN) and numerical-relativity (NR) waveforms in an overlapping time interval $[t_1, t_2]$. These hybrids are assumed to be the target signals that we want to detect. For the PN inspiral waveforms we choose the "TaylorT1" approximant [254] waveforms at 3.5PN [228] phase accuracy. This is motivated by PN-NR comparisons of equal-mass spinning binaries, in which the accuracy of the TaylorT1 approximant was found to be the most robust [208, 225]. We include the 3PN amplitude corrections to the dominant quadrupole mode [234] and the 2.5PN spin-dependent corrections [251], which greatly improved the agreement between PN and NR waveforms.

If $\mathsf{h}(t) = h_+(t) - \mathrm{i}h_\times(t)$ denote the time-domain waveform from a binary, we match the PN and NR waveforms, $\mathsf{h}^{\mathrm{PN}}(t)$ and $\mathsf{h}^{\mathrm{NR}}(t)$, by minimizing their integrated squared difference,

$$\mathcal{D} \equiv \min_{\Delta t, \Delta\varphi_0, a} \int_{t_1}^{t_2} \left| \mathsf{h}^{\mathrm{PN}}(t + \Delta t, \varphi_0 + \Delta\varphi_0) - a\, \mathsf{h}^{\mathrm{NR}}(t, \varphi_0) \right|^2 \left(\partial_t - \mathcal{L}_\beta\right) , \qquad (5.30)$$

where φ_0 is the initial phase of the wave and a is a scale factor that reduces the PN-NR amplitude difference. The NR waveforms are combined with the "best-matched" PN

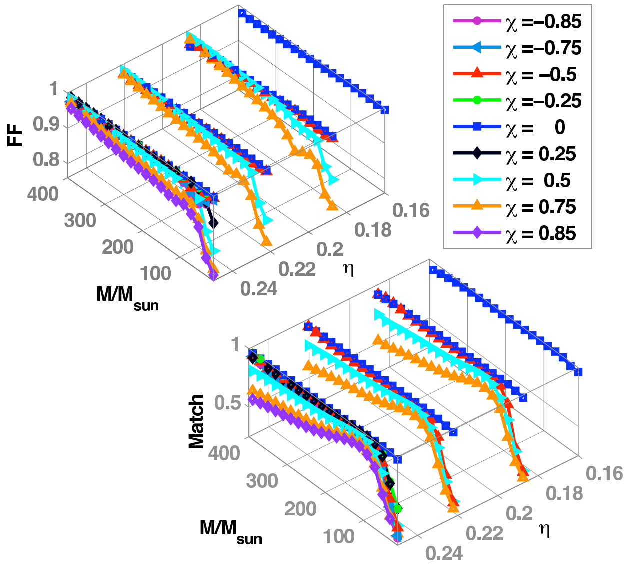

Figure 5.13: Fitting factor and faithfulness (in LIGO noise spectrum) of non-spinning phenomenological templates with spinning hybrid waveforms constructed from NR simulations sets (1), (2) and (3).

waveforms in the following way: $\mathsf{h}^{\rm hyb}(t) \equiv a\tau(t)\,\mathsf{h}^{\rm NR}(t) + (1-\tau(t))\,\mathsf{h}^{\rm PN}(t)$, where τ ranges linearly from zero to one for $t \in [t_1, t_2]$.

5.2.3 Efficiency of non-spinning IMR templates to search for binaries with non-precessing spins

It has been shown that PN inspiral signals from binaries with non-precessing spins can be detected using non-spinning PN templates without significant loss of SNR [255]. Here we show that, in the case of complete coalescence signals, significant loss of SNR is incurred upon neglecting the spin effects even in the absence of spin-induced precession. As a demonstration, we estimate the efficiency of the non-spinning IMR templates proposed in Refs. [14, 15, 209] in detecting GWs from binaries with non-precessing spins by computing the *fitting factor* [256] (FF) and *faithfulness* [236] of the non-spinning templates with the spinning hybrid waveforms discussed previously (Fig. 5.16). Given a target waveform, FF is the maximized *match* [257] between the target and templates drawn from the template bank, while the faithfulness is measured by taking the match between the target and the template with the same physical parameters. Note that the standard criteria for templates used in searches is that the FF exceed 0.97, which corresponds to a loss of no more than 10% of signals due to mismatch of signal and templates. FFs as low as 0.8 suggest that ∼50% binaries may go undetected if nonspinning IMR templates are employed to search for binaries with high spins (in the hang up configuration), while faithfulness as low as 0.3 suggest that the estimated parameters will be significantly biased.

5.2.4 Waveform templates for non-precessing binaries

The analytical waveforms family to model GWs from binaries with non-precessing spins that we construct can be written in the Fourier domain as $h(f) \equiv A(f)\, e^{-\mathrm{i}\Psi(f)}$, where

$$\begin{aligned} A(f) &\equiv C f_1^{-7/6} \begin{cases} f'^{-7/6}\,(1+\sum_{i=2}^{3}\alpha_i\, v^i) & \text{if } f < f_1 \\ w_m\, f'^{-2/3}\,(1+\sum_{i=1}^{2}\epsilon_i\, v^i) & \text{if } f_1 \le f < f_2 \\ w_r\, \mathcal{L}(f, f_2, \sigma) & \text{if } f_2 \le f < f_3, \end{cases} \\ \Psi(f) &\equiv 2\pi f t_0 + \varphi_0 + \frac{3}{128\eta v^5}\big(1+\sum_{k=2}^{7} v^k\, \psi_k\big). \end{aligned} \tag{5.31}$$

In the above expressions, $f' \equiv f/f_1$, $v \equiv (\pi M f)^{1/3}$, $\epsilon_1 = 1.4547\,\chi - 1.8897, \epsilon_2 = -1.8153\,\chi + 1.6557$, C is a numerical constant whose value depends on the sky-location and orientation of the binary as well as M and η, α_i ($\alpha_2 = -323/224 + 451\,\eta/168$ and $\alpha_3 = (27/8 - 11\,\eta/6)\chi$) are the PN corrections to the Fourier domain amplitude of the ($\ell = m = \pm 2$ mode) PN inspiral waveform [251], t_0 is the time of arrival of the signal at the detector and φ_0 the corresponding phase, $\mathcal{L}(f, f_2, \sigma)$ a Lorentzian function with width σ centered around the frequency f_2, w_m and w_r are normalization constants chosen so as to make $A(f)$ continuous across the "transition" frequencies f_2 and f_1, and f_3 is a convenient cutoff frequency such that the power of the signal above this frequency is negligible. The phenomenological parameters $\mu_j = \{f_1, f_2, \sigma, f_3\}$ and ψ_k are written in terms of the physical parameters of the binary as:

$$\begin{aligned} \pi M \mu_j &= a_0^j + a_1^j\,\eta + a_2^j\,\eta^2 + b_1^j\,\chi + c_{11}^j \eta\chi + c_{21}^j\,\eta^2\chi + b_2^j\,\chi^2 \\ &+ c_{12}^j\,\eta\chi^2 + +c_{22}^j\,\eta^2\chi^2 + b_3^j\,\chi^3 + c_{13}^j\,\eta\chi^3 + b_4^j\,\chi^4, \\ \psi_k &= a_0^k + a_1^k\,\eta + a_2^k\,\eta^2 + b_1^k\,\chi + c_{11}^k\,\eta\,\chi + c_{21}^k\,\eta^2\,\chi \\ &+ b_2^k\,\chi^2 + c_{12}^k\,\eta\,\chi^2 + c_{22}^k\,\eta^2\,\chi^2 + b_3^k\,\chi^3 + c_{13}^k\,\eta\,\chi^3, \\ \psi_k &= \sum_{i=1}^{3}\sum_{j=0}^{N} x_k^{(ij)} \nu^i \chi^j\,, \qquad \mu_k = \sum_{i=1}^{3}\sum_{j=0}^{N} \frac{y_k^{(ij)} \nu^i \chi^j}{\pi M}\,, \end{aligned} \tag{5.32}$$

where $N \equiv \min(3-i, 2)$ while $x_k^{(ij)}$ and $y_k^{(ij)}$ are tabulated in Table 5.6. Figure 5.12 plots the values of ψ_k and μ_j estimated from the hybrid waveforms, as well as the fits given by Eq. (5.32).

We match these waveforms to 2PN accurate adiabatic inspiral waveforms in the extreme-mass-ratio limit. These Fourier-domain waveforms are constructed from a PN expansion of the (exact) binding energy given in Ref. [258] and the 4PN-accurate GW luminosity given in Ref. [259]. In the $\eta \to 0$ limit, the phenomenological parameters reduce to the following quantities:

$$f_1 \to f_{\mathrm{ISCO}}, \;\; f_2 \to f_{\mathrm{QNM}}, \;\; \sigma \to f_{\mathrm{QNM}}/Q, \;\; \psi_k \to \psi_k^0, \tag{5.33}$$

where f_{ISCO} and f_{QNM} are the frequencies of the innermost stable circular orbit [258] and the dominant quasi-normal mode, and Q is the ring-down quality factor [260] of a

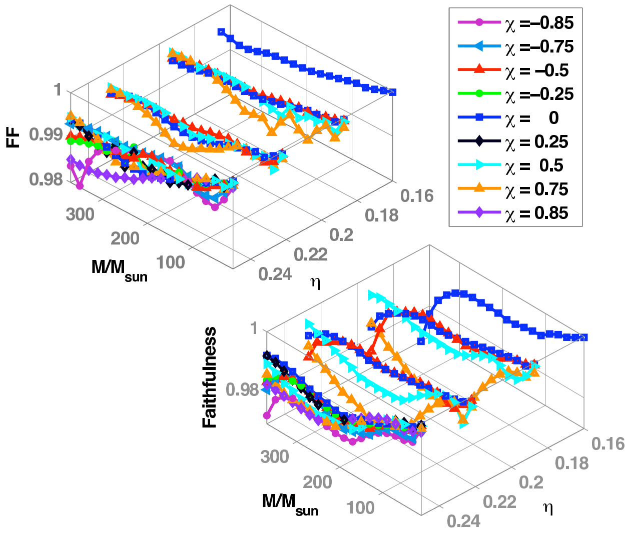

Figure 5.14: Fitting factor and faithfulness of the spinning templates with *equal-spin* hybrid waveforms (using Initial LIGO noise spectrum).

Kerr BH with mass M and spin χ, while ψ_k^0 are the Fourier domain phasing coefficients of a test-particle inspiralling into the Kerr BH, computed using the stationary-phase approximation.

The test-particle-limit waveforms suffer from two limitations: 1) we assume that the evolution of the GW phase at the merger and ringdown stages is a continuation of the adiabatic inspiral phase, and 2) in the absence of a reliable model for plunge, we approximate the amplitude of the plunge with $f'^{-2/3}\,(1+\sum_{i=1}^{2}\epsilon_i\,v^i)$. Nevertheless, in the test-mass limit, it is expected that the signal will be dominated by the long inspiral stage (followed by a quick plunge and ringdown), and the inspiral is guaranteed to be well-modelled by our waveform family. More importantly, the imposition of the appropriate test-mass limit in our fitting procedure ensures that the waveforms are well behaved even outside the parameter range where current NR data are available. Because of this, and the inclusion of the PN amplitude corrections, these waveforms are expected to be closer to the actual signals than the templates proposed in [14, 15] in the non-spinning limit (thus explaining the difference between the two waveform families).

5.2.5 Efficiency of the new templates

We have examined the "faithfulness" of the new templates in reproducing the hybrid waveforms by computing the *match* (noise-weighted inner product) with the hybrids. Loss of the SNR due to the "mismatch" between the template and the true signal is determined by the match maximized over the whole template bank – called *fitting factor* (FF). The standard criteria for templates used in searches is that FF > 0.97, which corresponds to a loss of no more than 10% of signals.

Match and FF of the analytical waveforms with the equal- (unequal-) spin hybrid waveforms are plotted in Fig. 5.14 (Fig. 5.15), using Initial LIGO design noise spec-

	a_0^k	a_1^k	a_2^k	b_1^k	c_{11}^k	c_{21}^k	b_2^k	c_{12}^k	c_{22}^k	b_3^k	c_{13}^k
ψ_0	$\frac{3}{128}$	0.0646073	-0.224362	0	-0.0716615	0.163815	0	-0.0516322	0.138573	0	-0.0215617
ψ_2	$\frac{3715}{32256}$	-22.6941	74.1756	0	25.8917	-59.3562	0	11.3617	-29.9764	0	6.82523
ψ_3	$-\frac{3\pi}{8}$	311.778	-975.843	$\frac{113}{128}$	-360.174	825.57	0	-99.9086	254.819	0	-87.6832
ψ_4	$\frac{15293365}{21676032}$	-1926.1	5810.99	0	2277.21	-5240.68	$-\frac{1215}{1024}$	238.604	-504.838	0	511.14
ψ_6	-6.52151	-12022.7	33859.1	$\frac{1135\pi}{64}$	15849.8	-36586.5	$\frac{75515}{12288}$	-4201.5	13246.1	0	3011.27
ψ_7	$\frac{77096675\pi}{10838016}$	10887.1	-30453.7	$-\frac{25150083775}{130056192}$	-14481.1	33615.9	$-\frac{2445\pi}{256}$	7029.33	-21536.9	$\frac{14585}{1024}$	-3011.14

	a_0^k	a_1^k	a_2^k	b_1^k	c_{11}^k	c_{21}^k	b_2^k	c_{12}^k	c_{22}^k	b_3^k	c_{13}^k	b_4^k
$f_{\rm cut}$	0.2444	0.2234	0.9619	0.05705	-0.1312	-0.0298	-0.002173	1.737	-6.862	0.02415	0.286	0.03336
$f_{\rm merg}$	0.06827	0.08025	-0.4084	0.04278	-0.8408	2.29	0.02721	-0.6356	1.243	0.06494	-0.2461	0.05771
$f_{\rm ring}$	0.1857	-0.1874	1.838	0.0905	-0.3844	0.9942	0.02188	0.6775	-2.859	0.03691	0.1113	0.03826
σ	0.09171	0.01898	-0.5766	0.007786	0.1434	-0.3237	-0.00496	-0.7896	3.608	-0.01951	-0.205	-0.02738

Table 5.6: Coefficients describing the amplitude and phase of the phenomenological waveforms. See Eq. (5.32).

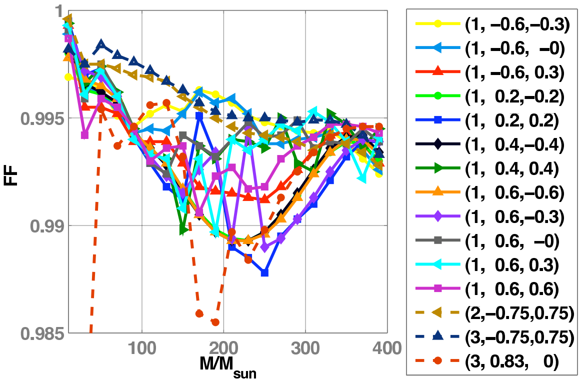

Figure 5.15: Fitting factor of the spinning templates with *unequal-spin* hybrid waveforms (using Initial LIGO noise spectrum). Parameters (q, χ_1, χ_2) of the hybrid waveforms are shown in legends.

trum [261]. Note that the analytical waveform family is constructed employing *only* the equal-spin hybrid waveforms. The PN–NR matching region used to construct the unequal-spin hybrids are also different from that used for equal-spin hybrids. These figures demonstrate the efficacy of the analytical templates in reproducing the target waveforms – templates are "faithful" (match $>$ 0.97) *either* when the masses *or* the spins are equal, while they are *always* "effectual" in detection (FF $>$ 0.97). These figures may be contrasted with Fig. 5.16, which details the effect of neglecting spin in the construction of the templates. This figure plots the matches of the non-spinning IMR template family proposed in [14, 15] with the equal-spin hybrid waveforms. FFs as low as 0.8 suggest that up to 50% binaries may go undetected if nonspinning IMR templates are employed to search for binaries with high spins (in the "hang-up" configuration), while matches as low as 0.3 suggest that the estimated parameters will be significantly biased.

Effective distance to optimally oriented BBHs (modeled by the new templates) producing optimal SNR of 8 at Initial LIGO noise spectrum is shown in Fig. 5.17, which demonstrates the dramatic effect of spin for detection of high-mass binaries; if most BBHs are highly spinning, then LIGO will be able to detect BH coalescences up to 1Gpc, thus increasing the event rates as much as five times compared to predictions based on models of nonspinning binaries. For Enhanced LIGO/Advanced LIGO detectors, the peak horizon distances are 2Gpc/19Gpc and similar improvements over the nonspinning templates are found.

5.2.6 Discussion

We find that as many as 50% of signals may be lost when non-spinning IMR templates are used to search for binaries with non-precessing spins aligned to the angular momentum. To address the need for spinning IMR templates, we combine state-of-the-art results from analytical and numerical relativity to construct for the first time a family of analytical IMR waveforms for BBHs with non-precessing spins from "first principles". These templates do not contain unphysical parameters, and we show that for the purposes of GW detection it is sufficient to represent the spins by a single parameter. This will considerably sim-

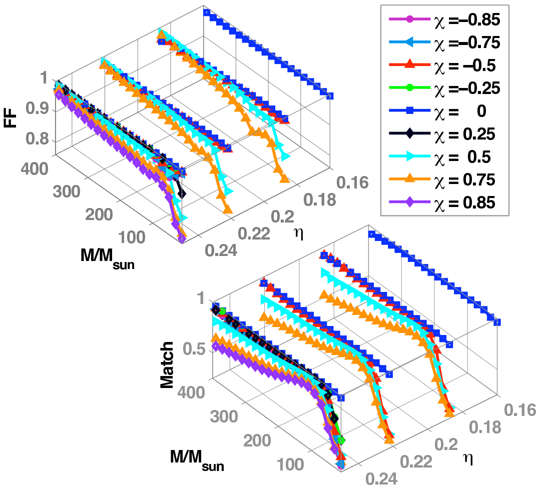

Figure 5.16: Match and FF of *non-spinning* IMR templates proposed in [14,15] with the equal-spin hybrid waveforms. A comparison with Fig. 5.15 demonstrates the effect of neglecting spins.

plify the use of our waveforms in GW searches in the near future. This method can readily be generalized to incorporate non-quadrupole spherical-harmonic modes, larger portions of the binary BH parameter space and further information from analytical approximation methods or numerical simulations which are more accurate or extend the parameter space. This will significantly accelerate the incorporation of NR results into the current effort for the first direct detection of GW signals. There are many other immediate applications of our waveforms: injections into detector data will help to put more realistic upper limits on the rate of BBH coalescences [245, 246] (thus directly leading to astrophysical results), and to compare the different algorithms employed in the search for GWs from BBHs [210], while employing these in population-synthesis studies will provide more accurate coalescence rates observable by the current and future detectors. Comparisons with precessing waveforms will help us to understand the implications of spin precession for detecting binaries with larger masses, and the waveforms will be used to characterize the effect of (non-precessing) spins in the parameter-estimation of BH binaries.

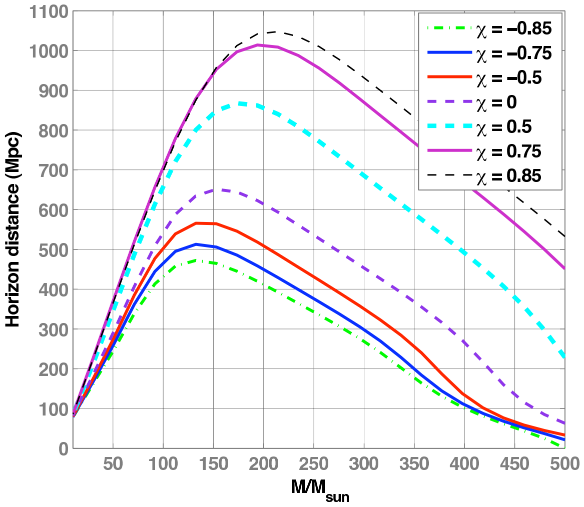

Figure 5.17: Effective distance to optimally-oriented, equal-mass binaries with (equal) spin χ producing optimal SNR 8 in Initial LIGO.

Chapter 6

Conclusions

Coalescing black-hole (BH) binaries are among the most promising candidate sources for the first direct detection of gravitational waves (GWs). Such observations will lead to precision tests of the strong-field predictions of general relativity as well as provide a wealth of information relevant to fundamental physics, astrophysics, and cosmology [262]. Computation of the expected waveforms from such sources is a key goal in current gravitational research. The results in this thesis are steps to assist in this process.

6.1 Boundary Conditions

Besides the importance of having a well-posed system, there is a practical consequence of defining correct conditions at the boundary. This is the fact that this choice allows one to place the boundary conditions, in principle, in any place where the linearized assumptions hold, thus reducing the need for making large numerical grids with the consequence of savings in computational resource requirements needed to simulate a given problem.

I have examined the initial boundary value problem for the second-order formulation of the Einstein equations in the generalized harmonic gauge. The system of evolution equations for this finite-difference harmonic code was derived in [40] where it was shown to be accurate, stable, and convergent for long-term evolutions of black hole space-times, such as head-on collisions of two black holes, isolated black holes, and binary black hole inspiral and merger. I described the derivation, implementation and testing of a new boundary treatment for this system. I demonstrated that this new treatment maintained the validity and convergence (to lower order) seen with the standard boundary treatments. I additionally showed that these conditions give us greater accuracy (for all reasonable resolutions), improved constraint preservation, improved boundary transparency, and greater stability in robust stability tests.

I have derived boundary conditions that preserve the constraints and lead to a well-posed initial-boundary value problem for the BSSN formulation based on the work of Dario Nuñez and Olivier Sarbach. These conditions are given in terms of the variable fields and its derivatives at the boundary. I have shown that the final system is indeed symmetric hyperbolic and preserves the constraints in the linear, constant coeeficient limit for conformally flat data. I have also given a discussion related the numerical implementation of these boundary conditions. Unlike standard methods, one does not over-specify the conditions on the boundary surface for the method proposed in Section [3.2].

With binary black hole evolutions now extending over multiple orbits, and thus many crossing times on conventional computational grids, boundary effects can potentially have a non-trivial influence on the late-time dynamics and extracted gravitational wave signals from such simulations. For sufficiently distant boundaries in the linearized regime, the boundary conditions described in the present work will help to make the numerical evolutions of relativistic spacetimes more robust. In terms of practical gain, there is still much work to be done in order to quantify the importance of using adequate boundary conditions. However, any improvement in accuracy and efficiency is a valuable contribution for the current state of the field of numerical relativity.

6.2 Physics

Using the results from a number of numerical simulations for binary black hole initial data, I have considered the spin vector of the BH produced by a BH binary merger as the sum of the two initial spins and of a third vector, parallel to the initial orbital angular momentum, and measures the orbital angular momentum not radiated. Without other fits than those already available to model aligned/antialigned binaries, I have measured the unknown vector and derived a formula that accounts for all of the 7 parameters describing a BH binary inspiralling in quasi-circular orbits. The equations (4.71) and (4.74), encapsulate the near-zone physics to provide a convenient, as well as robust and accurate prediction over a wide range of parameters, determination of the merger product of rather generic BH binaries.

Testing the formula against all of the available numerical data from recent publications and from our own simulations has revealed differences between the predicted and the simulated values of a few percent at most. This approach is intrinsically approximate and it has been validated on a small set of configurations. It can be improved: by reducing the χ^2 of the fitting coefficients as new simulations are carried out; by using fitting functions that are of higher-order than those in expressions (4.58) and (4.65); by estimating $\boldsymbol{J}^{\perp}_{\rm rad}$ through PN expressions or by measuring it via numerical simulations.

Overall, the data sample computed numerically consists of 38 values for $|v_{\rm kick}|$ and for $a_{\rm fin}$ which, for simplicity, we have considered to have constant error-bars of $8\ {\rm km/s}$ and 0.01, which represent, respectively, the largest errors reported in [87]. In both cases we have modelled the data with generic quadratic functions in a_1 and a_2 so that, in the case of the recoil velocity, the fitting function is

$$|v_{\rm kick}| = |c_0 + c_1 a_1 + c_2 a_1^2 + d_0 a_1 a_2 + d_1 a_2 + d_2 a_2^2|\,. \tag{6.1}$$

The fitting function on the right-hand-side of (6.1) is smooth everywhere but that its absolute value is not smooth along the diagonal $a_1 = a_2$. Using (6.1) and a blind least-square fit of the data, we obtained the coefficients (in ${\rm km/s}$) with a reduced-$\chi^2 = 0.09$. I can use the constraint that no recoil velocity should be produced for binaries having the same spin, *i.e.*, that $|v_{\rm kick}| = 0$ for $a_1 = a_2$, or the symmetry condition across the line $a_1 = a_2$. Enforcing both constraints yields

$$c_0 = 0\,, \quad c_1 = -d_1\,, \quad c_2 = -d_2\,, \quad d_0 = 0\,, \tag{6.2}$$

thus reducing the fitting function (6.1) to the simpler expression

$$|v_{\rm kick}| = |c_1(a_1 - a_2) + c_2(a_1^2 - a_2^2)|\,. \tag{6.3}$$

Performing a least-square fit using (6.3) we then obtain

$$c_1 = -220.97 \pm 0.78\,, \qquad c_2 = 45.52 \pm 2.99\,, \tag{6.4}$$

with a comparable reduced-$\chi^2 = 0.14$, but with error-bars that are much smaller on average. Because of this, we consider expression (6.3) as the best description of the data at second-order in the spin parameters.

In the same way we have first fitted the data for $a_{\rm fin}$, with a function

$$a_{\rm fin} = p_0 + p_1 a_1 + p_2 a_1^2 + q_0 a_1 a_2 + q_1 a_2 + q_2 a_2^2\,, \tag{6.5}$$

and found coefficients with very large error-bars. As a result, also for $a_{\rm fin}$ we resort to physical considerations to constrain the coefficients $p_0 \ldots q_2$. More specifically, at least at lowest order, binaries with equal and opposite spins will not contribute to the final spin and thus behave essentially as nonspinning binaries. Stated differently, we assume that $a_{\rm fin} = p_0$ for binaries with $a_1 = -a_2$. In addition, enforcing the symmetry condition across the line $a_1 = a_2$ we obtain

$$p_1 = q_1\,, \quad p_2 = q_2 = q_0/2\,, \tag{6.6}$$

so that the fitting function (6.5) effectively reduces to

$$a_{\rm fin} = p_0 + p_1(a_1 + a_2) + p_2(a_1 + a_2)^2\,. \tag{6.7}$$

Performing a least-square fit using (6.7) we then obtain

$$\begin{aligned} &p_0 = 0.6883 \pm 0.0003\,, \qquad p_1 = 0.1530 \pm 0.0004\,, \\ &p_2 = -0.0088 \pm 0.0005\,, \end{aligned} \tag{6.8}$$

with a reduced-$\chi^2 = 0.02$.

Being effectively a power series in terms of the initial spins of the two black holes, its zeroth-order term can be seen as the orbital angular momentum not radiated in gravitational waves and which amounts, at most, to $\sim 70\%$ of the final spin. The first-order term, on the other hand, can be seen as the contribution to the final spin coming from the initial spins of the two black holes and this contribution, together with the one coming from the spin-orbit coupling, amounts at most to $\sim 30\%$ of the final spin. Finally, the second-order term, which is natural to expect as nonzero in this view, can then be related to the spin-spin coupling, with a contribution to the final spin which is of $\sim 4\%$ at most.

We further performed simulations with an unequal masses and aligned spins (see Table 4.6) and obtained a third order polynomial fit for $|a_{\rm fin}|$ from arbitrary symmetric mass ratio $\nu \equiv M_1 M_2/(M_1+M_2)^2$ and the aligned equal spins of the initial BHs $a \equiv J/M^2$, *i.e.*, $a_{\rm fin} \equiv J_{\rm fin}/M^2_{\rm fin} = a_{\rm fin}(a,\, \nu)$

$$\begin{aligned} a_{\rm fin} = \quad & s_0 + s_1 a + s_2 a^2 + s_3 a^3 + s_4 a^2 \nu + s_5 a \nu^2 + \\ & t_0 a \nu + t_1 \nu + t_2 \nu^2 + t_3 \nu^3 \,. \end{aligned} \tag{6.9}$$

as shown in figure 4.17. Determining the remaining five coefficients from a least-square fit of the available data yielded

$$\begin{aligned} s_4 &= -0.129 \pm 0.012\,, & s_5 &= -0.384 \pm 0.261\,, \\ t_0 &= -2.686 \pm 0.065\,, & t_2 &= -3.454 \pm 0.132\,, \\ t_3 &= 2.353 \pm 0.548\,, \end{aligned} \tag{6.10}$$

we then ran simulations for misaligned spins (see table 4.7) and obtained a fit for arbitrary initial spins and mass ratio $q \equiv M_1/M_2$

$$\begin{aligned} |\boldsymbol{a}_{\rm fin}| = \frac{1}{(1+q)^2} \Big[& |\boldsymbol{a}_1|^2 + |\boldsymbol{a}_2|^2 q^4 + 2|\boldsymbol{a}_2||\boldsymbol{a}_1| q^2 \cos\alpha + \\ & 2\left(|\boldsymbol{a}_1|\cos\beta + |\boldsymbol{a}_2| q^2 \cos\gamma\right)|\boldsymbol{\ell}| q + |\boldsymbol{\ell}|^2 q^2 \Big]^{1/2}\,, \end{aligned} \tag{6.11}$$

where

$$\begin{aligned} |\boldsymbol{\ell}| = & \frac{s_4}{(1+q^2)^2}\left(|\boldsymbol{a}_1|^2 + |\boldsymbol{a}_2|^2 q^4 + 2|\boldsymbol{a}_1||\boldsymbol{a}_2| q^2 \cos\alpha\right) + \\ & \left(\frac{s_5 \nu + t_0 + 2}{1+q^2}\right)\left(|\boldsymbol{a}_1|\cos\beta + |\boldsymbol{a}_2| q^2 \cos\gamma\right) + \\ & 2\sqrt{3} + t_2 \nu + t_3 \nu^2 \,. \end{aligned} \tag{6.12}$$

These formulae give fairly accurate predictions for the final spin and kick of a merged black hole and will be useful for studies of the evolution of supermassive black holes and on statistical studies on the dynamics of compact objects in dense stellar systems, as well as significant effect on the waveform and impact on parameter estimation for gravitational wave detectors.

6.3 Analysis

We have considered in detail the issue of the detectability of binary system of black holes having equal masses and spins that are aligned with the orbital angular momentum. Such systems may be the preferred end-state of the inspiral of generic supermassive binary black-hole systems [201–203]. In view of this, we have computed the inspiral and merger of a large set of binary systems of equal-mass black holes with spins parallel to the orbital angular momentum but otherwise arbitrary. Attention is, thus, focused on the gravitational-wave emission so as to provide answers to questions such as what are the "loudest" and "quietest" configurations and what is the difference in SNR between the two.

Overall we find that the SNR ratio increases with the projection of the total black hole spin in the direction of the orbital momentum. In addition, equal-spin binaries with maximum spin aligned with the orbital angular momentum are more than "three times as loud" as the corresponding binaries with anti-aligned spins, thus corresponding to event rates up to 27 times larger. On average these considerations are only weakly dependent on the detectors, or on the number of harmonics considered in constructing the signal.

We have also investigated whether these binaries can lead to a degenerate patch in the space of templates. We do this by computing the mismatch between the different spinning configurations. Within our numerical accuracy we have found that binaries with opposite spins $\boldsymbol{S}_1 = -\boldsymbol{S}_2$ cannot be distinguished, whereas binaries with spin $\boldsymbol{S}_1 = \boldsymbol{S}_2$ have clearly distinct gravitational-wave emissions. This result may represent a serious obstacle towards a proper estimate of the physical parameters of binaries and will probably be removed only if the SNR is sufficiently high.

We find that as many as 50% of signals may be lost when non-spinning IMR templates are used to search for binaries with non-precessing spins aligned to the angular momentum. To address the need for spinning IMR templates, we combine state-of-the-art results from analytical and numerical relativity to construct for the first time a family of analytical IMR waveforms for BBHs with non-precessing spins from "first principles". These templates do not contain unphysical parameters, and we show that for the purposes of GW detection it is sufficient to represent the spins by a single parameter. This will considerably simplify the use of our waveforms in GW searches in the near future. This method can readily be generalized to incorporate non-quadrupole spherical-harmonic modes, larger portions of the binary BH parameter space and further information from analytical approximation methods or numerical simulations which are more accurate or extend the parameter space. This will significantly accelerate the incorporation of NR results into the current effort for the first direct detection of GW signals. There are many other immediate applications of our waveforms: injections into detector data will help to put more realistic upper limits on the rate of BBH coalescences [245, 246] (thus directly leading to astrophysical results), and to compare the different algorithms employed in the search for GWs from BBHs [210], while employing these in population-synthesis studies will provide more accurate coalescence rates observable by the current and future detectors. Comparisons with precessing waveforms will help us to understand the implications of spin precession for detecting binaries with larger masses, and the waveforms will be used to characterize the effect of (non-precessing) spins in the parameter-estimation of BH binaries.

Appendix A

Appendix

A.1 Well-posed boundary terms with SAT

Consider a domain represented by a discrete grid consisting of points $i = i_{min} \dots i_{max}$ and gridspacing $h = \frac{b-a}{i_{max}-i_{min}}$ covering $x \in [a, b]$. A 1D difference operator D on such a domain is said to satisfy SBP with respect to a scalar product (defined by its coefficients σ_{ij})

$$E = \langle u, v \rangle = h \sum_{ij} u_i \cdot v_j \sigma_{ij}, \tag{A.1}$$

if the property

$$\langle u, Dv \rangle + \langle v, Du \rangle = (u \cdot v) \mid_a^b \tag{A.2}$$

holds for all gridfunctions $u, v \in L^2[a, b]$. The scalar product is diagonal if $\sigma_{ij} = \sigma_{ij}\delta_{i,j}$. One advantage of 1D difference operators satisfying SBP with diagonal norms is that SBP is guaranteed to hold in several dimensions if the 1D operator is used on each direction (which is not known to hold in the non-diagonal case in general).

For the advection equation $\partial_t u = \partial_x u$ the semidiscrete equation with penalty term is written as

$$\dot{u}_i = \Lambda D u_i + \frac{\delta_{i,0} T}{h \sigma_{00}} (g - u_0). \tag{A.3}$$

Defining the energy as $E = \langle u, u \rangle$, and defining it's time derivative as

$$\dot{E} = (\Lambda - 2T) u_0^2 + 2 g u_0 T, \leq (\Lambda - T) u_0^2 + T g^2. \tag{A.4}$$

With positive speed, we can take $T = \Lambda + \delta_{i,0}$. For $g = 0$, we have $\dot{E} = (\Lambda - 2T) u_0^2$, thus showing that the energy won't increase.

Having a 1D operator that satisfies SBP with respect to a diagonal scalar product $\Sigma = (\sigma_{ij}) = \delta_{ij}\sigma_i$, one can construct a 3D operator by simply applying the 1D difference operator to each direction. The resulting 3D operator satisfies SBP with respect to a diagonal scalar product

$$(u, v)_\Sigma = h_x h_y h_z \sum_{ijk} \sigma_{ijk} u_{ijk} \cdot v_{ijk},$$

with $\sigma_{ijk} = \sigma_i \sigma_j \sigma_k$. Defining a 3D difference operator by just applying this one-dimensional one to each direction will satisfy SBP with respect to the trivial 3D scalar product.

Then, for some boundary conditions, the 3D semidiscrete equation for the 3D advection may be written as:

$$\dot{u}_{ijk} = \Lambda_l D u_{ijk} + \frac{\delta_{i,0} T}{h \sigma_{x00}} (g_x - u_{x0}) + \frac{\delta_{j,0} T}{h \sigma_{y00}} (g_z - u_{y0}) + \frac{\delta_{k,0} T}{h \sigma_{z00}} (g_z - u_{z0}). \quad \text{(A.5)}$$

Now we consider the system of Equations $\dot{u} = A^\mu \partial_\mu u = A^x \partial_x u + A^y \partial_y u$, where u is a vector-valued function and, A^x, and A^y are symmetric and constant coefficient matrices.

The 3D scalar product is defined as the product of the scalar product on each direction,

$$E = \langle u, v \rangle = h_x h_y \sum ij (u_{ij}, v_{ij}) \sigma_{(x)i} \sigma_{y(j)}, \quad \text{(A.6)}$$

where (u, v) is the Euclidean scalar product of two vectors. Then the semidiscrete equation with a SAT penalty term is:

$$\dot{u}_{ij} = A^\mu \partial_\mu u_{ij} - \frac{T}{h_y \sigma_{(y)j=0}} u_{i0}$$

and the time derivative of the energy of the system is then:

$$\dot{E} = h_x \sum i \sigma_{(x)i} [(u_{i,0}, (A^\mu - 2T) u_{i,0}]$$

With positive speed, we can take $T = \Lambda + \delta$. For $g_i = 0$, we have $\dot{E} = (A^\mu - 2T) u_{i,0}^2$, thus showing that the energy won't increase.

A.1.1 Second Derivatives

The first derivative operator works as in the 1D case, except at boundary edges and corners. SBP applied to the energy method will give a specific solution for the penalty term at the boundaries, as this depends on the space of the equations, I will give the wave equation solution in the next section. The second derivative is the same except that there is the question of the value of

$$D_2 = H^{-1}(-D_1^T H D_1 + BS) = H^{-1}(-A + BS) \quad \text{(A.7)}$$

for mixed coordinates ($D_2 = D_{ij}$ for $i \neq j$). These terms are derived in Section [3.1.1].

First I will introduce the terminology:

- S_i is the approximation of the first derivative operator at the boundaries. "S" is for stencil.

- $Q_i + Q_i^t = B_i = diag(-1, 0..., 1)$.
- $A_{ij} = D_i^T H D_j$ represents the part of the second derivative that is the square of the of the first derivative without a penalty term.
- $D_{+i} = H^{-1}(Q_i + R_i)$ is the upwind first derivative term.
- $D_{-i} = H^{-1}(Q_i - R_i)$ is the downwind first derivative term.
- $DI_i = H^{-1} R_i$ is the artificial dissipation term ($R = R^T$).

With this notation we use the second semidiscrete derivatives:

$$\begin{aligned}
D_{ii}^{(u)} &= \frac{1}{2}(D_{+i}D_{-i} + D_{-i}D_{+i}) = H^{-1}(-D_i^T H D_i + B_i D_i) - DI_i^T H DI_i \qquad \text{(A.8)} \\
D_{ij}^{(u)} &= \frac{1}{2}(D_i D_j + D_j D_i) = \frac{1}{4}[(D_{+i}D_{-j} + D_{-i}D_{+j}) + (D_{+j}D_{-i} + D_{-j}D_{+i})] \\
&= \frac{1}{4}H^{-1}[(Q_i + R_i)^T(Q_j - R_j) + (Q_i - R_i)^T(Q_j + R_j) \\
&+ (Q_j + R_j)^T(Q_i - R_i) + (Q_j - R_j)^T(Q_i + R_i)] \\
&= \frac{1}{2}H^{-1}[(Q_i^T Q_j + Q_j^T Q_i) - (R_i^T R_j + R_j^T R_i)] \\
&= \frac{1}{2}[(A_{ij} + A_{ji}) - (DI_i^T H DI_j + DI_j^T H DI_i)]
\end{aligned}$$

for the unmixed and mixed second derivatives, respectively.

A.1.2 Wave Equation in Flat Space

Here, as an instructive example, I will show the derivation of simultaneous approximation penatly terms (SAT) to enforce conservation of energy to ensure well posedness with artificial outer boundaries. The energy method applied to the wave equation in flat space $u_{tt} = u_{xx} + u_{yy} + u_{zz}$ gives:

$$\frac{d}{dt}\left(\|u_t\|^2 + \|u_x\|^2 + \|u_y\|^2 + \|u_z\|^2\right) = 2(u_t u_x \mid_{x=0}^{x=N_x} + u_t u_y \mid_{y=0}^{y=N_y} + u_t u_z \mid_{z=0}^{z=N_z}) \tag{A.9}$$

If we use the boundary conditions (assuming all g_0 and g_N are zero) then for the boundaries of $i = 0, 1 \ldots, N-1, N$

$$\begin{aligned}
[\delta_{i,0}(\alpha + D)_x + \delta_{j,0}(\alpha + D)_y + \delta_{k,0}(\alpha + D)_z]u_{ijk} &= -u_t(0)\,, \qquad \text{(A.10)} \\
[\delta_{i,N}(\beta + D)_x + \delta_{j,N}(\beta + D)_y + \delta_{k,N}(\beta + D)_z]u_{ijk} &= u_t(N)\,.
\end{aligned}$$

with $\alpha \leq 0$ and $\beta \geq 0$ so that an energy estimate is possible. The energy method leads to leads to:

$$\begin{gathered}\frac{d}{dt}\left(\|u_t\|^2 + \|u_x\|^2 + \|u_y\|^2 + \|u_z\|^2\right) = \\ (\langle u_t, u_{tt}\rangle + \langle u_{tt}, u_t\rangle) + (\langle u_i, u_{it}\rangle + \langle u_{it}, u_i\rangle) = \\ (\langle u_t, u_{ii}\rangle + \langle u_{ii}, u_t\rangle) + (\langle u_j, u_{jt}\rangle + \langle u_{jt}, u_j\rangle)\end{gathered} \tag{A.11}$$

By applying the SBP condition $\langle u, Dv\rangle + \langle v, Du\rangle = (uv) \mid_a^b$ this is:

$$\dot{E} = 2u_t u_i \mid_{x_i=0}^{x_i=N_i} \tag{A.12}$$

I do the same to the semidiscrete approximation of the wave equation in flat space

$$v_{tt} = H_{x_i}^{-1}(-A_{ii} + BS_i)v + \tau_0 H^{-1} E_0(\alpha_0 v_t + \beta_0 S_i v) + \tau_N H^{-1} E_N(\alpha_N v_t + \beta_N S_i v) \tag{A.13}$$

where are vectors of length N and $E_0^T = (1, 0, \ldots, 0)$ and $E_N^T = (0, 0, \ldots, 1)$. Applying the energy method I obtain

$$\dot{E} = 2u_t u_i \mid_{x_i=0}^{x_i=x_{N_i}} + 2\tau_0(\alpha_0 u_t^T E_0 u_t + \beta_0 u_t^T E_0 S_i u) + 2\tau_N(\alpha_N u_t^T E_N u_t + \beta_N u_t^T E_N S_i u) \tag{A.14}$$

In order to control the energy growth I must set the $u_t^T S_i u$ terms to zero, thus $\tau_0\beta_0 = 1$ and $\tau_N\beta_N = -1$. I also want $\tau_0(\alpha_0 L + \beta_0) = 1$ and $\tau_N(\alpha_N R + \beta_N) = -1$ for boundary conditions $u_t = \delta_{0,i} L u_i + \delta_{N,i} R u_i$ so for the wave equation I get

$$v_{tt} = H_{x_i}^{-1}(-A_{ii} + BS_i)v + H_{x_i}^{-1} E_0 S_i v - H_{x_i}^{-1} E_N S_i v \tag{A.15}$$

To prescribe boundary conditions at the corners and edges, you do not need a normal vector except for the spacing coefficient ($dx^2/(dx^2 + dy^2 + dz^2)$). One can just look at the contribution to the semidiscrete energy above from the edges (i.e. (x,y,z)=(0,0,z)) or corners (i.e. (x,y,z)=(0,0,N)).

A.1.3 Wave Equation in General

The energy method applied to the wave equation $u_{tt} = (\frac{-\gamma^{ij}}{\gamma^{tt}}\partial_i\partial_j - 2\frac{\gamma^{it}}{\gamma^{tt}}\partial_i\partial_t)u$ gives:

$$\begin{gathered}\frac{d}{dt}\left(\|u_t\|^2 + \|-\frac{\gamma^{ij}}{\gamma^{tt}} u_i u_j\|\right) = \\ (\langle u_t, u_{tt}\rangle + \langle u_{tt}, u_t\rangle) + -\frac{\gamma^{ij}}{\gamma^{tt}}(\langle u_i, u_{jt}\rangle + \langle u_{it}, u_j\rangle) = \\ -\frac{\gamma^{ij}}{\gamma^{tt}}(\langle u_t, u_{ij}\rangle + \langle u_{ij}, u_t\rangle + \langle u_i, u_{jt}\rangle + \langle u_{it}, u_j\rangle) - 2\frac{\gamma^{it}}{\gamma^{tt}}(\langle u_t, u_{it}\rangle + \langle u_{it}, u_t\rangle)\end{gathered} \tag{A.16}$$

By applying the SBP condition $\langle u, Dv\rangle + \langle v, Du\rangle = (uv)\mid_a^b$ this is:

$$\begin{aligned}\frac{\gamma^{ij}}{\gamma^{tt}}[(u_t^\top D_j u)\mid_{x_i=0}^{x_i=N_i} + (u_t^\top D_i u)\mid_{x_j=0}^{x_j=N_j}] + 2\frac{\gamma^{it}}{\gamma^{tt}}u_t^2\mid_{x_i=0}^{x_i=N_i} = \\ -2[\frac{\gamma^{ij}}{\gamma^{tt}}(u_t u_j)\mid_{x_i=0}^{x_i=N_i} + \frac{\gamma^{it}}{\gamma^{tt}}(u_t^2)\mid_{x_i=0}^{x_i=N_i}]\end{aligned} \tag{A.17}$$

Then applying the boundary conditions $u_t = \delta_{0,x_i}\alpha_i u_i + \delta_{N,x_i}\beta_i u_i$

$$\begin{aligned} - &\quad 2[(\gamma^{ij}\beta_i u_i u_j\mid_{x_i=N_i} + \gamma^{it}\beta_i u_i u_t\mid_{x_i=N_i}) \\ - &\quad (\gamma^{ij}\alpha_i u_i u_j\mid_{x_i=0} + \gamma^{it}\alpha_i u_i u_t\mid_{x_i=0})] \\ = &\quad -2[(\beta_i u_t^2 - \gamma^{it}u_t^2)\mid_{x_i=N_i} - (\alpha_i u_t^2 - \gamma^{it}u_t^2)\mid_{x_i=0}]\end{aligned} \tag{A.18}$$

So:

$$\frac{d}{dt}\xi = 2[E_{N_i}(\beta_i u_t^T u_t - \gamma^{it}u_t^T u_t) - E_0(\alpha_i u_t^T u_t - \gamma^{it}u_t^T u_t)] \tag{A.19}$$

If we start, again, with our wave equation and add the penalty terms before we derive the time derivative of the energy:

$$\begin{aligned} v_{tt} &= -\frac{\gamma^{ij}}{\gamma^{tt}}H^{-1}(-A_{ij} + BS_i)v - 2\frac{\gamma^{it}}{\gamma^{tt}}H^{-1}Q_i v_t \\ &+ \tau_0 H^{-1}E_0(\alpha_0 v_t + \beta_0 S_i v) + \tau_{N_i}H^{-1}E_{N_i}(\alpha_{N_i}v_t + \beta_{N_i}S_i v)\end{aligned} \tag{A.20}$$

We again calculate the time derivative of the energy norm:

$$\frac{d}{dt}\left(\|u_t\|^2 + \|-\frac{\gamma^{ij}}{\gamma^{tt}}u_i u_j\|\right) = (\langle u_t, u_{tt}\rangle + \langle u_{tt}, u_t\rangle) - \frac{\gamma^{ij}}{\gamma^{tt}}(\langle u_i, u_{jt}\rangle + \langle u_{it}, u_j\rangle) \tag{A.21}$$

And apply summation by parts in the integration:

$$\begin{aligned} - &\quad \frac{\gamma^{ij}}{\gamma^{tt}}[(v_t^\top S_j v)\mid_{x_i=0}^{x_i=N_i} + (v_t^\top S_i v)\mid_{x_j=0}^{x_j=N_j}] - 2\frac{\gamma^{it}}{\gamma^{tt}}v_t^\top v_t\mid_{x_i=0}^{x_i=N_i} \\ + &\quad 2\tau_{0_i}\alpha_{0_i}v_t^\top E_{0_i}v_t + 2\tau_{0_i}\beta_{0_i}v_t^\top E_{0_i}S_i v \\ + &\quad 2\tau_{N_i}\alpha_{N_i}v_t^\top E_{N_i}v_t + 2\tau_{N_i}\beta_{N_i}v_t^\top E_{N_i}S_i v \\ = &\quad 2(\tau_{N_i}\alpha_{N_i} - \frac{\gamma^{it}}{\gamma^{tt}})v_t^\top E_{N_i}v_t + 2(\tau_{0_i}\alpha_{0_i} + \frac{\gamma^{it}}{\gamma^{tt}})v_t^\top E_{0_i}v_t \\ + &\quad 2(\tau_{N_i}\beta_{N_i} - \frac{\gamma^{ij}}{\gamma^{tt}})v_t^\top E_{N_i}S_i v + 2(\tau_{0_i}\beta_{0_i} + \frac{\gamma^{ij}}{\gamma^{tt}})v_t^\top E_{0_i}S_i v\end{aligned} \tag{A.22}$$

In order to control the sign of the energy growth we need to set the $v_t^\top E_{N_i}S_i v$ terms to zero. We get: $\tau_0\beta_0 = -\frac{\gamma^{ij}}{\gamma^{tt}}$ and $\tau_N\beta_N = \frac{\gamma^{ij}}{\gamma^{tt}}$. So:

$$\frac{d}{dt}\left(\|u_t\|^2 + \|\frac{\gamma^{ij}}{\gamma^{tt}}u_i u_j\|\right) = 2(\tau_{N_i}\alpha_{N_i} - \frac{\gamma^{it}}{\gamma^{tt}})v_t^\top E_{N_i}v_t + 2(\tau_{0_i}\alpha_{0_i} + \frac{\gamma^{it}}{\gamma^{tt}})v_t^\top E_{0_i}v_t \tag{A.23}$$

$$= -2(\beta_{N_i}\frac{\gamma^{it}}{\gamma^{tt}} - \alpha_{N_i}\frac{\gamma^{ij}}{\gamma^{tt}})\beta_{N_i}^{-1} v_t^\top E_{N_i} v_t + 2(\beta_{0_i}\frac{\gamma^{it}}{\gamma^{tt}} - \alpha_{0_i}\frac{\gamma^{ij}}{\gamma^{tt}})\beta_{0_i}^{-1} v_t^\top E_{0_i} v_t$$

Given the maximally dissapative conditions: $\beta_{N_i}\gamma^{it} - \alpha_{N_i}\gamma^{ij} \leq 0$ and $\beta_{0_i}\gamma^{it} - \alpha_{0_i}\gamma^{ij} \geq 0$ we know that $\beta_{N_i} > 0$ and $\beta_{0_i} < 0$

$$p_t = -\frac{\gamma^{it}}{\gamma^{tt}} H^{-1} Q_i v_t - \frac{\gamma^{ij}}{\gamma^{tt}} H^{-1}(A + (E_0 - E_N)S)v \tag{A.24}$$

$$-\frac{\gamma^{ij}}{\gamma^{tt}\beta_{0_i}} H^{-1} E_0(\alpha_{0_i} v_t + \beta_{0_i} S_i v) + \frac{\gamma^{ij}}{\gamma^{tt}\beta_{N_i}} H^{-1} E_{N_i}(\alpha_{N_i} v_t + \beta_{N_i} S_i v)$$

If we set $\alpha = -\beta$

$$p_t = -\frac{\gamma^{it}}{\gamma^{tt}} D_{i+} p - (\gamma^{ij} - \frac{\gamma^{it}\gamma jt}{\gamma_{tt}}) H^{-1} A_{ij} v \pm \frac{2\gamma^{ij}}{h\gamma^{tt}}[(1 - \frac{\gamma^{it}\gamma^{jt}}{\gamma^{tt}} + \gamma^{tt} - \frac{\gamma^{it}}{\gamma^{tt}}) D_{i+} v - p] \tag{A.25}$$

To prescribe boundary conditions at the corners and edges, you do not need a normal vector except for the spacing coefficient (i.e. $dx^2/(dx^2 + dy^2 + dz^2)$). You can just look at the contribution to the semidiscrete energy above from the edges (i.e. (x,y,z)=(0,0,z)) or corners (i.e. (x,y,z)=(0,0,N)).

A.2 Proper Boundaries for Harmonic

Conditions for spherical waves in a cartesian grid:

$$(\partial_t - \partial_x)\left[r^2\left(g^{\mu\nu} - g_0^{\mu\nu}\right)\right] = 0 \tag{A.26}$$

Right side subtracted in penalty terms:

$$\begin{aligned} \partial_t Q^{\mu\nu} &= -\left(g^{ij} - \frac{g^{it}g^{jt}}{g^{tt}}\right) D_+ D_- g^{\mu\nu} - \frac{g^{it}}{g^{tt}} D_{-i} Q^{\mu\nu} + \tilde{S} \\ &+ \tau_{0_i} H^{-1} E_{0_i}(\alpha_{0_i} g_t^{\mu\nu} + \beta_{0_i} S_i g^{\mu\nu} + \gamma_{0_i} g^{\mu\nu} - e_{0_i} g_0) \\ &+ \tau_{N_i} H^{-1} E_{N_i}(\alpha_{N_i} g_t^{\mu\nu} + \beta_{N_i} S_i g^{\mu\nu} + \gamma_{N_i} g^{\mu\nu} - e_{N_i} g_N) \end{aligned} \tag{A.27}$$

Where E_{N_i} is zero everywhere except the upper x_i boundary, and E_{0_i} is zero everywhere except the lower x_i boundary.
We calculate the time derivative of the energy norm:

$$\frac{d}{dt}\left(\|u_t\|^2 + \|-\frac{\gamma^{ij}}{\gamma^{tt}} u_i u_j\|\right) = (\langle u_t, u_{tt}\rangle + \langle u_{tt}, u_t\rangle) - \frac{\gamma^{ij}}{\gamma^{tt}}(\langle u_i, u_{jt}\rangle + \langle u_{it}, u_j\rangle) \tag{A.28}$$

And apply summation by parts in the integration:

$$\begin{aligned} \dot{E} &= 2\frac{\gamma^{ij}}{\gamma^{tt}}(v_t^\top S_j v)\,|_{x_i=0}^{x_i=N_i} - 2\frac{\gamma^{it}}{\gamma^{tt}}(v_t^\top v_t)\,|_{x_i=0}^{x_i=N_i} \\ &+ 2\tau_{0_i}\alpha_{0_i} v_t^\top E_{0_i} v_t + 2\tau_{0_i}\beta_{0_i} v_t^\top E_{0_i} S_i v + 2\tau_{0_i}\gamma_{0_i} v_t^\top E_{0_i} v - 2\tau_{0_i} e_{0_i} v_t^\top E_{0_i} g_0 \\ &+ 2\tau_{N_i}\alpha_{N_i} v_t^\top E_{N_i} v_t + 2\tau_{N_i}\beta_{N_i} v_t^\top E_{N_i} S_i v + 2\tau_{N_i}\gamma_{N_i} v_t^\top E_{N_i} v - 2\tau_{N_i} e_{N_i} v_t^\top E_{N_i} g_N \end{aligned} \tag{A.29}$$

Which simplifies to:

$$\begin{aligned} \dot{E} &= 2(\tau_{N_i}\alpha_{N_i} - \frac{\gamma^{it}}{\gamma^{tt}})v_t^\top E_{N_i} v_t + 2(\tau_{0_i}\alpha_{0_i} + \frac{\gamma^{it}}{\gamma^{tt}})v_t^\top E_{0_i} v_t \\ &+ 2(\tau_{N_i}\beta_{N_i} - \frac{\gamma^{ij}}{\gamma^{tt}})v_t^\top E_{N_i} S_i v + 2(\tau_{0_i}\beta_{0_i} + \frac{\gamma^{ij}}{\gamma^{tt}})v_t^\top E_{0_i} S_i v \\ &+ 2(\tau_{N_i}\gamma_{N_i})v_t^\top E_{N_i} v + 2(\tau_{0_i}\gamma_{0_i})v_t^\top E_{0_i} v \\ &+ 2(\tau_{N_i}e_{N_i})v_t^\top E_{N_i} g_0 + 2(\tau_{0_i}e_{0_i})v_t^\top E_{0_i} g_0 \end{aligned} \tag{A.30}$$

In order to control the sign of the energy growth we need to set the $v_t^\top E_{N_i} S_i v$ terms to zero. We get: $\tau_0\beta_0 = -\frac{\gamma^{ij}}{\gamma^{tt}}$ and $\tau_N\beta_N = \frac{\gamma^{ij}}{\gamma^{tt}}$.
So:

$$\begin{aligned} \dot{E} &= -2(\beta_{N_i}\frac{\gamma^{it}}{\gamma^{tt}} - \alpha_{N_i}\frac{\gamma^{ij}}{\gamma^{tt}})\beta_{N_i}^{-1} v_t^\top E_{N_i} v_t \\ &+ 2(\beta_{0_i}\frac{\gamma^{it}}{\gamma^{tt}} - \alpha_{0_i}\frac{\gamma^{ij}}{\gamma^{tt}})\beta_{0_i}^{-1} v_t^\top E_{0_i} v_t \\ &+ 2(\tau_{N_i}\gamma_{N_i})v_t^\top E_{N_i} v + 2(\tau_{0_i}\gamma_{0_i})v_t^\top E_{0_i} v \\ &+ 2(\tau_{N_i}e_{N_i})v_t^\top E_{N_i} g_0 + 2(\tau_{0_i}e_{0_i})v_t^\top E_{0_i} g_0 \end{aligned} \tag{A.31}$$

Given the maximally dissipative conditions: $\beta_{N_i}\gamma^{it} - \alpha_{N_i}\gamma^{ij} \leq 0$ and $\beta_{0_i}\gamma^{it} - \alpha_{0_i}\gamma^{ij} \geq 0$ we know that $\beta_{N_i} > 0$ and $\beta_{0_i} < 0$.

For the harmonic system the interior is:

$$\partial_t Q^{\mu\nu} = \frac{\gamma^{it}}{\gamma^{tt}} D_{i+} Q^{\mu\nu} - (\gamma^{ij} + \frac{\gamma^{it}\gamma^{jt}}{\gamma^{tt}}) H^{-1} A_{ij} \gamma^{\mu\nu} \tag{A.32}$$

The full evolution equation with the Boundaries is then

$$\begin{aligned} \partial_t Q^{\mu\nu} &= -\frac{\gamma^{it}}{\gamma^{tt}} D_{i+} Q^{\mu\nu} - (\gamma^{ij} + \frac{\gamma^{it}\gamma^{jt}}{\gamma^{tt}}) H^{-1} (A_{ij} + (E_0 - E_N) S_i) \gamma^{\mu\nu} \\ &+ \frac{2\gamma^{ij}}{\gamma^{tt}\beta_0} H^{-1} E_{0_i} [(1 + \frac{\gamma^{it}}{\gamma^{tt}}) D_{i+}\gamma^{\mu\nu} - \frac{Q^{\mu\nu}}{\gamma^{tt}} + \frac{2x}{r^2}(\gamma^{\mu\nu} - g_0)] \\ &+ \frac{2\gamma^{ij}}{\gamma^{tt}\beta_N} H^{-1} E_{N_i} [(1 - \frac{\gamma^{it}}{\gamma^{tt}}) D_{i+}\gamma^{\mu\nu} + \frac{Q^{\mu\nu}}{\gamma^{tt}} + \frac{2x}{r^2}(\gamma^{\mu\nu} - g_N)] \end{aligned} \tag{A.33}$$

Where $\gamma_{\mu\nu} \equiv \sqrt{-g} g^{\mu\nu}$ and $Q^{\mu\nu} = g^{t\alpha}\partial_\alpha \gamma^{\mu\nu}$. Thus we can show that the energy growth of the system is bounded.

A.3 Constraint Preserving Boundary Conditions

The constraint equations

$$C^{\mu} = -\partial_t \gamma^{\mu t} - \partial_x \gamma^{\mu x} - \partial_y \gamma^{\mu y} - \partial_z \gamma^{\mu z} - \tilde{S}^{\mu} \tag{A.34}$$

are used to set the conditions for the four values $\gamma^0 \mu$. We plug these into Sommerfeld type conditions chosen to be (for the upper bound):

$$\left(\partial_x + \partial_t + \frac{1}{r}\right)\left(\gamma^{AB} - \gamma_0^{AB}\right) = 0 \tag{A.35}$$

giving us the conditions for the three γ^{AB}.

$$\left(\partial_x + \partial_t + \frac{1}{r}\right)\left(\gamma^{tA} - \gamma^{xa} - \gamma_0^{tA} + \gamma_0^{xA}\right) = 0 \tag{A.36}$$

giving us the two γ^{xA} since we know γ^{tA} from the constraints.

$$\left(\partial_x + \partial_t + \frac{1}{r}\right)\left(\gamma^{tt} - 2\gamma^{xt} + \gamma^{xx} - \gamma_0^{tt} + 2\gamma_0^{xt} - \gamma_0^{xx}\right) = 0 \tag{A.37}$$

Which finally gives us γ^{xx} since we know γ^{tt} and γ^{xt} from the constraints. Where AB are the directions prependicular to the boundaries and x is the direction outward of the boundary face. There are a number of ways to vary this, which could be experimented with.

This give the 10 conditions (at the x=1 boundary):

$$\left(\partial_x + \partial_t\right)\gamma^{00} = \partial_x \gamma^{00} - \partial_x \gamma^{01} - \partial_y \gamma^{02} - \partial_z \gamma^{03} - S^0$$

$$\left(\partial_x + \partial_t\right)\gamma^{01} = \partial_x \gamma^{01} - \partial_x \gamma^{11} - \partial_y \gamma^{12} - \partial_z \gamma^{13} - S^1$$

$$\left(\partial_x + \partial_t\right)\gamma^{02} = \partial_x \gamma^{02} - \partial_x \gamma^{12} - \partial_y \gamma^{22} - \partial_z \gamma^{23} - S^2$$

$$\left(\partial_x + \partial_t\right)\gamma^{03} = \partial_x \gamma^{03} - \partial_x \gamma^{13} - \partial_y \gamma^{23} - \partial_z \gamma^{33} - S^3$$

$$\left(\partial_x + \partial_t\right)\gamma^{11} = \left(\partial_x + \partial_t\right)\left(2\gamma^{01} - \gamma^{00}\right) - \frac{1}{r}\left(\gamma^{11} - 2\gamma^{01} + \gamma^{00}\right) + \left(\partial_x + \frac{1}{r}\right)\left(\gamma_0^{11} - 2\gamma_0^{01} + \gamma_0^{00}\right)$$

$$\left(\partial_x + \partial_t\right)\gamma^{12} = \left(\partial_x + \partial_t\right)\left(\gamma^{02} - \gamma_0^{02}\right) - \frac{1}{r}\left(\gamma^{12} - \gamma^{02}\right) + \frac{1}{r}\left(\gamma_0^{12} - \gamma_0^{02}\right) + \partial_x \gamma_0^{12}$$

$$\left(\partial_x + \partial_t\right)\gamma^{13} = \left(\partial_x + \partial_t\right)\left(\gamma^{03} - \gamma_0^{03}\right) - \frac{1}{r}\left(\gamma^{13} - \gamma^{03}\right) + \frac{1}{r}\left(\gamma_0^{13} - \gamma_0^{03}\right) + \partial_x \gamma_0^{13}$$

$$\left(\partial_x + \partial_t\right)\gamma^{22} = -\frac{1}{r}\left(\gamma^{22} - \gamma_0^{22}\right) + \partial_x \gamma_0^{22}$$

$$\left(\partial_x + \partial_t\right)\gamma^{23} = -\frac{1}{r}\left(\gamma^{23} - \gamma_0^{23}\right) + \partial_x \gamma_0^{23}$$

$$\left(\partial_x + \partial_t\right)\gamma^{33} = -\frac{1}{r}\left(\gamma^{33} - \gamma_0^{33}\right) + \partial_x \gamma_0^{33}$$

A.4 On the convergence tests

The effects of the initial transient modes can last for different amounts of time for the different resolutions. A comparison of the Q^{+}_{22} waveforms between the three resolutions confirms this shift in time – the waveform maxima are seen at slightly different times for the different resolutions. We attempt to undo this effect by manually shifting the time-coordinate of the medium and high resolution runs

$$t \to t + \delta t. \tag{A.38}$$

The value of δt is set for the medium and high resolution runs independently, using the minimization condition

$$\frac{\partial}{\partial(\delta t)} \int_{150}^{170} |Q(t \to t + \delta t) - Q_{\rm vhigh}|^2 dt = 0. \tag{A.39}$$

This effectively means aligning in time the peak amplitude of the three runs, at $t \approx 160\,M$. Solving Eq. (A.39) numerically for the Q^{+}_{22} waveforms gives

$$\delta t_{0.024} = 0.4756 \quad \text{and} \quad \delta t_{0.018} = 0.1078. \tag{A.40}$$

Applying the time-shifting condition Eq. (A.38) to the coarse and medium resolution data, and inserting the result into Eqs. (4.20)–(4.21) gives convergence rates that are consistent with the theoretical expectations.

In Table A.1 we report the convergence rates as calculated from Eq. 4.20 for the time interval $0 \leq u \leq 190$ (u is the retarded time as defined in Sec. 4.1.2) which excludes the initial burst but contains the rest of the waveform. We see close to fourth-order convergence for the $\ell = 2$ modes Q^{+}_{22} and $Q^{\times}_{21}$. The $\ell = m = 3$ mode Q^{+}_{33}, on the other hand, shows second order convergence in phase, which is most likely related to the fact that the magnitude of this mode is the same size as the finite difference error in Q^{+}_{22} and is a factor of 40 smaller than the magnitude of Q^{+}_{22} itself.

The final kick-velocity magnitude in units of $\mathrm{km/s}$ is

$$|v|_{\rm kick} = 263.49, \quad 259.75, \quad \text{and} \quad 261.00 \tag{A.41}$$

for the medium, high and very-high resolutions. This gives $\rho(|v|_{\rm kick}) = 2.98$ which can be inserted into Eq. (4.21) to obtain a calculated convergence rate of 4.32.

A.5 Details on the extraction of Ψ_4

The numerical solution of Eqs. (4.29) involves first an interpolation of Ψ_4 as calculated according to Eqs. (4.25) from its values on the Cartesian grid to those onto the extraction sphere by using fourth-order Lagrange interpolants. Because of the symmetry across the $z = 0$ plane the interpolation is effectively done on the upper hemisphere only, thus using a spherical coordinate system with $\theta, \phi \in [0, \pi/2] \times [0, 2\pi]$ and applying cell-centered

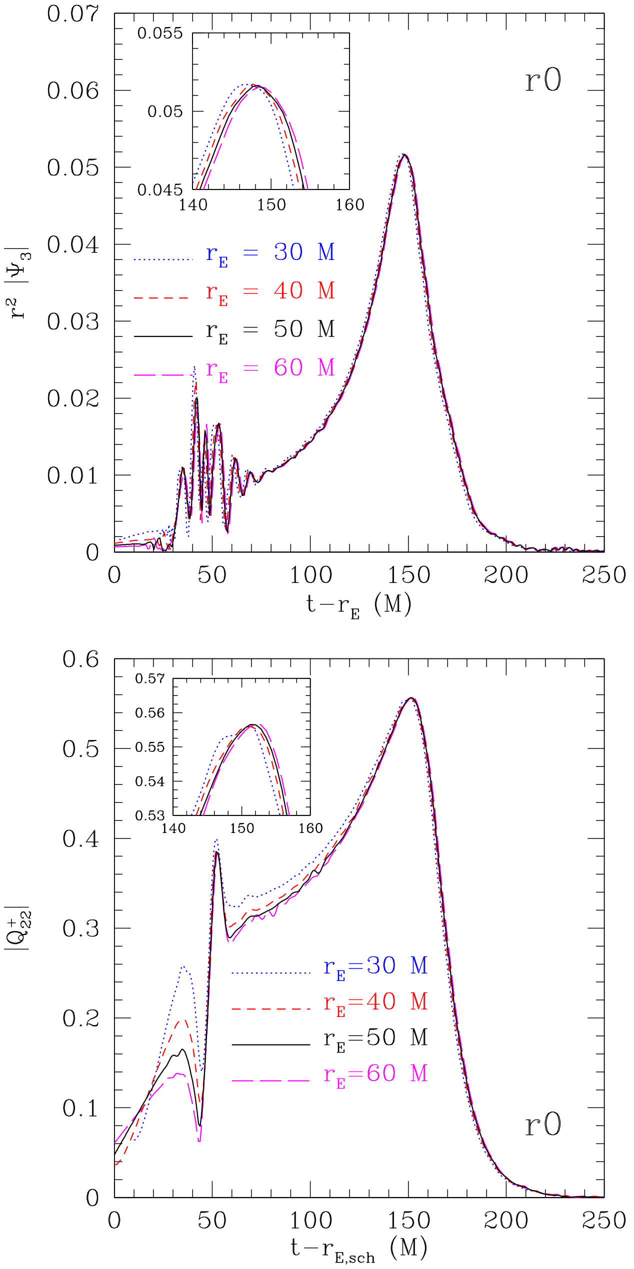

Figure A.1: *Left panel:* Evidence that the conditions for the Peeling theorem are met also for Ψ_3, which scales as r^{-2} when extracted at isotropic radii $r_{\rm E} = 30\,M$, $40\,M$, $50\,M$, and $60\,M$. This figure should be compared to the corresponding Fig. 4.5. *Right panel:* The same as the left panel but for the gauge-invariant quantity Q^+_{22}, which is shown to be constant when extracted at isotropic radii $r_{\rm E} = 30\,M$, $40\,M$, $50\,M$, and $60\,M$.

Table A.1: Integrated convergence rates of the Zerilli-Moncrief gauge-invariant variables providing the dominant contribution in the kick-velocity measurements. As the numbers indicate, we achieve at least third order convergence both in amplitude and phase. A time-shift as given by Eqs. (A.38)–(A.40) was made on the raw data to remove the near cancellation of the lowest-order error terms.

Q	$Q^{\times}_{21}$		Q^{+}_{22}		Q^{+}_{33}	
$r_{\rm E}/M$	amp	phase	amp	phase	amp	phase
30	4.51	3.95	4.65	4.31	4.32	2.13
40	4.08	3.70	4.61	4.34	4.26	2.62
50	3.83	4.44	4.35	4.76	4.02	2.39

discretization along the θ-direction to avoid the coordinate singularities at the poles on the sphere.

The angular resolution is chosen so that the spacings $\Delta\theta$ and $\Delta\phi$ are equal and of the same order as the corresponding Cartesian spacings of the refinement level in which the largest extraction 2-sphere is located. As an example, for the fiducial finest resolution of $h = 0.024\,M$, the largest extraction radius is at $r_{\rm E} = 60\,M$ and in a region covered by the second refinement level with spacing $\Delta^{0.024}_{rl=2} = 1.536\,M$. To obtain an equivalent spacing on the 2-sphere, we solve for $\Delta\theta$ and $\Delta\phi$ such that

$$r_{\rm E}\Delta\theta = r_{\rm E}\Delta\phi \approx \Delta^{0.024}_{rl=2} = 1.536\,M\,. \tag{A.42}$$

The resulting number of grid points is $N_\theta = 56$ along the θ-direction and $N_\phi = 224$ along the ϕ-direction.

After interpolation onto the extraction sphere, we first calculate the time integral of $\Psi_4|_{S^2}$ and afterwards, the surface integral of the absolute square of the former according to Eqs. (4.29). These integrals are both computed using fourth-order schemes. In particular, for the surface integral, we use Simpson's rule in the form

$$\begin{aligned}\int_{x_0}^{x_N} dx\, f(x) \quad \approx \quad & \Delta x \left[\frac{17}{48}f_0 + \frac{59}{48}f_1 + \frac{43}{48}f_2 + \frac{49}{48}f_3 \right. \\ & + \langle f_k \rangle \\ & \left. + \frac{49}{48}f_{N-3} + \frac{43}{48}f_{N-2} + \frac{59}{48}f_{N-1} + \frac{17}{48}f_N \right]\,, \end{aligned} \tag{A.43}$$

where $\langle f_k \rangle$ is the sum over all f_k with $3 < k < N-3$. The integral over $d\theta d\phi$ is obtained by computing the tensor product of the RHS of Eqs. (A.43), *i.e.*,

$$\int_{\theta_0}^{\theta_N} d\theta \int_{\phi_0}^{\phi_N} d\phi\, f(\theta,\,\phi) \approx \Delta\theta\Delta\phi \sum_{i=0}^{N_\theta}\sum_{j=0}^{N_\phi} c_i c_j\, f_{ij}\,, \tag{A.44}$$

where the c_i, c_j are the coefficients in the RHS of Eqs. (A.43).

The time integral of Eqs. (4.29) is generically calculated by using the fourth-order Simpson's rule in such a way that the integral for the time step k uses only past time steps i with $0 \leq i \leq k$. Care is required for the very first time steps, for which we have less than 7 evaluations of the integrand. In this case, we use the 2nd-order accurate trapezoid rule if $N = 1, 3$, or 5

$$\int_{x_0}^{x_N} dx\, f(x) \approx \Delta x \left[\frac{1}{2} f_0 + \langle f_k \rangle + \frac{1}{2} f_N \right] , \tag{A.45}$$

or the fourth-order accurate Simpson's rule

$$\begin{aligned} \int_{x_0}^{x_N} dx\, f(x) \quad &\approx \quad \Delta x \left[\frac{1}{3} f_0 + \frac{4}{3} f_1 \right. \\ &\qquad \left. + \langle \frac{2}{3} f_{2k} + \frac{4}{3} f_{2k+1} \rangle + \frac{1}{3} f_N \right] , \end{aligned} \tag{A.46}$$

if $N = 2, 4$ or 6. For $N \geq 7$ we simply use Simpson's rule in the form (A.43). It should be noted that the use of a higher-order time integration scheme improves the overall accuracy in the calculation of the final recoil velocity by more than a factor of 10.

A.6 A comparison of wave-extraction methods

In Fig. 4.5, we have shown that Ψ_4 as extracted at different radii correctly scales with the $1/r$ falloff as predicted by the peeling theorem. Here, we also check if all other components of the Weyl tensor exhibit the correct $r^{5-n}\Psi_n = \text{const.}$ scaling.

The left panel of Fig. A.1 indeed shows that the scaling property of all Ψ_n behave as expected. In the course of the same analysis, it is also worth looking at the waveforms as calculated by using the gauge-invariant formalism. In particular, we focus on the real part of the $\ell = 2, m = 2$ even parity wave mode Q^{+}_{22} and check for the correct scaling for the different extraction radii. The right panel of Fig. A.1 shows that Q^{+}_{22} is constant for all extraction radii as expected.

As a final remark, we will also compare the h_+ and $h_\times$ as calculated by using the odd and even master functions in the gauge-invariant formalism according to Eq. (4.31) and the spin-weighted spherical harmonic amplitudes of the Weyl component $\Psi_4^{\ell m}$ decomposed on the extraction spheres. Using these amplitudes, the metric perturbations $h_+, h_\times$ recovered by a double time integral of Eq. (4.27)

$$h_+ - \mathrm{i} h_\times = \lim_{r\to\infty} \sum_{\ell,m} \int_0^t dt' \int_0^{t'} dt'' \Psi_4^{\ell m} \,{}_{-2}Y_{\ell m} . \tag{A.47}$$

The numerical integration of Eq. (A.47) requires knowledge of an integration constant for the calculation of the second integral to eliminate the linear offset. This constant is determined by searching for minima in the $\Psi_4^{\ell m}$ mode and averaging over them. The resulting value is used as the integration constant. In both cases, we only consider the dominant contribution from mode $\ell = 2\,, m = 2$.

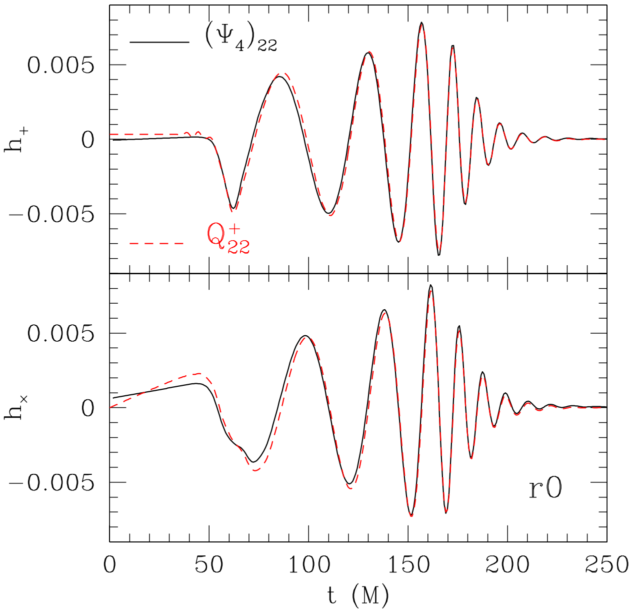

Figure A.2: Comparison of the two polarization amplitudes h_+ (upper graph) and $h_\times$ (lower graph) as computed with Ψ_4 (continuous black line) or with the gauge invariant quantities $Q^+_{\ell m}$ (dashed red line). Note the two polarizations are computed using the lowest (and dominant) multipole $\ell = 2,\ m = 2$ and are extracted at $r_{\rm E} = 50\, M$.

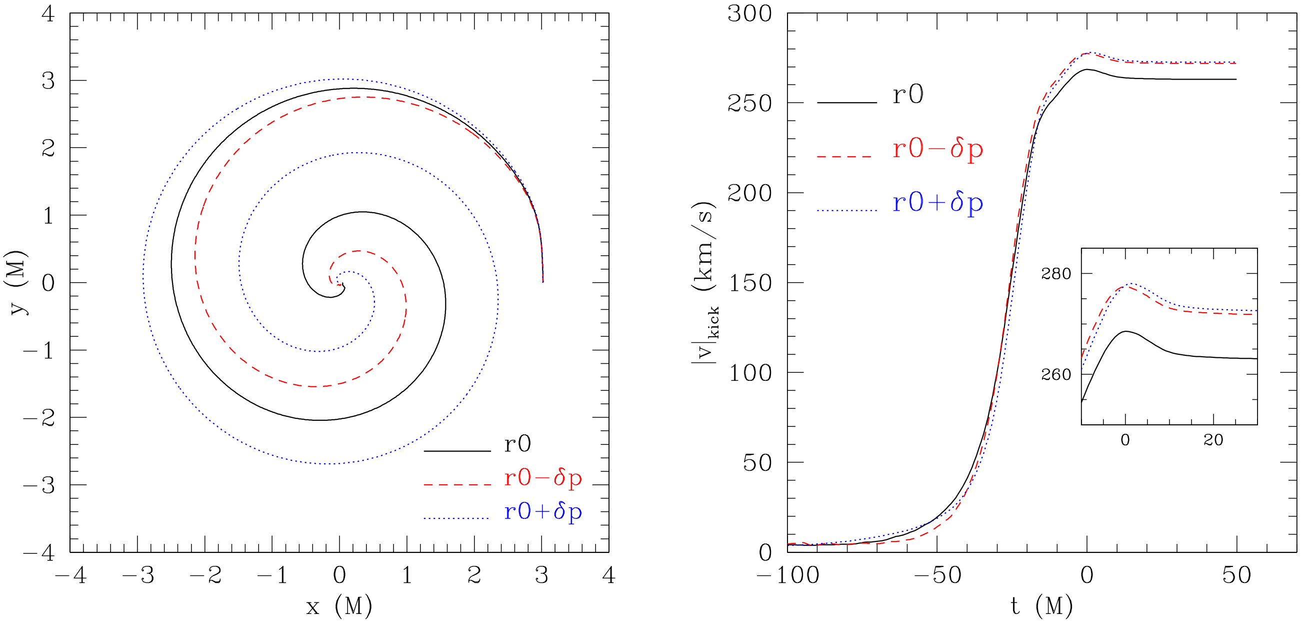

Figure A.3: *Left panel:* Coordinate trajectories for one of the black holes for the $r0$ compared with similar models where the initial linear momenta have been changed by $\pm 3\%$ in order to modify the eccentricity of the inspiral. *Right panel:* Recoil velocity for the $r0$ case is compared with similar models for which the initial eccentricity has been increased by adding and subtracting 3% of the initial linear momentum of the black holes relative to the $r0$ values. The effect of increased eccentricity in the final merger is to increase the size of the kick, by about 4% in both cases.

A.7 On the influence of orbital eccentricity

Another source of potential error in calculating a “physical” kick comes from the choice of initial data parameters. Our evolutions begin from fairly close separations, comprising at most the last 2-3 orbits. As such, parameters for quasi-circular orbits determined by the effective potential method, give only approximations to the true orbital parameters for black holes that have spiraled in from infinity, and it is known that the method produces a non-trivial residual eccentricity for initial data at close separation. This eccentricity can have significant effects on the orbital trajectories before merger, and a potential influence on the calculated recoil. To test this we have evolved two modified $r0$ models, one in which the initial linear momenta of the black holes is 3% larger than that specified in Table 4.1, and another in which the linear momenta are 3% smaller. The modified momenta have the effect of changing the orbital energy of the bodies from the minima determined by the effective potential method, introducing an additional eccentricity to the evolution. The resulting black hole trajectories and kick determinations are shown respectively in Fig. A.3. We see that although the level of applied eccentricity is large, and in fact much larger than the expected eccentricity due to the intrinsic inaccuracy of the effective potential method, it modifies the recoil by only about $10\,\mathrm{km/s}$, that is, 4%. Further, in both the high and low energy cases, the recoil is increased over the fiducial $r0$ case, suggesting that increased eccentricity generically leads to a slightly larger recoil.

A.8 Sensitivity curves

For convenience, we report below the sensitivity curves used to compute the SNRs that are often difficult to collect from the literature. For LISA we we use the same noise curve as for the LISA Mock Data Challenge 3 [263] as implemented by Trias and Sintes, and made available by the LISA Parameter Estimation Task Force [264]. The noise curve for advanced Virgo can be found in tabulated form in Ref. [220].

LIGO

$$S_h(f) = S_0 \left\{ \left(\frac{4.49f}{f_0}\right)^{-56} + 0.16 \left(\frac{f}{f_0}\right)^{-4.52} + 0.52 + 0.32 \left(\frac{f}{f_0}\right)^{2} \right\} , \qquad S_0 = 9 \times 10^{-46}, \quad f_0 = 150 \text{ Hz}\,,$$

AdLIGO

$$S_h(f) = S_0 \left\{ \left(\frac{f}{f_0}\right)^{-4.14} - 5 \left(\frac{f_0}{f}\right)^{2} + 111 \left(1 - \left(\frac{f}{f_0}\right)^{2} + \frac{1}{2}\left(\frac{f}{f_0}\right)^{4}\right) \left(1 + \frac{1}{2}\left(\frac{f}{f_0}\right)^{2}\right)^{-1} \right\} , \qquad S_0 = 10^{-49}, \quad f_0 = 215 \text{ Hz}\,,$$

Virgo

$$S_h(f) = S_0 \left\{ \left(\frac{7.87f}{f_0}\right)^{-4.8} + \frac{6}{17}\left(\frac{f_0}{f}\right) + \left[1 + \left(\frac{f}{f_0}\right)^{2}\right] \right\} , \qquad S_0 = 10.2 \times 10^{-46}, \quad f_0 = 500 \text{ Hz}\,. \tag{A.48}$$

References

[1] Rezzolla L *et al.* 2007 *ApJ* **708** (*Preprint* `0708.3999`)

[2] Marronetti P *et al.* 2008 *Phys. Rev.* **D77** 064010 (*Preprint* `0709.2160`)

[3] Berti E *et al.* 2007 *Phys. Rev.* **D76** 064034 (*Preprint* `gr-qc/0703053`)

[4] Buonanno A, Kidder L E, and Lehner L 2008 *Phys. Rev. D* **77**(2) 026004 (*Preprint* `0709.3839`)

[5] Damour T and Nagar A 2007 *Phys. Rev. D* **76**(4) 044003 (*Preprint* `0704.3550`)

[6] Berti E *et al.* 2008 *Class. Quant. Grav.* **25** 114035 (*Preprint* `0711.1097`)

[7] Buonanno A *et al.* 2007 *Phys. Rev.* **D76** 104049 (*Preprint* `0706.3732`)

[8] Rezzolla L *et al.* 2008 *ApJ* **674** L29–L32 (*Preprint* `0710.3345`)

[9] Campanelli M, Lousto C O, and Zlochower Y 2006 *Phys. Rev. D* **74** 084023

[10] Tichy W and Marronetti P 2007 *Phys. Rev.* **D76** 061502 (*Preprint* `gr-qc/0703075`)

[11] Herrmann F *et al.* 2007 *Phys. Rev.* **D76** 084032 (*Preprint* `0706.2541`)

[12] Lousto C O, Campanelli M, and Zlochower Y 2009 (*Preprint* `0904.3541`)

[13] Kesden M 2008 *Phys. Rev. D* **78**(8) 084030 (*Preprint* `0807.3043`)

[14] Ajith P *et al.* 2008 *Phys. Rev.* **D77** 104017 (*Preprint* `0710.2335`)

[15] Ajith P 2008 *Class. Quant. Grav.* **25** 114033 (*Preprint* `0712.0343`)

[16] Cutler C *et al.* 1993 *Phys. Rev. Lett.* **70** 2984–2987

[17] Flanagan E E 1998 *Phys. Rev. D* **58** 124030

[18] Price R 1972 *Phys. Rev. D* **5** 2419

[19] Pretorius F 2005 *Phys. Rev. Lett.* **95** 121101 (*Preprint* `gr-qc/0507014`)

[20] Campanelli M, Lousto C O, Marronetti P, and Zlochower Y 2006 *Phys. Rev. Lett.* **96** 111101 (*Preprint* `gr-qc/0511048`)

[21] Brügmann *et al.* 2004 *Phys. Rev. Lett.* **92** 211101 (*Preprint* `gr-qc/0312112`)

[22] Diener P *et al.* 2006 *Phys. Rev. Lett.* **96** 121101 (*Preprint* `gr-qc/0512108`)

[23] Imbiriba B *et al.* 2004 (*Preprint* `gr-qc/0403048`)

[24] Pfeiffer H P *et al.* (*Preprint* `gr-qc/0702106`)

[25] Choquet-Bruhat Y and Ruggeri T 1983 *Comm. Math. Phys* **89** 269–275

[26] Arnowitt R, Deser S, and Misner C W 1962 in L Witten, ed, *Gravitation: An introduction to current research* (New York: John Wiley) pp 227–265 (*Preprint* `gr-qc/0405109`)

[27] Nakamura T, Oohara K, and Kojima Y 1987 *Prog. Theor. Phys. Suppl.* **90** 1–218

[28] Shibata M and Nakamura T 1995 *Phys. Rev. D* **52** 5428

[29] Baumgarte T W and Shapiro S L 1998 *Phys. Rev. D* **59** 024007 (*Preprint* `gr-qc/9810065`)

[30] Alcubierre M, Brügmann B, Miller M, and Suen W M 1999 *Phys. Rev. D* **60** 064017 (*Preprint* `gr-qc/9903030`)

[31] Smarr L and York J W 1978 *Phys. Rev. D* **17** 1945

[32] Bona C and Massó J 1992 *Phys. Rev. Lett.* **68** 1097

[33] Alcubierre M *et al.* 2003 *Phys. Rev. D* **67** 084023 (*Preprint* `gr-qc/0206072`)

[34] Gundlach C and Martin-Garcia J 2004 *Phys. Rev. D* **70** 044031 (*Preprint* `gr-qc/0402079`)

[35] Friedrich H 1985 *Comm. Math. Phys.* **100** 525–543

[36] de Donder T 1921 *La Gravifique Einsteinienne* (Paris: Gauthiers-Villars)

[37] Bona C and Massó J 1992 in H Sato and T Nakamura, eds, *Sixth Marcel Grossman Meeting on General Relativity (Proceedings, Kyoto, Japan, 1991)* (Singapore: World Scientific) p 335

[38] Garfinkle D 2002 *Phys. Rev. D* **65** 044029

[39] Lindblom L *et al.* 2006 *Class. Quantum Grav.* **23** S447–S462 (*Preprint* `gr-qc/0512093`)

[40] Szilágyi B *et al.* 2007 *Class. Quantum Grav.* **24** S275–S293 (*Preprint* `gr-qc/0612150`)

[41] Alcubierre M *et al.* 2005 *Phys. Rev. D* **72** 124018 (*Preprint* `gr-qc/0507007`)

[42] Babiuc M C, Szilágyi B, and Winicour J 2006 *Class. Quantum Grav.* **23** S319–S342 (*Preprint* `gr-qc/0511154`)

[43] Kreiss H O, Reula O, Sarbach O, and Winicour J 2007 *Class. Quantum Grav.* **24** 5973–5984 (*Preprint* `gr-qc/0707.4188`)

[44] Gundlach C, Martin-Garcia J M, Calabrese G, and Hinder I 2005 *Class. Quantum Grav.* **22** 3767–3774 (*Preprint* `gr-qc/0504114`)

[45] Brodbeck O, Frittelli S, Hübner P, and Reula O A 1999 *J. Math. Phys.* **40** 909–923 (*Preprint* `gr-qc/9809023`)

[46] Reula O 1998 *Living Rev. Relativity* **1** 3 URL `http://www.livingreviews.org/lrr-1998-3`

[47] Motamed M *et al.* 2006 *Phys. Rev. D* **73** 124008 (*Preprint* `gr-qc/0604010`)

[48] Brügmann B 1996 *Phys. Rev. D* **54**(12) 7361–7372 (*Preprint* `gr-qc/9608050`)

[49] Brandt S and Brügmann B 1997 *Phys. Rev. Lett.* **78**(19) 3606–3609 (*Preprint* `gr-qc/9703066`)

[50] Brill D S and Lindquist R W 1963 *Phys. Rev.* **131**(1) 471–476

[51] Bowen J M and York J W 1980 *Phys. Rev. D* **21**(8) 2047–2056

[52] Ansorg M, Brügmann B, and Tichy W 2004 *Phys. Rev. D* **70** 064011 (*Preprint* `gr-qc/0404056`)

[53] Alcubierre M *et al.* 2001 *Phys. Rev. D* **64** 061501(R) (*Preprint* `gr-qc/0104020`)

[54] Misner C W 1963 *Ann. Phys.* **24** 102–117

[55] Bowen J M 1979 *Gen. Rel. Grav.* **11**(3) 227–231

[56] Bowen J M 1982 *Gen. Rel. Grav.* **14**(12) 1183–1191

[57] Kulkarni A D, Shepley L, and York J 1983 *Phys. Lett.* **96A**(5) 228

[58] York J W 1983 in N Deruelle and T Piran, eds, *Gravitational Radiation* (Amsterdam: North-Holland) pp 175–201 ISBN 0-444-86560-8

[59] Baker J G *et al.* 2006 *Phys. Rev.* **D73** 104002 (*Preprint* `gr-qc/0602026`)

[60] van Meter J, Baker J G, Koppitz M, and Choi D I 2006 *Phys. Rev. D* **73** 124011 (*Preprint* `gr-qc/0605030`)

[61] Hannam M *et al.* 2007 *Phys. Rev. Lett.* **99** 241102 (*Preprint* `gr-qc/0606099`)

[62] Courant R and Friedrichs K O 1976 *Supersonic flows and shock waves* (Berlin: Springer)

[63] Shu C W and Osher S J 1988 *J. Comput. Phys.* **77** 439

[64] Teukolsky S A 2000 *Phys. Rev. D* **61** 087501

[65] Choptuik M W and Unruh W G 1986 *Gen. Rel. Grav.* **18** 818–843

[66] Kreiss H O and Oliger J 1973 *Methods for the approximate solution of time dependent problems* (Geneva: GARP publication series No. 10)

[67] Gustafsson B, Kreiss H O, and Oliger J 1995 *Time dependent problems and difference methods* (New York: Wiley)

[68] Hawking S W and Ellis G F R 1973 *The large scale structure of spacetime* (Cambridge, England: Cambridge University Press) ISBN 0-521-09906-4

[69] York J W 1989 in C Evans, L Finn and D Hobill, eds, *Frontiers in Numerical Relativity* (Cambridge, England: Cambridge University Press) pp 89–109 ISBN 0-521-36666-6

[70] Thornburg J 2004 *Class. Quantum Grav.* **21**(2) 743–766 (*Preprint* `gr-qc/0306056`)

[71] Huisken G and Yau S T 1996 *Invent. Math.* **124** 281–311

[72] Ashtekar A, Beetle C, and Fairhurst S 1999 *Class. Quantum Grav.* **16** L1–L7 (*Preprint* `gr-qc/9812065`)

[73] Newman E T and Penrose R 1962 *J. Math. Phys.* **3**(3) 566–578 erratum in J. Math. Phys. 4, 998 (1963)

[74] Regge T 1961 *Nuovo Cim.* **19** 558–571

[75] Zerilli F J 1970 *Phys. Rev. Lett.* **24**(13) 737–738

[76] Moncrief V 1974 *Annals of Physics* **88** 323–342

[77] Teukolsky S A 1973 *Astrophys. J.* **185** 635–647

[78] Abrahams A, Anderson A, Choquet-Bruhat Y, and York J 1996 *C.R. Acad. Sci. Paris* **t. 323, Serie II** 835–841

[79] Hadamard J 1902 *Princeton University Bulletin* **8** 49–52

[80] Courant R and Hilbert D 1962 *Methods of Mathematical Physics* (New York: John Wiley and Sons, Inc) ISBN 0-85226-132-2

[81] Kreiss H O and Scherer G 1977 On the existence of energy estimates for difference approximations for hyperbolic systems Tech. rep. Dept. of Scientific Computing, Uppsala University

[82] Friedrich H and Nagy G 1999 *Commun. Math. Phys.* **201** 619–655

[83] Kreiss H O and Winicour J 2006 *Class. Quantum Grav.* **23** S405–S420 (*Preprint* `gr-qc/0602051`)

[84] Buchman L T and Sarbach O C A 2006 *Class. Quantum Grav.* **23** 6709–6744 (*Preprint* `gr-qc/0608051`)

[85] Rinne O 2006 *Class. Quantum Grav.* **23** 6275–6300 (*Preprint* `gr-qc/0606053`)

[86] Alcubierre M *et al.* 2001 *Int. J. Mod. Phys. D* **10**(3) 273–289 (*Preprint* `gr-qc/9908012`) URL `http://ejournals.worldscientific.com.sg/ijmpd/10/1003/S0218271801000834`

[87] Pollney D *et al.* 2007 *Phys. Rev.* **D76** 124002 (*Preprint* `gr-qc/0707.2559`)

[88] Husa S *et al.* 2008 *Phys. Rev.* **D77** 044037 (*Preprint* `0706.0904`)

[89] Allen G, Goodale T, Massó J, and Seidel E 1999 in *Proceedings of Eighth IEEE International Symposium on High Performance Distributed Computing, HPDC-8, Redondo Beach, 1999* (IEEE Press)

[90] Goodale T *et al.* 2003 in *Vector and Parallel Processing – VECPAR'2002, 5th International Conference, Lecture Notes in Computer Science* (Berlin: Springer)

[91] Toolkit C C `http://www.cactuscode.org`

[92] Mesh Refinement with Carpet URL `http://www.carpetcode.org/`

[93] Schnetter E, Hawley S H, and Hawke I 2004 *Class. Quantum Grav.* **21**(6) 1465–1488 (*Preprint* `gr-qc/0310042`)

[94] York J W 1979 in L L Smarr, ed, *Sources of gravitational radiation* (Cambridge, UK: Cambridge University Press) pp 83–126 ISBN 0-521-22778-X

[95] Alcubierre M *et al.* 2000 *Phys. Rev. D* **62** 044034 (*Preprint* `gr-qc/0003071`)

[96] Berger M J and Oliger J 1984 *J. Comput. Phys.* **53** 484–512

[97] Babiuc M C, Kreiss H O, and Winicour J 2007 *Phys. Rev.* **D75** 044002 (*Preprint* `gr-qc/0612051`)

[98] Mattsson K 2003 *J. Sci. Comput.* **18** 133–153

[99] Mattsson K and Nordström J 2004 *J. Comput. Phys.* **199**(2) 503–540

[100] Nordström J, Mattsson K, and Swanson C 2007 *J. Comput. Phys.* **225**(1) 874–890 ISSN 0021-9991

[101] Kreiss H O and Scherer G 1974 in C D Boor, ed, *Mathematical Aspects of Finite Elements in Partial Differential Equations* (New York: Academica Press)

[102] Strand B 1994 *J. Comput. Phys.* **110** 47

[103] Carpenter M, Nordström J, and Gottlieb D 1999 *J. Comput. Phys.* **148**(2) 341

[104] Babiuc M C, Szilágyi B, and Winicour J 2006 *Phys. Rev. D* **73** 064017 (*Preprint* `gr-qc/0601039`)

[105] Calabrese G *et al.* 2003 *Commun. Math. Phys.* **240** 377–395 (*Preprint* `gr-qc/0209017`)

[106] Calabrese G *et al.* 2003 *Class. Quantum Grav.* **20** L245–L252 (*Preprint* `gr-qc/0302072`)

[107] Seiler J, Szilagyi B, Pollney D, and Rezzolla L 2008 *Class. Quantum Grav.* **25** 175020 (*Preprint* `0802.3341`)

[108] Carpenter M, Gottlieb D, and Abarbanel S 1994 *J. Comput. Phys.* **111** 220–236

[109] Calabrese G and Gundlach C 2006 *Class. Quantum Grav.* **23** S343–S368 (*Preprint* `gr-qc/0509119`)

[110] Teukolsky S A 1982 *Phys. Rev. D* **26** 745–750

[111] Rinne O, Lindblom L, and Scheel M A 2007 *Class. Quantum Grav.* **24**(16) 4053–4078 (*Preprint* `gr-qc/0711.2084`)

[112] Rezzolla L *et al.* 1998 *Phys. Rev. D* **57** 1084–1091

[113] Abrahams A M *et al.* 1998 *Phys. Rev. Lett.* **80** 1812–1815 (*Preprint* `gr-qc/9709082`)

[114] Rezzolla L *et al.* 1999 *Phys. Rev. D* **59** 064001 (*Preprint* `gr-qc/9807047`)

[115] Eppley K R 1979 in L Smarr, ed, *Sources of gravitational radiation* (Cambridge, England: Cambridge University Press) p 275

[116] Brill D S 1959 *Ann. Phys. (N. Y.)* **7** 466–483

[117] Eppley K R 1977 *Phys. Rev. D* **16**(6) 1609–1614

[118] Holz D, Miller W, Wakano M, and Wheeler J 1993 in B L Hu and T A Jacobson, eds, *Directions in General Relativity: Proceedings of the 1993 International Symposium, Maryland; Papers in honor of Dieter Brill* (Cambridge, England: Cambridge University Press) p 339

[119] Alcubierre M *et al.* 2000 *Phys. Rev. D* **61** 041501 (R) (*Preprint* `gr-qc/9904013`)

[120] Pazos E *et al.* 2007 *Class. Quantum Grav.* **24**(12) S341–S368 (*Preprint* `gr-qc/0612149`)

[121] Alcubierre M *et al.* 2004 *Class. Quantum Grav.* **21** 589 (*Preprint* `gr-qc/0305023`)

[122] Szilágyi B, Gomez R, Bishop N T, and Winicour J 2000 *Phys. Rev. D* **62** 104006 (*Preprint* `gr-qc/9912030`)

[123] Apples With Apples: Numerical Relativity Comparisons and Tests URL `http://www.ApplesWithApples.org/`

[124] Szilágyi B, Schmidt B, and Winicour J 2002 *Phys. Rev. D* **65** 064015 (*Preprint* `gr-qc/0106026`)

[125] Calabrese G, Hinder I, and Husa S 2006 *J. Comput. Phys.* **218**(2) 607–634 ISSN 0021-9991 (*Preprint* `gr-qc/0503056`)

[126] Babiuc M C, Szilagyi B, and Winicour J 2006 *Class. Quant. Grav.* **23** S319–S342 (*Preprint* `gr-qc/0511154`)

[127] Beyer H and Sarbach O 2004 *Phys. Rev. D* **70** 104004 (*Preprint* `gr-qc/0406003`)

[128] Nagy G and Sarbach O 2006 *Classical and Quantum Gravity* **23** S477 (*Preprint* `gr-qc/0601124`)

[129] Reula O and Sarbach O 2005 *J. Hyperbol. Diff. Eq* **397** (*Preprint* `gr-qc/0409027`)

[130] Alcubierre M *et al.* 2000 *Phys. Rev. D* **62** 124011 (*Preprint* `gr-qc/9908079`)

[131] Buchman L T and Sarbach O C A 2007 *Class. Quantum Grav.* **24** S307–S326 (*Preprint* `gr-qc/0703129`)

[132] Baker J G *et al.* 2006 *Phys. Rev. Lett.* **96** 111102 (*Preprint* `gr-qc/0511103`)

[133] Pretorius F 2006 *Class. Quantum Grav.* **23** S529–S552 (*Preprint* `gr-qc/0602115`)

[134] Campanelli M, Lousto C O, and Zlochower Y 2006 *Phys. Rev. D* **73** 061501(R) (*Preprint* `gr-qc/0601091`)

[135] Baker J G *et al.* 2007 *Phys. Rev.* **D75** 124024 (*Preprint* `gr-qc/0612117`)

[136] Baker J G *et al.* 2006 *Astrophys. J.* **653** L93–L96 (*Preprint* `astro-ph/0603204`)

[137] Baiotti L and Rezzolla L 2006 *Phys. Rev. Lett.* **97** 141101 (*Preprint* `gr-qc/0608113`)

[138] Diener P *et al.* 2006 *Phys. Rev. Lett.* **96**(12) 121101 (*Preprint* `gr-qc/0512108`)

[139] Gonzalez J A *et al.* 2007 *Phys. Rev. Lett.* **98** 091101 (*Preprint* `gr-qc/0610154`)

[140] Campanelli M, Lousto C O, and Zlochower Y 2006 *Phys. Rev. D* **74** 041501 (*Preprint* `gr-qc/0604012`)

[141] Campanelli M *et al.* 2007 *Phys. Rev.* **D75** 064030 (*Preprint* `gr-qc/0612076`)

[142] Baker J G, Campanelli M, Pretorius F, and Zlochower Y 2007 *Class. Quant. Grav.* **24** S25–S31 (*Preprint* `gr-qc/0701016`)

[143] Thornburg J *et al.* 2007 *Class. Quantum Grav.* **24** 3911 (*Preprint* `gr-qc/0701038`)

[144] Peres A 1962 *Phys. Rev.* **128** 2471–2475

[145] Bekenstein J D 1973 *Phys. Rev.* **D7** 949–953

[146] Fitchett M J 1983 *Mon. Not. R. astr. Soc.* **203** 1049

[147] Fitchett M J and Detweiler S 1984 *Mon. Not. R. astr. Soc.* **211** 933–942

[148] Favata M, Hughes S A, and Holz D E 2004 *Astrophys. J.* **607** L5–L8 (*Preprint* `astro-ph/0402056`)

[149] Peters P C 1964 *Phys. Rev.* **136** B1224–B1232

[150] Hinder I *et al.* 2008 *Phys. Rev.* **D77** 081502 (*Preprint* `0710.5167`)

[151] Hughes S A and Blandford R D 2003 *Astrophys. J.* **585** L101–L104

[152] Buonanno A, Chen Y, and Damour T 2006 *Phys. Rev. D* **74**(10) 104005

[153] Bruegmann B *et al.* 2008 *Phys. Rev.* **D77** 124047 (*Preprint* `0707.0135`)

[154] Rezzolla L *et al.* 2007 *ArXiv e-prints* **712** (*Preprint* `0712.3541`)

[155] Koppitz M *et al.* 2007 *Phys. Rev. Lett.* **99** 041102 (*Preprint* `gr-qc/0701163`)

[156] Herrmann F, Shoemaker D, and Laguna P 2006 (*Preprint* `gr-qc/0601026`)

[157] Herrmann F *et al.* 2007 *Astrophys. J.* **661** 430–436 (*Preprint* `gr-qc/0701143`)

[158] Campanelli M, Lousto C O, Zlochower Y, and Merritt D 2007 *Astrophys. J.* **659** L5–L8 (*Preprint* `gr-qc/0701164`)

[159] Gonzalez J A *et al.* 2007 *Phys. Rev. Lett.* **98** 231101 (*Preprint* `gr-qc/0702052`)

[160] Campanelli M, Lousto C O, Zlochower Y, and Merritt D 2007 *Phys. Rev. Lett.* **98** 231102 (*Preprint* `gr-qc/0702133`)

[161] Misner C W, Thorne K S, and Wheeler J A 1973 *Gravitation* (San Francisco: W. H. Freeman)

[162] Thornburg J 1996 *Phys. Rev. D* **54**(8) 4899–4918 (*Preprint* `gr-qc/9508014`)

[163] Smarr L L 1973 *Phys. Rev. Lett.* **30** 71

[164] Christodoulou D 1970 *Phys. Rev. Lett.* **25**(22) 1596–1597

[165] Cook G B 1994 *Phys. Rev. D* **50**(8) 5025–5032

[166] Pfeiffer H P, Teukolsky S A, and Cook G B 2000 *Phys. Rev. D* **62** 104018 (*Preprint* `gr-qc/0006084`)

[167] Cook G B 2000 *Living Rev. Relativity* **3** 5 URL `http://www.livingreviews.org/lrr-2000-5`

[168] Damour T and Gopakumar A 2006 *Phys. Rev. D* **73** 124006 (*Preprint* `gr-qc/0602117`)

[169] Merritt D and Ekers R D 2002 *Science* **297** 1310–1313 (*Preprint* `astro-ph/0208001`)

[170] Merritt D *et al.* 2004 *Astrophys. J.* **607** L9–L12 (*Preprint* `astro-ph/0402057`)

[171] Redmount I H and Rees M J 1989 *Comments on Astrophysics* **14** 165–+

[172] Kidder L E 1995 *Phys. Rev. D* **52** 821–847 (*Preprint* `gr-qc/9506022`)

[173] Baker J G *et al.* 2007 *Astrophys. J.* **668** 1140–1144 (*Preprint* `astro-ph/0702390`)

[174] Schnittman J D and Buonanno A 2007 (*Preprint* `astro-ph/0702641`)

[175] Gunnarsen L, Shinkai H, and Maeda K 1995 *Class. Quantum Grav.* **12** 133–140 (*Preprint* `gr-qc/9406003`)

[176] Lehner L and Moreschi O M 2007 *Phys. Rev.* **D76** 124040 (*Preprint* `0706.1319`)

[177] Campanelli M and Lousto C O 1999 *Phys. Rev. D* **59** 124022 (*Preprint* `gr-qc/9811019`)

[178] Allen G, Camarda K, and Seidel E 1998 3D black hole spectroscopy: Determining waveforms from 3D excited black holes gr-qc/9806036

[179] Rupright M E, Abrahams A M, and Rezzolla L 1998 *Phys. Rev. D* **58** 044005

[180] Camarda K and Seidel E 1999 *Phys. Rev. D* **59** 064019 (*Preprint* `gr-qc/9805099`)

[181] Abrahams A M and Price R H 1996 *Phys. Rev. D* **53** 1963

[182] Nagar A and Rezzolla L 2005 *Class. Quantum Grav.* **22**(16) R167–R192 erratum-ibid. **23**, 4297, (2006)

[183] Baker J *et al.* 2000 *Phys. Rev. D* **62** 127701 gr-qc/9911017

[184] Font J A *et al.* 2002 *Phys. Rev. D* **65** 084024 (*Preprint* `gr-qc/0110047`)

[185] Thorne K 1980 *Rev. Mod. Phys.* **52**(2) 299

[186] Dreyer O, Krishnan B, Shoemaker D, and Schnetter E 2003 *Phys. Rev. D* **67** 024018 (*Preprint* `gr-qc/0206008`)

[187] Ashtekar A and Krishnan B 2003 *Phys. Rev. D* **68** 104030 (*Preprint* `gr-qc/0308033`)

[188] Schnetter E, Krishnan B, and Beyer F 2006 *Phys. Rev. D* **74** 024028 (*Preprint* `gr-qc/0604015`)

[189] Alcubierre M *et al.* 2005 *Phys. Rev. D* **72**(4) 044004 (*Preprint* `gr-qc/0411149`)

[190] Seidel E 1999 *Prog. Theor. Phys. Suppl.* **136** 87–106 URL `http://ptp.ipap.jp/link?PTPS/136/87/`

[191] Brandt S and Seidel E 1995 *Phys. Rev. D* **52**(2) 870–886 URL `http://link.aps.org/abstract/PRD/v52/p870`

[192] Poisson E 2004 *Phys. Rev.* **D70** 084044 (*Preprint* `gr-qc/0407050`)

[193] Martel K and Poisson E 2005 *Phys. Rev.* **D71** 104003 (*Preprint* `gr-qc/0502028`)

[194] Kupi G, Amaro-Seoane P, and Spurzem R 2006 *Mon. Not. R. Astron. Soc.* **371** L45–L49 (*Preprint* `astro-ph/0602125`)

[195] Cunningham C T, Price R H, and Moncrief V 1978 *Astrophys. J.* **224** 643

[196] Cunningham C, Price R, and Moncrief V 1979 *Astrophys. J.* **230** 870–892

[197] Boyle L, Kesden M, and Nissanke S 2008 *Phys. Rev. Lett.* **100** 151101 (*Preprint* `0709.0299`)

[198] Damour T 2001 *Phys. Rev. D* **64** 124013 (*Preprint* `gr-qc/0103018`)

[199] Buonanno A and Damour T 2000 *Phys. Rev.* **D62** 064015 (*Preprint* `gr-qc/0001013`)

[200] Damour T and Nagar A 2008 *Phys. Rev.* **D77** 024043 (*Preprint* `0711.2628`)

[201] Grandclement P *et al.* 2004 *Phys. Rev. D* **69** 102002 (*Preprint* `gr-qc/0312084`)

[202] Kalogera V 2004 *Pramana* **63** 673–+

[203] Bogdanovic T, Reynolds C S, and Miller M C 2007 (*Preprint* `astro-ph/0703054`)

[204] Barker B and O'Connell R 1970 *Phys. Rev. D* **2** 1428

[205] Jasiulek M and et al 2007 *in preparation*

[206] Damour T *et al.* 2008 *Phys. Rev.* **D77** 084017 (*Preprint* `0712.3003`)

[207] Reisswig C *et al.* 2009 (*Preprint* `0907.0462`)

[208] Ajith P *et al.* 2009 (*Preprint* `0909.2867`)

[209] Ajith P *et al.* 2007 *Class. Quant. Grav.* **24** S689–S700 (*Preprint* `arXiv:0704.3764[gr-qc]`)

[210] Aylott B *et al.* 2009 *Class. Quantum Grav.* **26** 165008 (*Preprint* `0901.4399`)

[211] Farr B, Fairhurst S, and Sathyaprakash B S 2009 *Class. Quantum Grav.* **26** 114009 (*Preprint* `0902.0307`)

[212] Santamaria L, Krishnan B, and Whelan J T 2009 *Class. Quantum Grav.* **26** 114010 (*Preprint* `0901.4696`)

[213] Babak S, Hannam M, Husa S, and Schutz B F 2008 (*Preprint* `0806.1591`)

[214] Barausse E and Rezzolla L 2009 *Astrophys. J. Lett.* **704** L40–L44 (*Preprint* `0904.2577`)

[215] Abbott B *et al.* (LIGO Scientific) 2009 *Rept. Prog. Phys.* **72** 076901 (*Preprint* `0711.3041`)

[216] Waldman S and (for the LIGO Science Collaboration) 2006 *Class. Quantum Grav. 23 (2006) S653 – S660*

[217] Adhikari R, Fritschel P, and Waldman S 2006 Enhanced ligo Tech. Rep. LIGO-T060156-01-I LIGO Scientific Collaboration

[218] Advanced LIGO `http://www.ligo.caltech.edu/advLIGO/`

[219] Acernese F *et al.* 2006 *Class. Quantum Grav.* **23** S635–S642

[220] Advanced Virgo Preliminary Design, Virgo internal report VIR-089A-08 (2008)

[221] Danzmann K *et al.* 1998 *Max-Planck-Inistitut für Quantenoptik, Report MPQ* **233** 184–209

[222] Danzmann K and Rüdiger A 2003 *Class. Quantum Grav.* **20** S1–S9 URL `stacks.iop.org/CQG/20/S2`

[223] Beig R and Murchadha N O 1994 *Class. Quantum Grav.* **11** 419–430 (*Preprint* `gr-qc/9304034`)

[224] Dain S and Friedrich H 2001 *Commun. Math. Phys.* **222** 569–609 (*Preprint* `gr-qc/0102047`)

[225] Hannam M *et al.* 2008 *Phys. Rev. D* **78** 104007

[226] Damour T, Jaranowski P, and Schaefer G 2001 *Phys. Lett.* **B513** 147–155 (*Preprint* `gr-qc/0105038`)

[227] Blanchet L, Faye G, Iyer B R, and Joguet B 2002 *Phys. Rev.* **D65** 061501 (*Preprint* `gr-qc/0105099`)

[228] Blanchet L, Damour T, Esposito-Farese G, and Iyer B R 2004 *Phys. Rev. Lett.* **93** 091101 (*Preprint* `gr-qc/0406012`)

[229] Poisson E 1998 *Phys. Rev.* **D57** 5287–5290 (*Preprint* `gr-qc/9709032`)

[230] Alvi K 2001 *Phys. Rev.* **D64** 104020 (*Preprint* `gr-qc/0107080`)

[231] Blanchet L, Buonanno A, and Faye G 2006 *Phys. Rev.* **D74** 104034 (*Preprint* `gr-qc/0605140`)

[232] Faye G, Blanchet L, and Buonanno A 2006 *Phys. Rev.* **D74** 104033 (*Preprint* `gr-qc/0605139`)

[233] Boyle M *et al.* 2007 *Phys. Rev.* **D76** 124038 (*Preprint* `0710.0158`)

[234] Blanchet L *et al.* 2008 *Class. Quantum Grav.* **25** 165003

[235] Flanagan E E and Hughes S 1998 *Phys. Rev. D* **57** 4535

[236] Damour T, Iyer B R, and Sathyaprakash B S 1998 *Phys. Rev. D* **57** 885–907 (*Preprint* `gr-qc/9708034`)

[237] Vaishnav B, Hinder I, Herrmann F, and Shoemaker D 2007 *Phys. Rev.* **D76** 084020 (*Preprint* `0705.3829`)

[238] Abbott B *et al.* (LIGO Scientific) 2006 *Phys. Rev.* **D73** 102002 (*Preprint* `gr-qc/0512078`)

[239] Hannam M *et al.* 2009 *Phys. Rev.* **D79** 084025 (*Preprint* `0901.2437`)

[240] Reisswig C, Bishop N T, Pollney D, and Szilagyi B 2009 (*Preprint* `0907.2637`)

[241] Bode N and Phinney S 2007 *APS Meeting Abstracts* pp 1010–+

[242] Megevand M *et al.* 2009 *Phys. Rev.* **D80** 024012 (*Preprint* `0905.3390`)

[243] Ajith P and Bose S 2009 *Phys. Rev. D* **79** 084032

[244] Damour T and Nagar A 2009 *Phys. Rev.* **D79** 081503 (*Preprint* `0902.0136`)

[245] Robinson C 2009 Talk given at Amaldi Meeting, New York.

[246] Pankow C *et al.* 2009 *Class. Quantum Grav.* **26** 204004 (*Preprint* `0905.3120`)

[247] Sesana A *et al.* 2009 *Astrophys. J.* **698** L129–L132 (*Preprint* `0903.4177`)

[248] Volonteri M, Madau P, Quataert E, and Rees M J 2005 *Astrophys. J.* **620** 69–77 (*Preprint* `astro-ph/0410342`)

[249] Gammie C F, Shapiro S L, and McKinney J C 2004 *Astrophys. J.* **602** 312–319 (*Preprint* `astro-ph/0310886`)

[250] Shapiro S L 2005 *Astrophys. J.* **620** 59

[251] Arun K G *et al.* 2009 *Phys. Rev. D* **79** 104023

[252] Husa S *et al.* 2008 *Class. Quantum Grav.* **25** 105006

[253] Brügmann B *et al.* 2008 *Phys. Rev. D* **77** 124047

[254] Damour T *et al.* 2001 *Phys. Rev. D* **63** 044023

[255] Apostolatos T A 1996 *Phys. Rev. D* **54**(4) 2421–2437

[256] Apostolatos T A 1995 *Phys. Rev. D* **52** 605–620

[257] Owen B J 1996 *Phys. Rev. D* **53** 6749–6761 (*Preprint* `gr-qc/9511032`)

[258] Bardeen J M *et al.* 1972 *ApJ* **178** 347–370

[259] Tagoshi H *et al.* 1996 *Phys. Rev. D* **54** 1439–1459

[260] Echeverria F 1989 *Phys. Rev. D* **40**(10) 3194–3203

[261] Abbott B *et al.* (LIGO Scientific) 2004 *Nucl. Instrum. Meth.* **A517** 154–179 (*Preprint* `gr-qc/0308043`)

[262] Sathyaprakash B and Schutz B F 2009 *Liv. Rev. Relativity* **12**(2) URL `http://www.livingreviews.org/lrr-2009-2`

[263] Babak S *et al.* 2008 *Class. Quantum Grav.* **25** 184026 (*Preprint* `0806.2110`)

[264] `http://www.tapir.caltech.edu/dokuwiki/lisape:home`

Curriculum Vitae

Personal

Date of Birth: May 5th, 1983
Place of Birth: Washington DC, United States
Citizenship: United States
Marital Status: Unmarried
First Language: English

Education

Albert Einstein Institute	*Ph.D. in Astrophysical Relativity*
Potsdam, Germany	Sept. 2005 - Jan. 2010
Adviser:	Bernard Schutz
University Affiliation:	Gottfried Wilhelm Leibniz Universität Hannover via the International Max Plank Research School (IMPRS)
Cornell University	*B.A. Physics*
Ithaca, NY	Aug 2001 - May 2005
Adviser:	Saul Teukolsky
Research Emphasis:	Computational Physics; Numerical Relativity
Hayfield Secondary School	*H.S. Honors A.P.*
Alexandria, VA	Sept 1997 - June 2001
Research Emphasis:	Physics; Architecture; Computer Science

Fellowships, Grants, and Awards

James Hartle Award: talk *Constraint Preserving Boundaries in 2nd Order Form*
NASA NY Space Grant 2003: For work under Saul Teukolsky on *DUSTVis*
Fermi National Accelerator Lab Internships for Physics Majors 2002:
BTeV Trigger Algorithm
US DoD's SEAP (Science and Engineering Apprenticeship Program) 2001
Award of Recognition of Outstanding Achievement, US Naval Research Laboratory
Recognition from Nat. Science Teachers Association
(for *Longitudinal Flow in Au-Au Collisions*)
Recognition from Graduate Women in Science (for *Acoustic Thermometry of Sea Water*)
Intel Science Talent Search Semifinalist 2001 (for *Longitudinal Flow in Au-Au Collisions*)
University of Southern California Young Scientist of the Year 2000
CIA Outstanding Young Scientist (for *Acoustic Thermometry of Sea Water*)
Armed Forces and Communications and Electronics scholarship and internship

Award of Recognition: the Society of Women Engineers (*Acoustic Thermometry of Sea Water*)
Intel Virginia State Science Talent Search 2nd (*Longitudinal Flow in Au-Au Collisions*)
Grand Prize alternate in the NOVA Intel Science and Engineering Fair
Physlink.com Young Scientist of the Year 2000 (for *Acoustic Thermometry of Sea Water*)

Research Experience

July 2005 - Present: I worked on numerical simulations of black hole spacetimes. My work was mostly with a code which uses a Generalized Harmonic formulation of the Einstein Equations. My focus was on well-posed constraint preserving boundary conditions. With additional work on constraint damping methods, and the use of Pade extrapolation for Apparent Horizon excision boundaries.

Dr. Bela Szilagyi: Bela.Szilagyi@aei.mpg.de

June 2004 - August 2004: I was a visitor to the Max-Planck-Institute for Gravitational Physics in Potsdam, Germany. Using an open-source toolbox in an environment called Cactus, I wrote a numerical code to simulate the propagation of gravitational waves off a potential in a three dimensional coordinate system. I wrote a generalization of the Zerilli Equation that reduced the problem to a radial equation expanded to three dimensions with spherical harmonics.

Dr. Denis Pollney: Denis.Pollney@aei.mpg.de

November 2002 - October 2004: I worked for Prof. Saul Teukolsky on software for the visualization of numerical simulations of relevant solutions to the Einstein equations. These included inspiraling neutron stars toward super-massive black holes, interacting black holes. Called DUSTVis, it is a OpenDX visualization program designed to be used with the Caltech/Cornell DUST algorithm. It is used to patch domains together visualize and reasonably interpolate them. We also worked on software for the visualization of warped neutron star accretion disks.

Prof. Saul Teukolsky: Saul@astro.cornell.edu

May 2002-August 2002: I participated in Fermi National Accelerator Laboratory's Internship for Physics Majors Program (IPM). I worked under supervisor Jin-yuan Wu on a project called BTeV. BTeV will be looking for rare B-meson and charm decays, trying to find a value for sine 2-beta and better understand rare decays. I coded parts of the tracking algorithm for the Level 1 Trigger Code. This code finds hits on the silicon pixel detectors in the central event region of the detector and tries to match them to tracks, find the location of primary events, and looks for detached tracks which may signify an interesting decay.

Dr. Jin yuan Wu: jywu168@fnal.gov

June 2001 - Sept. 2001: I worked at the Naval Research Laboratory in the Electronics Science & Technology Division on the optimization of natural growth of Silicon dioxide, SiGe, and SiC samples via Molecular Beam Epitaxy. I also experimented with the temperature and surface segregation dependencies of Phosphorous doping rates via MBE. During my time at the NRL I gained experience with XPS, SIMS, STMs, MBE, and SEMs. I also helped to update their old XPS data acquisition system by monitoring the GPIB communication between the XPS system, the Channeltron, and the server.

Dr. Philip Thompson: thompson@nrl.navy.mil
Dr. Glenn Jernigan: glenn.jernigan@nrl.navy.mil

May 2000 - August 2000: I worked in the National Superconducting Cyclotron at Michigan State University. I wrote data analysis code in C++ and did the analysis of data collected of Au on Au collisions at energies from 20-60 AMeV. I did analysis of the longitudinal flow in these collisions to work towards a nuclear equation of state to work towards better understanding of flow through in stellar core collapses.

Dr. Gary Westfall: westfall@nscl.msu.edu

Contributed Talks

"Final Spin from Binary Black Hole Coalescence"
Salamanca, Spain September 19, 2008
XXXI Spanish Relativity Meeting (E.R.E. 2008)

"From General Relativity to Black Hole Observation"
Salamanca, Spain September 19, 2008
XXXI Spanish Relativity Meeting (E.R.E. 2008) (plenary talk)

"Final Spin from Binary Black Hole Coalescence"
California Institute of Technology, Pasadena, CA, USA August 22, 2008
TAPIR Theoretical Astrophysics and Relativity Seminar

"2nd Order in Space Constraint Preserving Summation by Parts Boundaries"
Puerto de la Cruz, Tenerife, Spain September 10-14, 2007
XXX Spanish Relativity Meeting (E.R.E. 2007)

"Constraint Preserving Boundary Treatment in 2nd Order Form"
Sydney, Australia July 8-14, 2007
18th International Conference on General Relativity and Gravitation (GRG18)

"Boundary Treatments for the Einstein Equations in 2nd Order Form"
Palma de Mallorca, Spain September 4-8, 2006
XXIX Spanish Relativity Meeting (E.R.E. 2006)

"Generalised Harmonic Coordinates in 2nd Order "
AEI, Potsdam, Germany November, 2005
Sonder-Forschungsbereich / TransRegio 7 Video Seminars

"Generalised Harmonic Coordinates using Abigel"
Oberjoch, Germany October 10-14, 2005
2005 Oberjoch Seminars

Publications

L. Rezzolla, P. Diener, E. N. Dorband, D. Pollney, C. Reisswig, E. Schnetter, J. Seiler. **The Final Spin From the Coalescence of Aligned-spin Black-hole Binaries**. *Astrophys. J.* **674** *(2008) L29*. Preprint: arXiv.org:0710.3345 [gr-qc]

L. Rezzolla, E. Barausse, E. N. Dorband, D. Pollney, C. Reisswig, J. Seiler, S. Husa. **On the final spin from the coalescence of two black holes**. *Phys. Rev. D* **78** *(2008) 044002*. Preprint: arXiv:0712.3541[gr-qc]

J. Seiler, B. Szilagyi, D. Pollney. **Constraint Preserving Boundaries for a Generalized Harmonic Evolution Systems**. *Class. Quant. Grav.* **25** *(2008) 175020*. Preprint: arXiv:0802.3341 [gr-qc]

B. Aylott, *et al.* (including J. Seiler). **Testing gravitational-wave searches with numerical relativity waveforms: Results from the first Numerical INJection Analysis (NINJA) project**. *Classical and Quantum Gravity* **26**, *(2009) 165008*. Preprint: arXiv:0901.4399 [gr-qc].

B. Aylott, *et al.* (including J. Seiler). **Status of NINJA: the Numerical INJection Analysis project** *Classical and Quantum Gravity* **26**, *114008 (2009) 114008*. Preprint: arXiv:0905.4227[gr-qc]

C. Reisswig, S. Husa, L. Rezzolla, E. Dorband, D. Pollney, J. Seiler. **Gravitational-wave detectability of equal-mass black-hole binaries with aligned spins**. Preprint: arXiv:0907.0462[gr-qc]

P. Ajith, *et al.* (including J. Seiler). **“Complete” gravitational-waveforms for black-hole binaries with non-precessing spins**. Preprint: arXiv:0909.2867 [gr-qc]